LEABHARLANN CHOLÁISTE NA TRÍONÓIDE, BAILE ÁTHA CLIATH | TRINITY COLLEGE LIBRARY DUBLIN
Ollscoil Átha Cliath | The University of Dublin

Terms and Conditions of Use of Digitised Theses from Trinity College Library Dublin

Copyright statement

All material supplied by Trinity College Library is protected by copyright (under the Copyright and Related Rights Act, 2000 as amended) and other relevant Intellectual Property Rights. By accessing and using a Digitised Thesis from Trinity College Library you acknowledge that all Intellectual Property Rights in any Works supplied are the sole and exclusive property of the copyright and/or other IPR holder. Specific copyright holders may not be explicitly identified. Use of materials from other sources within a thesis should not be construed as a claim over them.

A non-exclusive, non-transferable licence is hereby granted to those using or reproducing, in whole or in part, the material for valid purposes, providing the copyright owners are acknowledged using the normal conventions. Where specific permission to use material is required, this is identified and such permission must be sought from the copyright holder or agency cited.

Liability statement

By using a Digitised Thesis, I accept that Trinity College Dublin bears no legal responsibility for the accuracy, legality or comprehensiveness of materials contained within the thesis, and that Trinity College Dublin accepts no liability for indirect, consequential, or incidental, damages or losses arising from use of the thesis for whatever reason. Information located in a thesis may be subject to specific use constraints, details of which may not be explicitly described. It is the responsibility of potential and actual users to be aware of such constraints and to abide by them. By making use of material from a digitised thesis, you accept these copyright and disclaimer provisions. Where it is brought to the attention of Trinity College Library that there may be a breach of copyright or other restraint, it is the policy to withdraw or take down access to a thesis while the issue is being resolved.

Access Agreement

By using a Digitised Thesis from Trinity College Library you are bound by the following Terms & Conditions. Please read them carefully.

I have read and I understand the following statement: All material supplied via a Digitised Thesis from Trinity College Library is protected by copyright and other intellectual property rights, and duplication or sale of all or part of any of a thesis is not permitted, except that material may be duplicated by you for your research use or for educational purposes in electronic or print form providing the copyright owners are acknowledged using the normal conventions. You must obtain permission for any other use. Electronic or print copies may not be offered, whether for sale or otherwise to anyone. This copy has been supplied on the understanding that it is copyright material and that no quotation from the thesis may be published without proper acknowledgement.

Modelling the thermal history of onshore Ireland, Britain and its offshore basins using low-temperature thermochronology

PhD Thesis

2017

Daniel Döpke

TRINITY COLLEGE DUBLIN
08 FEB 2017
ACADEMIC REGISTRY

PhD
NATURAL SCIENCES

Trinity College Dublin
Coláiste na Tríonóide, Baile Átha Cliath
The University of Dublin

50735286
50735286

THESIS
11410

TRINITY LIBRARY
0 8 AUG 2017
DUBLIN

Thesis 11410

Declaration

I declare that this thesis has not been submitted as an exercise for a degree at this or any other university and it is entirely my own work.

I agree to deposit this thesis in the University's open access institutional repository or allow the library to do so on my behalf, subject to Irish Copyright Legislation and Trinity College Library conditions of use and acknowledgement.

Summary

The main goal of this PhD thesis is to investigate the early Cenozoic exhumation history of Ireland and Britain. The causal mechanism for early Cenozoic exhumation on this sector of the NW European margin remains contentious, but broadly can be divided into two main competing hypotheses: i), exhumation caused by mantle-driven processes associated with the development of the proto-Iceland mantle plume and ii), exhumation related to compressional forces associated with the effects of the opening of the North Atlantic Ocean and the Alpine collision.

In this thesis, a combination of apatite fission track (AFT) and apatite (U-Th-Sm)/He (AHe) dating was employed to discriminate between these two hypotheses. Both of these low-temperature thermochronology techniques have the advantage that they can be applied in the absence of strata straddling the time of exhumation. This is the case for the Irish Sea region where onshore Cenozoic rocks are sparse. Sample locations were focused around the Irish Sea region, and extended into Wales, central and western Ireland and Scotland, so that the limits of hypothesised Cenozoic exhumation could be determined. Overall, 47 samples were analysed for AFT and AHe dating, including four pseudo-vertical profiles. The AFT results range from 43.3 ± 5.8 Ma (1σ) on the Isle of Arran (IoA-3) to 353.6 ± 12.1 Ma (1σ) in central Scotland (Sct-6). The AHe ages (1σ, F_T-corrected) range from 5.2 ± 0.4 Ma (Ire-10, a borehole at 1702 m) to 290.9 ± 23.3 Ma in central Scotland (Sct-9).

The key findings of the thermal history modelling reveal that late Permian to mid-Jurassic onshore exhumation in Ireland and Wales shows a clear temporal relationship between exhumation and rifting in the *immediately adjacent* offshore basins, which is related to the complicated break-up of Pangea and the subsequent initiation of rifting in the North Atlantic region. The Scottish massif appears rather unaffected by Pangea break-up and subsequent Mesozoic rifting, with most samples from Scotland generally showing slow cooling during Paleozoic and Mesozoic times.

The magnitude of the early Cenozoic exhumation event in Ireland and Britain is difficult to account for due to small amounts of exhumation involved (<1.5 km).

Thus, a key point in this study is that a combination of both AFT and AHe dating with pseudo-vertical profile analysis is necessary in order to improve resolution of the thermal models. With this combined approach it was possible to sub-divide the early Cenozoic exhumation history of Ireland and Britain into four different zones (colour-coded depending on intensity of the exhumation signal). The red zone is centred on the northern part of the Irish Sea region and experienced 2 to 3 km of early Cenozoic exhumation, assuming a paleogeothermal gradient of 25°C/km. The yellow zone in Wales and western Scotland experienced between 1.5 and 2 km exhumation and the green zone in southeast Ireland and in part of the Northern Highlands of Scotland experienced up to 1 km of exhumation. The white zone in south Wales, central Scotland and west Ireland shows no sign of early Cenozoic exhumation.

The results indicate a clear "dome-like" exhumation pattern centred on the northern part of the Irish Sea region, and more limited exhumation in south Wales and western Scotland. This focused exhumation event is in good agreement with previously published exhumation patterns but is better resolved, and is synchronous with the emplacement of the British Irish Paleogene Igneous Province (BIPIP). Thus, the results suggest that the early Cenozoic exhumation in Ireland and Britain was most likely caused by mantle-driven processes associated with the development of the proto-Iceland mantle plume. An elongate body of hot mantle material likely extended from beneath Greenland to beneath the Irish Sea region, emplacing a magmatic body into or beneath the lower crust corresponding approximately to the present-day limits of the BIPIP. This study identifies the emplacement of this magmatic body as the main cause of early Cenozoic exhumation. It is also possible that a component of the observed early Cenozoic exhumation was caused by dynamically supported uplift and mechanical erosion of the lithosphere.

The AFT and AHe dating systems are not temperature-sensitive enough to resolve the Neogene thermal history, but the presented thermal histories suggest small amounts of Neogene exhumation for Ireland, whereas the Scottish samples tend to show monotonic cooling during the Neogene.

Table of Contents

Summary i

List of Figures vii

List of Tables xii

1. Introduction 1

1.1 Methods employed for assessing exhumation 4

1.2 Rationale for employing low-temperature themochronology and the choice of study area 6

1.3 Far-field stress hypothesis 10

1.4 Mantle plume hypothesis 12

1.5 Comparison between compressional stress and mantle-driven processes 18

2. Regional geological setting and Mesozoic – Cenozoic exhumation of Ireland and Britain 19

2.1 Paleozoic to late Mesozoic tectonic setting 19

2.1.1 Caledonian orogeny: late Cambrian – early to mid Devonian 19

2.1.2 Variscan orogeny: mid-Devonian – Carboniferous 23

2.1.3 Permian – late Cretaceous 26

2.1.4 Late Cretaceous to Paleogene 29

2.2 Mesozoic and Cenozoic rocks onshore Ireland and Britain 29

2.3 Offshore sedimentary basins 32

2.3.1 Western Irish offshore basins 32

2.3.2 Southern Irish and British offshore basins 34

2.3.3 Irish Sea basin system 37

2.3.4 North Sea 38

2.4 Low-temperature thermochronology studies in Ireland and Britain 41

2.4.1 Southern England and the Irish Sea system 41

2.4.2 Scotland 46

2.4.3 Central England, Southern Uplands, Lake District and Pennines 47

2.4.4 Ireland and Northern Ireland 48

2.5 Mantle-driven processes in Ireland and Britain 49

2.6 How do previous studies support the far-field stress/mantle-driven hypotheses? 53

3. Thermochronology 55

3.1 Introduction 55

3.2 Apatite fission track dating 57

3.2.1 Track formation 58

3.2.2 From the general isotope age equation to the fission track age equation 60

3.2.3 External detector method 62

3.2.4 Zeta calibration 65

3.2.5 Apatite fission track age determination via LA-ICP-MS 67

3.2.6 Thermal annealing of fission tracks 70

3.2.7 Measuring track lengths and track length distributions 74

3.2.8 D_{par} 78

3.2.9 Durango apatite as a standard on low-temperature thermochronology 78

3.3 Apatite (Uranium-Thorium-Samarium)/Helium dating 79

3.3.1 ^{4}He production 80

3.3.2 AHe age Calculation 82

3.3.3 He diffusion in apatite 83

3.3.4 ^{4}He partial retention zone (PRZ) 85

3.3.5 Radiation damage 85

3.3.6 α-ejection correction (F_T) 87

3.3.7 ^{4}He implantation 91

3.4 Apatite uranium-lead dating 93

4. Analytical procedures 96

4.1 Mineral separation 96

4.2 AHe dating analytical procedure 100

4.2.1 Crystal selection and packing 100

4.2.2 ^{4}He degassing 103

4.2.3 U, Th and Sm analysis 104

4.3 Apatite fission track analytical procedure 105

4.3.1 AFT sample preparation 106

4.3.2 Track counting and track length measurements 107

4.4 LA-ICP-MS measurements for AFT and apatite U-Pb dating 110

4.4.1 Data reduction for AFT and U-Pb dating 111

5. Sample locations 114

6. Modelling 119

6.1 Introduction to modelling by QTQt 119

6.2 Theoretical basis of the approach 119

6.3 Applying QTQt to thermochronological data 121

6.4 Generating a QTQt modelling file 124

6.5 Applying the QTQt modelling procedure in this study 125

7. Results 127

7.1 Thermal history modelling results 150

7.1.1 Scotland 162

7.1.2 West and Central Ireland 165

7.1.3 South Ireland 168

7.1.4 Isle of Man and Isle of Arran 170

7.1.5 Wales 171

8. Discussion 175

8.1 Caledonian and post-Caledonian exhumation 176

8.2 Carboniferous deposition and Variscan exhumation 180

8.3 Pangea break-up and Mesozoic rifting event 183

8.3.1 South Ireland 183

8.3.2 Central east Ireland 185

8.3.3 West Ireland 186

8.3.4 Wales and Isle of Man 188

8.3.5 Scotland 190

8.3.6 Overall Mesozoic exhumation history 191

8.4 Early Cenozoic exhumation 191

8.4.1 Red zone exhumation *195*
8.4.2 Yellow zone exhumation *198*
8.4.3 Green zone *201*
8.4.4 Non-coloured study area (white zone) *204*
8.5 Neogene cooling 207
8.6 Causes for early Cenozoic exhumation 209
8.6.1 Far-field stress hypothesis *211*
8.6.2 Mantle-driven exhumation *214*
8.7 Early Cenozoic deposition centres 217
9. Conclusions 221
9.1 Paleozoic and Mesozoic exhumation 222
9.2 Early Cenozoic exhumation 223
10. Suggestions for future work 226
11. Acknowledgements 228
12. References 230
13. Appendix 263

List of Figures

Figure 1.1: Reconstruction of the North Atlantic region at ~62 Ma showing compressional stress originating from the opening of the North Atlantic and the Alpine collision (adapted after Nielsen et al. 2007). 3

Figure 1.2: Reconstruction of the North Atlantic region at ~62 Ma showing the lateral extension of the proto-Iceland mantle plume extending into the Irish Sea region (adapted after Nielsen et al. 2007). Proposed elongated tongue adapted after Al-Kindi et al. (2003). 4

Figure 1.3: Map of the offshore basins mentioned in this study adjacent to the British and Irish massifs (adapted after Woodcock and Strachan, 2012). 8

Figure 1.4: Exhumation caused by mantle-driven processes (adapted after Burov and Cloetingh, 2009). 15

Figure 1.5: Comparison of surface topography caused by (a) compressional stress and (b) mantle-driven processes. 18

Figure 2.1: Plate reconstruction of Laurentia, Baltica and Avalonia during the late Cambrian (~500 Ma). The Iapetus Ocean starts to close and an intra-oceanic island arc is colliding with the Laurentian margin. Volcanic arc is shown in green, subduction zones in blue (adapted after Chew and Stillman, 2009). 20

Figure 2.2: Plate reconstruction of Laurentia, Baltica and Avalonia during the late Ordovician (~450 Ma). The Grampian orogenic belt (red) has formed and the Iapetus Ocean between Baltica and Laurentia is closing. Volcanic arc is shown in green, subduction zones in blue (adapted after Chew and Stillman, 2009). 21

Figure 2.3: Plate reconstruction of Laurentia, Baltica and Avalonia during the late Silurian (420 Ma). The Scandian orogenic belt has formed (red) and the final continent – contient collision between Laurentia and Avalonia occurs. Subduction zones are shown in blue (adapted after Chew and Stillman, 2009). 22

Figure 2.4: Map of Ireland and Britain with major Caledonian and Variscan structures depicted. 24

Figure 2.5: Plate reconstruction of Laurentia, Baltica and Gondwana during the early Carboniferous (~356 Ma). The Rheic Ocean starts to close and the supercontinent Pangea starts to form. Red zone represents Variscan orogenic belt (adapted after Scotese and McKerrow, 1990 and Chew and Stillman, 2009). 25

Figure 2.6: Paleogeographic reconstruction of the North Atlantic during A: early Triassic and B: early Jurassic. The growing offshore basins show signs of extension associated with rifting (adapted after Tyrrell et al., 2007) 27

Figure 2.7: Late Jurassic and late Cretaceous rifting in the North Atlantic region (adapted after Peacock et al., 2004). 28

Figure 2.8: Map of Ireland and Britain with the distribution of post-Triassic sedimentary rocks and the British Irish Paleogene Igneous Province (BIPIP). 30

Figure 2.9: Map of the Irish Sea and southern Irish Sea basin systems (adapted after Woodcock and Strachan, 2012). 35

Figure 2.10: Map-based comparison of the denudation estimates from subsidence modelling and apatite fission track data from Jones et al. (2003) with the compiled AFT, VR and compaction data from Hillis et al. (2008). 42

Figure 2.11: Elongate tongue of hot mantle material originating from the proto-Iceland mantle plume beneath Greenland reaching into the Irish Sea system (adapted after Al-Kindi et al., 2003). 52

Figure 3.1: Temperature sensitivities ("closure temperatures") of different radiometric dating methods including the apatite U-Pb, fission track and (U-Th-Sm)/He dating methods used in this study (adapted after Carlson, 2011). 55

Figure 3.2: Temperature sensitivities of the apatite fission track dating (AFT) and apatite (U-Th-Sm)/He dating (AHe) methods. HePRZ: Helium partial retention zone for AHe dating (Wolf et al., 1998). PAZ: Partial annealing zone for AFT dating (Gleadow and Duddy, 1981). 57

Figure 3.3: The ion spike explosion model adapted from Fleischer et al. (1975). Black circles: ^{238}U atoms in the apatite crystal lattice. White circles: other atoms in the apatite crystal lattice. 59

Figure 3.4: Schematic image of a polished and etched apatite crystal. Red line (Region of interest): Area counted for AFT analysis. 60

Figure 3.5: Schematic diagram showing the preparation of an apatite grain for AFT analysis via the external detector method (Hurford and Green, 1982) and the LA-ICP-MS method. 63

Figure 3.6: Apatite grains with 30 µm laser spot. Dotted line shows ablations intervals for calculation of depth-weighted $^{238}U/^{43}Ca$ ratio. 68

Figure 3.7: Schematic diagram showing the annealing behavior of apatite fission tracks with temperature. Above 120°C the fission tracks will completely anneal. Between 120°C and 60°C the fission tracks will partially anneal (PAZ: partial annealing zone) resulting in the tracks shrinking with time. The higher the temperature, the shorter the tracks will become. Below 60°C the tracks are nearly "frozen", which means partially annealed tracks remain short and newly formed tracks essentially keep their initial length. 71

Figure 3.8: Determination of confined track lengths making an angle of >10° to the counting surface. 75

Figure 3.9: Top: Three possible time-temperature paths resulting in three different track length distributions displayed at the bottom of the figure. A: The narrow track length distribution indicates a rapid cooling of the sample through the PAZ. B: A wide distribution indicates slow cooling through the PAZ. C: The bimodal distribution indicates reheating of the sample into the temperature range of the PAZ. The pre-existing length population gets annealed and shortened while a younger track length population forms, recording the recent cooling path. 77

Figure 3.10: A: Schematic diagram of an apatite crystal showing accumulation and ejection of σ-particles. B: Evolution of the alpha retention from the centre of the apatite crystal to its rim. 81

Figure 3.11: Schematic diagram of an apatite crystal showing defects in the crystal lattice caused by the alpha decay of ^{238}U and a zone of a high concentration of these defects causing severe damage to the crystal lattice serving as a "trap" for ^{4}He. 87

Figure 3.12: Schematic diagram of ^{4}He implantation into apatite crystals. A: Implantation of ^{4}He due to an adjacent zircon ("bad neighbourhood"). B: Implantation of ^{4}He due to a zircon inclusion. 91

Figure 4.1: Jaw crusher with tungsten carbide plates used to disaggregate the sample. The fraction <300 µm is processed further. 96

Figure 4.2: Water operated shaking table to separate the light minerals (clay-size) from the heavier minerals. The heavy mineral fraction is then processed further. 97

Figure 4.3: Frantz magnetic separator used to separate the non-magnetic from the magnetic fraction. The non-magnetic fraction is then processed further. 98

Figure 4.4: Schematic diagram of heavy mineral separation in a separation funnel. A: Separation of "light" minerals such as quartz and feldspar from "heavy" minerals like apatite, zircon and pyrite with acetone diluted DIM (~2.8 g/cm^3). B: Separation of apatite and heavier minerals like zircon and pyrite with pure DIM (3.3 g/cm^3). 99

Figure 4.5: Selected apatite grain under normal light for AHe analysis. White dotted line shows the grain boundaries and both terminations (Grain Ire-8 grain a). 101

Figure 4.6: Schematic diagram of apatite grains for (U-Th)/He analysis. A: Grain with two "pyramidal" terminations (2T). B: One "pyramidal" termination (1T) and one broken end. C: Two broken ends (0T). 102

Figure 4.7: Reflected light image of a c-axis parallel apatite grain counted using the software package TrackWorks (Autoscan Systems). 108

Figure 5.1: Map with sample locations across Britain and Ireland. Samples which did not yield any apatite are not included on the map. 115

Figure 7.1: AFT age (Ma) versus F_T-corrected single grain AHe age (Ma) plot of all modelled results. Dashed line is the 1:1 ratio from AFT to Ft-corrected AHe age. Samples below the line have older AHe ages than AFT ages. A: Sample Ire-5 shows consistent older AHe than AFT ages. B: Three out of four AHe grains from sample Br-1 are older than the corresponding AFT age but only one grains is far away (out or error) from the 1:1 ratio. 127

Figure 7.2: Sample elevation (m) versus AFT age (Ma) divided by region for all samples in this study. Sample profiles are separated from their corresponding region. 129

Figure 7.3: Projected MTL (µm) versus AFT age (Ma) plot showing a slight negative correlation between MTL and AFT age. 130

Figure 7.4: Unprojected MTL (µm) versus AFT age (Ma) plot with previously published data from Ireland (empty symbols) and data from this study divided into the different geographical regions. 131

Figure 7.5: Sample elevation (m) versus single grain F_T-corrected AHe age (Ma) divided by region for all samples in this study. Sample profiles are separated from their corresponding region. 136

Figure 7.6: F_T-corrected AHe age (Ma) versus radius (μm) of each modelled single grain per sample used for modelling and divided into regions. 137

Figure 7.7: FT-corrected AHe ages (Ma) versus eU (ppm) of each modelled single grain per sample used for modelling and divided into regions. 137

Figure 7.8: AFT ages (Ma) versus F_T-corrected AHe ages (Ma) revealing five clusters with similar AFT to AHe age relationships. 138

Figure 7.9: AFT ages (Ma) versus F_T-corrected AHe ages (Ma) plot comparing the five clusters revealed by the data and five regional districts (Scotland, south Ireland, west and central east Ireland, Wales and the Isle of Man/Arran). 139

Figure 7.10: Thermal history models and track length distributions for samples Sct-3, Sct-5, Sct-8 and Sct-12 from central Scotland. 151

Figure 7.11: Thermal history models and track length distributions for samples Sct-6, Sct-7 and Sct-9 from central Scotland. 152

Figure 7.12: Thermal history models and track length distributions for samples Sct-10 and Sct-11 from western Scotland and sample An and Pb-1 from Wales. 153

Figure 7.13: Thermal history models and track length distributions for samples Sct-1, Sct-2 and the Isle of Arran in south Scotland. 154

Figure 7.14: Thermal history models and track length distributions for samples Ire-1, Ire-2, Ire-3 and Ire-4 from the west coast of Ireland. 155

Figure 7.15: Thermal history models and track length distributions for samples Ire-8, Ire-9 and Ire-10 from central east Ireland. 156

Figure 7.16: Thermal history models and track length distributions for samples LG-17, LG-18, LG-19 and LG-32 from south Ireland. 157

Figure 7.17: Thermal history models and track length distributions for profile Lugnaquilla (Lu) in south Ireland. 158

Figure 7.18: Thermal history models and track length distributions for samples IoM-1, IoM-2 and IoM-3 from the Isle of Man. 159

Figure 7.19: Thermal history models and track length distributions for profile Snowdonia (Cu) in north Wales. 160

Figure 7.20: Thermal history models and track length distributions for profile Brecon Beacons (Br) in south Wales. 161

Figure 7.21: Summary figure of all *major* cooling events revealed by thermal history modelling divided into regions. Blue: Cooling events. Green: Cooling events from forward modelling. Red: Depositional age. P.: sample profiles. Grey box represents the proposed timeframe for mantle-driven processes during early Paleogene. Cooling events labeled with a question mark are below recorded below 40°C and thus not well constraint. 174

Figure 8.1: Thermal history models from seven samples in Scotland and the Snowdonia (Cu) profile in Wales. Cross-referenced are the thermal models with predictions and TLD, where available. 177

Figure 8.2: Thermal history models from Wales. The constructed forward models for Anglesey (An; green dashed line) and Pembrokeshire (Pb-1; blue dashed line) are compatible with the inverse model from the Snowdonia profile (Cu; red and orange line) profile. Cross-referenced are the thermal models with predictions and TLD, where available. 179

Figure 8.3: Carboniferous reheating in Southern Scotland (Sct-2) and in the Brecon Beacons profile (Br) from south Wales. Cross-referenced are the thermal models with predictions and TLD, where available. 181

Figure 8.4: Thermal history models which show post-Variscan exhumation despite the fact that they lie north of the Variscan front. Cross-referenced are the thermal models with predictions and TLD, where available. 182

Figure 8.5: Onshore exhumation linked with syn-rift sedimentation in the adjacent offshore basins. Arrows show which adjacent offshore basins contain syn-rift sediments of the same age as exhumation is proposed by thermal models. The Paleozoic and Mesozoic exhumation is explained in more detail in chapter 9.1. 184

Figure 8.6: Map of Britain and Ireland with sample location coloured based on their amount of early Cenozoic cooling. 193

Figure 8.7: Proposed early Cenozoic exhumation map of Britain and Ireland with sample locations divided into three coloured zones based on their magnitude of exhumation. Exhumation is derived from modelled cooling events and an assumed paleo-geothermal gradient of 25°C/km. 194

Figure 8.8: AFT (Ma) versus F_T-corrected AHe (Ma) plot divided into zones based on the intensity of early Cenozoic exhumation. The white zone is further divided into Scotland, west Ireland and the Brecon Beacons (Br) profile in Wales, to emphasize that each region (Ireland, Scotland and Wales) contains samples which do not show early Cenozoic exhumation. Ire-7 is considered separately because this sample did not experience early Cenozoic exhumation but thermal relaxation following the emplacement of a nearby Palaeogene dyke. Dashed line: AFT and AHe ages 1:1 ratio. 196

Figure 8.9: Single grain F_T-corrected AHe age (Ma) versus eU (ppm) plot. 202

Figure 8.10: Sample Ire-1 compared to the bulk of the single grain F_T-corrected AHe ages (Ma) versus radius (μm). 204

Figure 8.11: Proposed early Cenozoic exhumation divided into three zones based on magnitude of exhumation compared with results from previous studies. 206

Figure 8.12: Map of Ireland and Britain showing focused early Cenozoic exhumation colour-coded according to the inferred magnitude of the exhumation pulse. The locus of early Cenozoic exhumation is compared with the postulated zone of magmatic underplating as proposed by Al-Kindi et al. (2003) and Tomlinson et al. (2006). 210

List of Tables

Table 3-1: Decay constants for the U-Th-Sm decay systems employed in low-temperature thermochronology (Lederer et al., 1967; Jaffey et al., 1971; Steiger and Jäger, 1977; Friedlander et al., 1981; Wagner and Van den Haute, 1992). 60

Table 3-2: Stopping distances for the alpha decay of ^{238}U, ^{235}U, ^{232}Th and ^{147}Sm (Farley et al., 1996; Ketcham et al., 2011). 88

Table 4-1: Mineral densities for apatite, zircon, pyrite and quartz 98

Table 5-1: Sample locations 116

Table 7-1: Apatite fission track results 132

Table 7-2: AHe age results for the modelled AHe grains. A more detailed table with all analysed grains is provided in the appendix. 140

Table 7-3: Apatite U-Pb age results. 148

Table 8-1: Observed ages and predictions from the inverse and forward model with QTQt from samples Anglesey (An) and Pembrokeshire (Pb-1) in Wales. 179

1. Introduction

This thesis investigates the Mesozoic – Cenozoic exhumation history of Ireland and Britain. This region is one of the classic areas for regional geology, stemming back to the early 19th century when the first geological map of England and Wales was drafted by William Smith in 1815. Since then a vast array of geological studies have been undertaken in Ireland and Britain. These include detailed field mapping along with studies investigating the regional tectonic, igneous and metamorphic histories and the biostratigraphical ages and palaeoenvironmental records of sedimentary successions (e.g. Woodcock and Strachan, 2012). When combined with abundant borehole records and seismic data from the offshore basins provided by the hydrocarbon industry, this makes Ireland and Britain one of the most geologically studied areas in the world. Despite their small geographical area, the geology of Ireland and Britain is extremely diverse, spanning from Archaean in NW Scotland (Lewisian gneiss with Ion microprobe U-Pb zircon ages between 2.85 and ca. 2.75 Ga; Whitehouse et al., 1997) to Quaternary times and comprising a large suite of rock types. A more detailed tectonostratigraphic overview of Ireland and Britain is given in the introduction to Chapter 2, and includes a review of the three Phanerozoic orogenic cycles (the Caledonian orogeny, the Variscan orogeny and the far-field effects of Alpine orogenesis).

The wealth of data from the hydrocarbon industry make Ireland and Britain a superb natural laboratory for exhumation studies. However with the exception of southeast Britain, Palaeozoic and older rocks dominate much of the onshore geology, and as a result geoscientists have had to turn to indirect techniques for the assessment of exhumation to help constrain the Mesozoic and Cenozoic history of the area. Over the past 25 years, the uplift and denudation history of Ireland, Britain and its offshore basins has been intensively investigated (e.g. Lewis et al., 1992; Brodie and White, 1994; White and Lovell, 1997; Allen et al., 2002; Doré et al., 2002; Hillis et al., 2008a; Holford et al., 2010; Cogné et al., 2014).

However despite 25 years of investigation, the Cenozoic exhumation history of Ireland and Britain is still in many ways poorly understood and remains contentious. Cenozoic exhumation controls the morphology of the surface, geological outcrop patterns and drainage systems, and also has important implications for the generation and migration of hydrocarbon resources (Hillis et al., 2008a). The hydrocarbon industry is interested whether possible source rocks have been buried both deeply and long enough to generate hydrocarbons. Furthermore, they want to know if suitable reservoir rocks were already in place and had formed traps before the migration of the hydrocarbons. Thus, reconstruction of the exhumation history can indicate if these conditions were achieved and also if late (e.g. Cenozoic) exhumation could have influenced or breached pre-existing traps.

There are primarily two competing hypothesis describing the Mesozoic – Cenozoic exhumation history in Ireland and Britain. The first hypothesis is related to the effects of the opening of the North Atlantic Ocean and the Alpine collision and is described in more detail in section 1.3. In essence, exhumation associated with far-field stress acting between the North Atlantic spreading centre and the Alpine orogenic belt (Figure 1.1) caused by the build-up of the stress in the plate interior and the release of this stress causes basin inversion and reactivation of old Variscan and Caledonian faults across Ireland and Britain. As stress has to be build up before it is released, the far-field stress hypothesis would result in spatially and temporally variable late Cretaceous – Neogene exhumation (Ziegler et al., 1995; Green et al., 2002; Holford et al., 2005b; Japsen et al., 2007; Hillis et al., 2008a; Holford et al., 2009b).

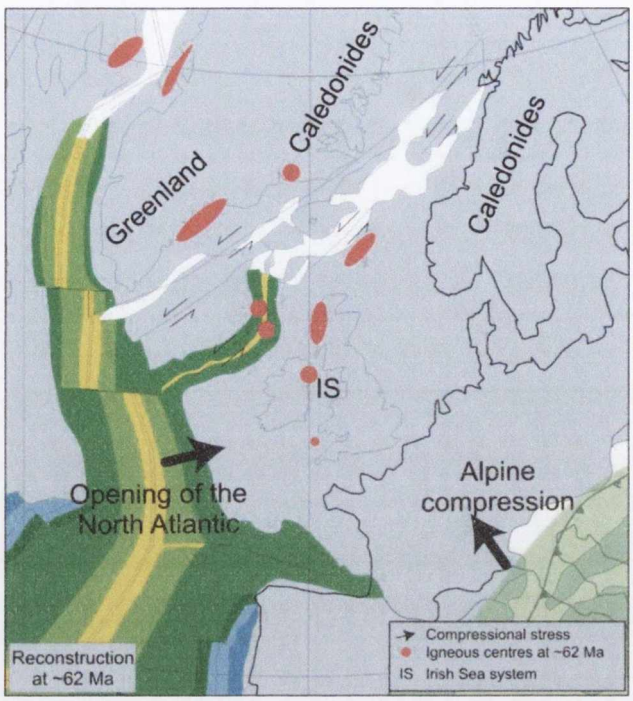


Figure 1.1: Reconstruction of the North Atlantic region at ~62 Ma showing compressional stress originating from the opening of the North Atlantic and the Alpine collision (adapted after Nielsen et al. 2007).

The second hypothesis is based on mantle-driven processes associated with the development of the proto-Iceland mantle plume affecting the Irish Sea region and is described in more detail in section 1.4. The plume is envisaged to have been an elongated tongue of hot mantle material in the asthenosphere (Al-Kindi et al., 2003) extending from beneath Greenland (Figure 1.2) and active during the Paleocene (66.0 – 56.0 Ma[1]) (i.e. White and Lovell, 1997; Jones and White, 2003; Tiley et al., 2004; Persano et al., 2007). The spatial and temporal distribution of exhumation associated with this plume would yield an asymmetric dome-like structure at ~60 Ma centred beneath the Irish Sea region (Al-Kindi et al., 2003; Jones and White, 2003).

[1] The International Chronostratigraphic Chart v2015/01 from the International Commission of Stratigraphy (www.stratigraphy.org) is used throughout this thesis when assigning absolute ages to the geological timescale unless otherwise stated.

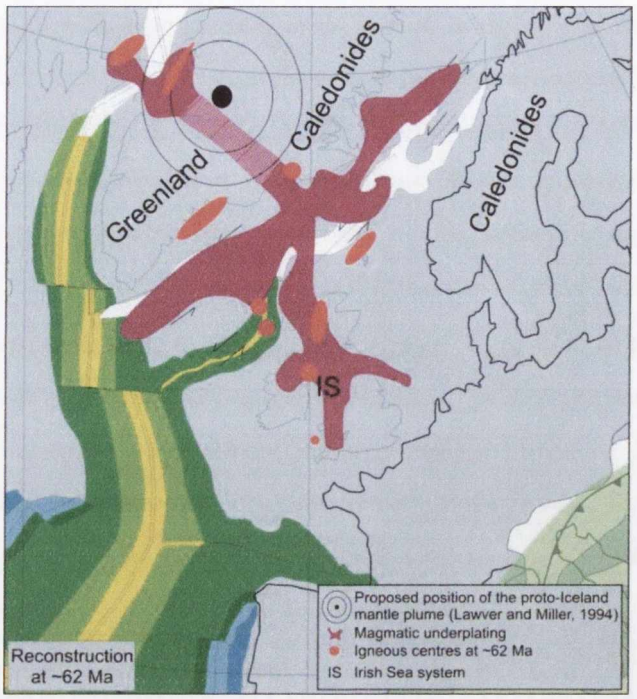


Figure 1.2: Reconstruction of the North Atlantic region at ~62 Ma showing the lateral extension of the proto-Iceland mantle plume extending into the Irish Sea region (adapted after Nielsen et al. 2007). Proposed elongated tongue adapted after Al-Kindi et al. (2003).

The major differences between these two hypotheses are how they predict the spatial patterns and timing of exhumation. Therefore, further investigation of the timing and spatial distribution of Cenozoic exhumation is needed to distinguish between these two competing hypotheses. The goal of this PhD thesis is to resolve the controversy between these two opposing hypotheses by undertaking a regional low-temperature thermochronology study employing apatite fission track (AFT) and apatite (uranium-thorium-samarium)/helium (AHe) dating.

1.1 Methods employed for assessing exhumation

Many different techniques can be used to estimate the timing and magnitude of exhumation (e.g. Corcoran and Doré, 2005). Depending on the area of interest (e.g. onshore or offshore) and the availability of samples or seismic profiles, some methods may be more applicable than others. Commonly used methods can be separated into four different groups, i) tectonic-based techniques (e.g. subsidence modelling), ii) compaction-based techniques (e.g. sonic velocity), iii)

stratigraphic correlations and iv) thermal history-based methods (e.g. vitrinite reflectance and low-temperature thermochronology).

Tectonic-based techniques such as subsidence modelling are intimately associated with the lithospheric stretching and cooling model of McKenzie (1978). This model predicts an initial phase of syn-rift (fault-related) subsidence, which is partially counteracted by the dynamic support of buoyant asthenospheric mantle underneath the thinned lithosphere. As the lithospheric mantle cools and thickens following lithospheric stretching, syn-rift subsidence is followed by an exponentially decreasing phase of post-rift (thermal) subsidence. The difference between the subsidence predicted using the McKenzie (1978) model and the observed tectonic subsidence is indicative of the magnitude and timing of exhumation. However, the stretching and cooling model of McKenzie (1978) is not always applicable. The model is invalid where protracted rifting occurred (such as the St. George's Channel Basin; Welch and Turner, 2000). Furthermore, erosion of syn-rift strata can result in anomalously low estimates of stretching factors which in turn influences the reconstruction of the exhumation history (Corcoran and Doré, 2005).

Compaction studies estimate the reduction in sediment volume (and hence porosity) during burial by employing sonic velocity data (Magara, 1976). The advantages of compaction studies are that sonic velocity data is widely available for offshore basins, and they do not require the collection of rock samples. However, the velocity and porosity are strongly lithology dependent, which can present problems if the investigated section shows no clear relationships between compaction and depth. Furthermore, diagenesis might also have affected the porosity of the studied section, so compaction data have to be evaluated carefully (Corcoran and Doré, 2005).

Stratigraphic correlation methods are based on the correlation of successions (with borehole ties) in seismic sections and the identification of unconformities. This can give some indications as to the magnitude and timing of exhumation events. However, stratigraphic correlations are strongly dependent on the availability of seismic sections and borehole records. It is difficult to estimate

exhumation if entire sequences have been removed from the basin (as in the Irish Sea region, sections 1.2, 2.3.3), as in such cases erosion estimates are likely to be significantly underestimated. Furthermore, stratigraphic units can vary substantially in terms of their depositional thickness, which also makes evaluation of basin-wide erosion estimates difficult (Corcoran and Doré, 2005).

Thermal history-based methods include vitrinite reflectance and low-temperature thermochronology. Vitrinite reflectance (VR) is based on the reflectivity of vitrinite, a coal maceral, under incident light, and is a proxy for thermal maturation (Stach et al., 1982). The degree of alteration (thermal maturation) of the particle is an indication of how deeply the sediment was buried and thus can be used to estimate the paleogeothermal gradient and to make evaluations of exhumation. However, the VR response is dominated by the maximum paleotemperature experienced by the sample, and does not preserve information on thermal events prior to this peak temperature episode. Furthermore, VR needs kerogen concentrates from the time period of interest otherwise it is impossible to provide timing constraints via VR for that time period (Corcoran and Doré, 2005). If such kerogen-bearing sedimentary rocks are absent, low-temperature thermochronological approaches such as apatite fission track dating (AFT) and apatite (uranium-thorium-samarium)/helium dating (AHe) are employed since they do not require samples from the time period of interest (Reiners, 2005). Low-temperature thermochronology provides insights into the thermal history of a region/basin that is not available from the inspection of the remnant rock record. Furthermore, low-temperature thermochronology has the key advantage that it can provide direct estimates on the *timing* of exhumation.

1.2 Rationale for employing low-temperature themochronology and the choice of study area

Many of the methods described above (e.g. subsidence modelling, compaction studies and stratigraphic correlation) are most commonly applied to offshore sedimentary basins (Figure 1.3). They have been widely applied to the hydrocarbon-prospective sedimentary basins around Ireland and Britain

(Japsen, 2000; Green et al., 2001a; Hall and Bishop, 2002; Holford et al., 2009c; Stoker et al., 2010), but exhumation estimates employing these techniques are hindered when the strata straddling the time period of interest (e.g. the late Mesozoic to Cenozoic in this study) are absent. There are only a few Cenozoic outcrops exposed on onshore Ireland and northern Britain (Allen et al., 2002). Although the offshore basins like the Porcupine Basin, Rockall Trough, Celtic Sea Basin and Cardigan Bay Basin (Figure 1.3) provide a more complete stratigraphical record from the Mesozoic to Cenozoic, this is not the case for the Irish Sea Basin system, the postulated locus of uplift caused by the proto-Iceland mantle plume during the Palaeocene (White and Lovell, 1997). In the Irish Sea basin system, the youngest sub-Quaternary rocks are Lower Jurassic siltstones in the Solway Firth and east of the Isle of Man. The lack of Cenozoic and Late Mesozoic rocks in the Irish Sea region indicates a significantly higher amount of Cenozoic exhumation than for the other offshore basins around Britain and Ireland, even compared to the adjacent Cardigan Bay Basin. The lack of onshore Cenozoic rocks around the Irish Sea region means that AFT and AHe dating are required to quantify the timing and spatial distribution of Cenozoic exhumation in this region, as both techniques have the advantage that they can be used in the absence of strata straddling the time of exhumation (Farley, 2002; Corcoran and Doré, 2005; Holford et al., 2005b).

One key criterion for distinguishing between mantle plume versus far-field stress hypotheses as the main cause of Late Mesozoic to Cenozoic exhumation in Ireland and Britain is its spatial distribution. Exhumation associated with magmatic underplating is postulated to have been centred on the Irish Sea region (Jones et al., 2001), whereas the far-field stress hypothesis predicts an irregular spatial distribution of denudation of varying magnitude across Ireland and Britain and their offshore basins (Holford et al., 2005b; Hillis et al., 2008a). Therefore, the focus of the sampling area in this thesis was centred on the Irish Sea region (East Ireland, Isle of Man, Isle of Arran, Southern Scotland and Wales). Furthermore, I reanalysed a subset of samples from a previous apatite fission track thermochronology project in Ireland (Allen et al., 2002) and obtained apatite concentrates from across Scotland provided by F. Stuart at the Scottish Universities Environmental Research Centre (SUERC).

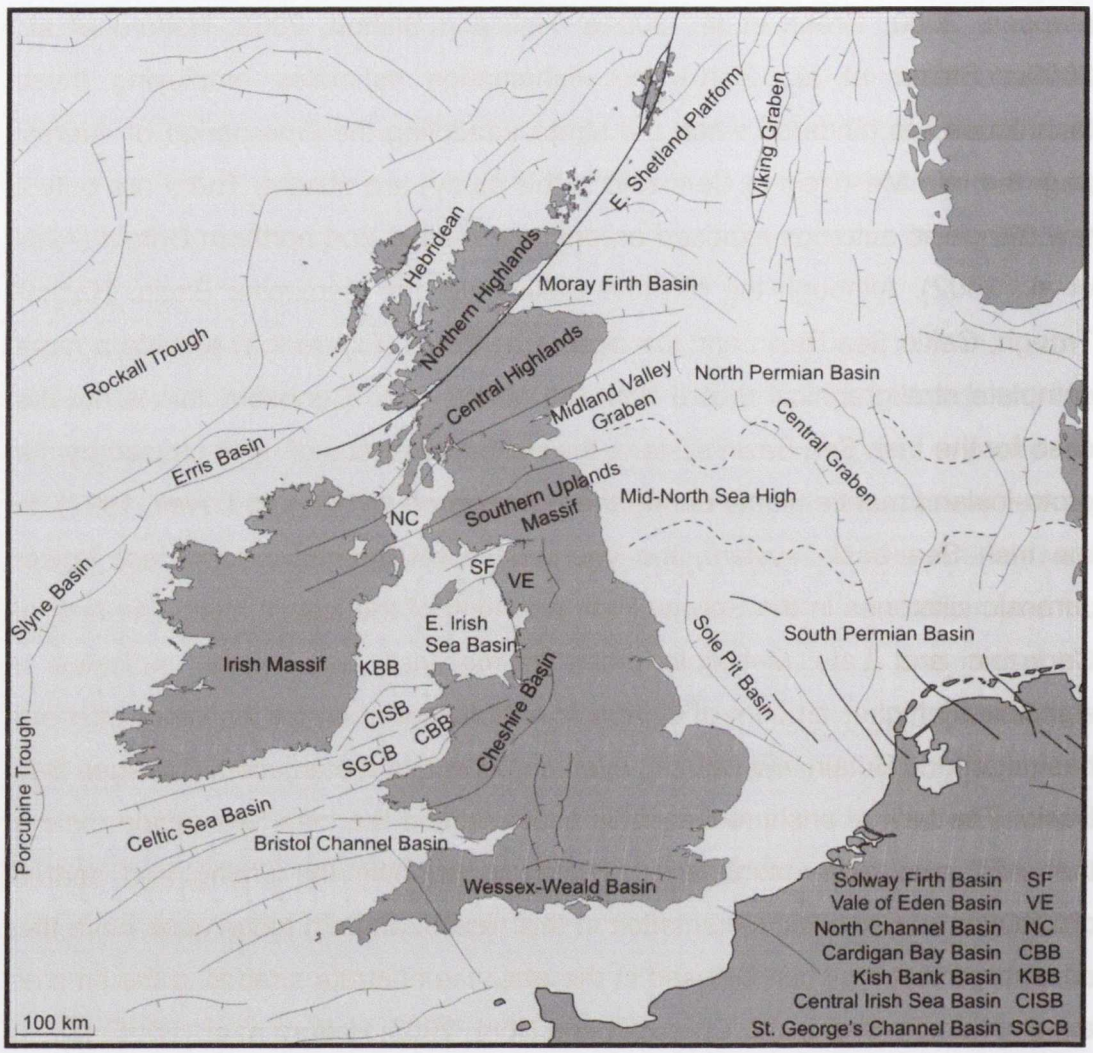


Figure 1.3: Map of the offshore basins mentioned in this study adjacent to the British and Irish massifs (adapted after Woodcock and Strachan, 2012).

Most previous studies investigating the exhumation history of Britain and Ireland and their offshore basins have employed AFT and/or VR data (e.g. Allen et al., 2002; Green et al., 2002; Holford et al., 2005b; Holford et al., 2010) and revealed that most of onshore Ireland and Scotland were already cooler than 60°C during Cenozoic times, and therefore below the temperature sensitivity of the AFT technique (Chapter 3). The insensitivity of the AFT technique below ~60°C therefore makes it difficult using AFT data to separate the possible effects of Neogene exhumation from earlier exhumation events during the Paleogene or late Mesozoic (Holford et al., 2008).

Therefore, one key aspect of this thesis was to combine AFT and AHe analysis and also to employ pseudo-vertical profile modelling. So far, only two studies have published AHe data from Ireland and Scotland (Persano et al., 2007; Cogné et al., 2014), and only Cogné et al. (2014) has combined AFT and AHe data to model the Cenozoic exhumation history. A combination of these two methods is necessary since AHe dating has a lower partial retention zone of 85 – 40°C (Wolf et al., 1998) compared to AFT dating with a partial annealing zone of 120 - 60°C (Gleadow and Duddy, 1981). AHe dating is therefore well suited to detecting small amounts of exhumation (below ~2 km for a typical geothermal gradient). Therefore a combination of AFT and AHe analysis provides a better understanding of the last ~2 km of exhumation which is the assumed amount of denudation around the Irish Sea system during Cenozoic times (Jones et al., 2002; Holford et al., 2005b).

This thesis uses pseudo-vertical profiles, where possible, and combines the samples in the modelling software QTQt to one single model (Gallagher, 2012). The modelling procedure will be explained in more detail in chapter 6 but is essentially based on the assumption that, the samples in the vertical profile experienced the same thermal history with a temperature offset between the top and bottom sample. Thus, combining the samples to generate one single thermal history improves the resolution and reduces uncertainties and the complexity of the model compared to modelling each sample individually (Gallagher et al., 2005a; Gallagher et al., 2005b).

Thus, this study employed combined AFT and AHe analysis with a vertical profile modelling focussed around the Irish Sea region to produce well constrained thermal histories capable of distinguishing between i) a dome-like structure of exhumation caused by the development of the proto-Iceland mantle plume around the Irish Sea region during the Paleocene or ii) irregularly distributed exhumation of varying magnitude, related to far-field stresses due to mid-Atlantic rifting and the Alpine collision.

1.3 Far-field stress hypothesis

Several studies have linked the late Mesozoic/early Cenozoic exhumation history around Britain and Ireland with the opening of the Atlantic Ocean, the collision of the African and the Eurasian plate or both, respectively (Figure 1.1) (Cloetingh et al., 1990; Lewis et al., 1992; Ziegler et al., 1995; Green et al., 2001a; Doré et al., 2002; Green et al., 2002; Holford et al., 2005b; Hillis et al., 2008a; Holford et al., 2009b). The main arguments for the far-field stress hypothesis are the apparent timing and spatial distribution of Cenozoic exhumation in Britain and Ireland (Hillis et al., 2008a). The synchronicity of tectonic events on the Atlantic margin and Alpine collision with exhumation events ~1500 km away in the plate interior recorded by multiple AFT, vitrinite reflectance (VR) and basin inversion studies, has been used to suggest that regional intraplate exhumation episodes are probably driven by major tectonic events at plate margins (Ziegler, 1989; Green et al., 2002; Holford et al., 2009b). Furthermore, the present-day stress field in many continental interiors such as Western Europe, South America, and North America is parallel to the stress field at the plate boundaries (Zoback, 1992; Hillis et al., 2008b). This has led many authors to believe that plate boundary forces are the dominant cause for intraplate uplift (e.g. Green et al., 2002; Hillis et al., 2008b; Holford et al., 2009b).

There are many examples in the literature (e.g. Australia, South America, Africa and Asia) that suggest that far-field stress can cause deformation and exhumation thousands of kilometres away from active plate margins. Hillis et al. (2008b) investigated the stress field orientations in Neogene to Recent structures developed on the southeastern and western Australian passive margins. The present-day stress originates from stress at the mid-ocean ridge between the Antarctic and Indo-Australian plate and the similarities between the present-day stress field and the Neogene paleostress field implies that the source of the Neogene stress was also transmitted from the Antarctic plate boundary. Therefore Hillis et al. (2008b) argue that intraplate exhumation on the Australian passive margin is dominated by plate boundary interactions thousands of kilometres away.

Far-field stresses causing exhumation on passive margins was also documented by Cogné et al. (2011; 2012) on the continental margin of SE Brazil. They recognized compressional phases on the Brazilian passive margin linked to far-field stresses between the Andean subduction zone and the mid-Atlantic ridge. These compressional phases are reflected in different phases of cooling on the passive margin which were detected by modelling AFT and AHe data with QTQt. The main phase of cooling occurred during the early Cretaceous and was contemporaneous with break-up and rifting in the South Atlantic (Nürnberg and Müller, 1991). The post-rift history is further divided into i) late Cretaceous ii) Paleogene and iii) Neogene cooling episodes. The post-rift phases are all linked to phases of Andean orogenesis, and resulted in the reactivation of transfer zones and deformation in the Brazilian offshore basins as well as the emplacement of alkaline intrusive bodies (Cogné et al., 2011; Cogné et al., 2012). Similar results were found by Cobbold et al. (2007), who examined active tectonics using seismological and Global Positioning System (GPS) data from South America. They produced fault maps that spanned different phases (mid-Cretaceous, late Cretaceous, Paleogene and Neogene) of the Andean orogeny, and demonstrated that more deformation occurred on the passive continental margin than in the cratonic plate interior (Cobbold et al., 2007).

Another well-documented example for deformation and exhumation associated with far-field stress occurred on both sides of the South Atlantic, in SE Brazil and southern Africa. Initial rifting took place during the early to mid-Cretaceous and is related to the initial opening of the South Atlantic and the break-up of Gondwana (Hudec and Jackson, 2002; Moore et al., 2008; Turner et al., 2008). AFT and VR data reveal cooling episodes linked to the break-up of Gondwana and compressional shortening during the mid-Cretaceous at both margins and also during the early Cretaceous in West Africa, which is consistent with major unconformities in the offshore basins (Turner et al., 2008). The mid-Cretaceous cooling episode was also recognized by Moore et al. (2008), who linked volcanic activity in southern Africa with changes in the spreading regime in the South Atlantic and with major unconformities in the offshore basins.

One modern day example is the West Siberian Basin, which is experiencing long-wavelength surface uplift accommodated by discrete faults and faulting (Allen and Davies, 2007). This uplift is likely associated with far-field stress associated with the India-Eurasian collision. This uplift is taking place ~1500 km north of the northern limit of Himalayan orogenesis, which is in turn an additional ~2000 km north of the main Himalayan collisional suture zone (Allen and Davies, 2007; Holford et al., 2009b).

1.4 Mantle plume hypothesis

Earth's topography is largely caused by the isostatic response to physical, chemical or thermal perturbations to the lithosphere. Anomalous regional-scale, long-wavelength (> ca. 10^2 km) uplift which is not associated with compressional faulting and folding must be related to mantle-driven processes caused by chemical and/or thermal differences within the mantle (McKenzie, 1984; Lithgow-Bertelloni and Silver, 1998; Braun, 2010). The isostatic responses to physical thickening/thinning and chemical changes in the lithosphere (i.e. density changes due to crystallisation of phases) are permanent, whereas the isostatic response to a thermal perturbation is transient and only lasts as long as the thermal anomaly. It is also important to note that mantle processes and the thermal, chemical and physical anomalies within the lithosphere which yield an isostatic response are not limited to one discrete process (such as dynamic uplift, lithospheric thinning or magmatic underplating). Usually, there is more than one process active and it can be hard to distinguish which mantle-related process caused the uplift. Furthermore, the less dense mantle material can also traverse horizontally along the bottom of the lithosphere, probably using weak zones at the base of the lithosphere (Sleep, 1990). This in turn leads to uplift further away from the centre of upwelling of the mantle plume (Jones and White, 2003). For example, Al-Kindi et al. (2003) proposed a linear lateral extension from the proto-Iceland mantle plume beneath Greenland extending beneath Ireland and Britain which is ~1200 to ~1300 km away from the proposed centre of the mantle plume (Figure 1.2). A modern melt channel with a similar spatial extent has been proposed by

Rickers et al. (2013) based on full-waveform tomography modelling, suggesting that Britain and Ireland are still dynamically supported today.

Unfortunately, the mantle cannot be directly observed or sampled and thus mantle dynamics are poorly constrained. Mantle dynamics rely on indirect observations such as seismic tomography and gravity anomalies. By convention, gravity maps are presented following a free-air correction. Free-air gravity anomalies are differences in the gravity field after correcting for collection elevation to a reference level, usually the geoid (surface of equal gravitational potential, approximately corresponding to mean sea level; Bonvalot et al., 2012), and can indicate that mantle-driven processes are active. Thus, it is difficult to make estimates about mantle-driven processes in the geological past, since we cannot use seismic interpretation or free-air gravity to resolve anomalous uplift. Therefore, indirect observations of mantle processes are needed, such as the exhumational response to regional uplift where this is not associated with evidence for regional compression.

Several studies suggested that uplift around Britain and Ireland was caused by mantle-driven processes probably originating from the proto-Iceland mantle plume (White and Lovell, 1997; Jones et al., 2002; Al-Kindi et al., 2003; Jones and White, 2003; Arrowsmith et al., 2005; Tomlinson et al., 2006; Davis et al., 2012). A mantle plume is a region in the mantle where hotter and/or less dense mantle material is constantly uprising from a deep source (i.e. core-mantle boundary; Burov and Cloetingh, 2009) even until it reaches the lithosphere. In general, a mantle plume is described as mushroom shaped (see Figure 1.4) but, as described above, the plume can also form lateral extensions, like spokes, reaching further away from the centre of the upwelling.

Mantle-driven processes caused by the mantle-plume can be divided into three main causes: i) dynamically supported uplift (e.g., Braun, 2010), ii) the isostatic response caused by thinning and erosion of the base of the lithosphere (Burov and Cloetingh, 2009) and iii) magmatic underplating (McKenzie, 1984; Lithgow-Bertelloni and Silver, 1998; Maclennan and Lovell, 2002; Braun, 2010).

However, all processes can occur at the same time, which makes quantification of the relative proportion of each process difficult.

Which mantle-driven process is responsible for uplift cannot readily be resolved by indirect observations of uplift on the Earth's surface such as the low-temperature thermochronology methods employed in this thesis. Nevertheless, it is important to give a brief description of each process since they have been discussed and implicated in various studies (e.g. Al-Kindi et al., 2003; Jones and White, 2003; Arrowsmith et al., 2005) concerning Palaeogene uplift and exhumation around Ireland and Britain.

(i) Dynamically-driven uplift is caused by buoyant mantle upwelling induced by thermal or chemical density variations in the mantle. These density variations will cause the less dense mantle (comprised of hotter material with an anomalously low seismic velocity) material to rise (Lithgow-Bertelloni and Silver, 1998; Braun, 2010). If deep-seated low-density material is continuously rising from the core-mantle boundary for a long period of time through the mantle and impinges on the base of the lithosphere, then the rising material is commonly termed a mantle plume (Morgan, 1972; Burov and Cloetingh, 2009). The buoyant ascending mantle material will induce stress at the base of the lithosphere and thus cause vertical motion (Figure 1.4a). The dynamic topography caused by the upwelling is only transient and varies as the mantle flow changes and is characterized by a small amplitude (~1000 m) and a long wavelength that is proportional to the scale and depth of the mantle flow, and can range from several hundred to several thousand kilometres across (Burov and Cloetingh, 2009; Braun, 2010). The isostatic response to the thermal anomaly will decay as the material cools and once the cause of upwelling has ceased, the lithosphere will return to its compositionally-controlled isostatic state.

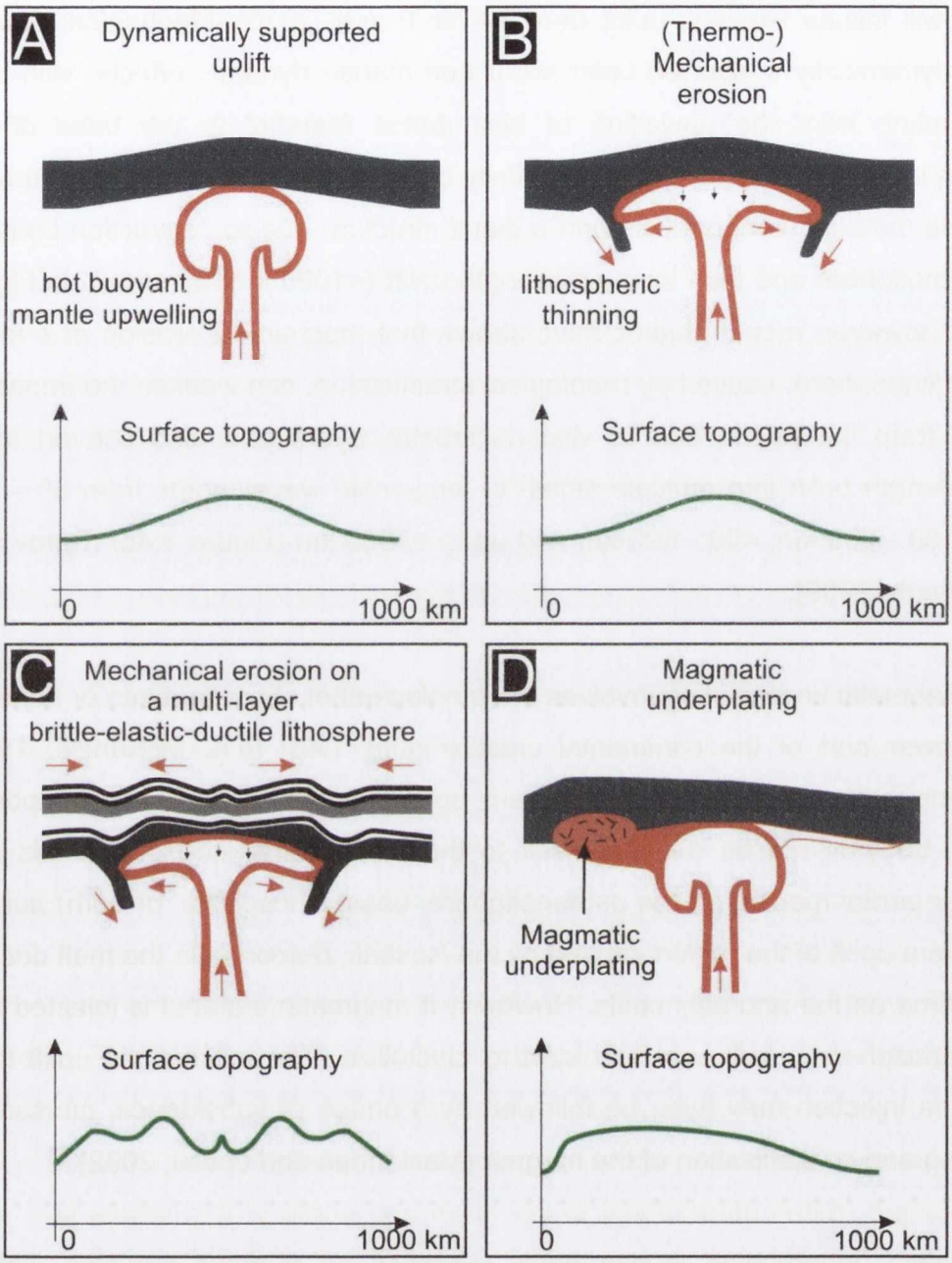


Figure 1.4: Exhumation caused by mantle-driven processes (adapted after Burov and Cloetingh, 2009).

(ii) The isostatic response to thinning and erosion of the base of the lithosphere can occur if buoyant asthenospheric mantle ascends to the base of the lithosphere. This induces partial melting by decompression of the upwelling asthenospheric mantle and results in thinning by (thermo-)mechanical erosion of the base of the lithosphere due to convecting asthenospheric material (Figure 1.4b). The replacement of mantle lithosphere with lower density mafic

melt will initiate isostatic uplift (Bird, 1979; Braun, 2010). Mechanical erosion and dynamically supported uplift are linked mantle dynamic effects, with both originating from the upwelling of less dense material to the base of the lithosphere and thus both can potentially occur at the same time. The buoyant mantle material is thought to form a diapir structure due to convection beneath the lithosphere and thus long-wavelength uplift (~1000 km) as shown in Figure 1.4b; however, recent studies have shown that mechanical erosion of a multi-layer lithosphere, caused by rheological stratification, can weaken the impact of uplift from the plume due to viscous crustal layers and also convert long-wavelength uplift into multiple small- to long-scale wavelengths from 50 - 100 km, 150 - 300 km, 400 - 500 km and up to ~1000 km (Figure 1.4c) (Burov and Cloetingh, 2009).

(iii) Magmatic underplating involves the emplacement of magma into or beneath the lower part of the continental crust (Figure 1.4d) (e.g. McKenzie, 1984) causing both transient and permanent uplift. As with dynamically supported uplift, buoyant mantle material rises to the base of the lithosphere: this can trigger partial melting (of the asthenosphere, basal lithosphere, or both) but the transient uplift of the region caused by the isostatic response to the melt decays with time as the anomaly cools. However, if magmatic material is injected into the lithosphere, it will cool and start to crystallize. The initial rapid uplift from magma injection may even be followed by a phase of subsidence, caused by cooling and crystallisation of the magma (Maclennan and Lovell, 2002).

Magmatic underplating is commonly modelled as a mafic intrusion with a gabbroic composition due to partial melting of the mantle (e.g. Maclennan and Lovell, 2002). In this paradigm, the emplacement of the still relatively dense gabbro (~3.1 g/cm^3) into or beneath the crust may still cause permanent uplift, even after the initial dynamic support is ceased, due to the lower density of the gabbro compared to that of bulk upper mantle peridotite (~3.2 - 3.3 g/cm^3) and crustal thickening (Braun, 2010). The actual amount of potential permanent uplift is difficult to quantify since several parameters (themselves difficult to quantify) must be considered. Firstly, the thickness of the emplaced body; secondly, the true density relationships between upper mantle (fairly well known

for peridotite: ~3.2 - 3.3 g/cm^3), the emplaced body (assumed as gabbro) and the lower crust (not well known as it can be quite heterogeneous, but usually assumed to be 2.8 g/cm^3; Hacker et al., 2015) and thirdly, the potential thinning/erosion of the lithosphere which took place during the initial emplacement phase.

Modelling the isostatic effects of magmatic underplating is challenging. The lower continental crust is much more compositionally diverse than the oceanic crust (Braun, 2010; Hacker et al., 2015). Furthermore, the injection of magmatic material can occur in multiple phases and thus cause several uplift and erosion followed by subsidence events over a geologically short period of time which are not easily resolvable with low-temperature thermochronometers such as AFT and AHe.

From the description of the three processes, dynamically-driven uplift, isostatic response to thinning and erosion and magmatic underplating, it is obvious that mantle-driven processes occur to some degree together. If the buoyant mantle material causing the dynamically supported uplift ascends to the base of the lithosphere, then it can possibly cause lithospheric thinning by mechanical erosion which then results in isostatic uplift. The hot ascending mantle is also subject to heat loss due to convective cooling from contact with the cooler lower lithosphere which in turn would promote crystallisation of partial melts, triggering magmatic underplating. Therefore, it is difficult to discriminate between these three mechanisms with low-temperature thermochronometers such as AFT and AHe dating, used in this study. Nevertheless, all mantle-driven processes are characterised by exhumation of a relative long-wavelength (~1000 km), even though mechanical erosion can cause exhumation of a smaller-scale wave-length in addition to the long-wavelength pattern (Figure 1.4c; Burov and Cloetingh, 2009).

1.5 Comparison between compressional stress and mantle-driven processes

Exhumation related to compressional stress originating from the opening of the North Atlantic Ocean and the Alpine collision would generate a more localised (tens of kilometres; Figure 1.5a), spatially and temporally variable (late Cretaceous to Neogene) exhumation pattern across Ireland and Britain. Onshore exhumation would be likely focussed along reactivated major structures and faults.

On the other hand, exhumation related to mantle-driven processes will show a regional-scale, dome-like structure with the highest exhumation occurring at the locus of upwelling/underplating, and decreasing in intensity away from this region (Figure 1.5b). The exhumation event is temporally limited to the timing of mantle plume activity at ~60 Ma. The dome-like structure would not be expected to have been affected by major faults, however, major faults might have undergone some minor reactivation during the regional-scale uplift and doming.

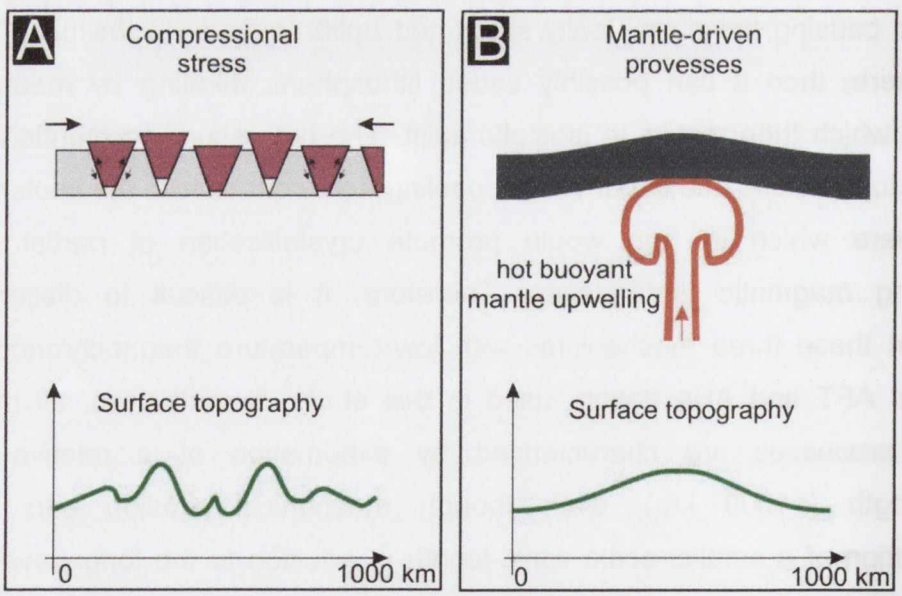


Figure 1.5: Comparison of surface topography caused by (a) compressional stress and (b) mantle-driven processes.

2. Regional geological setting and Mesozoic – Cenozoic exhumation of Ireland and Britain

In this chapter a brief tectonic and geological review of Ireland and Britain and neighbouring parts of the NW European shelf is presented. This review is intended to provide a geological context to the succeeding chapters, but given the vast literature on the subject it cannot be completely comprehensive. More detailed reviews of the tectonic history of this segment of the NW European margin can be found in various papers and books (Ziegler et al., 1995; Peacock, 2004; McCann et al., 2006; Ziegler and Dezes, 2006; Anell et al., 2009; Holland and Sanders, 2009).

2.1 Paleozoic to late Mesozoic tectonic setting

Today, Britain and Ireland are located close to the continental shelf of the North Atlantic passive margin. Britain and Ireland were affected by at least two major Paleozoic orogenic cycles, the Caledonian orogeny (late Cambrian – late Silurian/Devonian) and the Variscan orogeny (Devonian – Carboniferous). The effects of far-field Alpine orogenesis on southern Ireland and Britain are less significant and are discussed later.

2.1.1 Caledonian orogeny: late Cambrian – early to mid Devonian

During the late Neoproterozoic north-west Ireland and Scotland formed part of the Laurentian continent (Laurentia), and were separated by the Iapetus Ocean (Figure 2.1; Harland and Gayer, 1972) from southeast Ireland and southern Britain which formed part of the microcontinent Avalonia. During the Cambrian the Iapetus Ocean started to close, and initiated a series of tectonic events which have been attributed to the Caledonian orogeny (McKerrow et al., 2000; Chew and Strachan, 2014).

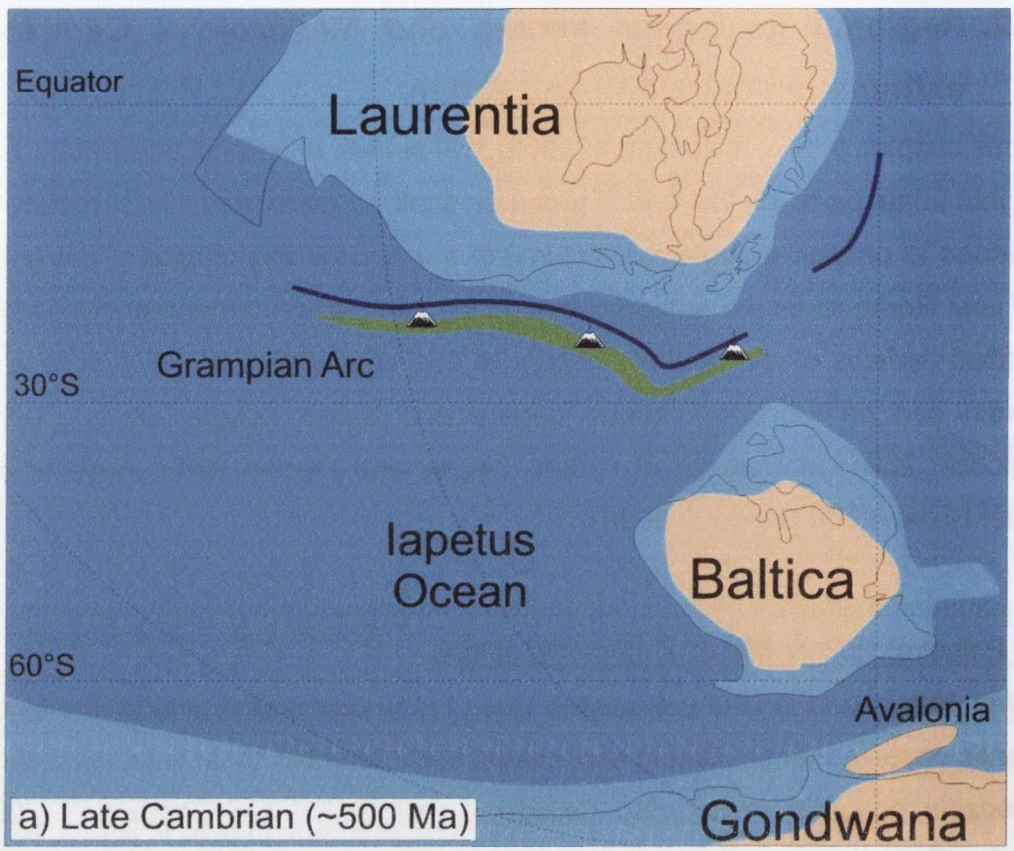


Figure 2.1: Plate reconstruction of Laurentia, Baltica and Avalonia during the late Cambrian (~500 Ma). The Iapetus Ocean starts to close and an intra-oceanic island arc is colliding with the Laurentian margin. Volcanic arc is shown in green, subduction zones in blue (adapted after Chew and Stillman, 2009).

The Caledonian orogeny can be divided into three major tectonic phases (McKerrow et al., 2000) The first tectonic phase is termed the Grampian orogeny and took place from early to mid – Ordovician (475 – 460 Ma). The Grampian orogeny is related to the collision of the Laurentian margin with an intra-oceanic island arc terrane (Figure 2.2) which was generated by the subduction of oceanic lithosphere within the Iapetus Ocean (Dewey and Shackleton, 1984).

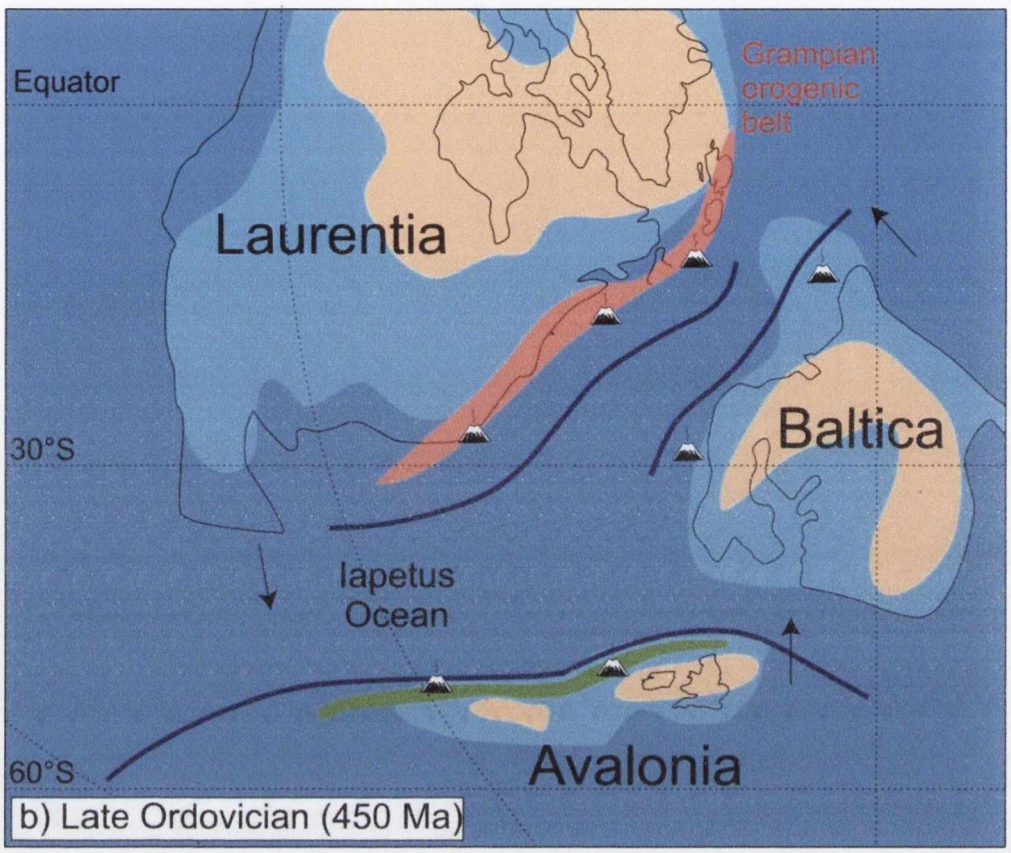


Figure 2.2: Plate reconstruction of Laurentia, Baltica and Avalonia during the late Ordovician (~450 Ma). The Grampian orogenic belt (red) has formed and the Iapetus Ocean between Baltica and Laurentia is closing. Volcanic arc is shown in green, subduction zones in blue (adapted after Chew and Stillman, 2009).

The second phase, the Scandian event (Thigpen et al., 2013), occurred during the Silurian and ranges from ~435 – 425 Ma. This tectonic phase was related to the closure of the Iapetus Ocean between Laurentia and Baltica (essentially modern day Scandanavia) (Figure 2.3). The later collision between Laurentia and Baltica caused deformation restricted to the Northern Highland Terrane in Scotland (Figure 2.4) between the Moine Thrust Zone and the Great Glen Fault (Baker, 1976; Chew and Strachan, 2014; Cawood et al., 2014).

The Iapetus Ocean between Avalonia and Baltica closed during the late Ordovician along the "Tornquist" line (see Figure 2.3; Torsvik and Rehnström, 2003; Waldron et al., 2014). During the Silurian (Figure 2.3), Waldron et al. (2014a) proposed that Laurentian fragments between Laurentia and Avalonia are transported northwards following arc collision and emplaced onto Baltica

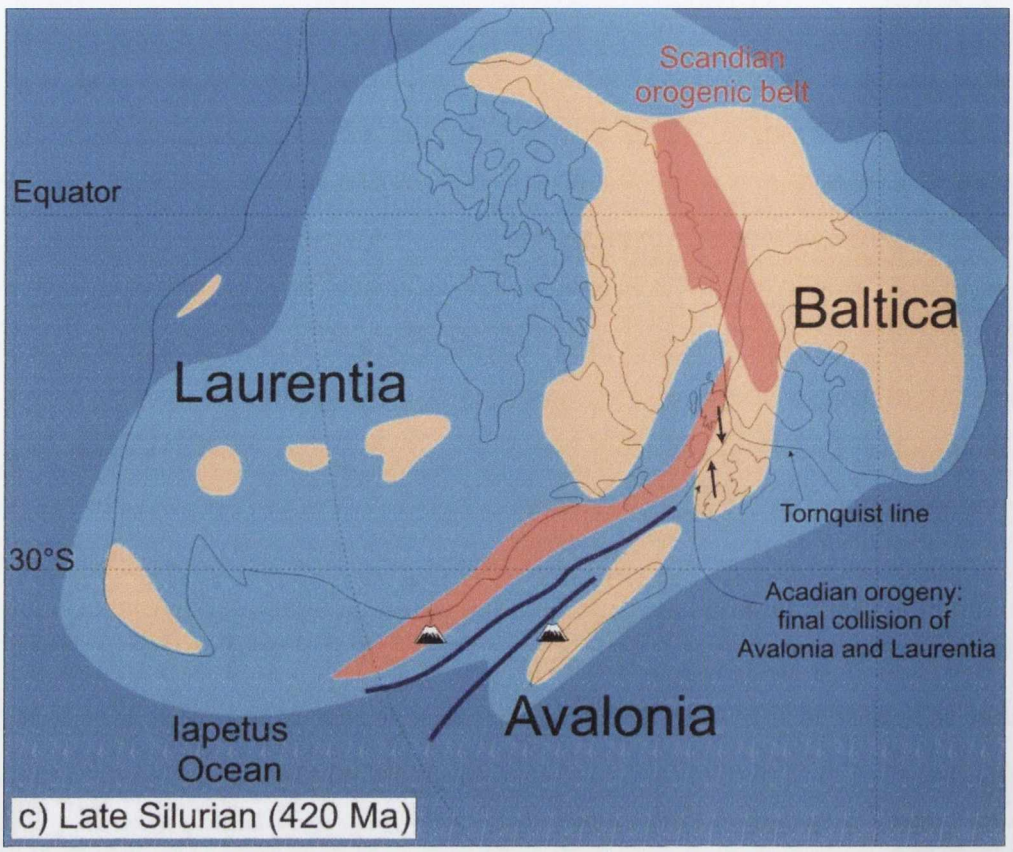


Figure 2.3: Plate reconstruction of Laurentia, Baltica and Avalonia during the late Silurian (420 Ma). The Scandian orogenic belt has formed (red) and the final continent – contient collision between Laurentia and Avalonia occurs. Subduction zones are shown in blue (adapted after Chew and Stillman, 2009).

The last stage, continent – continent collision between Laurentia and the connected Avalonia and Baltica, has affect Ireland and Britain, is called the Acadian event (Figure 2.3), is the third tectonic phase of the Caledonian orogenic cycle, and occurred during early – mid Devonian time (~405 – 390 Ma; Woodcock et al., 2007; Chew, 2009; Chew and Stillman, 2009). However, the origin of this event is still debated since it post-dates the closure of the Iapetus Ocean by ~20 – 25 Ma. Woodcock et al. (2007) associate the deformation with the subduction of the Rheic Ocean in the south and proposed to assign the deformation to a "proto-Variscan" event rather than to the late Caledonian orogeny.

The closing of the Iapetus Ocean resulted in the continent – continent collision between Laurentia and Avalonia and Ganderian microplate (Rogers et al.,

2006; Waldron et al., 2014b). Ganderia is a fragment, similar to Avalonia originating from Gondwana, which occurs in south east Ireland and central Newfoundland (Rogers et al., 2006). The contact zone between these plates is termed the Iapetus Suture Zone and is oriented NE-SW separating the Southern Uplands and the Lake District in northern England, crosses the northern pinnacle of the Isle of Man and across central Ireland (Figure 2.4). The collision was "soft" and did not produce a lot of crustal thickening (Chew and Stillman, 2009) and instead was accompanied by oblique, sinistral strike-slip transpression (Soper et al., 1992; Dewey and Strachan, 2003) and abundant granitic magmatism (Chew and Stillman, 2009).

Avalonia, Laurentia and Baltica were thus amalgamated into one large continent, termed Laurussia, by the end of the Caledonian orogeny. The major tectonic structures from the Caledonian orogeny in Ireland and Britain are NE – SW oriented and have been reactivated during subsequent tectonic events (Lefort, 1989; Peacock, 2004).

2.1.2 Variscan orogeny: mid-Devonian – Carboniferous

The Variscan orogeny resulted from the collision of the continent of Laurussia to the north (which encompassed Ireland and Britain) with the continent of Gondwana to the south (comprising South America, Africa, India, Australia and Antarctica). The Variscan orogeny in Europe is dominated by the collision of several micro-continental blocks derived from Gondwana during its late Ordovician – Silurian fragmentation (Scotese and McKerrow, 1990; Matte, 2001). Laurussia and Gondwana were originally separated by the Rheic Ocean (Nance et al., 2010).

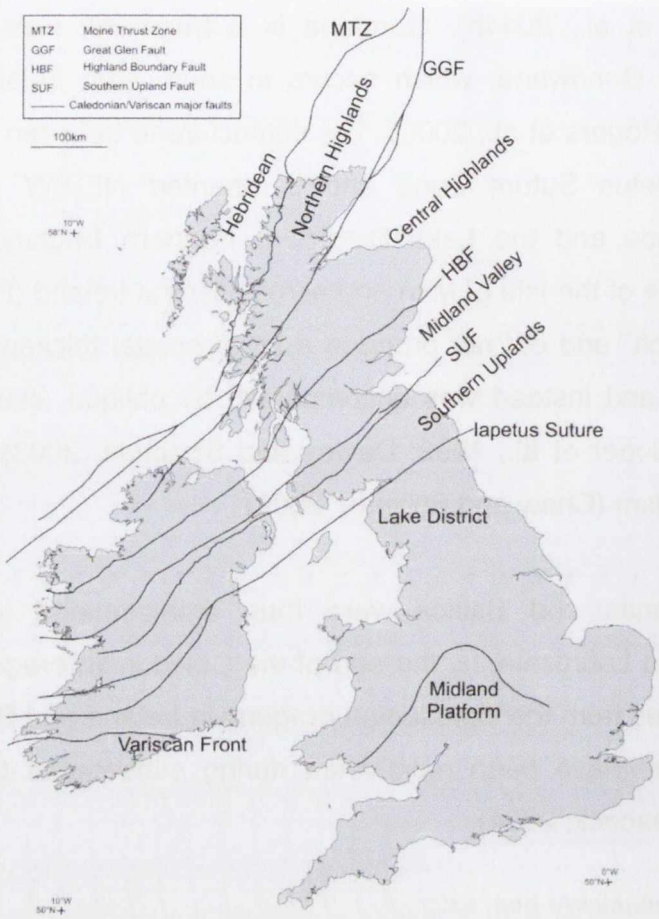


Figure 2.4: Map of Ireland and Britain with major Caledonian and Variscan structures depicted.

The Rheic Ocean started to close during the mid- to late Devonian (~395 – 370 Ma; Cartier and Faure, 2004; Nance et al., 2010). The Devonian sedimentary successions in Ireland and Britain show a switch from mainly transpressional strike-slip deformation, linked to the final stages of continent-continent collision of Laurentia and Avalonia at the end of the Caledonian orogenic cycle, to a more purely extensional regime. The latter is related to the initiation of subduction of the Rheic Ocean and therefore associated with the onset of the Variscan orogeny (Graham, 2009a; Kroner and Romer, 2013; Richmond and Williams, 2015).

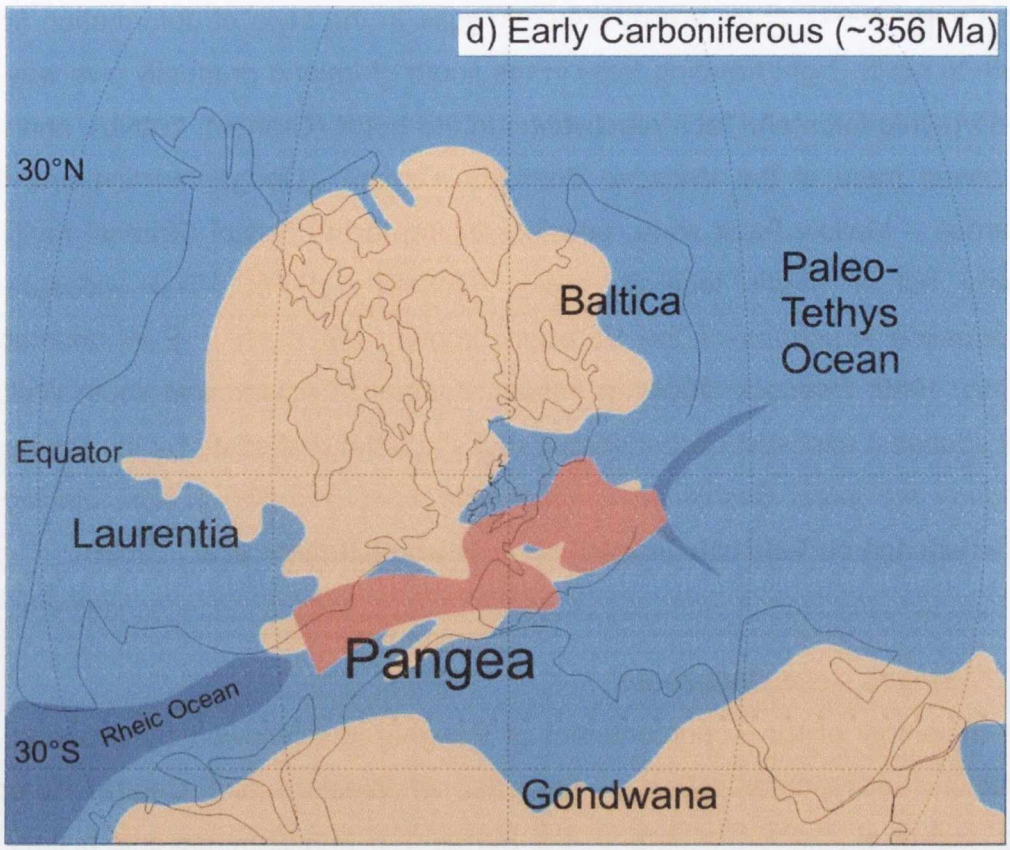


Figure 2.5: Plate reconstruction of Laurentia, Baltica and Gondwana during the early Carboniferous (~356 Ma). The Rheic Ocean starts to close and the supercontinent Pangea starts to form. Red zone represents Variscan orogenic belt (adapted after Scotese and McKerrow, 1990 and Chew and Stillman, 2009).

At around ~360 Ma Laurussia collided with Armorica and Gondwana, closing the Rheic Ocean (Figure 2.5) and initiating the formation of the supercontinent Pangea (Faure et al., 1997). However, Variscan orogenesis did not terminate after the initiation of collision but rather continued to build the Variscan orogenic belt across Central Europe, North Africa and North America until late Carboniferous to early Permian times (Figure 2.5; Matte, 2001).

Ireland and Britain were situated in a back-arc setting during the closure of the Rheic Ocean (Cartier and Faure, 2004) and therefore were situated outside of the internal Variscan orogenic belt, in the foreland (Cartier and Faure, 2004; McCann et al., 2006). Although southwest Ireland and the southernmost part of England (south of the Bristol Channel) have been considered to form the northern Variscan front (Matte, 1991; Unrug et al., 1999; Matte, 2001; Cartier

and Faure, 2004), there are obvious changes in the style of deformation from south to north. Tight trending folds in the south of Ireland gradually give way to broad gentle folds and fault reactivation in the north (Graham, 2009b), and the supposed trace of the Variscan front (the Dingle – Dungarvan line and the Killarney – Mallow Fault zone, possibly linking to the Bristol Channel fault) is clearly not a major tectonic break (Graham, 2009b). The widespread deformation structures of the Variscan orogeny are mainly ~E-W orientated (Lefort, 1989; Peacock, 2004) in Ireland, southern England and south Wales. The youngest exposed Carboniferous rocks in Ireland affected by the Variscan Orogeny are latest Bashkirian (Westphalian B; c. 315 Ma) in age, placing a maximum age on Variscan Orogenesis in Ireland (Graham et al., 2009b).

2.1.3 Permian – late Cretaceous

The assembly of the supercontinent of Pangea was followed by a period of instability and reorganisation of the crust of Western and Central Europe (McCann et al., 2006). In Ireland, the Permian to Mesozoic tectonic history is hard to determine precisely due to the limited occurrence of onshore Permian and Mesozoic sediments (Simms, 2009). Ireland and Britain were located in the foreland of the Variscan mountain belt and show limited basin development until the onset of the break-up of Pangea during the Triassic (Scotese and Langford, 1995; Peacock, 2004; McCann et al., 2006; Simms, 2009).

The break-up of Pangea started during the late Permian – early Triassic (Figure 2.6a) in the Barents Sea and the Norwegian-Greenland Sea rift (Ziegler and Dezes, 2006). During the Mesozoic, the rifting propagated southwards into the North Atlantic and finally into the Central Atlantic connecting with a second major rift propagating northwards from the Central Atlantic Rift System (Figure 2.6b) (Ziegler and Stampfli, 2001; Peacock, 2004). Transtensional deformation associated with this rifting event led to the development of a complex network of basins across the North Atlantic margin including Ireland and Britain (McCann et al., 2006; Stolfova and Shannon, 2009).

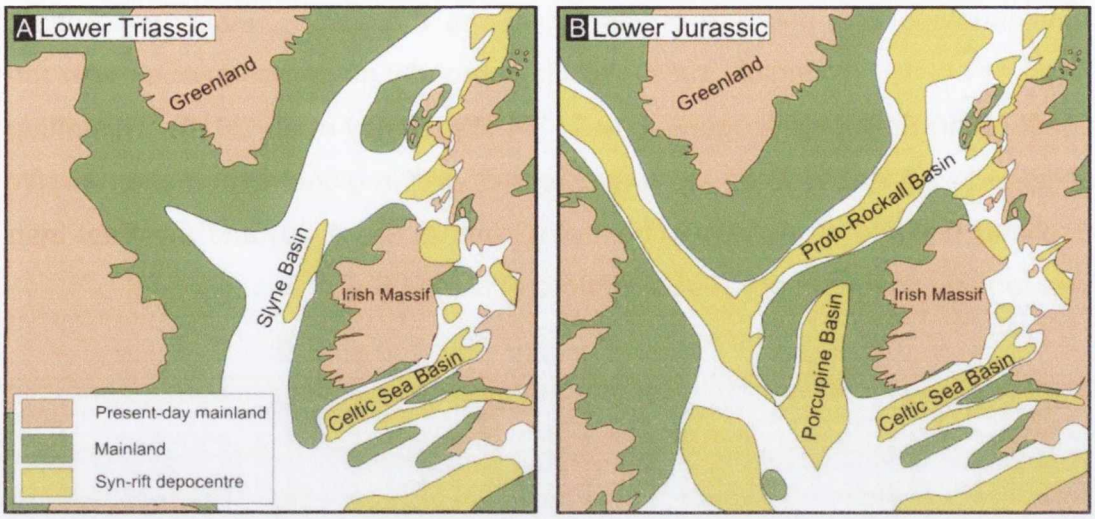


Figure 2.6: Paleogeographic reconstruction of the North Atlantic during A: early Triassic and B: early Jurassic. The growing offshore basins show signs of extension associated with rifting (adapted after Tyrrell et al., 2007)

The Permo-Triassic basins on the western Atlantic Irish margin (such as the Rockall Trough, Figure 1.3) are mainly oriented ~NE–SW and thereby are parallel to the major Caledonian structures (Murphy et al., 1991; Clift and Turner, 1998; Doré et al., 1999; Stolfova and Shannon, 2009). In contrast, basins offshore southern Ireland and southern Britain are orientated ~E–W which is sub-parallel to the Variscan structural grain (Figure 1.3). These basins include the Bristol Channel, the Celtic Sea Basin, Central English Channel, the basins within the Irish Sea region and the Wessex and Weald Basin (Coward, 1990; Floodpage et al., 2001; Blundell, 2002; Peacock, 2004). This indicates that the development of basins around Britain and Ireland was strongly dependent on the orientation of major pre-existing structural elements.

During the early to mid-Jurassic, rifting took place along the Norwegian – Greenland rift extending southwards into the Rockall – Faeroe Basin (Figure 2.6b) and the North Sea (Ziegler, 1989; Peacock, 2004). From the late Jurassic until early Paleogene, rifting also propagated northwards from the Central Atlantic into the North Atlantic and during the early to mid-Jurassic, major seafloor spreading initiated between North America and North Africa and propagated northwards (Figure 2.7a) (Ziegler, 1989; McHone, 2000; Peacock, 2004). The spreading propagated northwards into the North Atlantic between

Newfoundland and the Bay of Biscay, during the early Cretaceous (Aptian; Keen et al., 1977; Ziegler, 1989), which is broadly contemporaneous with the onset of the Eo-Alpine orogeny (~140 – 84 Ma, Handy et al., 2010). This rifting episode is also associated by some authors with regional exhumation in NW Scotland (Holford et al., 2010), Ireland (Green et al., 2000) and the East Irish Sea region (Holford et al., 2005b; Holford et al., 2009b).

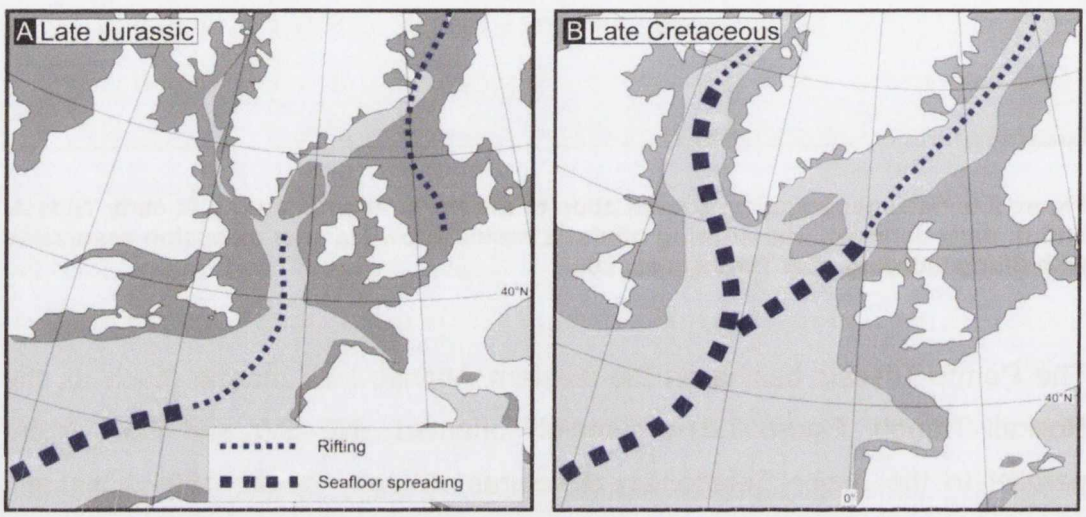


Figure 2.7: Late Jurassic and late Cretaceous rifting in the North Atlantic region (adapted after Peacock et al., 2004).

Ultimately during the Cretaceous, the two major rift systems, the Norwegian – Greenland rift and the Central Atlantic Rift System, merged west of the Irish continental margin to form one composite rift system (Figure 2.7b) separating Greenland, North and South America from Norway, Western Europe and Africa.

Early AFT studies from Ireland indicated at least two cycles of exhumation and reburial in Ireland during the mid-Jurassic and early Cretaceous. However, based on AFT and AHe data from vertical profiles, Cogné et al. (2014) proposed that the Mesozoic exhumation history of western Ireland was instead likely to represent one diachronous event linked to rift-related uplift which started at ~180 Ma in Donegal in NW Ireland to ~125 Ma in Kerry in SW Ireland.

AFT data from Holford et al. (2010) implied multiple phases of exhumation in NW Scotland during both the Triassic (~245 – 225 Ma; 225 – 190 Ma) and early Cretaceous (140 – 130 Ma; 110 – 90 Ma). They suggest that the Triassic (~245 – 225 Ma) exhumation event in NW Scotland was caused by localized footwall uplift and that the Triassic – Jurassic exhumation event (225 – 190 Ma) represents a regional final stage of post-Caledonian unroofing. The early Cretaceous exhumation events are linked by Holford et al. (2005b) to exhumation in southern Britain and, associated with the onset of seafloor spreading in the North Atlantic. The Mesozoic exhumation episode will be discussed in more detail in section 8.3.

2.1.4 Late Cretaceous to Paleogene

Britain and Ireland are situated on the North Atlantic "passive" margin hence would be expected to have experienced little post-rift exhumation. Yet, this segment of the North Atlantic "passive" margin has experienced post-rift exhumation of up to ~1.5 – 2.5 km during the late Cretaceous to Cenozoic (Holliday, 1993; Green, 2002; Hillis et al., 2008a). The late Cretaceous to Paleogene tectonic history for Ireland and Britain remains highly contentious and is based around two main hypotheses: far-field stress and mantle plume, as discussed in chapter 1.

2.2 Mesozoic and Cenozoic rocks onshore Ireland and Britain

The distribution of Mesozoic and Cenozoic rocks in Ireland and Britain can give important insights into the exhumation history of the region. However, basing the exhumation history entirely on the occurrence or absence of Mesozoic/Cenozoic rocks is ambiguous, since it is usually unclear how much rock was initially in place, how much was removed or if it corresponds to a period of no deposition.

The main region of Mesozoic and Cenozoic outcrops in the region is in SE Britain (Figure 2.8), where the broad disposition of units shows that they get progressively younger from Triassic terrestrial sandstones near the Irish Sea to Cretaceous chalk and Paleogene sandstones near the English Channel.

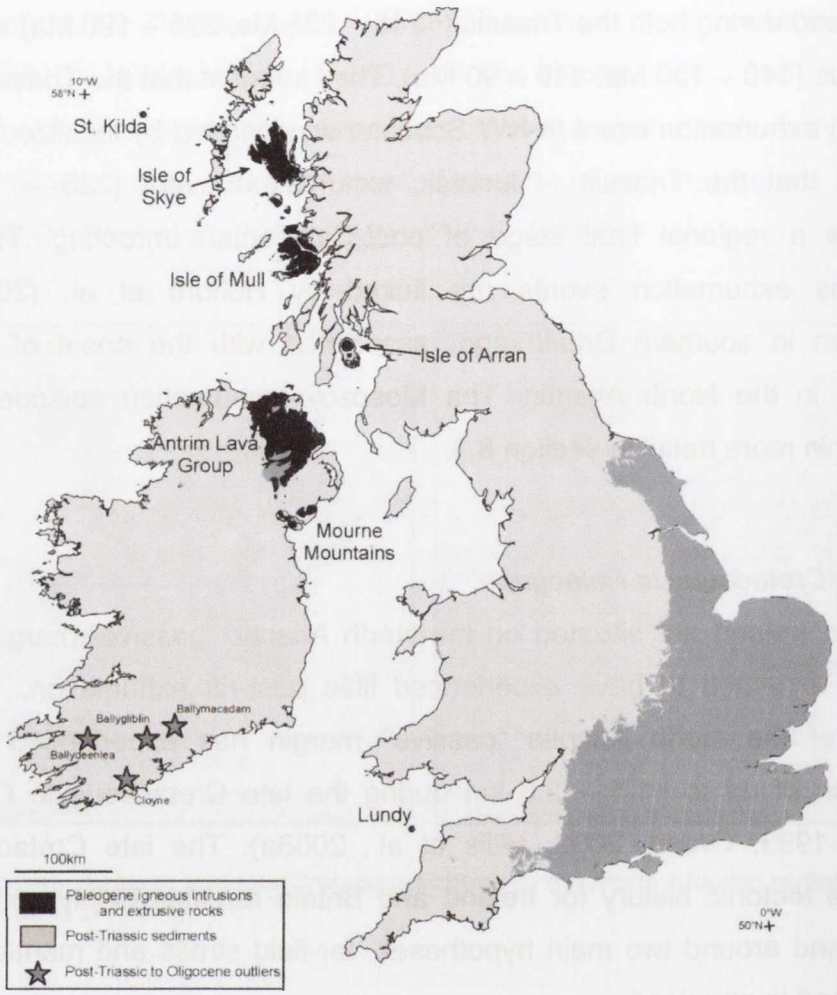


Figure 2.8: Map of Ireland and Britain with the distribution of post-Triassic sedimentary rocks and the British Irish Paleogene Igneous Province (BIPIP).

Other non-igneous Mesozoic and Cenozoic outcrops are sparse in Britain and Ireland. On the Isle of Skye in western Scotland and adjacent to the Moray Firth Basin in north Scotland some Triassic and Jurassic sediments crop out. In Cloyne in southern Ireland is a mid-Jurassic (~180 Ma) clay outcrop (Higgs and Beese, 1986; Figure 2.8) and across southern Ireland are a few local Cenozoic outcrops, the oldest of Oligocene age in Ballygiblin, Co Cork (Simms and Boulter, 2000) and Ballymacadam, Co. Tipperary (Watts, 1957) (Figure 2.8). However, most of them are undated or poorly dated as Miocene to Pliocene (Coxon and McCarron, 2009). A key outcrop is the Ballydeenlea chalk in Co. Kerry (Figure 2.8) which has been dated as Campanian (83.6 ±0.2 Ma to 72.1

±0.2 Ma; Barr, 1966). Vitrinite reflectance data indicates that the Ballydeenlea chalk was heated up to approximately 80°C which was then interpreted as burial beneath 1 to 1.5 km of, probably, later Cretaceous and earliest Paleogene sediments (Evans and Clayton, 1998).

Another important region of Mesozoic/Cenozoic outcrops is in Northern Ireland, where thick sequences of Permian – Triassic and lower Jurassic mudstones are preserved in the Lough Neagh, Rathlin and Larne basins (Holford et al., 2009a). Furthermore, a nearly complete succession of Upper Cretaceous limestone is unconformably overlain by the Antrim Lava Group (Figure 2.8) which erupted between 62.6 – 59.6 Ma (Ganerød et al., 2010) and obtains a maximum thickness of 780 m (Walker, 1995; Mitchell, 2004; Holford et al., 2009a). The preservation of the thick sequences of the Antrim Lava Group could indicate little exhumation has happened in this part of Ireland. However, it is uncertain how thick the Tertiary basalt lava pile initially was, and so it is difficult to access the total amount of exhumation in this part of Northern Ireland. High-degree cementation (thermally induced textural alteration) in the Upper Cretaceous chalk indicate burial depths of the chalk of up to 1.5 – 2 km, which would indicate an initially much thicker sequence of basalts lying on top of the Lava group (Maliva and Dickson, 1997). Additional evidence for significant Cenozoic exhumation in Northern Ireland is provided by the Mourne Mountain granite. The granite intruded at ~ 56 Ma (Gamble et al., 1999) and is today on the surface, indicating a strong phase of Cenozoic exhumation at least in the southern part of Northern Ireland.

The eruption of the Antrim Lava group and the intrusion of the Mourne Mountains were accompanied by considerable amounts of igneous activity in the North Atlantic, across western and central Scotland as well as in north Ireland (Figure 2.8). This Paleogene igneous activity is known as the North Atlantic Igneous Province (NAIP). This phase of Paleogene igneous activity in Britain and Ireland is here called the British Irish Paleogene Igneous Province (BIPIP) and is dated by the $^{40}Ar/^{39}Ar$ and zircon U-Pb methods to 62.6 ± 0.3 to 55.6 ± 0.2 Ma (Chambers et al., 2005; Ganerød et al., 2010). Additional Paleogene igneous activity can be found in the East Irish Sea region

(Fleetwood dyke swarm), smaller dyke swarms offshore NW Wales and in the north of Ireland, and an igneous intrusion in the Bristol Channel on the island of Lundy (Figure 2.8).

2.3 Offshore sedimentary basins

Mesozoic and Cenozoic sedimentary rocks in the offshore basins are much more abundant than on onshore Ireland and Britain. As described in section 2.1.3, the basins around Britain and Ireland initially formed during the Permo-Triassic and follow the major Caledonian structures on the western Irish Atlantic margin (~NE – SW) and are sub-parallel to Variscan structures to the south of Ireland and Britain (Figure 1.3) (Murphy et al., 1991; Doré et al., 1999; Stolfova and Shannon, 2009). Thus, in most cases, the basin fill consists of syn-rift and post-rift sediments of Permo-Triassic to Cenozoic age.

2.3.1 Western Irish offshore basins

The western Irish offshore basin system comprises several small basins and some bigger basins as the Slyne, Erris, Porcupine and Rockall basins (Figure 1.3) which developed during several extensional episodes with NE-SW oriented trends inherited from Caledonian structures. The rifting phases in the western Irish offshore basin system were diachronous, and were initiated by the break-up of Pangea during Permo-Triassic (Figure 2.6a), but rifting also occurred during the mid-Jurassic (Figure 2.6b), late Jurassic to early Cretaceous (Figure 2.7a) and mid- to late Cretaceous (Figure 2.7b; Moore, 1992; Chapman et al., 1999; Dancer et al., 1999; Shannon et al., 1999; Haughton et al., 2005; Naylor and Shannon, 2005).

In general, the Mesozoic-Cenozoic record of the western Irish offshore is characterized by extended periods of thermal subsidence however, the diachronous rifting phases resulted in a more variable tectonostratigraphic record than in either the Irish Sea or the Celtic Sea basins (Shannon, 1992; McDonnell and Shannon, 2001). The larger basins (Porcupine and Rockall basins) contain thick Cenozoic successions (Shannon and Naylor, 1998) whereas the Slyne Basin contains only very thin (~40 m thick) Cenozoic

sediments and early Cenozoic basaltic lavas (Dancer et al., 2005) and a thin Cenozoic layer is present in the Erris Basin (see Figure 1.3 for basin locations; Chapman et al., 1999). Additionally, the Porcupine – Rockall region is characterized by widespread intrusive and extrusive magmatism, which is associated with either the opening of the Atlantic Ocean (Ritchie et al., 1999; Walsh et al., 1999; Johnston et al., 2001; Haughton et al., 2005) and/or the emplacement of the proto-Iceland mantle plume (Jones and White, 2003).

The biggest depocentres in the western Irish offshore system are the Rockall and Porcupine Basins (Figure 1.3), where the main phase of rifting occurred during the late Jurassic to mid-Cretaceous (Walsh et al., 1999; Johnston et al., 2001; Haughton et al., 2005). The Rockall Basin consists of up to 6 km of Mesozoic and Cenozoic sedimentary rocks which are comprised of Cretaceous limestones and Cenozoic siltstones and claystones (Haughton et al., 2005). Additionally, the Rockall Basin is boarded by smaller basins which contain up to 5 km of strata, such as the Erris Basin which locally encompasses over 1 km of Cretaceous sediments (Chapman et al., 1999). However, the timing of extension, igneous activity and sedimentological evolution in the Rockall Basin are poorly understood due to limited amount of boreholes and seismic data available (e.g. Haughton et al., 2005).

The Porcupine Basin (Figure 1.3) consists of sedimentary sequences up to 12 km thick (Shannon, 1992; Ryan et al., 2009) of which the Cretaceous and Cenozoic successions comprise up to 7 km (Croker and Klemperer, 1989; Jones et al., 2001). Haughton et al. (2005) investigated three drill-cores from the Porcupine High with relative thin Cenozoic layers due to their location (two on the western slope and one on the northern flank of the high), and revealed inversion of Jurassic successions sometime during the late Jurassic or early Cretaceous (Haughton et al., 2005). During the Paleogene, uplift of the Porcupine High probably caused an influx of clastic sediments into the Porcupine and Rockall basins (McDonnell and Shannon, 2001). This is evident in reflection seismic data from the Porcupine Basin which show a clear change from carbonate to clastic sedimentation during the late Cretaceous to early Paleogene throughout the basin (Shannon, 1992). Another possible source for

clastic sediments in the Porcupine Basin is the Irish mainland. The west coast of Ireland does not show early Cenozoic exhumation (Cogné et al., 2014), however, there is possibility of a Paleo-Shannon transporting clastic sediments from the east coast and the Irish Sea region into the western Irish offshore basins. This will be further discussed in section 8.7. Despite the evidence for small amounts of uplift and basin inversion, the Cretaceous and Cenozoic successions in the Porcupine – Rockall region show essentially no faulting (Croker and Klemperer, 1989; Jones et al., 2001). The Oligocene to present-day succession is dominated by deep-marine shales (Shannon, 1992).

2.3.2 Southern Irish and British offshore basins

The offshore basins of southern Ireland and Britain comprise the Celtic Sea, Cardigan Bay, St. George's Channel, Bristol Channel and Wessex-Weald basins (Figure 2.9). The structural framework developed during rifting associated with the break-up of Pangea during Permo-Triassic times, similar to the western Irish offshore basins. However, these basins follow old Variscan E-W oriented structures, unlike the western Irish offshore basins which follow older Caledonian NE-SW structures (Blundell, 2002). All southern Irish and British offshore basins show gentle folding caused by Cenozoic basin inversion and uplift which is likely associated with far-field compression from the Alpine orogeny (Blundell, 2002).

The Celtic Sea Basin is located to the south of Ireland (Figure 2.9) and consists of sedimentary successions up to 9 km thick (Shannon and Naylor, 1998). The majority of the sedimentary rocks consist of marine Lower and Middle Jurassic successions resting conformably on Triassic red beds. This sequence is followed by an unconformity with the overlying Lower and Upper Cretaceous successions over 1 km thick (Shannon and Naylor, 1998). The Cenozoic succession is quite thin compared to the Mesozoic rocks and is only up to 1 km thick (Robinson et al., 1981). Murdoch et al. (1995) recognised two Cenozoic uplift episodes in the Celtic Sea Basin which removed more than 1 km of sediments during Paleocene and Oligo - Miocene times (Shannon and Naylor, 1998).

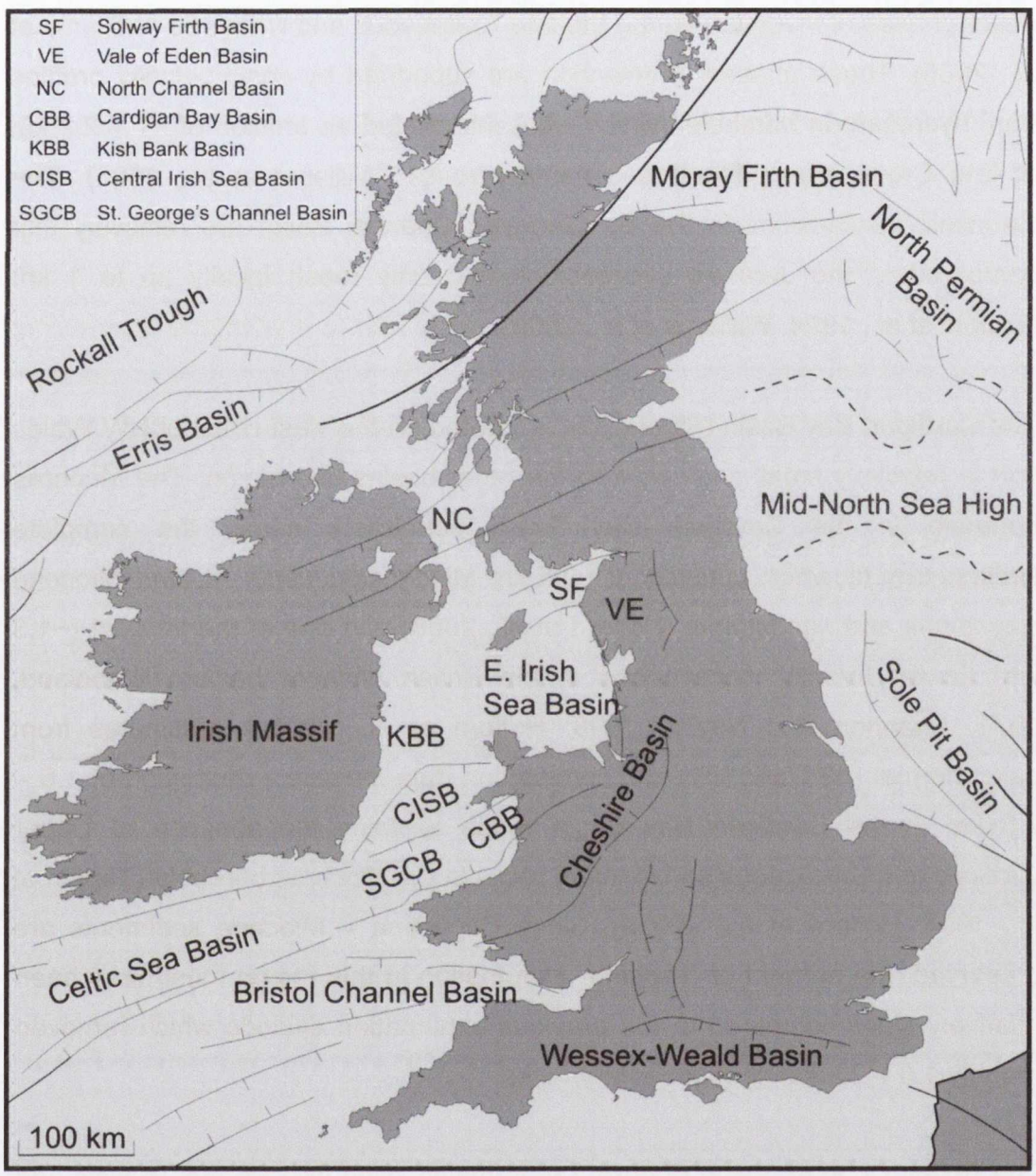


Figure 2.9: Map of the Irish Sea and southern Irish Sea basin systems (adapted after Woodcock and Strachan, 2012).

The St. George's Channel Basin (Figure 2.9) contains up to 12 km of post-Carboniferous successions (Welch and Turner, 2000b). Jurassic subsidence accompanied by extensional faulting resulted in Middle to Upper Jurassic successions attaining local maximum thicknesses of more than 5 km (Welch and Turner, 2000b; Holford et al., 2005a), which is one of the thickest Jurassic successions on the Irish and British continental shelf (Williams et al., 2005). Extensive seismic mapping of the St. George's Channel Basin revealed two

major phases of inversion during the late Cretaceous and Neogene (Williams et al., 2005). These phases of inversion are supported by sonic velocity profiles from hydrocarbon boreholes which were interpreted as erosion of ~1 – 2.2 km of late Cretaceous post-rift sedimentary rocks (Williams et al., 2005). The Cenozoic successions in the St. George's Channel Basin are relatively thin compared to the Jurassic successions and only reach locally up to 1 km (Tappin et al., 1994; Williams et al., 2005).

The Cardigan Bay Basin (Figure 2.9) is located on the west coast of NW Wales and is relatively small compared to the other basins this region. The Mochras borehole in the Cardigan Bay Basin penetrates nearly the complete sedimentary fill which consists of ~0.5 km Middle Oligocene – Lower Miocene claystones and sandstones (Holford et al., 2008) and one of the thickest (~1.3 km) Lower Jurassic successions in the British offshore basins (Woodland, 1971; Shannon and Naylor, 1998; Holford et al., 2005a). Estimates from paleothermal (AFT and VR) and compaction data indicate exhumation of 1.5 – 2.5 km in the Cardigan Bay Basin which explains the absence of Upper Jurassic and Cretaceous sedimentary rocks in the Mochras borehole (Tappin et al., 1994; Holford et al., 2005a). Since Oligocene – Miocene sediments are preserved, the amount of Neogene exhumation in this region must have been relatively small compared to the previous exhumation episode which removed roughly 1.5 – 2.5 km of sedimentary rocks.

The Bristol Channel Basin (Figure 2.9) is mainly filled with Permo-Triassic and early Jurassic sedimentary rocks up to 3.3 km thick (Kamerling, 1979) which crop out on the southern margins of the basin (Glen et al., 2005). Mid- to late Jurassic successions in the centre of the Bristol Channel Basin are documented in boreholes and seismic lines and indicate mid- to late Jurassic extension which was followed by thermal relaxation and subsidence (Glen et al., 2005). Cretaceous and Cenozoic successions occur only scattered across the Bristol Channel Basin (Tappin et al., 1994) which suggest that most Cretaceous and Cenozoic sediments were removed some time after deposition. Kamerling (1979) and Tappin et al. (1994) inferred from the stratigraphic evidence that the main pulse of exhumation in the Bristol Channel Basin occurred during the

Cretaceous and to a smaller extent during the Paleogene. This amount of exhumation is consistent with fission track studies from Holford et al. (2005b) who reported up to 3 km of exhumation during the Cretaceous and up to 2 km for the Palaeogene in the Irish Sea basin system.

Comparing the Cretaceous and Cenozoic strata in the southern Irish and western British offshore basins with the western Irish offshore basins reveal a clear trend in the thickness of the successions. The southern Irish and western British basins consist of mainly Triassic – Jurassic strata covered by only a thin Cretaceous and Cenozoic cover which is locally up to 2 km thick in the Celtic Sea Basin (Shannon and Naylor, 1998), whereas the western Irish offshore basins consists of 6 to 7 km of Cretaceous – Cenozoic successions in the Porcupine Basin and Rockall Trough, respectively.

2.3.3 Irish Sea basin system

The Irish Sea basin system comprises the North Channel, Solway Firth, the Kish bank, East Irish Sea and the Central Irish Sea basins (Figure 2.9). The region consists predominantly of Permo-Triassic sedimentary rocks and some Early Jurassic sedimentary rocks in the East Irish Sea Basin and the Solway Firth Basin (Figure 2.9).

The East Irish Sea Basin (Figure 2.9) contains up to ~5 km of Permian to Lower Jurassic sedimentary rocks resting on Carboniferous basement (Jackson et al., 1995). In general, post-Lower Jurassic successions are absent from the Irish Sea basin system (Shannon and Naylor, 1998), with the exception of a ~200 m thick succession of poorly dated Paleogene (Pleistocene or older; Naylor et al., 1993) sediments in the Kish Bank Basin. Beneath this thin layer of Paleogene sediments are up to 3 km of Permo-Triassic (Naylor et al., 1993) and Lower Jurassic successions in the Kish Bank basin (Broughan et al., 1989), and 3 km of Permo-Triassic sequences in the Central Irish Sea Basin (Maddox et al., 1995) which consisting of continental red beds and evaporites (Shannon and Naylor, 1998). Similar sequences were recognized in the Larne borehole onshore Northern Ireland (Holford et al., 2009a).

Several studies using AFT, compaction and seismic data (White and Lovell, 1997; Green et al., 2001a; Holford et al., 2005b), link the absence of post Lower Jurassic sediments in the Irish Sea basin system with pronounced exhumation (>3 km) in this region during Cretaceous and Paleogene (Cope, 1984; Lewis et al., 1992; Holford et al., 2005b). As outlined in the introduction to this thesis, constraining the timing and spatial distribution of exhumation around the Irish Sea basin system is the key goal of this study.

2.3.4 North Sea

The North Sea is divided into the northern North Sea Basin and the Southern North Sea Basin. For the purpose of this study, the focus is set to the western part of both regions. The northern North Sea Basin comprises the East Shetland Platform, East Shetland Basin, the Moray Firth Basin (Inner and Outer), Viking Graben and the Northern Permian Basin (Figure 1.3). The northern and southern parts of the North Sea are separated by the Mid-North Sea High and the Central Graben. The southern North Sea Basin comprises the Sole Pit Basin and the South Permian Basin (Figure 1.3).

In the northern part, the East Shetland Platform is surrounded by the Outer Moray Firth Basin, the South Viking Graben, and the East Shetland Basin. The East Shetland Basin developed during the Caledonian orogeny and is filled with mainly Devonian to recent sedimentary rocks and experienced two phases of rifting in the early Triassic and late Jurassic which is followed by a phase of thermal subsidence in the early to mid-Jurassic and Cretaceous respectively (Thomas and Coward, 1995).

The Paleocene successions are up to ~1 km thick and show at least 14 short duration sequences of mudstones representing maximum flooding events associated with transgression. These are unconformably overlain by sandstones and reworked chalks deposited in slope or basinal settings within extensive submarine fan systems around the East Shetland Platform during the Paleocene to earliest Eocene (~65 to 54 Ma; Mudge and Jones, 2004). Mudge

and Jones (2004) argue that these sequences were caused by fluctuation in dynamically supported uplift or by melt injected into the base of the crust which subsequently crystallized and had caused magmatic underplating. The initial uplift from the emplacement of the melt will eventually cease as the melt crystallizes and cause subsidence. This process of injecting melt and subsequent cooling occurs in multiple phases and thus causes multiple transgressive-regressive sequences (Maclennan and Lovell, 2002; Mudge and Jones, 2004). The submarine fans recognized by Mudge and Jones (2004) are comparable in age and size with the submarine fans from the Porcupine Basin (Shannon, 1992).

The Moray Firth Basin (Figure 1.3, Figure 2.9) developed during Permo-Triassic times and exhibits a second late Jurassic to early Cretaceous rifting episode (Andrews et al., 1990) and has not undergone any crustal shortening since at least earliest Cretaceous times (Mackay et al., 2005). The basin is up to 6 km deep (McQuillin et al., 1982) and consists mainly of Jurassic, Cretaceous and Cenozoic sedimentary rocks. The oldest exposed rocks are located close to the coastline of Scotland, and get progressively younger towards the eastern border of the Moray Firth Basin (Mackay et al., 2005). The oldest rocks in the west part of the basin show signs of burial and were subsequently uplifted and gently tilted up eastwards. The amount of removed sediment is quantified by extrapolating seismic profiles and is on the order of ~1 km (McQuillin et al., 1982). The Cretaceous succession is up to 3 km thick, and the upper Jurassic and lowermost Cretaceous sedimentary rocks are intercalated with Mesozoic syn-rift mass flow deposits (Gray, 2013). The Cenozoic sediments in the Inner and Outer Moray Firth Basin are around 1 km thick (Hillis, 1995) and contain a significant number of submarine fans of Paleogene and Eocene age (Shannon, 1992).

During Cenozoic times, Mackay et al. (2005) suggest that the Moray Firth Basin experienced both transient and permanent uplift caused by the proto-Iceland mantle plume by analysing the subsidence history of 50 boreholes within the Moray Firth Basin. Based on their results, Mackay et al. (2005) suggest that the whole Moray Firth Basin was dynamically uplifted by a distal part of the proto-

Iceland mantle plume during the early Paleocene (65 - 61 Ma). During the early Eocene, the Moray Firth Basin shows sign of subsidence which suggest that the effect of the mantle plume was waning at that stage. However, the subsidence analysis by Mackay et al. (2005) revealed that Inner Moray Firth was permanently uplifted by up to 1.3 ± 0.1 km decreasing from west to east, which they associate with the emplacement of the British Irish Paleogene Igneous Province in Scotland (BIPIP Scotland: 60.1 ± 0.6 Ma at Faeroes to 59.35 ± 0.6 at Arran; Ganerød et al., 2010).

Mass balance calculations suggest that the entire volume of Paleogene submarine fans in the northern North Sea Basins can be accounted for by less than 1 km of uplift of the East Shetland Platform and Scottish Highlands (Den Hartog Jager et al., 1993). In the southern part of the North Sea, the submarine fans are absent. Nevertheless, sonic velocity studies from the southern North Sea show that the centre of the southern North Sea region experienced nearly no exhumation, and exhumation steadily increases eastwards to approximately 1.5 km exhumation in eastern England (Hillis, 1995). This shows that exhumation took place even when the clastic fans are absent in the offshore basins, suggesting that the main successions eroded from the Lake District and Midlands Platform were chalk, Jurassic shales and Carboniferous limestone which would explain the lack of submarine fans in the southern part of the North Sea (Den Hartog Jager et al., 1993).

One basin located on the western margin of the Southern North Sea Basin system which does not show submarine fans is the Sole Pit Basin. It developed during Permo-Triassic times and was an area of continuous sedimentation and subsidence from the Permian to Jurassic (Van Hoorn, 1987b). During the Cretaceous and Paleogene, this basin was inverted associated with compressional stress, most likely from the Alpine foreland (Van Hoorn, 1987b; Green et al., 2001b).

2.4 Low-temperature thermochronology studies in Ireland and Britain

Understanding the causes of exhumation in Ireland and Britain as well as the uplift/subsidence history of the offshore basins requires knowledge of the timing and amount of exhumation. Several low-temperature thermochronology studies have examined the timing, distribution and magnitude of exhumation onshore, as well as the thermal histories of the offshore basins. Because Britain and Ireland have been intensively investigated using low-temperature thermochronology, the studies have been sub-divided by region, and focus on the broader regional conclusions rather than concentrating on the thermal histories of individual basins.

2.4.1 Southern England and the Irish Sea system

Hillis et al. (2008a) compiled 329 estimates of exhumation predominantly from southern and central England, Ireland and the Irish Sea region based on AFT, VR and compaction data. The resultant exhumation map was not in agreement with previously published maps supporting exhumation caused by underplating related to the Proto-Iceland mantle plume (e.g., Jones et al., 2002).

The compiled exhumation data of Hillis et al. (2008) shows three major differences to the map published by Jones et al. (2002; Figure 2.10). Firstly, the exhumation data shows variations of up ~1 km in exhumation over short distances (~10 km). Such short-wavelength variations are clearly not compatible with regional uplift associated with magmatic underplating. Secondly, magmatic underplating (e.g. as postulated by Jones and White, 2003) would cause exhumation sited on the area of the underplating assuming that the isostatic response to underplating is only local. However, the compiled exhumation data of Hilllis et al. (2008) shows significant exhumation outside of the zone of postulated plume-related denudation. Lastly, the timing of exhumation in the compiled exhumation data set of Hillis et al. (2008) indicates multiple exhumation events during the early Cretaceous, Paleogene and Neogene, whereas underplating would result in a single, major, Paleocene exhumation event.

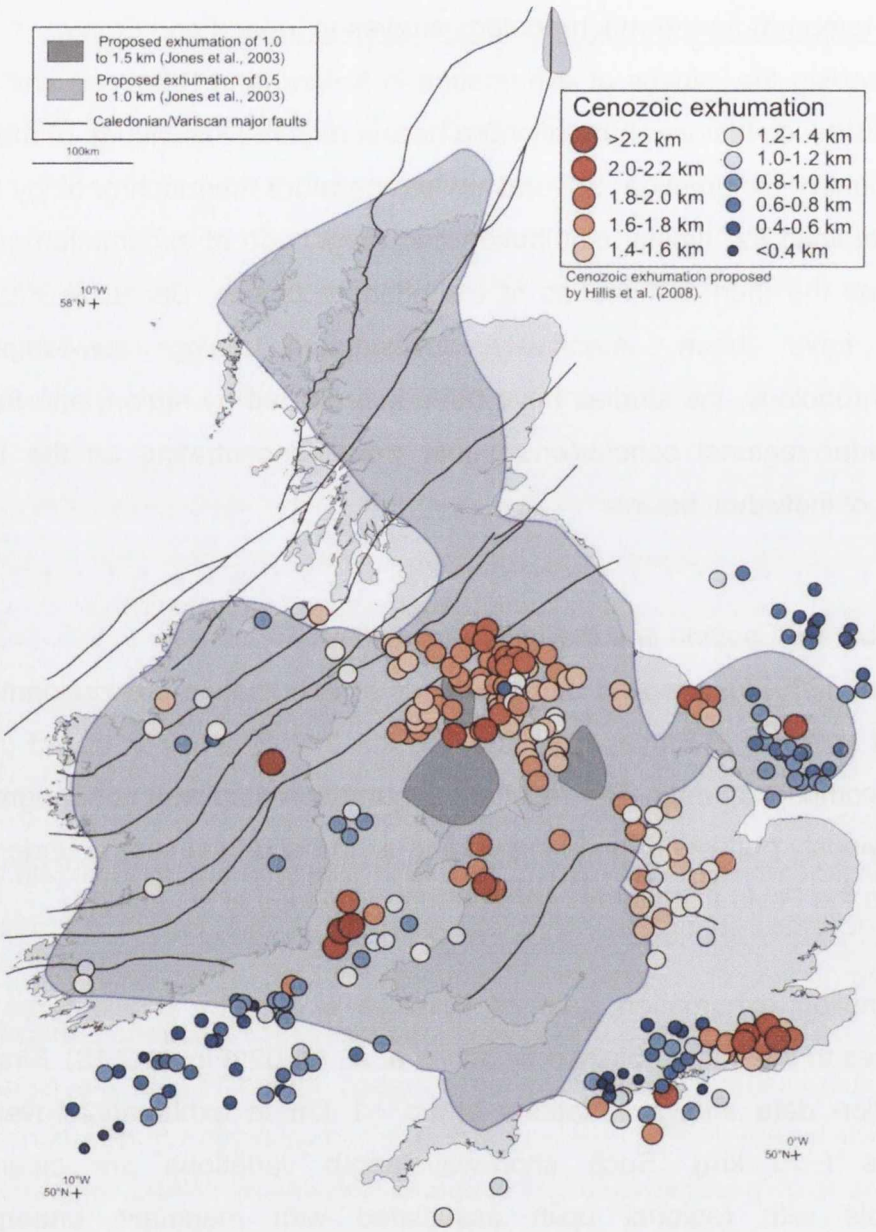


Figure 2.10: Map-based comparison of the denudation estimates from subsidence modelling and apatite fission track data from Jones et al. (2003) with the compiled AFT, VR and compaction data from Hillis et al. (2008).

These differences are in contradiction to exhumation caused solely by a mantle plume, and indicate that another tectonic mechanism must have occurred during Mesozoic and Cenozoic times. Therefore, Hillis et al. (2008a) concluded that exhumation was linked to crustal compression as a result of plate boundary stress transmitted into the plate interior rather than by magmatic underplating.

Holford et al. (2009b; 2010) proposed a similarly complex exhumation history for the Irish Sea basin system and NW Scotland, respectively. Their exhumation histories are similar to that published by Hillis et al. (2008a) and hence the Irish Sea basin system exhumation history of Holford et al. (2009b) is discussed in this section. Holford et al. (2009b) recognized four cooling episodes at around 120 – 115 Ma (early Cretaceous), 65 – 55 Ma (early Paleogene), 40 – 25 Ma (late Paleogene) and 20 – 15 Ma (early Neogene) by using onshore AFT data and comparing the results with major unconformities in the sedimentary record of the NW Atlantic margin (Praeg et al., 2005; Stoker et al., 2005a; Stoker et al., 2005b) as well as with deformation events at the plate boundaries. Each of these cooling episodes was of regional extent (~10^6 km^2) and involved removal of up to 1 km of strata (Holford et al., 2009b).

The first suggested exhumation episode took place in the early Cretaceous (120 – 115 Ma) and was related to the onset of seafloor spreading in the North Atlantic between the Bay of Biscay and Newfoundland during the Aptian (c. 118 Ma; Johnston et al., 2001; Holford et al., 2005b). The second exhumation episode occurred during the early Paleogene (65 – 55 Ma) at the same time as postulated magmatic underplating (Brodie and White, 1994; Jones et al., 2002). However, Holford et al. (2009b) instead relates early Paleogene exhumation to far-field stresses from either continental rifting to the NW of the Britain and Ireland which separated Greenland from Europe at around 55 Ma (Doré et al., 1999) and was accompanied by subaerial volcanism (White and McKenzie, 1989), and/or to the compressional stress caused by collision of the Alpine collision front with flexural basins and continental terranes in the European foreland. In both cases, compressional stress was inferred to have been transmitted >1500 km across the plate causing exhumation of up to 1 km and more (Ziegler et al., 1995; Dèzes et al., 2004; Holford et al., 2009b).

The third exhumation episode proposed by Holford et al. (2009b) took place during the late Paleogene (40 - 25 Ma). They linked this exhumation with unconformities along the North Atlantic margin and with possible uplift in Scandinavia (Japsen et al., 2007), along with the termination of seafloor spreading in the Labrador Sea and the associated "unification" of Greenland

with the North American plate (Doré et al., 1999; Holford et al., 2009b). Another possible explanation for this exhumation episode is related to compressional deformation in the Alpine orogeny (Pyrenean phase; Ziegler et al., 1995; Dèzes et al., 2004).

The last proposed exhumation episode occurred during the Neogene (20 – 15 Ma). At this time, the European plate changed its motion from north-directed drift to a more eastward motion and North Atlantic mid-ocean ridge exhibits increased spreading rates (Mosar et al., 2002). This change in plate motion may have led to a plate-wide phase of uplift and deformation during the mid-Miocene (Holford et al., 2009b). Furthermore, major magmatic events lead to the development of the "Iceland Plateau" during the mid-Miocene (Dore et al., 2008; Holford et al., 2009b). The formation of the "Iceland Plateau" at the mid-oceanic ridge may have increased compression along the NW Atlantic margin. There is also strong convergence between Africa and Europe along the Alpine orogenic belt in the Neogene (Dewey, 2000).

The basins located within the Irish Sea region contain no Cenozoic cover. However, the Celtic Sea Basin, St. George's Channel Basin, Cardigan Bay Basin, Bristol Channel and Wessex Basin (Figure 2.9) exhibit a more complete Mesozoic record with some Cenozoic strata present (Tappin et al., 1994; Williams et al., 2005). The Cardigan Bay Basin is of interest for the Mesozoic-Cenozoic exhumation history as it contains ~0.5 km Cenozoic sedimentary rocks which range in age from the mid-Oligocene to lower Miocene (~29 - 20 Ma), and about ~1.3 km of lower Jurassic rocks (Herbert-Smith, 1979; Tappin et al., 1994; Holford et al., 2005a).

Holford et al. (2005a) proposed only two major cooling events for the Cardigan Bay Basin, during the early Cretaceous (120 – 115 Ma) and the Neogene (20 – 0 Ma). The two cooling episodes are roughly in agreement with the exhumation episodes recognized by Hills et al. (2008a) for the southern Irish Sea System, however the late Cretaceous – early Paleogene exhumation episode is absent. The Holford et al. (2005a) exhumation models for the Cardigan Bay Basin suggest a maximum of 0.8 km exhumation, which is far less than anticipated for

a basin close to the locus of proposed plume-related Paleogene exhumation (Cope, 1984; Jones et al., 2002; Holford et al., 2005a).

To the southwest of the Cardigan Bay Basin, similar sequences of sedimentary rocks are encountered in the St. George's Channel Basin. Here, the successions consist of locally up to ~5 km of mid- to upper Jurassic strata (Welch and Turner, 2000b; Holford et al., 2005a), and locally up to 1.5 km of Eocene – Oligocene sedimentary rocks (Tappin et al., 1994; Williams et al., 2005). Williams el al. (2005) recognized late Cretaceous – Paleogene exhumation based on reflection seismic profiles. The profiles show mainly Jurassic sequences overlain by Eocene sedimentary rocks and separated by a Cenozoic unconformity. Williams et al. (2005) associates this early Paleogene exhumation episode with tectonic inversion in response to NW-directed compression which would be consistent with Alpine convergence at this time (Ziegler et al., 1995). However, Williams et al. (2005) do not rule out a regional component and suggests the tectonic inversion is superimposed on a magmatic underplating event. Due to the paucity of Cenozoic sedimentary rocks around the Irish Sea Basin system, is it difficult to constrain the timing and distribution of exhumation on a regional basis based only on reflection seismic profiles.

The seismic reflection data from the St. George's Channel Basin indicates compressional shortening during the Neogene. This is coeval with compressional shortening in southern England and the Cardigan Bay Basin (Holford et al., 2005a; Hillis et al., 2008a). Holford et al (2008) suggested that compression at the North Atlantic margin might be responsible for intraplate exhumation and shortening of sedimentary basins >1500 km away from the plate boundary. They claim that up to 1 – 1.5 km of Neogene exhumation was caused by compressional shortening and the resultant thickening and uplift of the Cenozoic sedimentary basin fill in southern England and the Irish Sea Basin system (Holford et al., 2008).

2.4.2 Scotland

The exhumation events recognized by Holford et al. (2010) in NW Scotland are similar to those detected in southern England (e.g. Hillis et al., 2008a) and the Irish Sea basin system (e.g. Holford et al., 2005b; Hillis et al., 2008; Holford et al., 2009b). However, the timing of the episodes differs slightly compared to the Irish Sea Basin system. Holford et al. (2010) recognized two distinct cooling episodes in NW Scotland during early to mid-Cretaceous (140 – 130 Ma and 110 – 90 Ma), whereas the Irish Sea basin system shows only one cooling episode at 120 – 115 Ma (Holford et al., 2005b). The Paleogene cooling episode lasted only ~5 Ma (65 – 60 Ma) in Scotland and about 10 Ma in the Irish Sea basin (65 – 55 Ma). Additionally, Neogene cooling in Scotland started about 5 Ma later (15 – 10 Ma) than in the Irish Sea Basin system (20-15 Ma) (Holford et al., 2005b; Holford et al., 2010). The differences in the timing of cooling between NW Scotland and the Irish Sea region results in some uncertainty in the correlation of cooling episodes onshore and with unconformities offshore.

Furthermore, an additional exhumation pulse was recognized during the Triassic (245 – 225 Ma) in NW Scotland, that was not detected in the Irish Sea Basin system, or southern England (Holford et al., 2009b; Holford et al., 2010). Holford et al. (2010) suggested that this cooling episode represents a final stage of post-Caledonian unroofing prior to reburial beneath thick Triassic and Jurassic sequences that were inferred to cover the Scottish Highlands. Holford et al. (2010) linked the exhumation pulses in NW Scotland with the sedimentary record in the offshore basins (Rockall and Faroe-Shetland basin) in northwest Britain (Stoker et al., 2010), and attributed the cooling histories to exhumation due to plate boundary stresses from the North Atlantic oceanic ridge system and from Alpine compression. Only the early Paleogene cooling was not linked to tectonic activity and instead was linked with burial beneath lava or hydrothermal and contact heating widespread across Scotland and the north of Ireland at that time (Holford et al., 2010).

Persano et al. (2007) investigated two vertical profiles from the Outer Hebrides and the western Scottish mainland to constrain the timing and magnitude of

early Cenozoic denudation using both AFT and AHe dating. Their AFT ages range from 186 ± 6 Ma to 257 ± 12 Ma and their AHe ages ranges from 77 ± 8 Ma to 265 ± 27 Ma (F_T-corrected). However, the AFT and AHe results were not modelled together. The AFT results were modelled separately using the AFTSolve software (Ketcham et al., 2000) and the AHe results were forward modelled using DECOMP (Dunai et al., 2003). Persano et al. (2007) recognized a rapid cooling event between 65 and 47 Ma from the AHe forward modelling.

The amount of early Cenozoic denudation was estimated by Persano et al. (2007) by deriving the geothermal gradient for each profile via the predicted t-T paths for the AHe ages at 65 Ma, and using the temperature difference between the bottom and top sample to constrain the geothermal gradient. A geothermal gradient of 19 ± 6 °C/km was obtained for the Outer Hebrides and 39 ± 9 °C/km for the western Scottish Mainland, resulting in denudation estimates of 2250 ±750 m denudation for the Outer Hebrides and 1330 ±230 m in the western Scottish mainland. These denudation estimates are in broad agreement with geophysical models proposing mantle upwelling, magmatic activity and magmatic underplating beneath the western part of Scotland and the Irish Sea region (Brodie and White, 1994; Al-Kindi et al., 2003; Arrowsmith et al., 2005).

2.4.3 Central England, Southern Uplands, Lake District and Pennines

Northern England was among the first regions where AFT dating was used to estimate the amount of exhumation in Britain and Ireland (Green, 1986). AFT data from Green (1986) and Green et al. (2012) show similar late Cretaceous to Paleogene ages for most parts of northern England, with some older Permo-Triassic ages, mainly from the east coast. Green (1986) stated that the region was subjected to kilometre-scale uplift at ~60 Ma, whereas Green et al. (2012) inferred Paleogene exhumation to have been modest and presumably short-lived and related to heating effects associated with underplating at the base of the crust. Thus, they concluded that Paleogene cooling in northern England was caused by the decrease in an elevated geothermal gradient of ~55 to 61

°C km^{-1}, probably linked to the BIPIP emplacement, to the present-day gradient of 38 °C km^{-1} (Green et al., 2012).

AFT and VR data from the Midlands in Central England show evidence for two exhumation episodes during the early and late Paleogene (Green et al., 2001b). However, the data indicates a complex pattern of cooling which would not coincide with a magmatic underplating model. Instead, Green et al. (2001b) correlated the exhumation pattern with the distribution of Paleozoic basins and suggests that far-field stress has reactivated the basin-bounding faults at different times, causing spatial and temporal variable exhumation across Central England.

2.4.4 Ireland and Northern Ireland

Ireland is well covered by AFT and VR data (Clayton et al., 1989; McCulloch, 1993; Green et al., 2000; Corcoran and Clayton, 2001; Allen et al., 2002). The wealth of data suggest cycles of exhumation and reburial during the mid-Jurassic, early Cretaceous and early Cenozoic (Green et al., 2000; Cogné et al., 2014), which is in broad agreement with studies from Britain (Hillis et al., 2008a; Holford et al., 2009b; Holford et al., 2010) and Northern Ireland (Holford et al., 2009a). However, other authors suggest a more monotonic exhumation history for Ireland during the Mesozoic, with a restricted phase of reburial during the late Cretaceous and a rapid exhumation episode during the Cenozoic (Allen et al., 2002).

The western margin of Ireland was recently examined by Cogné et al. (2014) using the AFT and AHe techniques, combined with vertical profile modelling using the QTQt software of Gallagher et al. (2005b; 2012). Their results suggest a progressive cooling event starting during the mid- to late Jurassic in NW Ireland and occurring in the late Jurassic to early Cretaceous in SW Ireland. Green et al. (2000) proposed similar cooling events for onshore Ireland from early to mid-Jurassic (180 – 170 Ma), Cretaceous (125 – 110 Ma), early Paleogene (65 – 55 Ma) and early Neogene (25 – 15 Ma). However, Green et al. (2000) argued that each event is a single cooling event with subsequent

reburial, whereas Cogné et al. (2014) linked this progressive north to south cooling episode to one diachronous exhumation event caused by rift-shoulder uplift and subsequent erosion. The late Cretaceous and Cenozoic exhumation history of western Ireland remains ambiguous since the low-temperature thermochronology techniques are not sensitive enough below ~40°C and therefore cannot constrain for small amounts of cooling during that time. However, QTQt modelling suggest reburial of western Ireland beneath ~1.5 km of sedimentary rocks during the late Cretaceous to early Cenozoic and removal of this cover during the Neogene probably related to compressional stress at the plate boundaries and possible enhanced erosion associated with Pleistocene glaciation (Cogné et al., 2014).

Northern Ireland shows similar cooling (exhumation) events for Mesozoic times but the occurrence of flood basalts (62.3 ± 0.3 to 59.6 ± 0.3 Ma; Ganerød et al., 2010) and igneous intrusions of Paleogene age (microprobe U-Pb age: 56.4 ± 1.4 Ma; Gamble et al., 1999) complicate the Cenozoic exhumation history (Holford et al., 2009a). Recent studies suggest that the Upper Cretaceous Chalk preserved beneath the Antrim flood basalts were buried up to ~1.5 - 2 km deeper which would indicate a much thicker sequence of flood basalts (Holford et al., 2009a). AFT and compaction data from the Larne No. 2 borehole indicate exhumation episodes during the mid-Jurassic and early Cretaceous and indicate deeper burial of the preserved sections by up to 1.3 km before late Cenozoic exhumation. The removed section could have included considerable amounts of flood basalt (Holford et al., 2009a). The Mourne Mountains is a Paleogene igneous intrusion in southern Northern Ireland, which is slightly younger than the flood basalts (microprobe U-Pb age: 56.4 ± 1.4 Ma; Gamble et al., 1999). The occurrence of an igneous intrusion which is now at the surface indicates substantial amounts of exhumation after the emplacement of the intrusion.

2.5 Mantle-driven processes in Ireland and Britain

Several studies have investigated the presence of magmatic underplating beneath the Irish Sea region, SW Scotland and beneath the North Atlantic shelf

and linked the underplating with the activity of the proto-Iceland mantle plume (Brodie and White, 1994; White and Lovell, 1997; Jones et al., 2002; Maclennan and Lovell, 2002; Al-Kindi et al., 2003; Arrowsmith et al., 2005). The main argument is a temporal and spatial correlation between uplift in Britain and Ireland, magmatic activity of the proto-Iceland mantle plume (Nielsen et al., 2002; Jones and White, 2003) as constrained by magmatism in the North Atlantic region, including the BIPIP between 62.6 ± 0.3 to 59.2 ± 1.4 Ma (Figure 2.8; Ganerød et al., 2010). Evidence for mantle-driven processes is based on examination of the stratigraphy in the offshore basins (Brodie and White, 1994; Brodie and White, 1995; White and Lovell, 1997; Jones et al., 2002; Praeg et al., 2005) and geophysical data including long-wavelength free-air gravity anomalies, wide-angle seismic data (Al-Kindi et al., 2003) and low-velocity seismic anomalies (Arrowsmith et al., 2005).

The basins within the Irish Sea Basin system can be used to study Paleogene uplift. The observed syn-rift subsidence can be used to calculate the post-rift subsidence by using the lithospheric stretching and cooling model (McKenzie, 1978). However, the basins around the Irish Sea region often do not contain any significant amount of Cenozoic sedimentary rocks. It would be unusual if the basins failed to subside after earlier rifting events and not be filled by a thermal subsidence succession (Brodie and White, 1994). Therefore, it is likely that up to ~3 km of post-rift sediments were removed from the basins due to uplift (Brodie and White, 1994).

Since Mesozoic sedimentary rocks are still preserved in southwest Britain, the simplest way to achieve this structure is to uplift Britain in the northwest (Brodie and White, 1994). This is also compatible with the deposition and geometry of turbidite fans and debris flows in the North Sea during the Paleogene (Shannon, 1992; White and Lovell, 1997). In particular, between 62 and 54 Ma a series of major submarine fans were deposited around Scotland (Mudge and Jones, 2004). Simultaneous pulses of fan sedimentation are recognized in the North Sea, Porcupine Basin, southeast England and in the Faeroe – Shetland Basin (White and Lovell, 1997).

Al-Kindi et al. (2003) used forward and inverse modelling of wide-angle seismic data and free-air gravity data to determine the three-dimensional shape of the magmatic underplating body. Their measurements for a high velocity, and therefore dense, body beneath the Irish Sea region are consistent with the crystallization of partial melt derived from the mantle into gabbro (Maclennan and Lovell, 2002). These results suggest that a linear sheet of hot mantle material was emplaced into the lithosphere and could directly cause uplift in and around the Irish Sea region and parts of Scotland (Figure 2.11). The model of Al-Kindi et al. (2003) also shows layering of the magmatic body which most likely suggest multiple injections of magma which would correspond with periodic sedimentation of 0.5 – 1 m.y. submarine fan cycles in offshore Scotland and the North Sea (White and Lovell, 1997). Furthermore, the modelled position of the underplated body (Al-Kindi et al., 2003) broadly coincides with gravity anomalies and the occurrence of igneous intrusions in Scotland, Ireland, the Irish Sea region and northern England as well as with the Antrim flood basalts in Northern Ireland (Ganerød et al., 2010). At 55 Ma magmatism ceased and the rate of sedimentation declined, which corresponds with the onset of sea-floor spreading between Greenland and Europe (White and Lovell, 1997).

Jones et al. (2003) associates the Paleogene exhumation in Ireland and Britain as well as the emplacement of the BIPIP with dynamic supported uplift caused by a horizontally-traversing hot mantle layer beneath the lithosphere originating from the incipient proto-Iceland mantle plume system. Normally, post-rift sedimentary basins should subside monotonically through their post-rift phase; however, the Outer Moray Firth, North Sea and Porcupine basin indicate phases of transient uplift within the post-rift sediments. This indicates a phase of transient uplift after the initial rifting phase at least in the offshore basins.

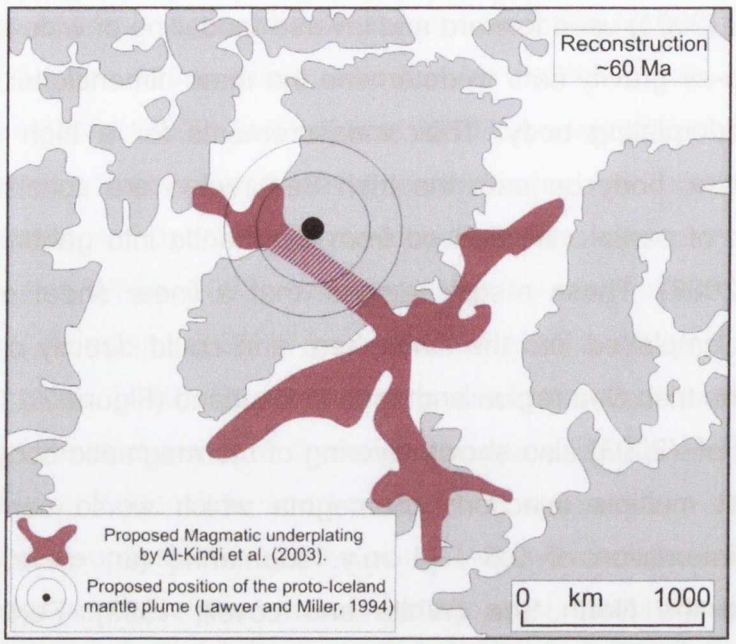


Figure 2.11: Elongate tongue of hot mantle material originating from the proto-Iceland mantle plume beneath Greenland reaching into the Irish Sea system (adapted after Al-Kindi et al., 2003).

Jones et al. (2002) investigated long wave-length gravity and bathymetric anomalies across the North Atlantic, and estimated the amplitude of dynamic uplift caused by the proto-Iceland mantle plume using the present-day dynamic supported uplift above Iceland and surrounding areas as constraints. Today, Iceland experiences ~1.5 to 2 km dynamically supported uplift and the NW European shelf experiences ~0.5 km associated with the Icelandic mantle plume. Similar amounts are inferred for the proto-Iceland mantle plume and its effects on Ireland and Britain. Based on mass balance calculations, which are in agreement with the amount of denuded material and the volume of sediments deposited in the northern North Sea and the Rockall Trough, Jones et al. (2002) concluded that a sub-vertical sheet of anomalously hot asthenosphere welled up beneath an axis from Faroes through the Irish Sea towards Lundy in the Bristol Channel and generated magmatic underplating.

A comprehensive geophysical receiver function study across Ireland, Britain and parts of NW Europe was carried out by Davis et al. (2012) to estimate the crustal thickness beneath Britain and Ireland. They assembled 3200 receiver functions for 1055 seismic events using 51 three-component broadband

seismometers. Their results indicate that the crustal thickness varies across Ireland and Britain between 24 and 36 km, whereby the thickest crust can be found beneath north Wales and central Scotland. Crustal thickness decreases towards NW Scotland and NW Ireland but the decrease negatively correlates with elevation and free-air gravity anomalies. Davis et al. (2012) suggest that elevation in NW Scotland and NW Ireland nowadays is linked to sub-lithospheric isostatic supported uplift caused by a hot buoyant "tongue" of asthenosphere originating from the Icelandic mantle plume. Jones et al. (2002) used free-air gravity anomalies and oceanic bathymetric anomalies to estimate the todays dynamic support from the Iceland mantle plume on the NW European shelf (including Ireland and Britain) to be less than 0.5 km. Additionally to the dynamic support, Davis et al. (2012) argue that a thick layer of high-velocity lower crustal rock exists beneath Scotland and expands further south, which is spatially consistent with the occurrence of Cenozoic magmatism and Paleogene denudation and is consistent with a zone of magmatic underplating (White and Lovell, 1997).

2.6 How do previous studies support the far-field stress/mantle-driven hypotheses?

The reviews of low-temperature, geophysical and stratigraphic studies above reveal a "correlation" between the techniques employed and the inferred cause for early Cenozoic exhumation in Ireland and Britain. In general, geophysical deeper crust and mantle studies (i.e. Al-Kindi et al., 2003; Arrowsmith et al., 2005; Davis et al., 2012) support a mantle-driven process, whereas AFT studies support far-field stress (i.e. Green et al., 2000; Holford et al., 2005b; Holford et al., 2010). The exception is the study by Persano et al. (2007) who used AFT and AHe dating and suggested magmatic underplating as cause for Cenozoic exhumation. The difference between the other AFT studies and that of Persano et al. (2007) was the use of the AHe system as an additional low-temperature thermochronology method. The advantage of combining AFT with AHe dating will be discussed in chapter 3. Cogné et al. (2014) also used AFT and AHe dating to investigate the western Irish onshore region, but their thermal models do not support far-field stress nor mantle-driven processes

during the Early Cenozoic. However, the western Irish onshore region is ~300 km away from the Irish Sea region and thus from the postulated region of maximum early Cenozoic exhumation.

3. Thermochronology

3.1 Introduction

Thermochronology is the study of the thermal history of minerals, rocks and geological terranes through time by using temperature-sensitive radiometric dating methods (Reiners, 2005) (Figure 3.1). Many common rock-forming and in particular accessory minerals contain radioactive isotopes (parent isotopes) which decay at a known rate and produce daughter products such as other radiogenic isotopes (or alternatively damage tracks) in the crystal lattice. Over time, the daughter product accumulates in the mineral.

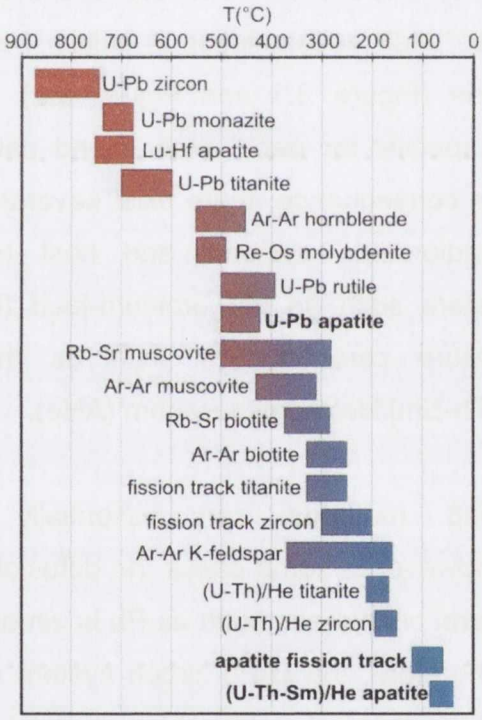


Figure 3.1: Temperature sensitivities ("closure temperatures") of different radiometric dating methods including the apatite U-Pb, fission track and (U-Th-Sm)/He dating methods used in this study (adapted after Carlson, 2011).

The principle behind radiometric dating methods is based on the fact that each parent isotope has a specific decay rate, and by using this decay rate and the ratio of the parent isotope to daughter product it is possible to calculate the time since the daughter product accumulated in the host mineral (e.g. Rutherford, 1905). However, the accumulation of the daughter product is not only dependent on the decay rate and the time elapsed, but also on the diffusion

loss (or annealing) of the daughter product in the mineral which is thermally activated (i.e. it is a function of temperature). Thermally activated diffusion means that the diffusion rates are higher at higher temperatures, resulting in the daughter product being prevented from accumulating in the host mineral. With decreasing temperature the rate of diffusion (annealing) decreases. The time where daughter products start to accumulate in the host mineral because the diffusion rate (annealing) is lower than the generation of daughter products is called the "closure temperature" (T_c) (Dodson, 1973). However, the concept of an apparent age T_c is oversimplified as there is a transition zone where diffusion (annealing) is happening but daughter products are also accumulated in the host mineral. The temperature zone between the closure temperature and the temperature of "total" accumulation is called the "partial retention" or "partial annealing" zone (Figure 3.1 and Figure 3.2). The zone of partial retention/annealing is specific for each mineral and parent/daughter system used (Figure 3.1). As a consequence, there exist several thermochronometers employing different radiometric systems and host minerals, from high-temperature chronometers such as the uranium-lead (U-Pb) zircon system down to low-temperature chronometers such as the (uranium-thorium-samarium)/helium ([U-Th-Sm]/He) apatite system (AHe).

All radiometric dating methods can essentially be regarded as thermochronometers, however in some cases the diffusion rate is already very low when the host mineral crystallizes such as Pb in zircon (>900°C; (Cherniak and Watson, 2000). Therefore, the U-Pb zircon system does not yield useful information concerning the thermal cooling history, but instead constrains the timing of crystallization of the mineral. Thus, the U-Pb zircon system is regarded as a geochronometer which yields absolute ages on the timing of a magmatic, metamorphic or hydrothermal event. The main difference between thermochronology and geochronology is therefore that thermochronology can resolve both temporal and thermal aspects of minerals, and thus give estimates on the timing and magnitude of a diverse suite of geological processes (Reiners, 2005).

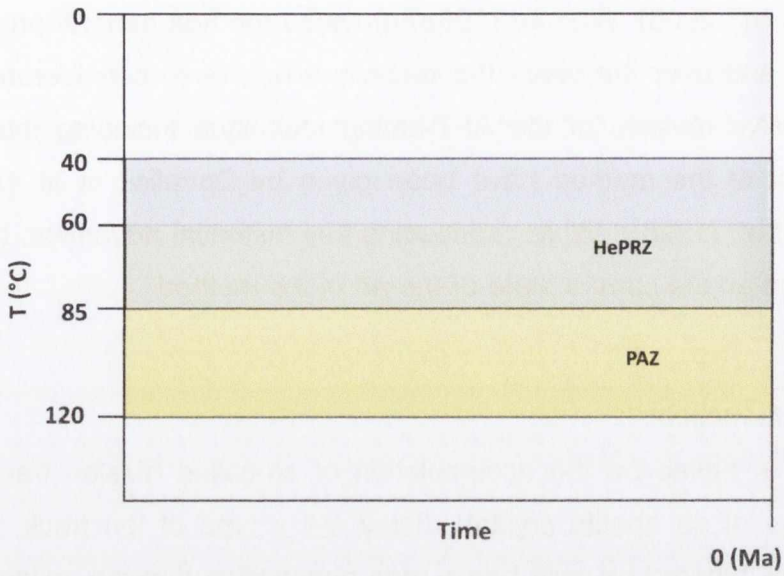


Figure 3.2: Temperature sensitivities of the apatite fission track dating (AFT) and apatite (U-Th-Sm)/He dating (AHe) methods. HePRZ: Helium partial retention zone for AHe dating (Wolf et al., 1998). PAZ: Partial annealing zone for AFT dating (Gleadow and Duddy, 1981).

The application of low-temperature thermochronometers to examining cooling histories below ~120°C has become more popular in recent years, because these thermochronometers are capable of investigating earth-surface processes and the interactions between tectonics, erosion and climate (Reiners, 2005). Since the goal of this study is to investigate the late Mesozoic to Cenozoic exhumation history of Ireland and Britain, low-temperature thermochronometers (apatite fission track (AFT) dating and apatite (U-Th-Sm)/He (AHe) dating) with an effective temperature range of 120 - 40°C were employed (Figure 3.2). Therefore, this chapter provides an overview of these methods. Furthermore, an overview of the U-Pb apatite system is also given, as this medium-high temperature thermochronometer (500 - 425°C, Chamberlain and Bowring, 2001) is a very useful "by product" of the LA-ICP-MS apatite fission track approach employed in our laboratory, which can be used as a high-temperature constraint on thermal history models.

3.2 Apatite fission track dating

The apatite fission track (AFT) dating method has been widely used for constraining low-temperature thermal histories over the past four decades

(Donelick et al., 2005). Wagner (1968) provided the first general procedure for AFT dating and over the years the technique has been considerably refined. Comprehensive reviews of the AFT-dating technique including the historical development of the method have been given by Donelick et al. (2005) and Gallagher et al. (1998). While mentioning key historical advances, this review focuses more on the current state-of-the-art of the method.

3.2.1 Track formation

AFT dating is based on the accumulation of so-called "fission tracks" in the crystal lattice of an apatite crystal. They are a type of ion track, which are damage trails created by swift heavy ions penetrating through solids. Several models have been put forward in the literature to describe ion track formation (including fission tracks) including the ion explosion spike model (Figure 3.3), the electron collision cascade model and the thermal spike model; the ion spike explosion model of Fleischer et al. (1975) is described here. During spontaneous fission of radioactive ^{238}U nuclei, which are unstable due to their atomic structure, two highly charged heavy particles are produced, releasing ~200 MeV (milli-electron volt) of energy, which is released in the movement of the two fragments (Friedlander et al., 1981). The charged particles recoil as a result of Coulomb repulsion and interact with other atoms in the crystal lattice by stripping away electrons (ionization), which is followed by further deformation in the crystal lattice because the ionized atoms in the lattice repel each other (Gallagher et al., 1998) (Figure 3.3). The interaction with the crystal lattice and the electron capturing leads to a loss of kinetic energy and eventually the particles come to rest, leaving behind defects in the crystal lattice termed fission tracks (e.g. Gallagher et al., 1998).

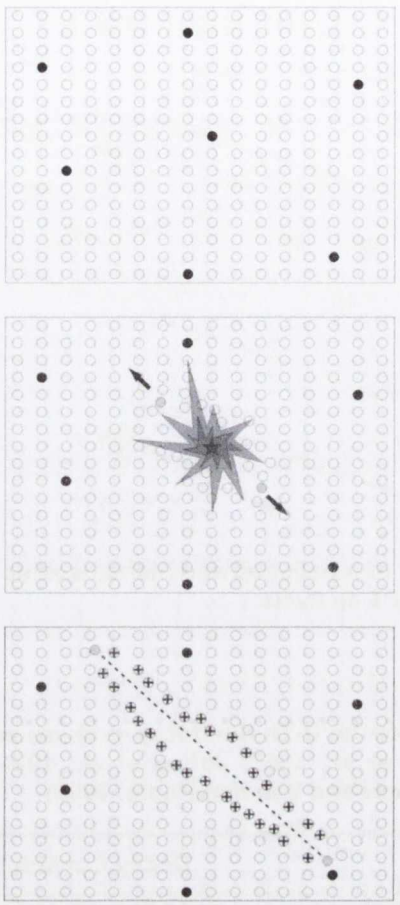


Figure 3.3: The ion spike explosion model adapted from Fleischer et al. (1975). Black circles: ^{238}U atoms in the apatite crystal lattice. White circles: other atoms in the apatite crystal lattice.

The defects are usually only ~3 – 14 nm wide (Paul and Fitzgerald, 1992) and therefore apatite grain surfaces are chemically etched so they can be seen under an optical microscope (Figure 3.4). In this study we used the etching "recipe" of Carlson et al. (1999) which uses 5.5 N HNO_3 for 20.0s (± 0.5s) at 21°C (± 1°C) to etch fission tracks, as most modern fission-track annealing protocols are calibrated against this and similar etching protocols (Ketcham et al., 1999; Ketcham et al., 2007a; Ketcham et al., 2007b). Etched fission tracks in apatite are up to 16.3 µm long and usually ~2 µm wide (Fleischer et al., 1975), and can be characterised under a petrological microscope at high magnification. ^{235}U and ^{232}Th undergo far fewer spontaneous fission reactions with time, so that their contribution to the overall accumulated fission track density in a mineral can be neglected.

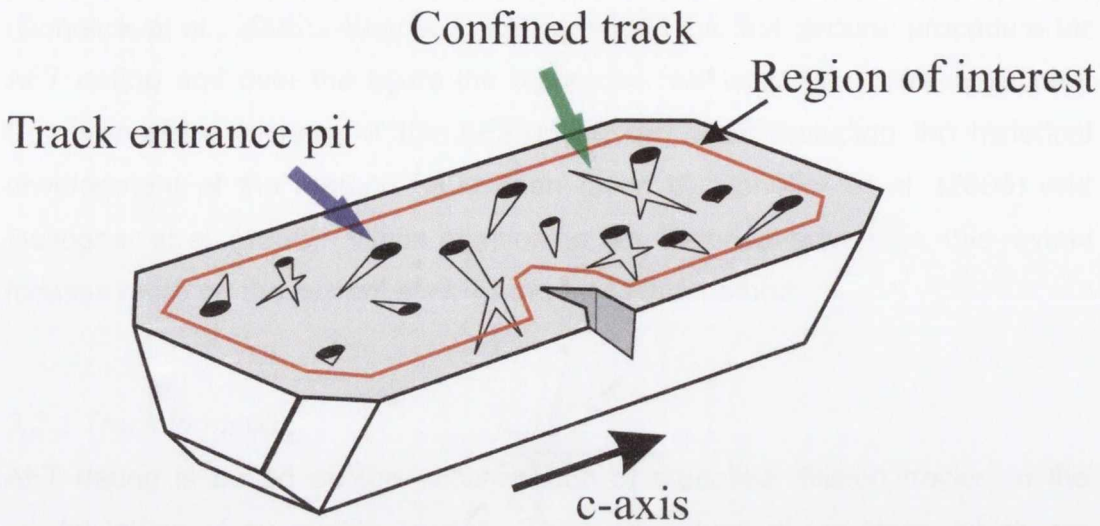


Figure 3.4: Schematic image of a polished and etched apatite crystal. Red line (Region of interest): Area counted for AFT analysis.

Table 3-1: Decay constants for the U-Th-Sm decay systems employed in low-temperature thermochronology (Lederer et al., 1967; Jaffey et al., 1971; Steiger and Jäger, 1977; Friedlander et al., 1981; Wagner and Van den Haute, 1992).

Isotope	Decay Constant (yr^{-1})
^{238}U	1.552×10^{-10} yr^{-1} (α)
	~7.5×10^{-17} yr^{-1} (s.f.)
^{235}U	9.848×10^{-10} yr^{-1} (α)
^{232}Th	4.947×10^{-11} yr^{-1} (α)
^{147}Sm	6.538×10^{-12} yr^{-1} (α)

Notes:

α: alpha-decay series

s.f.: spontaneous fission decay

3.2.2 From the general isotope age equation to the fission track age equation

In principle, each thermochronometric dating system is based on the ratio of an isotope (daughter isotope) produced by radioactive decay of an unstable isotope (parent isotope) in a mineral (Braun et al., 2006). Thus, constraining the isotopic age depends on the rate at which the unstable isotopes decays (decay constant λ; Table 3-1), as well the abundance of both parent (N_p) and daughter isotopes (N_d).

Under the assumption that the crystal is a closed system, which means no loss or implantation of daughter and/or parent isotopes (Dodson, 1973; Braun et al., 2006), the general isotopic age equation is given by

$$t = \frac{1}{\lambda} \ln\left(1 + \frac{N_d}{N_p}\right)$$

Equation 1

where, N_d is the amount of daughter isotope, N_p the amount of parent isotope and λ the total decay constant.

Equation 1 only applies if the parent isotope decays by one pathway (i.e. only alpha-decay). If the parent isotope decays into for example two daughter isotopes (N_{d1} and N_{d2}) with different decay constants (λ_1 and λ_2), then the isotopic age for one of these systems can be calculated by:

$$t = \frac{1}{\lambda} \ln\left(1 + \frac{\lambda}{\lambda_1} \frac{N_{d1}}{N_p}\right)$$

Equation 2

^{238}U decays not only by alpha and beta decay but also via spontaneous fission decay, which does not produce a measureable daughter isotope, but instead leaves behind fission tracks (i.e. damage-trails represent the daughter product) in the crystal lattice as explained in section 3.2.1. These fission tracks are counted on a polished and etched apatite grain surface. Thus, the number of daughter products is given by the counted number of spontaneous tracks (N_s) and the total abundance of ^{238}U represents the parent isotope. The general age equation can be changed to the fission track age equation by:

$$t = \frac{1}{\lambda} \ln\left(1 + \frac{\lambda}{\lambda_{fission}} \frac{N_s}{^{238}U}\right)$$

Equation 3

where, $\lambda_{fission}$ is the spontaneous decay constant (~7.5 x 10^{-17} y^{-1}; Roberts et al., 1968; Wagner and Van den Haute, 1992) and λ the total decay constant for ^{238}U (1.552 x 10^{-10} y^{-1}). Thus, to generate a fission track age, the ^{238}U abundance (parent) and the amount of fission tracks (daughter product) have to be determined.

However, it is not possible to determine the total amount of fission tracks in a whole apatite grain and therefore the fission tracks are counted in a single plane of the apatite crystal (the polished surface in Figure 3.4). The total number of spontaneous tracks (N_s) is replaced with the spontaneous track density (ρ_s) in a unit area which is proportional to the concentration of ^{238}U intersecting the same counted plane over time (t) in which accumulation of spontaneous fission tracks took place. Thus, the ^{238}U content has to be determined in the same plane (area) where we counted the spontaneous fission tracks. Nowadays, the ^{238}U abundance can be determined by either the external detector method or via *in situ* micro-beam measurements, which was the method used in this study. Both methods are explained below.

3.2.3 External detector method

The U content in apatite typically ranges from 1 to 100 pm and modern *in situ* micro-beam techniques such as LA-ICP-MS (laser-ablation inductively coupled plasma mass spectrometry) or SIMS (secondary ion mass spectrometry) facilitate the measurement of the trace-element parent ^{238}U isotope at the ppm level. However, in the early 1980s, when the routine application of the AFT method was being developed, such instrumentation did not exist. The amount of ^{238}U in the analysed crystal was determined using an elegant approach known as the external detector method (EDM) (Hurford and Green, 1982; Hurford and Green, 1983). In this approach, the polished grain surfaces of the counted apatite crystals are placed in intimate contact with low-U bearing "detector" mica, and bombarded with thermal (slow-moving or low-energy) neutrons in a nuclear reactor (

Figure 3.5). This induces fission of ^{235}U in the apatite lattice, while induced fission of ^{238}U is not possible as the binding energy released by thermal neutron

bombardment of ^{238}U is less than the critical energy. Induced fission of ^{235}U atoms within half a track length of the apatite grain surface can be registered in the mica detector. The amount of induced ^{235}U tracks on the mica can be related to the ^{238}U content by employing the natural $^{238}U/^{235}U$ ratio of 137.88 (Steiger and Jäger, 1977).

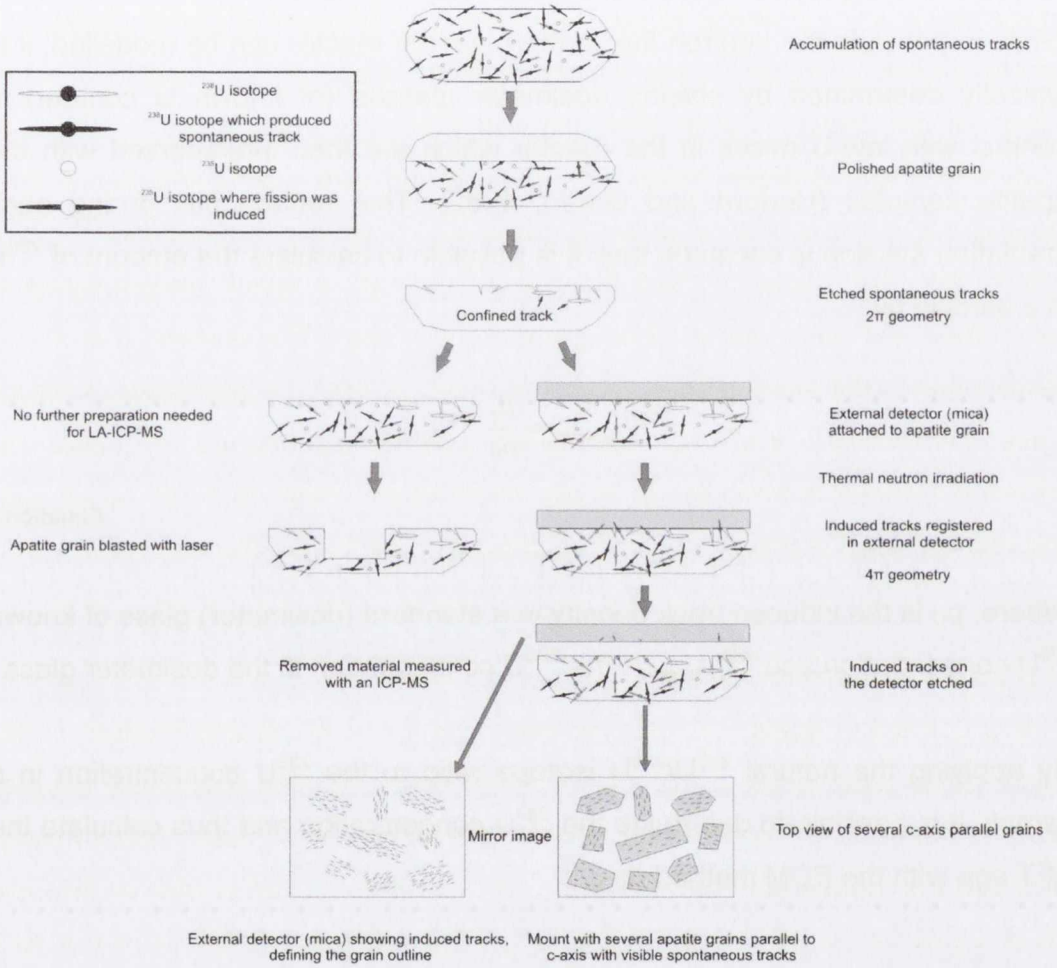


Figure 3.5: Schematic diagram showing the preparation of an apatite grain for AFT analysis via the external detector method (Hurford and Green, 1982) and the LA-ICP-MS method.

The induced track density (ρ_i) is proportional to the amount of ^{235}U in the apatite, the neutron flux per unit volume (Φ) from the irradiation and the thermal neutron fission cross-section for ^{235}U (σ = 580.2 x 10^{-24} cm^{-2}; Hanna et al., 1969; Green and Hurford, 1984), and thus can be calculated by,

$$\rho_i = q^{235}U\Phi\sigma$$

Equation 4

where, q is a plane drawn through a given volume where the induced fission tracks are counted (Galbraith, 2005).

While in principle the neutron flux in the research reactor can be modelled, it is typically determined by placing dosimeter glasses (of known U content) in contact with low-U micas in the reactor which are then interspersed with the apatite samples (Hurford and Green, 1982). The neutron flux during each irradiation session is constant, thus it is possible to calculate the amount of ^{235}U in a sample by:

$$^{235}U_{sample} = \frac{\rho_i}{\rho_D} {}^{235}U_{glass}$$

Equation 5

Where, ρ_D is the induced track density in a standard (dosimeter) glass of known ^{235}U concentration and $^{235}U_{glass}$ is the ^{235}U concentration in the dosimeter glass.

By applying the natural $^{235}U/^{238}U$ isotope ratio to the ^{235}U concentration in a sample it is possible to determine the ^{238}U concentration and thus calculate the AFT age with the EDM method (t_{EDM}):

$$t_{EDM} = \frac{1}{\lambda}\ln\left(1 + \frac{\lambda}{\lambda_{fission}}\frac{\rho_s\Phi\sigma Ig}{\rho_i}\right)$$

Equation 6

where I is the $^{235}U/^{238}U$ isotope ratio (7.253 x 10^{-3}; Galbraith, 2005), σ the thermal neutron fission cross-section (Hanna et al., 1969) and g is the geometry factor which represents a 2π (g=1) versus 4π geometry (g=0.5 in equation 6) caused by polishing into the apatite grain (

Figure 3.5). Therefore, the counted surface within the apatite (4π geometry) has spontaneous tracks derived from ^{238}U fission from both sides of the counted grain surface, but induced tracks are derived from only the side of the apatite in contact with the external detector mica (
Figure 3.5) (Green and Hurford, 1984; Gallagher et al., 1998; Donelick et al., 2005).

Evaluating Equation 6 reveals some difficulties calculating the AFT age with the EDM since some parameters are subject to analyst bias and the exact value for spontaneous fission decay constant ($\lambda_{fission}$) is uncertain. Hence a calibration factor is applied to the AFT age equation, called the zeta-calibration factor (ζ) which is expanded upon below.

3.2.4 Zeta calibration

Hurford and Green (1982) created the zeta calibration factor which corrects for several parameters which are not well-known or are subject to change as mentioned above. While the total decay constant for ^{238}U is well known (λ = 1.552 x 10^{-10} y^{-1}, Jaffey et al., 1971), the spontaneous fission decay constant is uncertain and only approximated at 7.5 x 10^{-17} y^{-1} (Roberts et al., 1968; Wagner and Van den Haute, 1992). Individual analysts count fission tracks slightly differently (i.e. they may sometimes disagree on what is a track and what is not) and thus the spontaneous (ρ_s) and induced (ρ_i) track densities are different from analyst to analyst. Therefore, a correction factor has to also account for the analyst bias to ensure that each AFT age is independent from the analyst who counted the tracks.

3.2.4.1 Zeta calibration for EDM

The zeta factor for the EDM involves placing both counted unknowns and standards of known age (e.g. Durango or Fish Canyon tuff apatite) into the same irradiation package. Since both standards and unknowns have an identical spontaneous fission decay constant, experienced the same neutron flux and are subject to the same ambiguities in track identification, these uncertainties are removed. Thus, the zeta-factor can be defined as:

$$\zeta = \frac{\left(e^{\lambda t_{std}} - 1\right)}{\lambda(\rho_s/\rho_i)_{std} g \rho_d}$$

Equation 7

where, t_{std} is a well-known and characterised age standard, $(\rho_s/\rho_i)_{std}$ the ratio of spontaneous to induced track densities in the standard and g is the geometry factor. By including the zeta calibration factor ζ into Equation 6, the EDM age calculation can be simplified as:

$$t_{EDM} = \frac{1}{\lambda} \ln \left[1 + \lambda \zeta g \left(\frac{\rho_s}{\rho_i}\right) \rho_D\right]$$

Equation 8

3.2.4.2 Zeta calibration for LA-ICP-MS

As mentioned previously (section 3.2.3), the EDM was established due to the difficulties measuring the U content in counted apatite grains. Nowadays, due to improved mass spectrometry instrumentation, it is possible to measure the ^{238}U content *in situ* in an apatite, which eliminates the need for the EDM and correction for the neutron flux in the reactor. But, the zeta calibration factor is still applied in the LA-ICP-MS method (Donelick et al., 2005) due to the uncertainties in the $\lambda_{fission}$ constant and in analyst bias (e.g. uncertainties in counting). Thus, the modified zeta-calibration factor for the LA-ICP-MS method removes the neutron flux and replaces the ρ_s/ρ_i ratio of the standard with the spontaneous tracks (N_s) per $^{238}U/^{43}Ca$ ratio in the counted area Ω (in cm^2).

$$\zeta = \frac{\left(e^{\lambda t_{std}} - 1\right)}{\lambda \left[\frac{N_s}{(^{238}U/^{43}Ca)\Omega}\right]_{std} g}$$

Equation 9

In all LA-ICP-MS fission-track dating studies, the background-corrected ^{238}U abundance is normalised to the ^{43}Ca content of the apatite (Hasebe et al.,

2004; Donelick et al., 2005). Ca is assumed to be stoichiometric in apatite, and employing ^{43}Ca as an internal standard accounts for variation in the quality of the ablation, or long-term variations within a session in signal intensities (session drift). Minor session drift in $^{238}U/^{43}Ca$ ratios is also possible and hence a primary zeta-factor is calculated during an extensive LA-ICP-MS session where each counted standard grain (typically Durango apatites) is analysed several times. Subsequently, in each following ICP-MS session with unknowns, a secondary zeta calibration factor is determined and normalized to the primary session value to account for variations in ICP-MS sensitivity between different sessions as a result of differences in instrument tuning parameters (Hasebe et al., 2004; Donelick et al., 2005).

Furthermore, employing LA-ICP-MS instead of the EDM method increases the speed of data acquisition since the samples do not have to be irradiated and "cool-down" after irradiation, and it also removes the need to count the induced tracks on external detector micas on unknowns and dosimeter glasses.

3.2.5 Apatite fission track age determination via LA-ICP-MS

In principle, AFT dating using LA-ICP-MS requires the same parameters as the EDM to calculate the age, i) the content of ^{238}U per unit area, ii) the amount of spontaneous fission tracks per unit area, iii) the decay constant for ^{238}U (Table 3-1) and an adjusted zeta calibration factor. However, the use of laser ablation bypasses the need to determine the induced track density and instead directly measures the $^{238}U/^{43}Ca$ ratio which substitutes for the induced track density (Figure 3.5). Equation 10 describes the age calculation for a single fission track age using the LA-ICP-MS approach:

$$t = \frac{1}{\lambda}\ln\left(1 + \lambda\zeta g \frac{N_s/\Omega}{^{238}U/^{43}Ca}\right)$$

Equation 10

Where, g is the geometry factor, λ is the total decay constant of ^{238}U ($1.552e^{-10}$ y^{-1}) while ζ represents the adjusted calibration factor zeta (section 3.2.4.2), N_s is

the amount of spontaneous fission tracks in apatite grains counted parallel to their crystallographic c-axis and Ω is the counted area in cm^2. The abundance of ^{238}U is determined using the depth-weighted $^{238}U/^{43}Ca$ ratio measured by LA-ICP-MS spot analysis so that the $^{238}U/^{43}Ca$ concentrations close to the grain surface (which contributes more fission tracks to the spontaneous track density) are weighted more heavily than $^{238}U/^{43}Ca$ concentrations at depth.

The depth-weighted $^{238}U/^{43}Ca$ ratio is calculated during the data reduction step in Iolite but is essentially based on the ablation rate, which is calculated from the depth of the laser pit (typically ~16 µm, as determined by in-house measurement after ablation) and the laser settings (225 shots of the laser in 45 seconds), and from the dimensions of the laser spot which is half a sphere derived from the laser spot size (30 µm) and the pit depth (~16 µm; Figure 3.6). Since the depth-weighted $^{238}U/^{43}Ca$ ratio is only determined for the position of the laser spot so it is important to closely match the position of the laser spot to the counted area (Ω). Otherwise possible variations in the $^{238}U/^{43}Ca$ ratio (e.g. zonation in the apatite grain) might have an influence on the calculated AFT age.

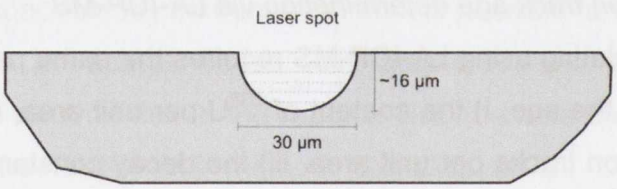


Figure 3.6: Apatite grains with 30 µm laser spot. Dotted line shows ablations intervals for calculation of depth-weighted $^{238}U/^{43}Ca$ ratio.

The calculation of the symmetrical error for a single AFT grain is given by Equation 11:

$$\sigma = \left\{ \frac{1}{N_s} + \left[\frac{\sigma_{(^{238}U/^{43}Ca)}}{^{238}U/^{43}Ca} \right]^2 + \left(\frac{\sigma_\zeta}{\zeta} \right)^2 \right\}^{1/2}$$

Equation 11

Where $\sigma_{(U/Ca)}$ is the error for the $^{238}U/^{43}Ca$ ratio and σ_ζ is the zeta-calibration factor error.

There are three commonly used approaches to present an AFT age: the pooled, central and mean age (Galbraith, 2005). The mean age is simply the statistical arithmetic mean of the single grain ages.

The pooled age (t_{pooled}) is the sum of the spontaneous track count divided by the sum of the weighted $(U/Ca)_j$ ratio multiplied by the counted area on each apatite grain.

$$t_{pooled} = \frac{1}{\lambda} \ln \left[1 + \lambda \zeta g \frac{\sum_1^j N_{s,j}}{\sum_1^j \left({}^{238}U/{}^{43}Ca \right)_j \Omega_j} \right]$$

Equation 12

In general, the pooled age is valid when the apatite grains derive from the same source and have a similar chemical composition (i.e. crystalline basement samples or volcanic apatites). They should therefore show the same annealing behaviour and yield a similar age. The exceptions are slowly cooled samples which have spent a long time in the PAZ and thus can show different single grain AFT ages despite being from the same source rock. Additionally, detrital samples in sedimentary basins can have multiple source areas. AFT studies on such samples (i.e. provenance studies) can show a wide spread in AFT ages along with variations in apatite chemistry which may influence annealing behaviour (section 3.2.6). AFT ages from one single source should show a Poissonian distribution around the "true" age (Galbraith, 2005). To test if the sampled grains derived from a single source, a standard X^2 test for over dispersion, by convention at a 5% level (Yates, 1934), was employed. If grains of one sample fail this test, it would indicate that either the grains are from different populations (such as in detrital samples) or that the U distribution is inhomogeneous in a grain which can influence the track measurement (Galbraith, 1981). Furthermore, extremely slow-cooled samples also can also show large age dispersion since slight changes in chemistry and temperature can affect the annealing behaviour. In the case that the samples fail the X^2 test, the central age is preferred.

The central age was developed by Galbraith and Laslett (1993) and is the weighted mean of the log normal distribution of the single grain ages (Gallagher et al., 1998). The central age is weighted for the precision of track counts from each grain, providing a geometric mean age (Gallagher et al., 1998). The central age can be calculated from:

$$t_{central} = \frac{1}{\lambda}\log\left[1 + \lambda\zeta g\frac{\eta}{(1-\eta)}\right]$$

Equation 13

where η is the weighted average of single-grain variance and η/(1- η) the equivalent of N_s/N_i. In general the central age as calculated by QTQt was employed in the modelling and in the results tables unless otherwise noted.

3.2.6 Thermal annealing of fission tracks

As mentioned in section 3.1, the diffusion (or annealing) behaviour of radiometric dating methods is thermally activated. The spontaneous fission of ^{238}U results in defects in the crystal lattice which are repaired (or annealed) at temperatures above the closure temperature. A borehole-based study by Gleadow and Duddy (1981) in the Otway Basin in southeast Australia determined AFT ages in Cretaceous volcaniclastic sandstones and concluded that at ~125°C the AFT ages were completely reset (i.e. yielding ages of 0 Ma) due to total annealing of fission tracks (Figure 3.7). Additionally, well-controlled laboratory experiments have constrained the annealing characteristics of fission tracks in apatite, using the Durango standard apatite from Mexico (Green et al., 1986).

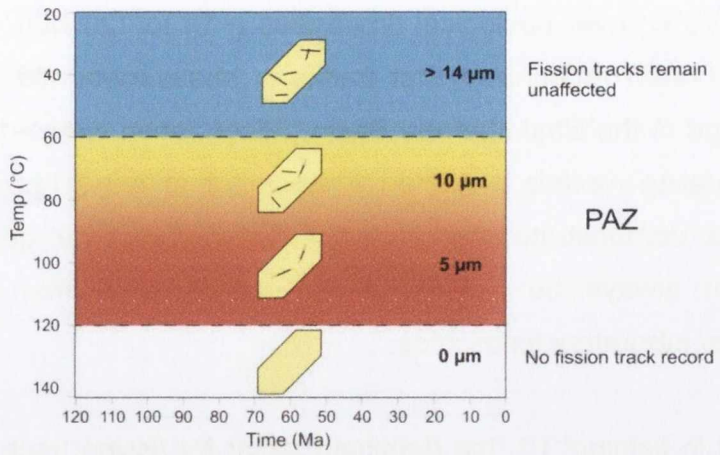


Figure 3.7: Schematic diagram showing the annealing behavior of apatite fission tracks with temperature. Above 120°C the fission tracks will completely anneal. Between 120°C and 60°C the fission tracks will partially anneal (PAZ: partial annealing zone) resulting in the tracks shrinking with time. The higher the temperature, the shorter the tracks will become. Below 60°C the tracks are nearly "frozen", which means partially annealed tracks remain short and newly formed tracks essentially keep their initial length.

These studies concluded that above ~120°C (on average), all generated spontaneous fission track anneal rapidly and are removed over geological timescales (Figure 3.7). Cooling below 120°C, spontaneous tracks remain in the crystal lattice much longer, but are subject to length shortening (Figure 3.7). These tracks slowly anneal, but the rate of annealing is lower than that at which new tracks form. These new tracks are also subject to shortening until the sample cools below the lower limit of the zone of track annealing at ~60°C (Gleadow and Duddy, 1981). This zone between ~60 – 120°C where shortening of fission tracks takes place is termed the "partial annealing zone" or PAZ (Wagner, 1979). Fission tracks generated below ~60°C are nearly unaffected by partial annealing (Figure 3.7). However, Green (1988) recognized a systematic length difference between natural occurring fission tracks and fresh or latent fission tracks (induced tracks produced in a nuclear reactor) which are usually 1 to 1.5µm longer. Induced tracks in apatite are typically 16.3 ± 0.9 µm long (Fleischer et al., 1975) whereas spontaneous tracks rarely exceed 15 µm (Green, 1988). This shortening clearly implies that some annealing occurs between ~60°C and surface temperatures over geological time scales (Gallagher et al., 1998). This is supported by a study by Spiegel et al. (2007) who identified track shortening of between 4 – 11% from deep ocean volcanogenic sediments which have been exposed to temperatures below the

PAZ (~10 – 70°C) over geological timescales (~15 to 120 Ma). Additionally, Vrolijk et al. (1992) recognized that tracks in shallowly-buried sediments of Cretaceous age in the East Mariana Basin, SE of Japan were ~14.6 µm long, whereas annealing models predicted a length of at least 14.8 to 15.9 µm. These studies demonstrate that annealing processes over geological time scales cannot always be determined by extrapolation from experiments conducted over laboratory timescales.

As mentioned in section 3.1, the dominant factor for fission track annealing in apatite is temperature but chemical composition and crystallographic orientation are also important (Gallagher et al., 1998; Donelick et al., 2005). The most common variety of apatite in the crust is near end-member fluorapatite. However, F^- can be substituted by other anions such as Cl^- or OH^-. Chlorine-rich apatites are more resistant to annealing than the pure end-member fluorapatites (Gleadow and Duddy, 1981; Green et al., 1986; Donelick, 1991; O'Sullivan and Parrish, 1995; Barbarand et al., 2003a). Therefore, characterising apatite chlorine content (Cl wt%) is very important for apatite annealing behaviour and thus has implications for the resultant thermal history models (Donelick et al., 2005). Other substitutions for Ca within the apatite crystal lattice such as Mn, Sr or coupled substitutions of Ca with the rare earth elements (REE) or P with Si are less prevalent and their role in the annealing behaviour is less well understood and not included in any annealing models thus far (Crowley et al., 1991; Ravenhurst et al., 1992; Brown et al., 1994; O'Sullivan and Parrish, 1995; Bergman and Corrigan, 1996; Gallagher et al., 1998; Barbarand and Pagel, 2001; Barbarand et al., 2003a; Spiegel et al., 2007).

The crystallographic orientation of the apatite grain is also an important factor on annealing behaviour. The process of etching and annealing in apatites is anisotropic in relation to their crystallographic orientation (Donelick, 1991; Donelick et al., 2005; Ketcham et al., 2007a). Tracks which are parallel to the crystallographic c-axis etch faster than tracks perpendicular to the c-axis (Gallagher et al., 1998), while annealing of tracks parallel to the c-axis is slower than tracks perpendicular to the c-axis (Green et al., 1986). Thus, only grains

which are parallel to the crystallographic c-axis should be used in AFT analysis for both fission-track age and track-length determinations (Figure 3.4).

Several studies (Barbarand et al., 2003a; Barbarand et al., 2003b; Ketcham, 2005b; e.g. Ketcham et al., 2007a; Ketcham et al., 2007b) have characterised the annealing behaviour of apatites relative to the c-axis and incorporated the anisotropy into an annealing model. Identification of c-axis parallel apatite grains is commonly accomplished by ensuring all fission-track etch pit entrances are parallel to each other (Figure 3.4). The length of the etch pits are also a good proxy (kinematic indicator) for the annealing behaviour of apatites and will be discussed in section 3.2.8.

The first detailed annealing algorithm was presented by Laslett et al. (1987) and is based on track shortening within F-rich Durango apatite from Mexico (Young et al., 1969). However, no chemical composition is incorporated into this annealing model, but since F-rich apatite dominates in natural apatite population the predictions of the Laslett et al. (1987) model generally fit well the observed track shortening in nature (Green, 1988). However, since the annealing of tracks at low-temperatures is not incorporated into the Laslett et al. (1987) model, the resultant thermal histories tend to show an artificial Neogene cooling pulse (Gunnell, 2000; Redfield, 2010) as they need to keep the sample within the PAZ until close to the present-day as the annealing model does not account for recent track shortening.

Another study investigating the annealing behaviour of apatite was carried out by Green et al. (1989) who examined Cretaceous volcaniclastic horizons containing abundant volcanic apatites from the Otway basin in SE Australia. The apatites started accumulating tracks immediately following eruption and were slowly buried in the basin, which increased the temperature and thus initiated annealing. Thus, the basin yields apatites in the temperature range from ~10°C (surface temperature) to ≥125°C. The results from the study show that the annealing behaviour of AFT is similar for both laboratory experiments and over geological time scales (Green et al., 1989). Furthermore, the study showed that the annealing behaviour is not only dependent on the temperature,

but also on the Cl/(Cl+F) ratio in apatite crystals. Apatite crystals with a similar composition as the Durango apatite (Cl/(Cl+F) ~0.1) also show a similar annealing behaviour, whereas crystals which are enriched in their Cl content (Cl/(Cl+F) ~0.8) show less annealing (and thus longer tracks) than Durango apatite (Green et al., 1989). Thus, for other chemical compositions (e.g. Cl-rich apatite), the Laslett annealing model is inadequate and an annealing model which includes chemical composition is required.

In this thesis, the multi-kinetic model of Ketcham et al. (2007a; 2007b), an improved version of the earlier multi-kinetic model of Ketcham et al. (1999), is used. The multi-kinetic model is based on the relationship between the measured D_{par}, length of a fision track etch pit entrance (explained in more detail in section 3.2.8), and the D_{par} values from well-defined apatite standards, such as Durango apatite (employed in this study) or Fish Canyon Tuff apatite as determined by Carlson et al. (1999), to determine the annealing behaviour of fission tracks. Furthermore, the annealing model incorporates c-axis projected track length distributions which improve the reproducibility and predictions of track length measurements (Ketcham et al., 2007a; 2007b).

3.2.7 Measuring track lengths and track length distributions

AFT dating provides an AFT age (sections 3.2.4, 3.2.5) and a fission-track length distribution (TLD) which essentially records the cooling history progression of a sample through the PAZ. The ability of the AFT system to provide continuous thermal histories is a major advantage over other radiometric dating methods which typically only provide an age of cooling below their respective closure temperatures. The track length distribution is comprised of "confined tracks" which are etched fission tracks completely beneath the surface of the crystal and horizontal to the polished surface (Bhandari et al., 1971). They are intersected by other etchable features such as other fission tracks or defects (Donelick and Miller, 1991), which penetrate the surface and thus act as conduits for the etching acid to penetrate and etch the confined track (Figure 3.4).

Only confined tracks which are approximately within ±10° of the horizontal of the polished surface should be measured (Donelick, 1991). The ratio of the measured (apparent) confined track length to the true confined track length is equal to the cosine of the angle the confined track makes to the horizontal polished surface. Cosine(10°) equals 0.985 (i.e. close to unity) and thus within the measurement uncertainty of a single fission-track length (Donelick, 1991; Donelick et al., 2005).

In this study the Autoscan software TrackWorks (Autoscan Systems) was employed, with an additional module that can measure confined tracks that make an angle >10° to the polished surface. The application is based on the Pythagorean theorem ($a^2+b^2 = c^2$), where a is the measured length of the track parallel to the polished grain surface, b is the vertical distance from tip to tip of the inclined fission track and c is the true length of the confined track (Figure 3.8). Length b is determined by focussing on the tip ends and employing the vertical difference in stage heights recorded by the microscope, and also takes into account the refractive index of apatite.

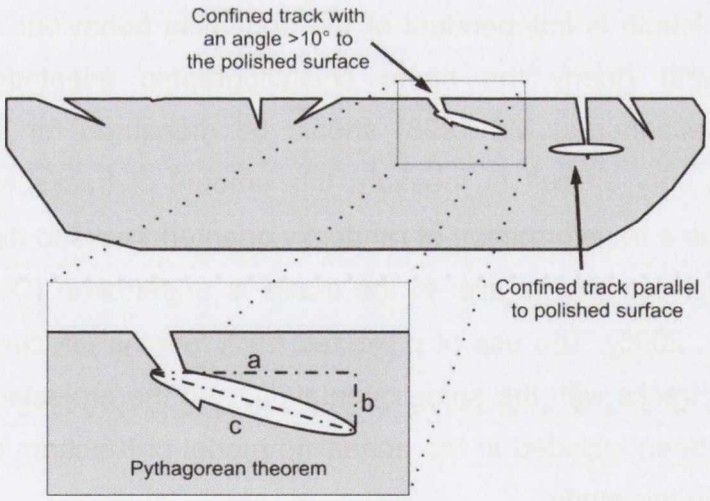


Figure 3.8: Determination of confined track lengths making an angle of >10° to the counting surface.

Only confined tracks which are fully etched and with both ends clearly visible should be measured. Furthermore, there exist two different types of confined tracks; confined tracks which are intersected by another fission track called

TINTs (Track IN Track) and confined tracks which are intersected by defects called TINCLEs (Track IN CLEavage) (Donelick and Miller, 1991). Usually only TINTs should be included within the track length distribution since TINCLE tracks can exhibit abnormal annealing behaviour (Barbarand et al., 2003b; Donelick et al., 2005). TINCLE tracks are only measured under certain conditions. A TINCLE track was only measured if it was intersected by a polishing scratch mark and thus there was no reason to believe the TINCLE track would have either annealed abnormally or that the confined track had opened up by movement on a cleavage or fracture plane. Furthermore, the number of TINCLE tracks is typically very small per sample (less than 3) indicating that exclusion would not materially change the track length distributions.

At least 100 track lengths should be measured, for statistically viable TLD data. However, as explained in Section 3.2.6, the annealing and etching behaviour of fission tracks depends on the orientation to the crystallographic c-axis. Confined tracks at a high angle to the c-axis anneal faster than tracks parallel to the c-axis. In order to derive cooling information from the TLD it is important that the track length is independent of the annealing behaviour and therefore only tracks with nearly the same crystallographic orientation (±15° by convention; Gallagher et al., 1998) should be measured for each sample. However, it is very difficult to measure this amount of tracks with the same orientation, thus a transformation of randomly oriented tracks to their equivalent "projected" track lengths parallel to the c-axis is undertaken (Donelick, 1991; Donelick et al., 2005). The use of projected track lengths effectively increases the amount of tracks with the same orientation, and the projected track-length algorithm has been included in the annealing model of Ketcham et al. (2007b) which is used in this study.

For each AFT sample, I attempted to count at least 100 confined track lengths and subsequently plot them in a histogram with 1µm intervals (Figure 3.9). The TLD is usually biased towards the longer tracks because i), longer tracks have a higher probability of being intersected by a track connected to the surface and ii), longer tracks are easier to detect than short tracks. However, the TLD still

contains more detailed information about the thermal history of a sample than nearly all other thermochronometers (Laslett et al., 1987).

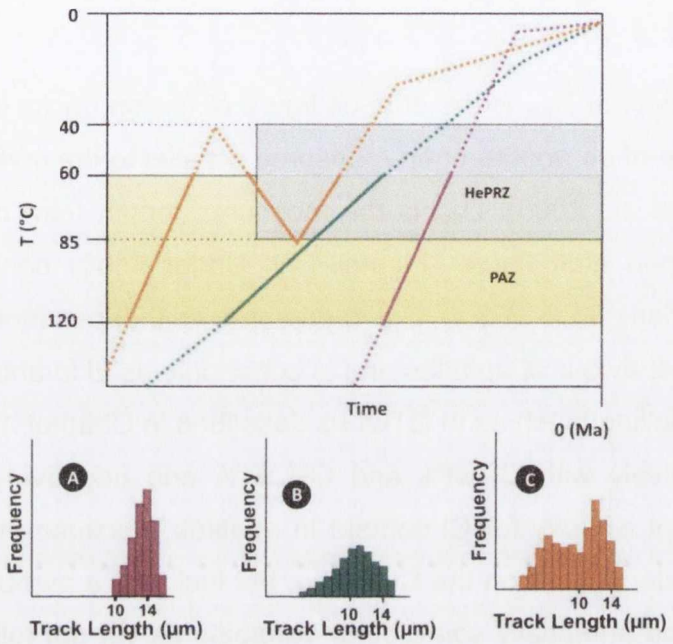


Figure 3.9: Top: Three possible time-temperature paths resulting in three different track length distributions displayed at the bottom of the figure. A: The narrow track length distribution indicates a rapid cooling of the sample through the PAZ. B: A wide distribution indicates slow cooling through the PAZ. C: The bimodal distribution indicates reheating of the sample into the temperature range of the PAZ. The pre-existing length population gets annealed and shortened while a younger track length population forms, recording the recent cooling path.

The crucial parameter controlling the track length distribution is the cooling rate while passing though the PAZ (Figure 3.7). Samples that enter the PAZ at the same time but that cool at different rates will record a different TLD and thus also a different age. For example, a sample passing very quickly through the PAZ (high cooling rate) will have a narrow TLD and a long mean track length (MTL) (Figure 3.9a), whereas samples that cool slowly through the PAZ (low cooling rate) will exhibit a broad TLD skewed towards long track lengths and with a long tail of short tracks (Figure 3.9b). A bimodal TLD might indicate a reheating event into the PAZ after the sample has already cooled below ~60°C (Figure 3.9c) or a change in the cooling rate while the sample was still in the PAZ. This last example also reveals that thermal histories based on TLDs are non-unique. Several different cooling histories through the PAZ could yield

similar TLDs, and without additional information is it not possible to determine which one is the most realistic cooling history.

3.2.8 D_{par}

The kinetic parameter D_{par} is the etch-pit figure of fission tracks intersecting the polished surface of an apatite grain measured parallel to the crystallographic c-axis (Donelick et al., 2005). D_{par} is the measured length from tip to tip of the hexagonal shaped etch figure (Figure 4.7). Under tightly controlled etching conditions (sections 3.2.1, 4.3.1), D_{par} represents an independent parameter for the annealing behaviour of apatites and is commonly used in annealing models for thermal modelling (such as in QTQt as described in Chapter 4). D_{par} typically correlates positively with Cl wt% and OH wt% and negatively with F wt%. However it is not a proxy for Cl content in apatites, because the geometry of D_{par} is not only dependent on the Cl/F ratio, but includes a number of chemical compositions and potentially some other variables as yet not fully investigated (Donelick, 1993; Donelick et al., 2005).

A relatively low value for Dpar (<1.75 µm) indicates fast annealing and can be considered a near end-member fluorapatite whereas apatites with D_{par} with high values (>1.75 µm) usually anneal slower (Carlson et al., 1999).

3.2.9 Durango apatite as a standard on low-temperature thermochronology

Durango apatite is almost certainly the best-characterised fluorapatite, and has been widely analysed for example for its hydroxyl content by using infrared spectroscopy (Baumer et al., 1985), element diffusion studies including rare earth elements (Cherniak, 2000), high-temperature petrology studies (Harlov and Förster, 2004; Antignano and Manning, 2008) and the oxygen and hydrogen isotope compositions by secondary ion mass spectrometry (SIMS) (Hallis et al., 2012). Furthermore, the Durango apatite has been used for AFT annealing and length studies (Laslett et al., 1984; Green et al., 1986), helium diffusion studies for AHe dating (Wolf et al., 1996; Farley, 2000) and in situ AHe dating (Boyce and Hodges, 2005) and is therefore a widely used standard in AFT and AHe dating.

Durango apatites are typically coarse-grained (> 1 cm), euhedral crystals that formed in an ore deposit at Cerro de Mercado near Durango City, Mexico (Young et al., 1969). The iron ore deposit is bracketed by two ignimbrite eruptions which have been dated by the $^{40}Ar/^{39}Ar$ method, yielding an age of 31.44 ± 0.18 Ma (2σ) for the iron ore deposit and Durango apatite itself (McDowell et al., 2005). AHe dating of Durango apatite in the same study has yielded an age of 31.02 ± 1.01 Ma (1σ) which is in good agreement with the $^{40}Ar/^{39}Ar$ age data (McDowell et al., 2005). Green et al. (1986) conducted laboratory annealing experiments on the annealing behaviour of Durango apatite, with experiment durations ranging from 20 minutes to 500 days and temperatures ranging from 95°C to 400°C. The resultant fanning Arrhenius plot constrained the PAZ for apatites and these data were subsequently used in the first empirical model for the annealing behaviour of induced tracks in apatite (Laslett et al., 1987).

Studies linking annealing behaviour to apatite composition (including Durango apatite) were carried out by Carlson et al. (1999) and Barbarand et al. (2003a). Durango apatite, usually used as a standard for AFT and AHe dating, has a relatively high chlorine content (0.43 Cl wt%) compared to most natural occurring apatites. These compositional differences mean that the chemical composition (including the chlorine content) and / or the kinetic parameter D_{par} should be analysed in apatite unknowns. These data are then incorporated into the thermal history models in order to account for the compositional differences and thus the different annealing behaviour between apatite unknowns and Durango apatite.

3.3 Apatite (Uranium-Thorium-Samarium)/Helium dating

The decay of uranium and thorium to helium was one of the first radiometric dating systems applied to be applied to the absolute dating of rocks (Rutherford, 1905). However, the method was subsequently found to yield helium dates much younger than independent estimates of the rock crystallisation age, and the method was abandoned. Only in the 1980s with

advances in the understanding of radiometric dating methods (e.g. different closure temperatures for different isotope-mineral systems) did interest revive in helium dating, particularly when applied to the minerals apatite and zircon. Zeitler et al. (1987) determined that AHe ages resulted from loss of radiogenic helium due to diffusion, and it was discovered that AHe dating records cooling information in the temperature range between 40 – 85°C (Zeitler et al., 1987; Wolf et al., 1998) (Figure 3.1).

3.3.1 ^{4}He production

AHe dating is based on the accumulation of ^{4}He nuclei (α-particles) in the apatite crystal (Figure 3.10a) due to the series decay of ^{238}U, ^{235}U and ^{232}Th to ^{206}Pb, ^{207}Pb and ^{208}Pb respectively, and the α-decay of ^{147}Sm to ^{143}Nd (Farley, 2002). The ^{4}He production of all four isotopes can be summarized by Equation 14:

$$^{4}He = 8^{238}U\left(e^{\lambda 238t} - 1\right) + 7^{235}U\left(e^{\lambda 235t} - 1\right) + 6^{232}Th\left(e^{\lambda 232t} - 1\right) + 1^{147}Sm\left(e^{\lambda 147t} - 1\right)$$

Equation 14

where ^{4}He, U, Th and Sm correspond to the present-day amounts in the crystal (atoms), t is the accumulation time (AHe age) and λ is the decay constant of the corresponding isotope (see Table 3-1). The coefficients in front of the U, Th and Sm contents are the amount of α-particles emitted during their respective radioactive decay series (Farley, 2002).

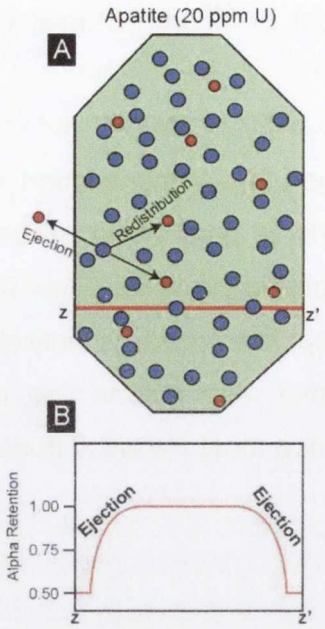


Figure 3.10: A: Schematic diagram of an apatite crystal showing accumulation and ejection of σ-particles. B: Evolution of the alpha retention from the centre of the apatite crystal to its rim.

Equation 14 can be simplified by replacing the amount of ^{235}U with the natural ratio of $^{235}U/^{238}U$ (1/137.88) to:

$$^4He = 8^{238}U\left(e^{\lambda 238t} - 1\right) + 7\left(\frac{1}{137.88}\right)^{238}U\left(e^{\lambda 238t} - 1\right) + 6^{232}Th\left(e^{\lambda 232t} - 1\right) + 1^{147}Sm\left(e^{\lambda 147t} - 1\right)$$

Equation 15

Thus, only the ^{238}U isotope has to be measured which is advantageous since it is more difficult to measure ^{235}U precisely due to the lower amounts present. ^{147}Sm only makes up 15% of all total samarium in the solar system and it only produces one α-particle with a long half-life. Thus the amount of α-particles produced by ^{147}Sm is very small and ^{147}Sm is often not measured. However, some studies have shown that especially in low U (<5 ppm) apatite, the Sm/U ratio can reach up to 100-200 which can therefore lead to erroneously old AHe age if the ^{147}Sm content is not measured (Spiegel et al., 2009). Therefore I measured at least a subset of apatite grains for ^{147}Sm in each sample to

demonstrate that the amount of ^{147}Sm is small enough to disregard ^{147}Sm-produced ^{4}He.

Equation 15, which describes ^{4}He accumulation with time, is based on the assumption that no initial ^{4}He is present. In general, this assumption is valid since the amount of atmospheric He is very low (only 5ppm) so that trapped atmospheric He within an apatite crystal is unlikely (Farley, 2002). The high diffusion rate of He in apatite also means that inherited He from previous cooling events is unlikely, since most He will diffuse very fast out of the apatite crystal (Zeitler et al., 1987).

3.3.2 AHe age Calculation

The calculation of the AHe age is more computationally difficult compared to AFT dating because several parent isotopes (^{238}U, ^{235}U, ^{232}Th and ^{147}Sm) produce the same daughter isotope (^{4}He). Thus, it is not possible to rearrange the ^{4}He accumulation equation (Equation 15) to directly calculate the AHe age, and up until the middle of the last decade AHe age determinations typically employed Taylor Series iterations. This approach involves assuming an age for "t" in equation 15 and calculating the amount of ^{4}He produced which is then subsequently compared with the measured ^{4}He content. When the measured and calculated ^{4}He are equal, then "t" yields the correct AHe age.

However, Meesters and Dunai (2002b; 2005) developed a non-iterative method to calculate the AHe age by calculating the total current ^{4}He production rate P, where:

$$P = 8 * \lambda_{238_U} + 7 * \lambda_{235_U} + 6 * \lambda_{232_{Th}} + 1 * \lambda_{147_{Sm}}$$

Equation 16

and replacing the decay constant of all four isotopes with a single weighted mean decay rate λ_{wm}, involving the relative production rates for each isotope:

$$\lambda_{wm} = \frac{8 * \lambda_{238_U}}{P} + \frac{7 * \lambda_{235_U}}{P} + \frac{6 * \lambda_{232_{Th}}}{P} + \frac{1 * \lambda_{147_{Sm}}}{P}$$

Equation 17

These modifications to the age equation mean the ^{4}He accumulation formula (Equation 15) has only one effective mean parent instead of four:

$$^4He = \frac{P}{\lambda_{wm}} \ln\left(e^{\lambda_{wm} t} - 1\right)$$

Equation 18

Converting Equation 18 for t enables the calculation of an approximate age t_{app} by,

$$t_{app} = \frac{1}{\lambda_{wm}} \ln\left[\frac{\lambda_{wm}}{P}\left(He_{prd}\right) + 1\right]$$

Equation 19

where He_{prd} is the total amount of measured ^{4}He in atoms. Thus, it is possible to directly calculate an approximate AHe age using an effective weighted mean of all four ^{4}He-producing isotopes. Theoretical calculations (involving different concentrations of parent isotopes) show that the deviation of the approximate direct solution from the true AHe age is only ~0.1% for ages as old as 500 Ma (Meesters and Dunai, 2005). As the error in AHe dating is dominated by analytical uncertainties in the U, Th, Sm and He concentrations as well as the alpha-ejection correction (section 3.3.6) the small error introduced by the direct solution age equation can be disregarded. Thus, the direct solution is a viable substitution for the iterative method and is easier to employ (Meesters and Dunai, 2005).

3.3.3 He diffusion in apatite

Knowledge of the diffusion behaviour of ^{4}He in apatite is critical to correctly interpret (U-Th-Sm)/He data. Diffusion is dominated by temperature (i.e. it is a

thermally-activated process) and thus rapidly cooled samples are easier to model since the amount of time between "total" diffusion and complete ^{4}He retention is very small. Slowly cooled samples however, require precise knowledge of how diffusion scales with temperature (Farley, 2002). Laboratory experiments investigating the He diffusion apatite have shown that diffusion obeys an Arrhenius relationship (Equation 20) which suggest that He diffusion in apatite is thermally activated volume diffusion process (Farley, 2002):

$$\frac{D_{(T)}}{a^2} = \frac{D_o}{a^2} e^{-E_a/RT}$$

Equation 20

Where, $D_{(T)}$ is the diffusivity, D_o is the diffusivity at infinite temperature, a is the diffusion domain radius (which in AHe dating is assumed to be the radius of the apatite crystal as the radius of the apatite crystal is the shortest pathway for He diffusion), E_a is the activation energy, R is the gas constant and T is the temperature (in Kelvin) (Farley, 2002; Dobson, 2006). One of the first studies on He diffusion in apatite was by Farley (2000) who recognised based on Durango apatite that they obeyed an Arrhenius relationship for temperatures <265°C. The Arrhenius plot is curved above 300°C which indicates more complex diffusion behaviour which is not fully understood but possibly related to structural changes in the apatite crystal and/or compositional modifications (Farley, 2000). Since the diffusion only changes above 300°C it is unlikely that the changes are relevant for the helium diffusion in natural settings (Wolf et al., 1998; Farley, 2002).

In addition to the temperature history, the shape of the apatite crystal is also important for the diffusion (Figure 3.10). Apatite grains are ideally prism shaped, and thus the shortest distant for He loss is the radius perpendicular to the c-axis (Reiners and Farley, 2001; Farley, 2002). Since the diffusion domain is the grain itself, the prism radius a is the relevant dimension for the diffusivity shown in Equation 20 (Farley, 2002). The influence of crystal size on diffusion is most pronounced in grains which have remained in the partial retention zone of ^{4}He for a long time period (>10^7 years) (Reiners and Farley, 2001). Meesters

and Dunai (2002a) showed that for different grain geometries, the surface area to volume ratio of the crystal is the key controlling factor on He diffusion for a given temperature history. Hence differences in the diffusion behaviour between different geometries is negligible if their surface area to volume is identical (Meesters and Dunai, 2002a).

3.3.4 ^{4}He partial retention zone (PRZ)

Equation 20 can be used to calculate the effective closure temperature (t_c) and cooling rate for a given crystal size (Dodson, 1973), which corresponds to the temperature where retention of He in the apatite crystal starts. Further studies investigating the retention and diffusion of He in apatite showed that for typical apatite crystal sizes (30 – 100 µm), retention begins as soon as the temperature falls below ~85°C and diffusion essentially ceases at ~40°C (Figure 3.1; Wolf et al., 1998). These results led to the definition of the "helium partial retention zone" (PRZ; Figure 3.2), which is defined as the zone between where 5% diffusion occurs and 95% retention (Wolf et al., 1998). However, recent studies (Shuster et al., 2006; Shuster and Farley, 2009) have found that in addition to the grain size and cooling rate (°C/Myr), the AHe closure temperature and thus the PRZ also depends on the amount of radiation damage in the crystal lattice which is discussed below.

3.3.5 Radiation damage

Another factor influencing the He diffusion in apatite (and thus the t_c and AHe age) is radiation damage in the apatite crystal (Figure 3.11). Radiation damage occurs mainly from the alpha decay of U and Th, which causes recoil damage in the crystal lattice. As zircon and titanite typically exhibit high U and Th contents, they usually show much more radiation damage than apatite. In these phases, the accumulation of large amounts of radiation damage promotes He loss because the connected radiation damage generates pathways for the He to leave the crystal more easily (Hurley, 1952; Flowers et al., 2009; Guenthner et al., 2013). In contrast, radiation damage in apatite impedes He mobility (Shuster et al., 2006) as the lower U and Th contents encountered in apatites means that the amount of radiation damage is not enough to generate linked

diffusion pathways but instead produces "traps" (Figure 3.11). Once in a trap, a helium nucleus becomes captured in the radiation damage trap as it has to overcome a much higher energy barrier (activation energy) to leave the radiation trap again (Shuster et al., 2006). As there is presently no direct proxy for radiation damage in apatite, Shuster et al. (2006) developed a predictive kinetic model based on the assumption that the fraction of induced traps in the crystal is proportional to the concentration of α-particle producing isotopes (expressed as the effective uranium content, or eU – Equation 21). The model predicts that for temperatures low enough to accumulate radiation damage, high eU contents will result in more traps being developed and hence a higher t_c for ^{4}He diffusion. eU is the weighted concentration of uranium, thorium and samarium isotopes for their proportional α-particle production rate and is calculated as:

$$eU = U + 0.235Th + 0.005Sm$$

Equation 21

where U, Th and Sm are the contents in ppm. Several empirical field based studies have now shown a positive correlation between AHe age and eU content (Shuster et al., 2006) that has been ascribed to the effects of radiation damage (Figure 3.11).

The laboratory experiments of Shuster and Farley (2009) show an increase in the t_c in apatite with increasing radiation damage, but that this effect is also reversible by thermal annealing. Thus, Flowers et al. (2009) developed a new kinetic model called the "radiation damage accumulation and annealing model" (RDAAM) which is based on the evolution of the diffusivity of ^{4}He in apatite in response to radiation damage accumulation and annealing adopted from the effective fission track density. This kinetic model is used for all the AHe ages modelled in this thesis.

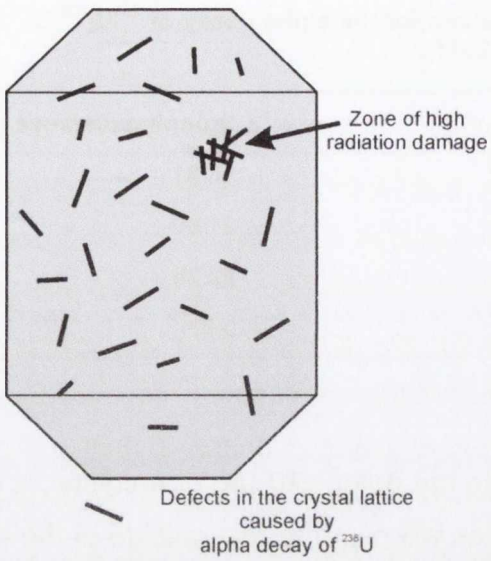


Figure 3.11: Schematic diagram of an apatite crystal showing defects in the crystal lattice caused by the alpha decay of ^{238}U and a zone of a high concentration of these defects causing severe damage to the crystal lattice serving as a "trap" for ^{4}He.

3.3.6 α-ejection correction (F_T)

The ejection of α-particles has to be considered when using the AHe dating method (Figure 3.10; Farley, 2002; Farley and Stockli, 2002). Large amounts of energy are released during the decay of ^{238}U, ^{235}U, ^{232}Th and ^{147}Sm, resulting in the movement of α-particles which can result in the ejection of helium atoms out of the crystal (Farley, 2002) (Figure 3.10). The distance that α-particles travel until they stop is called the stopping distance (Zeigler, 1977), and is different for each isotope system and is also a function of the density of the host mineral (Table 3-2; Farley et al., 1996; Ketcham et al., 2011). α-particles derived from U and Th decay typically travel ~20 µm in a straight line within an apatite crystal. The direction of the α-particle path is random, and the final particle position can be modelled as defining any position on the surface of a sphere with a radius of 20 µm, centred around the atom that emitted the α-particle.

Table 3-2: Stopping distances for the alpha decay of ^{238}U, ^{235}U, ^{232}Th and ^{147}Sm (Farley et al., 1996; Ketcham et al., 2011).

Isotope	Stopping distance (μm)
^{238}U	18.81
^{235}U	21.80
^{232}Th	22.25
^{147}Sm	5.93

If α-decay occurs within the outer ~20 μm of a crystal, a certain percentage of the generated α-particles will come to rest outside of the crystal (Figure 3.10a). Assuming that α-particle generation is homogeneous (i.e. there is no zoning of parent U, Th or Sm) and that α-particles are only lost due to ejection (based on a 20 μm radius of a sphere), then the retention of α-particles in an apatite crystal greater than ~40 μm in diameter will decrease from 100% retention in the core to 50% retention on the outer rim of the crystal (Figure 3.10b), assuming that the surface of the grain is flat and only about 40% retention at apices (Farley, 2002). The fraction of α-particles retained in the apatite crystal is defined as F_T (Farley et al., 1996). Another possibility is implantation of ^4He into the apatite grain from surrounding grains, which will be discussed further in section 3.3.7.

There are two general ways to correct for α-ejection, i) mechanical removal of the outermost ~20 μm of the crystal and ii) calculating the F_T correction factor which considers ^4He loss due to diffusion in relation to the geometry of the grain (Farley et al., 1996). The rim of the crystal is the region which undergoes ^4He ejection and possible implantation, and mechanically removing the outer ~20 μm rim removes this ^4He depleted zone. However, removing the outer part of an apatite crystal is challenging due to its small size (usually ~100 μm) and means that the single crystal is usually crushed. Yet, after crushing the crystal it is difficult to be sure if the picked fragment is only part of the inner core or from the outer rim. Thus, with the mechanical removal method it is still possible to analyse a fragment which is depleted in^4He and therefore this method should be avoided. The exceptions to this rule are large (i.e. centimetre size) apatite

crystals, like the Durango standard, where the probability of picking a fragment from the outer rim is small.

The second approach which involves correcting for α-ejection by calculating the F_T correction factor assumes that i) the amount of implanted ^4He is insignificant because the U concentration is usually much higher in apatite than in the host rock, and only direct contact of the dated apatite with another high U-bearing mineral would violate this assumption (Farley, 2002) and ii) the U, Th and Sm distribution is homogenous across the crystal (Farley et al., 1996; Farley, 2002; Farley and Stockli, 2002). The F_T correction factor, the fraction of ^4He retained in the crystal, is strongly dependent on the surface to volume ratio of the crystal (β) and the α-stopping distance (Farley et al., 1996).

There are different ways to calculate the F_T factor, firstly, by using simple geometrical forms such as a sphere, hexagonal prism or cylinder and assuming a mean stopping distance for U and Th of ~20 µm (Farley et al., 1996). Using a mean stopping distance is possible as Monte Carlo modelling demonstrates that minimal errors are introduced by using an average stopping distance instead of the actual stopping distances (Table 3-2) for U and Th (Farley, 2002). The F_T factor calculated for a simple sphere using this approach is:

Sphere:

$$F_T = 1 - \frac{3S}{4R} + \frac{S^3}{16R^3}$$

Equation 22

where, S is the mean stopping distance and R the radius of the sphere. Similar equations are possible for both a hexagonal prism and cylinder:

Hexagonal prism:

$$F_T = 1 - \frac{S(2.31L + 2R)}{4(RL)}$$

Equation 23

Cylinder:

$$F_T = 1 - \frac{S[2(R+L)]}{4(RL)}$$

Equation 24

where, L is the length of the crystal. However, these equations (22, 23 and 24) are only approximations, as an ideal apatite crystal is a hexagonal prism with pyramidal terminations on either end.

Gautheron et al. (2006) and Gautheron and Tassan-Got (2010) developed a code based on Monte Carlo modelling which can approximate a true 3D geometry, including pyramidal terminations or broken terminations for apatite crystals (i.e. a hexagonal prism). Ketcham et al. (2011) subsequently added to this model by i) reparametrizing the empirical polynomials to easily account for any future changes in the stopping distances datasets, ii) expanding the types of crystal shapes covered to include habits for all crystal systems and iii) calculating F_T factors by correcting the F_T-calculation for the contribution and stopping distance of the parent isotopes (i.e. the U/Th ratio). The model calculates the minimal volume, distributes the parent isotopes homogenously and computes the F_T factor by counting the α-particles remaining in the crystal after 10^7 decay events. This code is written into the program (Qtft), which was used in this study to calculate all F_T factors. It is beyond the scope of this thesis to present the detailed suites of equations used to calculate the F_T factor, and so the reader is directed to Meesters and Dunai (2002b) for the mathematical background and to Gautheron (2006), Gautheron and Tassan-Got (2010) and Ketcham et al. (2011)for an in-depth discussion. Once the F_T factor has been determined, the F_T corrected age is simply calculated by:

$$corrected\ age = \frac{measured\ age}{F_T}$$

Equation 25

3.3.7 ^{4}He implantation

When calculating the approximate AHe age using Equation 19, it is assumed that all ^{4}He is produced by the decay of ^{238}U, ^{235}U, ^{232}Th and ^{147}Sm from within the apatite crystal. There are two possible sources of ^{4}He implantation. The first is from surrounding minerals (Figure 3.12a) (termed helium implantation by "bad neighbours"; Spiegel et al., 2009), while the second potential source is from mineral inclusions inside the apatite crystal itself (Figure 3.12b).

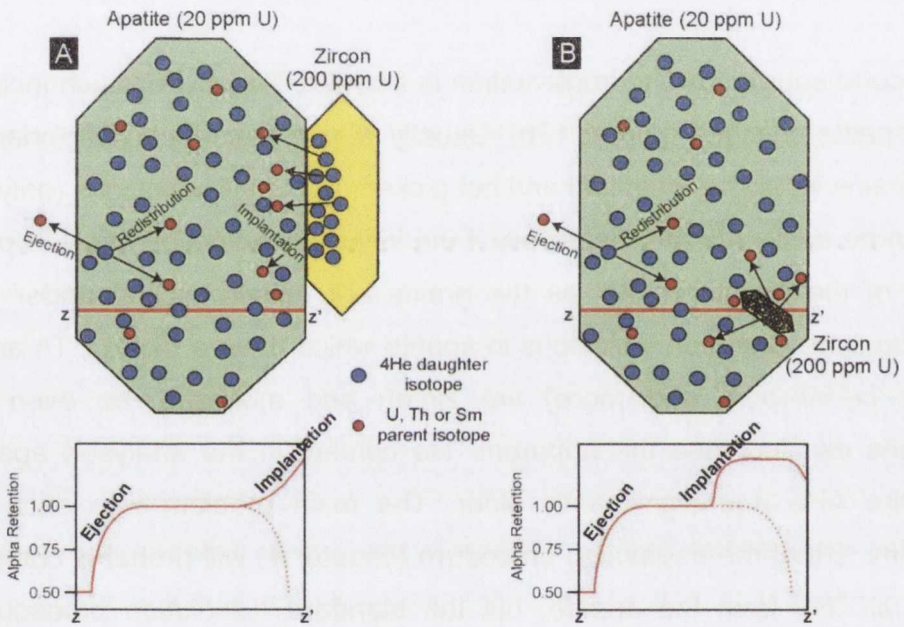


Figure 3.12: Schematic diagram of ^{4}He implantation into apatite crystals. A: Implantation of ^{4}He due to an adjacent zircon ("bad neighbourhood"). B: Implantation of ^{4}He due to a zircon inclusion.

A "bad neighbourhood" implies that minerals surrounding the analysed apatite grain have high U and Th contents, and α-emission from these grains can travel into the rim of the analysed apatite grain (Figure 3.12a) (Spiegel et al., 2009). However, although U and Th contents tend to be lower in apatite than in other accessory minerals such titanite or zircon, they are nevertheless much higher than in most common rock-forming minerals. Thus when comparing the effects of implantation and ejection, the effects of ejection will usually be far more pronounced (Farley, 2002). In most sedimentary and metamorphic rocks (with

the possible exception of sedimentary protoliths with concentrations of accessory minerals in heavy mineral-rich laminae), the effects of implantation are usually negligible. However, in igneous rocks, apatites are more likely to be in direct contact with other apatites, zircons or monazites which have a high enough U or Th content to influence the relationship between implantation and ejection (Dobson, 2006). In the case of a rock sample that yields older AHe ages than expected, the distribution of the accessory minerals in thin section should be examined in detail to see if the apatites are commonly encountered in contact with other high U- and Th-bearing phases.

The second source for ^{4}He implantation is from U-, Th- and Sm-rich inclusions in the apatite crystal (Figure 3.12b). Usually during grain selection (chapter 4) these grains would be identified and not picked, but small inclusions (only a few μm) can be easily missed, especially if the inclusion extinction angle is parallel to that of the apatite crystal as the grains are usually picked under cross-polarised light. Common inclusions in apatite which have a high U, Th and Sm content (>100 ppm and more) are zircon and monazite, so even small inclusions can increase the apparent ^{4}He content in the analysed apatite to make the AHe age significantly older. The main problem with such small inclusions is that the degassing procedure (chapter 4) will probably completely extract all ^{4}He from the apatite, but the standard dissolution procedure for apatite solution-ICP-MS analysis (5% ultra-pure HNO_3) will not dissolve inclusion like zircon or monazite. Thus, the ^{4}He from the inclusion will be measured during ^{4}He extraction, but no U, Th or Sm from the inclusion will be measured. Sometimes referred to as "parentless He", this effect results in older and non-reproducible AHe ages (Dobson, 2006).

While conducting AFT analysis on the sample, it is useful to note if small zircon inclusions are a common feature inside the counted apatite grains. The AFT scope has high-quality reflected-light optics and can easily detect small inclusions at high magnification. Knowledge of the presence of small inclusions (particularly small c-axis parallel inclusions) is advantageous for subsequent AHe picking. It may also help explain why in some samples the AHe ages are older than expected or even older than the respective AFT ages.

3.4 Apatite uranium-lead dating

The fission track laboratory in Trinity College Dublin uses a LA-ICP-MS approach to calculate uranium contents for apatite fission-track analysis. The laboratory protocol also generates U-Pb apatite ages for the grains. In this thesis, the apatite U-Pb ages were only used as the initial high-temperature constraint for the thermal history modelling and hence this method description only covers the fundamentals of the technique. A more comprehensive summary on the principles of the U-Pb apatite LA-ICP-MS technique can be found in Chew et al. (2011, 2014) and Thomson et al. (2012), while Chew and Donelick (2012) provide an overview of combined apatite fission track and apatite U-Pb dating.

LA-ICP-MS U-Pb dating on apatite is a relatively recent dating technique (Chew et al., 2011; Thomson et al., 2012) in comparison to LA-ICP-MS U-Pb dating of zircon, which is now a mature, widely employed method in the literature (Schoene, 2013). The main challenges involved with LA-ICP-MS U-Pb dating of apatite is that the U and Pb concentrations are commonly an order of magnitude lower than in zircon, and that apatite has a high common Pb to radiogenic Pb ratio which requires a common Pb correction to both standards and unknowns (Chew and Donelick, 2012). U-Pb dating of U-bearing accessory phases is normally undertaken by sample-standard bracketing (Chew et al., 2011) as the raw isotope ratios produced by the LA-ICP-MS method normally deviate from the accepted values due to mass discrimination from ablation to the mass spectrometer detector. Data reduction in LA-ICP-MS U-Pb apatite dating is greatly complicated by variable incorporation of common Pb into the reference material, and this is probably the main reason that LA-ICP-MS U-Pb dating of apatite was only developed relatively recently.

However recent advances in ICP-MS data reduction software, such as the freeware Iolite package of Paton et al. (2011), not only facilitate rapid processing of ICP-MS data but allow customised data reduction schemes to be incorporated into the software. In this thesis I used a data reduction scheme

(VizualAge_UcomPbine) within the Iolite package that can correct for variable amounts of common Pb in any U-Pb accessory mineral standard as long as the standard is concordant in the U-Pb systems after common Pb correction (Chew et al., 2014).

While AFT is a low temperature technique, the U-Pb apatite system has a temperature sensitivity of ~425 – 500°C (Chamberlain and Bowring, 2000; Schoene and Bowring, 2007). Therefore, while it does not directly date the timing of apatite crystallization, except in low-grade metamorphic rocks or rapidly cooled igneous rocks, it acts as a valuable constraint in constraining the high-temperature thermal histories of the samples. While this is the main use of the U-Pb apatite system in this thesis, combined LA-ICP-MS apatite fission track and U-Pb dating has other potential advantages, particularly in sedimentary provenance analysis.

In clastic rocks, zircon is chemically and mechanically robust, which means zircons can survive multiple erosion cycles and thus can be easily recycled making identification of source regions difficult (Morton and Hallsworth, 1999). In contrast, apatite dissolves more easily in acidic groundwater and weathering horizons and apatite only shows restricted mechanic stability during sedimentary transport, which means that apatite represents usually first cycle detritus (Morton and Hallsworth, 1999). Thus, one powerful application of LA-ICP-MS apatite U-Pb dating is in sedimentary provenance studies where it can offer complementary information to LA-ICP-MS U-Pb dating of zircons (i.e. Mark et al., 2016). Furthermore, apatite occurs in both felsic and mafic igneous rocks, whereas zircons primarily occur in felsic igneous rocks, and hence source fertility of zircon can be an issue in detrital provenance studies (Bernet, 2005).

The main difference between a LA-IPC-MS session employed solely for U-Pb apatite geochronology and a session where both AFT and U-Pb dating are undertaken is the spot size. Usually for LA-ICP-MS AFT dating a 30 µm spot size is employed. The spot size cannot be changed during an analytical session as it will affect the aspect ratio of the laser spot pit which in turn affects the

U/Pb and U/Ca fractionation behaviour. Hence a 30 μm is employed so that small apatite grains can be analysed. The spot can also not stray on the outermost 10 μm rim of an apatite crystal, as this region is not counted in fission track analysis as the outermost 10 μm represent a transition zone from the 2π geometry to 4π geometry, assuming the U distribution is homogenous within the grain (Donelick et al., 2005).

However, for U-Pb dating a spot size as large as the diameter of the largest apatite population (typically 50 μm – 60 μm) is advised since the apatite Pb content is generally low and so a larger volume of material has to be ablated to produce accurate and precise isotopic ratios. The U-Pb apatite system is not particularly significant for determining Cenozoic exhumation histories in slowly cooled terranes such as Ireland and Britain other than providing a high temperature constraint for thermal history modelling. Hence samples on which combined AFT and U-Pb dating were undertaken employed a 30 μm spot size and were not reanalysed with larger spot sizes to improve the precision on the U-Pb ages.

4. Analytical procedures

In this chapter, the sample preparation and analytical procedure followed for AFT, AHe and apatite U-Pb dating in the Trinity College Dublin laboratory is described. Since all methods are based on apatite, the sample preparation steps for mineral separation are identical. The protocols then diverge for AHe and AFT/U-Pb sample preparation. The AFT and U-Pb sample preparation and analytical measurements are identical, and only differ in the final treatment of the mass spectrometry data.

4.1 Mineral separation

Apatite is an accessory mineral in most igneous, sedimentary and metamorphic rocks, thus the collected samples typically weighed several kilograms to ensure sufficient apatite yield. From each sample a hand-sized piece of rock was kept aside for later thin-section analysis if deemed necessary. The sample was then split using a hydraulic press and washed and dried, before being disaggregated in a Retsch BB200 jaw crusher with tungsten carbide plates (Figure 4.1). The sample was passed through the jaw crusher using a successively smaller plate spacing and removing the < 300 µm fraction with a sieve following each pass. Grains >300 µm were crushed again until ~80-90% of the material was smaller than 300 µm. The use of a disk mill should be avoided since the apatite crystals should be ideally intact for AHe dating.



Figure 4.1: Jaw crusher with tungsten carbide plates used to disaggregate the sample. The fraction <300 µm is processed further.

Once enough sample was crushed, the <300 µm fraction was separated using a Gemini (Rogers) shaking table. The dry sample is poured onto the table using a wall-mounted funnel, and passes down the table through riffles with running water, which separates the light minerals from the heavier minerals (Figure 4.2). The advantage of the shaking table as a first step of mineral separation is that it both removes fine, clay-size grains and additionally concentrates the heavy minerals in the sample. Typically the <300 µm heavy mineral fraction is less than 10% of the original sample volume and this thus reduces the amount of sample processed for magnetic and heavy liquid separation. However, separation with the shaking table means that the sample has to be dried before it can be processed further. The samples were dried for 1-2 days in an oven at 60°C. Heating the sample for such a short time at temperatures within the apatite PRZ does not affect the AHe age based on our knowledge of helium diffusion of apatite (i.e. applying these diffusion parameters to the Arrhenius plot of Dodson, 1973).

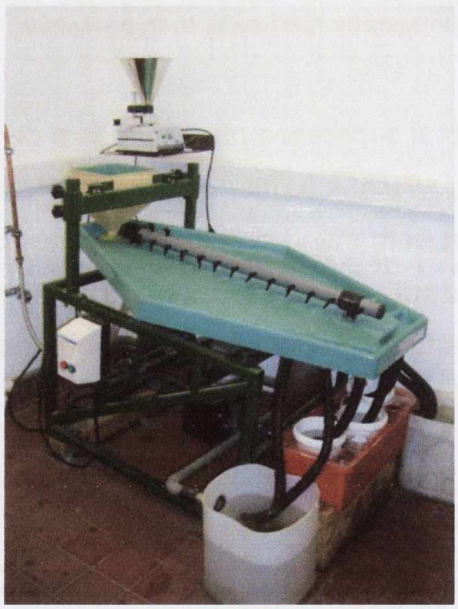


Figure 4.2: Water operated shaking table to separate the light minerals (clay-size) from the heavier minerals. The heavy mineral fraction is then processed further.

After the sample was dried in the oven, the heavy mineral separate from the shaking table is put into a Frantz magnetometer at different currents, starting with 0.5 A at a forward slope of ~20° and a side tilt of ~10° (Figure 4.3).

Afterwards, the non-magnetic fraction is run again at 1.0 A and 1.5 A, respectively. The non-magnetic fraction after 1.5 A usually contains the apatite separate. However, in some cases apatite can be enriched in Fe and thus can be found in the more magnetic fractions (Carlson et al., 1999).

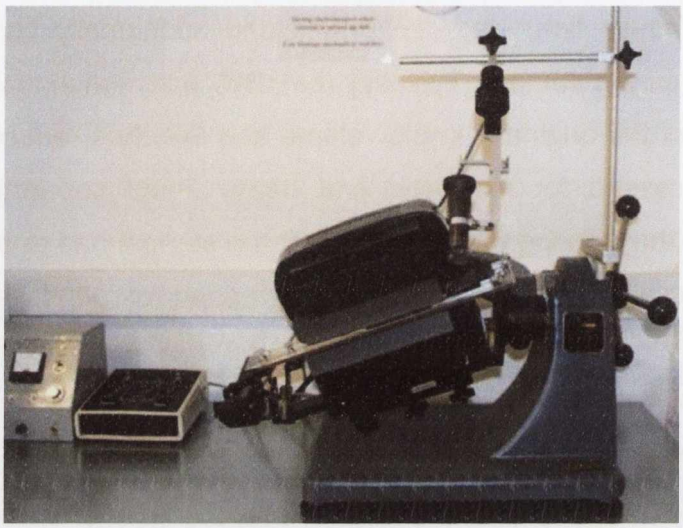


Figure 4.3: Frantz magnetic separator used to separate the non-magnetic from the magnetic fraction. The non-magnetic fraction is then processed further.

The last part of the mineral separation procedure is a density separation (Table 4-1) with a heavy liquid, which is further separated into two steps (Figure 4.4). The heavy liquid used in both steps is di-iodomethane (DIM: 3.3 g/cm^3), which is an organic-based fluid with a low viscosity and a low reactivity with minerals but it is toxic which means the separation has to be undertaken under a fume hood (Donelick et al., 2005).

Table 4-1: Mineral densities for apatite, zircon, pyrite and quartz

Mineral	Density range (g/cm^3)	Density average (g/cm^3)
Apatite	3.16 – 3.22 (3.21)	3.19
Zircon	4.6 – 4.7	4.65
Pyrite	5 – 5.02	5.01
Quartz	2.6 – 2.65	2.62
Feldspar (Plagioclase)	2.61 – 2.76	2.68

The first step is separation with DIM diluted with acetone to 2.8 g/cm^3 in a separation funnel with a stopcock at the bottom (Figure 4.4a). The sample inside the funnel is swirled to get all grains temporarily in suspension and then let settle for 30 minutes. Dense minerals such as apatite, zircon and pyrite will fall to the bottom of the funnel in DIM diluted to 2.8 g/cm^3 and the less-dense minerals like quartz and feldspar float on top of the liquid. This shaking and decanting procedure is repeated until no material sinks to the base of the funnel. The dense fraction is rinsed in acetone, air-dried and poured into a second funnel with undiluted DIM at 3.3 g/cm^3 (Figure 4.4b). This step is identical to before, only that the zircons will still fall to the bottom of the funnel but now the apatite will float on top of the liquid. Ideally, after this second step there will be a reasonably pure apatite and a zircon concentrate from the sample.

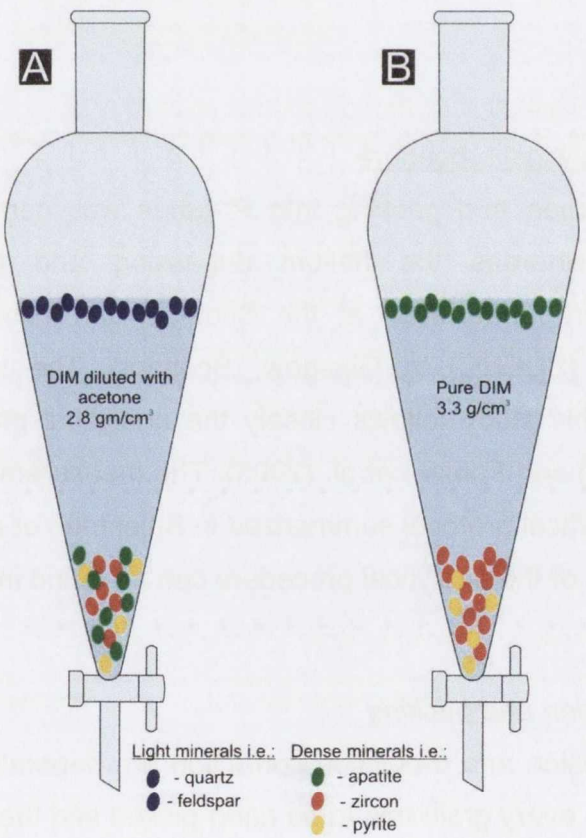


Figure 4.4: Schematic diagram of heavy mineral separation in a separation funnel. A: Separation of "light" minerals such as quartz and feldspar from "heavy" minerals like apatite, zircon and pyrite with acetone diluted DIM (~2.8 g/cm^3). B: Separation of apatite and heavier minerals like zircon and pyrite with pure DIM (3.3 g/cm^3).

After mineral separation, all separates should be checked under the microscope for their mineral content and purity. Sometimes quartz or feldspar grains can sink during the 2.8 g/cm^3 separation step due to inclusions in the grains which increase their density, or because the quartz/feldspar grains were "swirled" into the base of the funnel and could not escape. If there is sufficient contamination by less dense minerals (quartz and feldspar) in the apatite concentrate to make apatite identification and picking difficult, the heavy liquid separation procedure employing 2.8 g/cm^3 DIM is performed again. Because the sample size is now much smaller (typically less than a gram), the separation procedure is more efficient than during the first pass where untreated sample size is typically 10-100 grams. For samples with a small amount of apatite, it is advisable to pick the apatite grains for AHe dating before making the AFT mounts as the latter procedure requires more sample. Hence the analytical procedure for AHe dating is described first and is followed by AFT dating protocol.

4.2 AHe dating analytical procedure

Apatite grain selection and packing into Pt-tubes was carried out at Trinity College Dublin, whereas the helium degassing and U, Th and Sm measurements were undertaken at the Scottish Universities Environmental Research Centre (SUERC) in Glasgow, Scotland. The helium degassing protocol used in this study follows closely the analytical protocol outlined in House et al. (2000) and Foeken et al. (2006). The measurements of U, Th and Sm follow the analytical protocol summarized in Balestrieri et al. (2005). A more general description of the analytical procedure can be found in Farley (2002).

4.2.1 Crystal selection and packing

Since the ^{4}He diffusion and α-ejection correction are dependent on the crystal size and geometry, every grain has to be hand-picked and the dimensions have to be measured. Apatite picking for AHe dating was undertaken with a high magnification Nikon SMZ 1500 trinocular microscope, usually with a magnification of 150x (15x ocular and adjustable magnification of up to 10x) using transmitted light and switching between "normal light" and crossed-

polarizers. The first step for picking apatite grains for AHe dating is usually a quick pre-selection of apatite grains. The reason for the pre-selection is that the apatite concentrate does not purely consist of apatite grains and also apatite grains required for AHe dating should have a nearly idiomorphic crystal structure, which is, depending on the sample, rarely the case. Thus, during the pre-selection only nearly idiomorphic apatite grains are selected and transferred onto a second glass plate for further inspection.

After the pre-selection all picked grains are checked in detail for inclusions and cracks by using alcohol to increase the transparency of the grains and by switching between normal (Figure 4.5) and cross-polarized light. Mineral inclusions are easier to spot under cross-polarizers because inclusions that are not aligned to the crystallographic orientation of the host apatite will appear as a bright spots inside an apatite crystal which has an otherwise dark appearance.

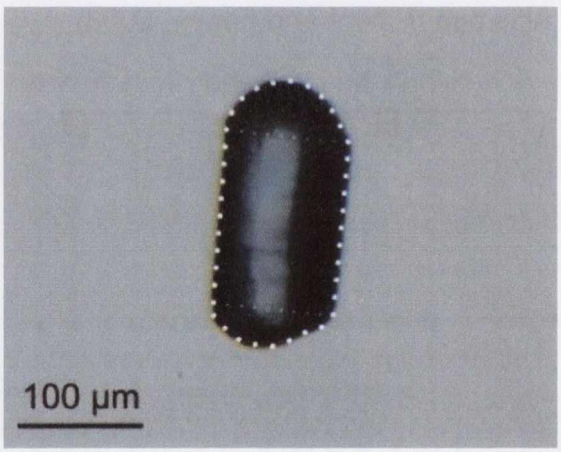


Figure 4.5: Selected apatite grain under normal light for AHe analysis. White dotted line shows the grain boundaries and both terminations (Grain Ire-8 grain a).

It is important to exclude all apatite crystals with inclusions or cracks because they can significantly change the age of the AHe measurements. Inclusions might induce a significant amount of "parentless" ^{4}He (section 3.3.7) into the apatite crystal (Figure 3.12b) and thus increase the AHe age. On the other hand, cracks in apatite crystals, which were not caused by the mineral separation and already existed when the crystal was in the PRZ might serve as fast pathways for ^{4}He diffusion and thus might yield younger AHe ages. Cracks

in apatite crystals are typically orientated perpendicular to the c-axis due to the crystal structure. Therefore, pre-existing cracks and cracks produced during the mineral separation (crushing) are indiscernible and thus should be avoided for AHe analysis.

Each apatite grain selected for AHe measurement was photographed using a Nikon D200 digital SLR camera connected to the trinocular eyetube of the Nikon microscope at magnification 150x (Figure 4.5). The pictures were subsequently analysed in the photo software "ImageJ" and the length, width and height were measured, along with information on whether the crystal has two broken ends (Figure 4.6c), one broken end and a pyramidal termination (Figure 4.6b) or two terminations (Figure 4.6a). Grain measurements were calibrated against a Psyer-SGI microscope graticule. Only apatite grains with a diameter >60 µm were selected otherwise the fraction of ^{4}He retained in the crystal would fall below ~60% and the error on the F_T correction factor would dominate the actual AHe age (Ehlers and Farley, 2003).

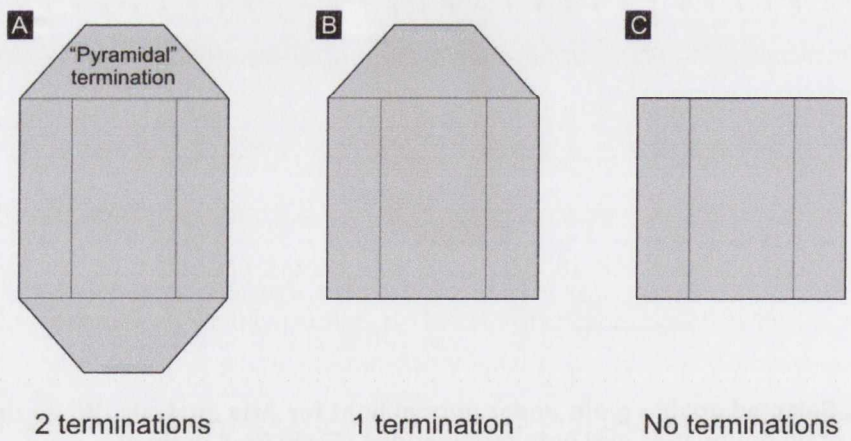


Figure 4.6: Schematic diagram of apatite grains for (U-Th)/He analysis. A: Grain with two "pyramidal" terminations (2T). B: One "pyramidal" termination (1T) and one broken end. C: Two broken ends (0T).

After the grain dimensions were measured, the single grain was carefully packed into a Pt-tube for degassing. Usually, ~5 single grains were picked per sample for AHe analysis. This is because even in well-behaved samples, there can be a moderate dispersion in AHe ages from grain to grain and still represent a good estimate for the true AHe age, taking into account the error for

the analytical procedure which is in this case ~2% (1σ) and an assumed error of 10% on the F_T correction (Farley, 2002).

Further reasons for dispersion in AHe ages include: i) small inclusions not detected during picking, ii) uncertainties in calculating the surface and volume ratio for broken crystals as shown in Figure 4.6 iii) uncertainties associated with the grain measurement as apatite crystals are usually not a perfect prism while the terminations often are not a perfect pyramid and iv) the U and Th distribution is not always uniform which has implications for 4He diffusion (e.g. U and Th enriched zones can lead to much older AHe ages).

4.2.2 ^{4}He degassing

The laser extraction system in SUERC used for the degassing of apatite crystals uses a diode laser (25 W, 808 nm) with a 2 mm spot size connected to one eyepiece of a binocular microscope. A small video camera is connected to the other eyepiece to observe the movement of the stage where the sample is located and to monitor the heating of the Pt-tube during degassing. Pt-tubes are used to "indirectly" heat the crystal by avoiding direct contact between the laser and crystal to prevent U and Th loss (House et al., 2000). The Pt-tubes are loaded in small holes drilled within a high purity Cu planchet. The Cu planchet can hold up to ~70 samples and is loaded into a stainless steel chamber on a moveable stage under the binocular. The chamber is part of a line system including several valves, pumps and a Hiden HAL3F Quadrupole mass spectrometer. Once the samples are loaded and the line has been pumped to vacuum overnight, the system can degas and measure ~70 samples within ~4 days.

The mass spectrometer calibration is undertaken with a ^{4}He-filled tank. At the start and end of each day and between every three to five samples, two calibration measurements are undertaken. These are compared with the mean calibration values of the day and the overall measurements since the last refilling of the ^{4}He tank or when the settings for the mass spectrometer were last changed. In general, the change during the calibration value was around 2 -

3% during each day. Additionally, at the beginning and the end of each session as well as once in between, empty Pt-tubes are heated for blank corrections. These heated Pt-tubes experienced the same dissolution procedure and were subsequently used as blanks for the U, Th and Sm analysis.

The degassing was undertaken with a defocused diode laser beam for 1 minute at approximately 500 – 600°C. This temperature is only an estimate derived from the yellow incandescence of the heated Pt-tube since the extraction system has no temperature sensor. Nevertheless, the temperature is sufficient to degas the apatite crystal without causing any U and Th loss which was demonstrated by the degassing experiments of Foeken et al. (2006). To ensure the apatite crystal is properly degassed, each Pt-tube is heated twice and the second run should be devoid of ^{4}He. If the second run yielded some ^{4}He, then a third run is undertaken and the process repeated until the crystal does not yield any more ^{4}He. However, a third run is usually only necessary if the apatite crystal was very large and therefore did not degas completely during the first two runs. This may happen during degassing of fragments of the Durango standard which can exceed 250 µm in diameter. Unknowns which did not degas on the first run were usually zircons (misidentified as apatites) which require a much higher degassing temperature (1100 – 1300°C) and a longer extraction time with the laser (~25 minutes) (Foeken et al., 2006).

4.2.3 U, Th and Sm analysis

After the ^{4}He degassing, the Pt-tubes are retrieved from the Cu planchet and put into pre-cleaned Teflon beakers for U, Th and Sm analysis. The beakers were pre-cleaned in several steps including HNO_3, HCl and a cleaning solution containing HF to ensure all beakers are free of any residual material from previous runs.

Each beaker was filled with 0.03g ±0.003g of an isotope tracer (or spike) mixture, containing ^{235}U, ^{230}Th and ^{149}Sm which was precisely measured with a high precision scale and balance (readability of 0.0001g) and 2 ml of 5% ultra-pure nitric acid (HNO_3) to dissolve the apatite. The beakers were subsequently

left on a hot plate for 48 hours to dissolve the apatite and afterwards the solution was transferred into small vials for U, Th and Sm analysis with a Agilent 7500ce Octopole Reaction System quadrupole ICP-MS (Balestrieri et al., 2005).

Each sample was measured in two sessions, since all six isotopes cannot be measured at the same time with the SUERC system. The first session measured ^{235}U, ^{238}U, ^{230}Th and ^{232}Th and the second session determined ^{149}Sm and ^{147}Sm contents. Fractionation in the mass spectrometer was monitored with the U500 standard (ratio of $^{235}U/^{238}U$ = 0.9997) every three unknowns or the Sm10 standard (ratio of $^{149}Sm/^{147}Sm$ = 0.94) every 10 unknowns, respectively. Each session on the mass spectrometer analysed 1-3 Durango standards for monitoring the overall session behaviour and total process blanks (empty Pt-tubes as mentioned above) for the blank correction of U, Th and Sm.

Based on the reproducibility of the Durango standards, the minimum analytical error for AHe measurements at SUERC is about 2% (1σ) assuming that the concentrations of U, Th and ^{4}He are well above blank level and excluding the error for α-ejection (Farley, 2002). Farley (2002) obtained a similar analytical precision of 2% with pure standard gases and aqueous standard solutions but in actual practice a reproducibility of ~6% (2σ).

4.3 Apatite fission track analytical procedure

After apatite grains were picked for AHe analysis, the rest of the apatite concentrate can be used to make AFT mounts. In general, two mounts were prepared for each sample provided enough material was available, to ensure enough apatite grains were polished for counting as well as for track length measurements. A comprehensive sample preparation protocol with alternative options for mounting and etching can be found in appendix 1 in Donelick et al. (2005).

4.3.1 AFT sample preparation

For mounting the apatite grains I used the epoxy-only approach (Donelick et al., 2005). The advantage of epoxy-only compared to a standard glass mount covered with epoxy is that the individual apatite grains are already near the surface prior to polishing. Thus, polishing the epoxy-only mounts is less time intensive than for glass mounts.

First, a glass slide (~ 75 by 25 mm) is covered with double-sided Scotch tape and two small plastic rings (washers ~1.5 mm high and 15mm in diameter) are mounted on them. Afterwards, the apatite grains are carefully poured from a folded piece of aluminium foil or a weighing paper onto the tape inside the ring to ensure the grains are evenly distributed inside the washer ring. Using double-sided Scotch tape ensures the apatite grains do not rise due to surface tension when the epoxy is subsequently poured into the ring. The volume of resin should barely exceed the internal diameter of the rings. Both filled rings are then covered by a second glass mount, which is also covered with double-sided Scotch tape which facilitates easy removal when the mounts have been cured. The mounts are cured in an oven at ~45°C for 24 hours.

Once the mount is hard, the glass slides can be removed with a razorblade and the plastic ring can be cut off using pincers. The epoxy-only mount is then loaded into a Struers Lapopol-21 polishing machine with a pressure-adjustable sample holder (Struers LaboForce 3). The polishing machine uses a rotating wheel at 300 rpm, and the grinding and polishing plates on the wheel have magnetic backs so they can be changed to use different polishing media.

The first polishing plate is a coarse composite plate (Struers MD-Allegro) with a mean grain size of 9 µm. It is used to grind the apatite mount, and is employed typically for ~10 s to remove any residual resin from the double-sided tape and to bring the apatite grains to the surface. The second plate is made of felt cloth (Struers MD-NAP) and is constantly sprinkled with a mixture of 6 µm diamond suspension fluid and lubricant via an automated doser (Struers Labodoser). During this step, the samples are regularly checked every ~3 minutes to see if all large polishing marks from the grinding stage are removed. The final polishing stage also uses a felt cloth plate but dosed with a 1 µm diamond fluid

and lubricant. This step takes 5 minutes but does not remove a lot of material, only removing small scratches and irregularities which would impede fission track counting.

After polishing, the apatite grains are etched to reveal spontaneous fission tracks. The etching recipe of Carlson et al. (1999) was used in this study. It employs 5.5 N HNO_3 for 20.0 s (±0.5 s) at 21°C (±1 °C). After etching, the mounts are directly placed into distilled water for several seconds and then moved into a second bath with distilled water for several seconds to remove the acid from the mounts. Subsequently, the mounts are dried and placed in open air for several hours allowing any remaining acid to dissipate without causing any uncontrolled etching (Donelick et al., 2005).

4.3.2 Track counting and track length measurements

For calibrating counting positions and for navigation on the mount during fission track analysis (and re-locating the counted areas during subsequent LA-ICP-MS measurements), three Cu SEM target grids (Agar Scientific) were glued onto each mount. Each of the three target grids has a letter (A, L or Q) in the centre of the target grid, and a reference point on each letter was defined to yield three reference points for each mount. The counting and track length measurements were undertaken on a Zeiss AxioImager Z1m with a maximum magnification of 1000x (100X Epiplan Neofluar DIC lens, 10X eyepiece magnification). The software used for counting and track length measurements is TrackWorks (Autoscan Systems) with included a module to measure confined track lengths which deviate by more than 10° from the horizontal polished surface (Section 3.2.7).

The first step in track counting is to coordinate the sample with help of the three SEM target grids. This facilitates adding more grains to the counted sample at a later stage, and prevents possible double counting of the same grain or re-measuring the same confined track length. This coordinate system is also used to retrieve the positions of counted grains on the mount for subsequent LA-ICP-MS analysis.

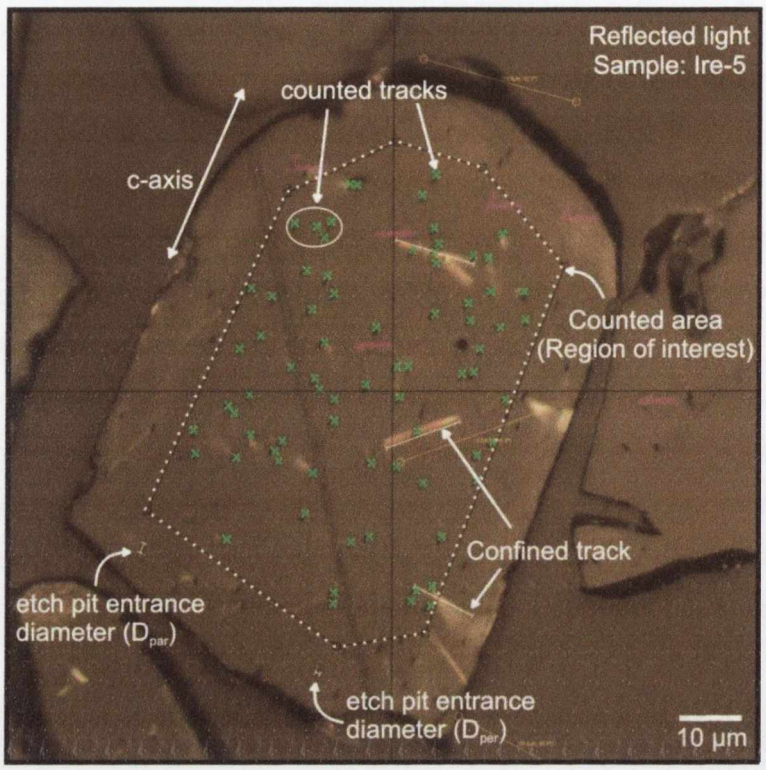


Figure 4.7: Reflected light image of a c-axis parallel apatite grain counted using the software package TrackWorks (Autoscan Systems).

Once the sample is coordinated, apatite grains parallel to the crystallographic c-axis are selected for counting (Figure 4.7). These are identified using a variety of criteria. The Zeiss AxioImager Z1m microscope in Trinity College Dublin has two circular polarizing plates, one below the stage and one above the stage but below the analyser. In circular polarization a plane-polarized ray is decomposed into two plane-polarized rays whose vibration directions (electric vectors) are at 90° to one another, with one ray retarded by a quarter wavelength behind the other. When added vectorially the resultant electric vector spirals as the ray propagates. In circular polarization all mineral grains exhibit their highest order interference colours for a given orientation of crystallographic axes relative to the plane of the stage, regardless of stage orientation. In other words is no change in interference colours when you rotate the stage or mount, facilitating rapid recognition of c-axis parallel apatite grains which will appear with the highest order interference colours. Potential C-axis parallel grains are then examined and screened in reflected light based on the alignment of etch-pit

figures and the characteristic appearance of etched polishing scratches on c-axis parallel surfaces.

Importantly, the apatite grain has to be at least 50 µm in diameter to avoid measuring too close to the rim (the outermost 10 µm) as the outermost 10 µm represent a transition zone from the 2π geometry to 4π geometry, assuming the U distribution is homogenous within the grain (Donelick et al., 2005) and to facilitate a 30 µm laser spot. Furthermore, the apatite grain should be as clear as possible, without too many defects which will impede the track counting and lead to misinterpretation of defects as tracks and vice versa.

Once an apatite grain is selected, the c-axis is defined using the alignment of the track etch pit figures in reflected light, and a region of interest (ROI) is defined on the grain (Figure 4.7), avoiding the outermost 10 µm of the grain along with areas that contain cracks or lots of defects within the crystal. Furthermore, the ROI should be selected carefully with regards to the spontaneous fission track distribution. In other words, a region of interest (the counted area) should not be defined to limit an area with a high spontaneous track density within a crystal with a variable spontaneous track density, since this indicates uranium zoning within the crystal. Instead regions of interest should be representative of the spontaneous track density of either the entire crystal or a large area within the crystal, so if the 30 µm spot LA-ICPMS is not positioned perfectly (e.g. due to minor stage drift on the laser ablation system), it still yields a representative U concentration of the counted area. Therefore the ROI (counted area) and the position of the laser spot need to be carefully defined. Once all spontaneous tracks have been counted, D_{par} (the length of the etch pit in reflected light) and D_{per} (the width of the fission track ethc pit) (Figure 4.7) for at least three spontaneous tracks per grain are measured. Any confined tracks present in the counted grains are also counted (Figure 4.7).

Per sample a total of 100 confined tracks were targeted; if 100 confined tracks were not found in the counted grains, further c-axis parallel grains were examined. In samples which yield relatively old AFT ages such as in thesis, ~20-25 grains counted grains are normally sufficient to yield enough confined

tracks. The kinetic parameters D_{par} and D_{per} are also measured for grains where only confined tracks were measured. Laser ablation is a destructive method and since it might be necessary to reinvestigate the counted grains in the case of grains that yield anomalous AFT ages, high-resolution 3-D stacked images were acquired in both transmitted and reflected light, as well as images with overlays showing the counted tracks, the measured confined tracks and the defined ROI.

4.4 LA-ICP-MS measurements for AFT and apatite U-Pb dating

LA-ICP-MS measurements for combined AFT and apatite U-Pb dating were acquired using a Photon Machines Analyte Exite 193 nm ArF Excimer laster-ablation system coupled to a Thermo Scientific iCAP Qc at Trinity College Dublin. The most important isotopes for integrated AFT and apatite U-Pb dating are ^{35}Cl, ^{43}Ca, ^{202}Hg, ^{204}Pb, ^{206}Pb, ^{207}Pb, ^{208}Pb, ^{232}Th and ^{238}U. Additional isotopes were measured for apatite trace-element determinations which may yield useful information for sedimentary provenance studies and apatite fission-track annealing behaviour (Chew and Donelick, 2012). These isotopes are ^{31}P, ^{55}Mn, ^{86}Sr, ^{89}Y, ^{139}La, ^{140}Ce, ^{141}Pr, ^{146}Nd, ^{147}Sm, ^{153}Eu, ^{157}Gd, ^{159}Tb, ^{163}Dy, ^{165}Ho, ^{166}Er, ^{169}Tm, ^{172}Yb, and ^{175}Lu. A 30 µm laser spot, with a 5 Hz repetition rate and a fluence of 3.31 J/cm^2 was employed. Each analysis lasted 45 s with a subsequent 25 s washout to clean the line from the previous analysis before the next analysis starts. Baseline isotope values between analyses were acquired using the last 10 s of signal of the washout.

During each ICP-MS session, a suite of standards was analysed comprising four Durango "zeta" standards (DUR) as the primary standard for AFT dating (section 3.2.9), followed by three NIST612 standard glass analyses (a homogenous standard glass doped to ~40 ppm for over a suite of trace elements, followed by three Madagascar apatites (MAD), three McClure Mountain syenite apatites and two Bamble chlorine apatite standards. Madagascar apatite and McClure Mountain apatites are described below and are the primary and secondary standards employed for apatite U-Pb dating. The primary AFT zeta standard (Durango apatite) is also employed as an

apatite U-Pb secondary standard. Bamble chlorapatite contains 6.3 wt% chlorine (Carlson et al., 1999; Donelick et al., 1999) and is the primary standard for LA-ICP-MS chlorine determinations in apatite (Chew et al., 2014). Following this block of standards, 20 apatite "unknowns" were analysed, followed by the next block of standards. For the start of the run, the block of standard analyses commenced with eight NIST612 analyses.

The NIST612 trace element standard glass is used to monitor long-term drift in U/Ca ratios during a LA-ICP-MS session. Madagascar apatite (Thomson et al., 2012) is the primary standard for apatite U-Pb dating, and the crystal fragments used in the Trinity College Dublin laboratory have yielded a ^{204}Pb-corrected ID-TIMS Concordia age of 473.5 ±0.7 Ma (Cochrane et al., 2014). McClure Mountain apatite was used as a secondary standard for U-Pb dating. McClure Mountain apatite has yielded a high-precision ID-TIMS crystallization age of 523.51 ± 2.09 Ma (weighted mean ^{207}Pb/^{235}U age, corrected for common Pb) and a well-defined initial Pb isotopic composition calculated from a 3-D total Pb-U isochron (^{206}Pb/^{204}Pb = 17.54 ± 0.24; ^{207}Pb/^{204}Pb = 15.47 ± 0.04) (Schoene and Bowring, 2007).

4.4.1 Data reduction for AFT and U-Pb dating

Data reduction of a LA-ICP-MS AFT and apatite U-Pb dating session is for the most parts identical, thus they are described together and only the differences between AFT and apatite U-Pb analysis are highlighted. The raw isotope data from the ICP-MS session is processed using the free software package IOLITE of Paton et al. (2011) running under the WaveMetrics package, IGOR Pro, a platform that was originally developed for time-series analysis, but has since then evolved and covers other applications such as curve fitting and image processing.

The first step in the data reduction is to establish a user-defined baseline correction and apply this correction session-wide to all isotopes. Baselines are defined typically for the last 10 s of the washout immediately preceding the next analysis. The apatite standard and unknown analyses are defined using a time-

stamped file (laser logfile) that is produced by the laser-ablation system, and temporally matched to the time-resolved signal intensities acquired by the mass spectrometer. These steps are common to both AFT and apatite U-Pb dating.

Typically there is variation in terms of the signal intensity in stoichiometric elements in apatite (linked to the quality of ablation between analyses, often ranging between ~10 - 20%). Hence U concentration measurements, if uncorrected for this effect would be significantly inaccurate. Hence for AFT dating by LA-ICP-MS, ^{43}Ca is employed as an internal standard, meaning that U signal intensities are normalised to the ^{43}Ca signal which is assumed to be stoichiometric in apatite. U/Ca drift during the session is corrected by fitting a smooth-fit curve (termed a "spline" in Iolite) through the NIST612 primary standard, and then applying this model U/Ca drift curve to all unknowns that are interspersed between standards.

An additional effect which needs to be taken into account is that the "effective" or "final" U concentration needs to be weighted more heavily towards the U concentration near the surface of the crystal compared to U deeper in the crystal, as U near the surface contributes more toward the production of spontaneous fission tracks (see chapter 3.2.5 for more information on the depth-weighted $^{238}U/^{43}U$ ratio). The analysis pit needs to extend to a distance of 10 µm (broadly half a fission track length) below the apatite grain surface and it is therefore also important that the depth of the ablated spot can be calculated accurately. In this thesis, the depth of ablation was monitored by measuring the depths of ablated spots by focusing on the bottom and tops of spot ablation pits using the z-stage of the AxioImager Z1m.

U-Pb data reduction is quite similar but it uses a modified version of the VizualAge data reduction scheme (VizualAge_UcomPbine) by Petrus and Kamber (2012), which accounts for a variable common Pb in the primary standard (Chew et al., 2014). The application of the data reduction scheme requires a user-specified down-hole correction model for U-Th-Pb fractionation which is fit through the common Pb-corrected U-Th-Pb ratios of the primary standard, Madagascar apatite. Afterwards this model downhole U-Th-Pb

fractionation curve for is applied to all secondary standards and unknowns. Long-term drift in isotopic and elemental ratios during the LA-ICP-MS session is then corrected for by normalizing all ratios to those of the U-Pb primary reference standard (Chew et al., 2014).

5. Sample locations

The sampling locations were selected to include the region putatively affected by the Proto-Iceland mantle plume along with neighbouring regions, so that the limits of plume-related Cenozoic exhumation can be determined or if the exhumation pattern exceeds the limits of the putatively mantle plume region. Therefore, the focus of the sampling area was situated around the Irish Sea region and also extended into Wales, central and western Ireland and Scotland. The sampling sites are displayed on Figure 5.1 and grid references in Table 5-1. In addition to their location relative to the inferred Irish Sea dome, fieldwork sites were also selected based on their rock-type and elevation. The preferred collected rock type for AFT and AHe analysis were felsic intrusive rocks (e.g. granites or granodiorites; see Table 5-1) as they typically yield coarse, euhedral apatite with reasonable U contents. Where possible, a pseudo-vertical sampling profile (i.e. steep mountainsides with a vertical sample spacing of c. 150 m) was adopted to facilitate vertical profile modelling within QTQt.

Some apatite separates were obtained from previous geochronology and thermochronology studies on Ireland and Scotland. Samples Ire 1 to Ire 7 along with the LG sample suite (LG 17, -18, -19 and -32) are a subset of samples analysed in previous AFT studies by Allen et al. (2002) and Bennett (2006). These samples were reanalysed in this thesis while also undertaking AHe on these samples. Samples Sct 1 to Sct 12 were supplied by Fin Stuart and colleagues at the Scottish Universities Environmental Research Centre (SUERC), as a suite of non-magnetic heavy mineral fractions from granites and gneisses in Scotland. All of the samples obtained from these previous dating studies are single samples and thus cannot be used for vertical profile modelling.

The additional fieldwork sites sampled for this thesis were situated on the Isle of Man (IoM), east/central Ireland (Ire 8 - 10; MM 1 - 5), Wales (An, Br, Cu, My, Pb and Yg) and the Isle of Arran (IoA) in Scotland. Overall, six vertical profiles were sampled on the Isle of Arran (IoA), the Mourne Mountains (MM) and from the Brecon Beacons (Br) and Snowdonia (Cu, My and Yg) in Wales (Figure

5.1). Two samples from the same granite body were sampled on the Isle of Man (IoM) but the vertical difference between the two locations is only ~80 m and thus very small. Nevertheless, these two samples were modelled together.

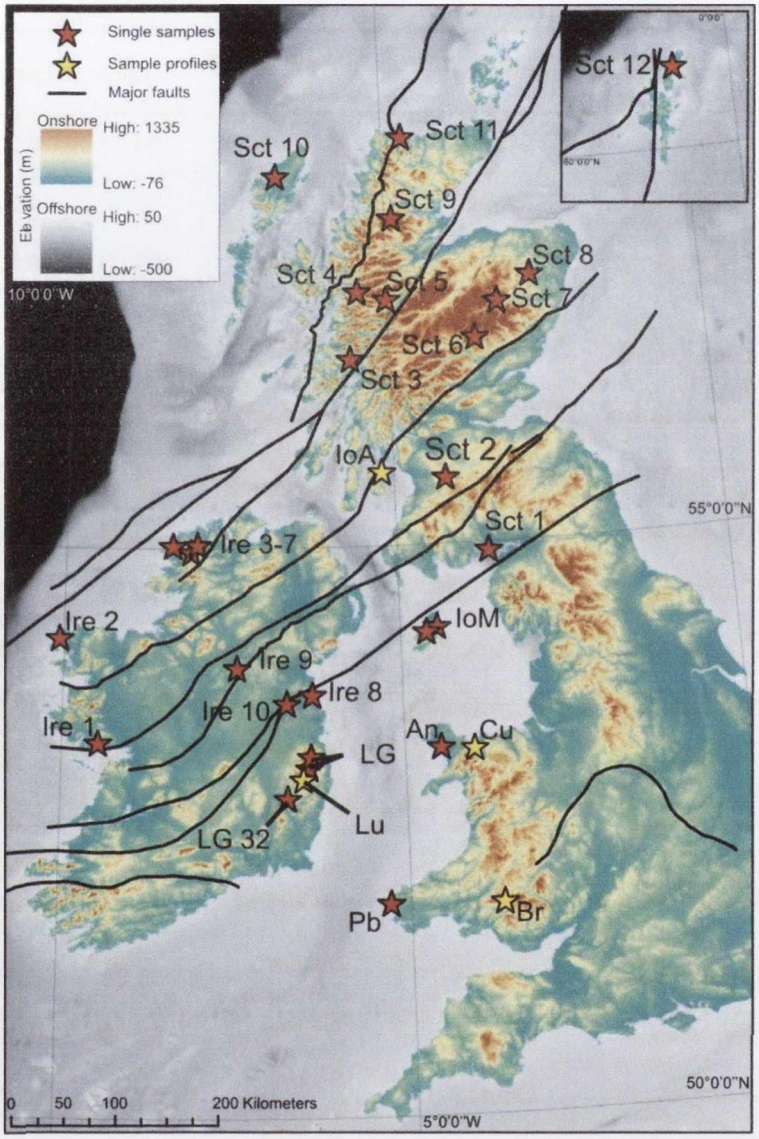


Figure 5.1: Map with sample locations across Britain and Ireland. Samples which did not yield any apatite are not included on the map.

One additional profile was sampled by Nathan Cogné from Lugnaquilla (Lu) in SE Ireland. From this profile three samples (Lu 1, 3 and 6) were chosen for AHe broken grain analysis (Beucher et al., 2013; Brown et al., 2013) and ~25 apatite grains were picked for AHe analysis but the AFT analysis was undertaken by N. Cogné. Unfortunately, the AHe broken grain analysis was not

modelled in this thesis due to extensive modelling time for ~25 AHe grains per sample (>12 hours for 1000 iterations in QTQt).

Table 5-1: Sample locations

Sample Name	Location	Lithology	Stratigraphic age	Lat.	Long.	Elevation (m)
IoM 1	Dhoon	Granite	Devonian	54.15	-4.23	239
IoM 2	Dhoon	Granite	Devonian	54.15	-4.22	162
IoM 3	Foxdale	Granite	Devonian	54.09	-4.37	174
Ire 1	Bovroughaun	Granite	Silurian - Devonian	53.30	-9.47	165
Ire 2	Binghamstown	Orthogneiss	Mesoproterozoic	54.21	-10.07	0
Ire 3	Bingorms	Granodiorite	Silurian - Devonian	54.98	-8.12	665
Ire 4	Kincasslagh	Granodiorite	Silurian - Devonian	55.03	-8.40	0
Ire 5	Glenveagh	Granodiorite	Silurian - Devonian	55.04	-8.03	640
Ire 6	Glenveagh	Granodiorite	Silurian - Devonian	55.04	-8.03	360
Ire 7	Kincasslagh	Granodiorite	Silurian - Devonian	55.04	-8.40	0
Ire 8	Drogheda	Granite	Silurian - Devonian	53.72	-6.33	3
Ire 9	Crossdoney	Granite	Silurian - Devonian	53.95	-7.44	120
Ire 10	Tara Mines	Sandstone	Ordovician - Silurian	53.64	-6.71	-1702
LG 17	Carrigshouk	Granite	Silurian - Devonian	53.09	-6.37	517
LG 18	Carrigshouk	Granite	Silurian - Devonian	53.09	-6.36	553
LG 19	Glenmacnass	Granite	Silurian - Devonian	53.07	-6.34	389
LG 32	Tullow Hill	Granite	Silurian - Devonian	52.80	-6.72	122
Sct 1	Criffel	Granite	Silurian - Devonian	54.94	-3.63	559
Sct 2	Distinkhorn	Granite	Silurian - Devonian	55.59	-4.22	240
Sct 3	Strontian	Granodiorite	Silurian - Devonian	56.64	-5.62	190
Sct 4	Ratagain	Granite	Silurian - Devonian	57.22	-5.48	350
Sct 5	Cluanie	Granite	Silurian - Devonian	57.15	-5.02	230

continues next page

Sample Name	Location	Lithology	Stratigraphic age	Lat.	Long.	Elevation (m)
Sct 6	Ben Vuirich	Foliated granite	Neoproterozoic	56.79	-3.64	670
Sct 7	Glen Gairn	Pink biotite granite	Silurian - Devonian	57.10	-3.26	410
Sct 8	Insch	Gabbro	Ordovician - Silurian	57.31	-2.72	200
Sct 9	Ardclach	Granite	Neoproterozoic	57.85	-4.88	507
Sct 10	West Lewis	Lewisian gneiss	Archaen	58.24	-6.76	45
Sct 11	Durness	Lewisian gneiss	Archaen	58.55	-4.67	30
Sct 12	Shetland	Granodiorite	Neoproterozoic	60.72	-1.01	15
An 1	Anglesey	Granite	Neoproterozoic	53.23	-4.49	29
Br 1	Brecon Beacons	Sandstone	Late Devonian	51.88	-3.71	801
Br 2	Brecon Beacons	Sandstone	Early Devonian	51.85	-3.69	505
Br 3	Brecon Beacons	Sandstone	Early Devonian	51.84	-3.68	251
Cu 1	Snowdonia	Granite	Ordovician - Silurian	53.18	-3.95	802
Cu 2	Snowdonia	Granite	Ordovician - Silurian	53.19	-4.00	731
Cu 3	Snowdonia	Granite	Ordovician - Silurian	53.19	-3.98	871
Cu 4	Snowdonia	Granite	Ordovician - Silurian	53.21	-3.99	316
Cu 5	Snowdonia	Granite	Ordovician - Silurian	53.27	-3.95	53
Pb 1	Pembrokeshire	Granite	Neoproterozoic	51.87	-5.28	5
Pb 2	Pembrokeshire	Granite	Neoproterozoic	51.87	-5.28	10
IoA 1	Isle of Arran	Granite	Paleogene	55.63	-5.19	852
IoA 2	Isle of Arran	Granite	Paleogene	55.63	-5.19	746
IoA 3	Isle of Arran	Granite	Paleogene	55.62	-5.18	535
IoA 4	Isle of Arran	Granite	Paleogene	55.62	-5.18	468
IoA 5	Isle of Arran	Granite	Paleogene	55.62	-5.18	385
IoA 6	Isle of Arran	Granite	Paleogene	55.67	-5.21	93

continues next page

Sample Name	Location	Lithology	Stratigraphic age	Lat.	Long.	Elevation (m)
Lu 1	Lugnaquilla	Granite	Silurian - Devonian	52.97	-6.46	901
Lu 3	Lugnaquilla	Granite	Silurian - Devonian	52.98	-6.44	502
Lu 6	Lugnaquilla	Granite	Silurian - Devonian	52.97	-6.38	126
Yg 1	Snowdonia	Granite	Ordovician - Silurian	53.12	-4.05	805
Yg 2	Snowdonia	Granite	Ordovician - Silurian	53.12	-4.02	305
My 1	Snowdonia	Granite	Ordovician - Silurian	53.07	-4.18	698
My 2	Snowdonia	Granite	Ordovician - Silurian	53.08	-4.17	145
Pb 3	Pembrokeshire	Granite	Ordovician - Silurian	52.00	-5.08	105
MM 1	Mourne M.	Granite	Paleogene	54.14	-5.98	715
MM 2	Mourne M.	Granite	Paleogene	54.14	-5.98	579
MM 3	Mourne M.	Granite	Paleogene	54.14	-5.99	411
MM 4	Mourne M.	Granite	Paleogene	54.13	-5.99	282
MM 5	Mourne M. core	Granite	Paleogene	54.12	-6.00	
-600						-600
-515						-515
-437						-437
-344						-344
-253						-253
-179						-179
-86						-86
-21						-21

Notes:
Mourne M.: Mourne Mountains

6. Modelling

6.1 Introduction to modelling by QTQt

The modelling of all AFT and AHe data was undertaken with the QTQt software package (version 5.4.1) designed by K. Gallagher (Gallagher, 2012). QTQt is a modelling program which can infer the thermal history of low-temperature thermochronological data, including from multiple samples in one vertical profile (Gallagher et al., 2005), which is one of the main approaches of this thesis. This chapter provides a general overview about the modelling approach and the techniques that can be implemented in QTQt and a more comprehensive explanation can be found in Gallagher (2012).

Currently, the software is capable of modelling data from the apatite and zircon fission track, apatite and zircon (U-Th-Sm)/He, vitrinite reflectance, $^{4}He/^{3}He$ and $^{40}Ar/^{39}Ar$ systems (Gallagher, 2015). Furthermore, other mineral-isotope systems (e.g. U-Pb thermochronometry) can be added by simply changing the activation energies and diffusivities. For AFT dating, QTQt supports the Durango-based annealing model of Laslett et al. (1987) as well as the multi-kinetic annealing model of Ketcham et al. (1999 and 2007a; 2007b). For AHe studies, the radiation-damage accumulation and annealing model (RDAAM) of Flowers et al. (2009) and Gautheron et al. (2009) are included. The RDAAM model from Flowers et al. (2009), see chapter 3.3.5, is based on the effective fission track density as proxy for accumulated radiation damage while the Gautheron et al. (2009) based on a quantitative model which includes α-recoil damage, annealing and He diffusion kinetics. In this thesis, the AFT annealing model of Ketcham et al. (2007a; 2007b) and the AHe RDAAM of Flowers et al. (2009) were employed in modelling.

6.2 Theoretical basis of the approach

The inverse modelling of the data with QTQt uses a Bayesian trans-dimensional Markov Chain Monte Carlo (MCMC) approach which is an iterative sampling method. It is explained in detail, including the mathematical background, in Gallagher et al. (2009; 2012).

The Bayesian approach refers to a statistical method which is based on conditional probabilities. Of interest is the posterior probability defined as the probability of a (thermal history) model, conditional on, or given, the observed data. The posterior probability is proportional to product of the likelihood, the probability of the observed data given a (thermal history) model, and the prior probability for the (thermal history) model. See Gallagher et al. (2009) and references therein for further explanations relevant to on Bayes' theorem.

The prior probability distribution is essentially defined as what we think is reasonable in the absence of data. In the case of QTQt, this means constraints on the range of possible time and temperature values for the thermal history and additional information such as the annealing kinetics or diffusion parameters. The likelihood is a value describing how well the model fits the observed data, given the underlying modelling parameters (Gallagher et al., 2009).

To produce the posterior probability distribution a MCMC approach is used, which is an iterative sampling method. The general principle behind a Markov chain is that it produces a sequence of models which represents the posterior distribution. This process involves perturbing a current model to produce a proposed model which is either accepted or rejected depending on specified acceptance criterion. The criterion is essentially the ratio of the posterior probabilities for the proposed and the current model. If the ratio is greater than 1, the proposed model is always accepted, otherwise it is accepted with a probability defined by the posterior ratio.

The iterations for the MCMC approach can be separated into two parts. The first part (burn-in) represents the first initial exploration of the modelling space and these models are subsequently discarded; however, this stage helps define the space of acceptable thermal histories. The second part (post-burn-in) is used to approximate the posterior probability distribution by keeping all accepted thermal histories (Gallagher, 2012).

The combined Bayesian-MCMC approach enables QTQt to investigate the whole modelling space constrained by the prior information and determine the likelihood to represent how well each model fits the observed data for each proposed model. The transdimensional approach implemented in QTQt allows the data to infer the complexity of the thermal history, which is different to other modelling programs (i.e. HeFTy; Ketcham, 2005) where the thermal history is characterised by a user specified number of time – temperature constraints which determines the complexity of the model in advance.

The complexity of a model is defined by the number of point time – temperature points (t-T) used to predict the thermal history. The Bayesian approach naturally prefers simpler solutions for the thermal model because as the number of t-T points increases, the posterior probability decreases, and thus the acceptance probability for a more complex thermal history will be lower than a simpler model, if they both fit the data to a similar degree (Gallagher, 2012). As a consequence of preferring simpler thermal models, the Bayesian approach reduces problems of over interpretation of inferred thermal histories (i.e. complexity or modelling artefacts not required by the data).

6.3 Applying QTQt to thermochronological data

A wide range of thermal histories can be explored within the limits defined by the general prior information (the starting "box" for the thermal history in t-T space), which is by default a time interval spanning double the oldest age in the thermochronological dataset and a temperature range of 70 ± 70°C (which covers the temperature sensitivity range of the commonly employed AFT and AHe systems). Additional information can be added, including a temperature offset for vertical profiles, and additional time-temperature constraints if known (e.g. the depositional age of a detrital sample, or the crystallisation age of a magmatic sample). In this thesis, magmatic samples typically employed the apatite U-Pb age (obtained by the LA-ICP-MS AFT dating approach, sections 3.4, 4.4) as a high-temperature constraint.

In QTQt, the first model is randomly drawn from the given prior distributions including the general prior (the specified time-temperature range), additional time-temperature constraints (in the case of this study apatite U-Pb ages) and the present-day surface temperature. This forms the first current model, and we calculate its likelihood (how well the model fits the observed data. By multiplying the likelihood and the prior probability, we obtain the posterior probability. In each subsequent iteration, one parameter is changed in the model to produce a proposed model. Predictions from the proposed model are used to calculate its likelihood and posterior, latter being compared to that for the previous model as the acceptance condition.

Possible changes in the model include: i) changing the temperature of a t-T point, ii) changing the time of a t-T point, iii) removing a t-T point, iv) create a new t-T point, v) changing the kinetic parameter for AFT dating (e.g. D_{par}), vi) change the temperature offset value (in vertical profile models) or vii) "resampling" one observed data value (e.g. the AFT kinetic parameter, AFT data or an AHe age). Resampling the observed data is a way to deal with general noise (e.g. spread in AHe ages) caused by uncertainties in, for example, grain size measurements for apatite grains (AHe dating) and simplified assumptions (i.e. uncertainties within the annealing or diffusion model) (Gallagher, 2012). Resampling the observed data means that instead of using the observed age to calculate the likelihood for the proposed model, a value is sampled from a normal distribution centred on observed age with the observed error as the standard deviation. The sampled value is then treated as the observed age for the likelihood calculation (Gallagher, 2012). Allowing the observed data to vary will increase the uncertainty in the inferred models. However, as some parameters are difficult to measure or calculate (grain dimensions for AHe dating) and other are uncertain (annealing and diffusion models) it is a reasonable assumption that the error is larger than the measurement error and the conservative approach of resampling observed data is reasonable (Gallagher, 2012).

After one of above listed parameters is changed, the thermal history model is run again and the software compares if the predicted data for this new thermal

history (e.g. the AFT or AHe ages, AFT track lengths etc.) fit the observed data better than the previous model. If the proposed thermal model yields better predictions (higher probability) than the current one, then the new model will tend accepted and so become the "current" thermal history model. However, predicted models with lower likelihoods can also be accepted as a viable thermal history as a consequence of the probabilistic nature of the acceptance criterion (Gallagher, 2012).

The acceptance probability is calculated from the prior model and the likelihood from the proposed and current model and is always between 0 and 1 (Gallagher, 2012). The criterion is then compared with a randomly generated number calculated using a uniform distribution (between 0 and 1). If the acceptance criterion is bigger than the randomly generated number, then the proposed thermal history is accepted. If a proposed model is rejected, then a copy of the current model is added to the posterior probability distribution. By adopting this approach, QTQt quantifies the range of accepted models as a probability distribution, and thus ensures that a spectrum of possible thermal histories are accepted, as opposed to identifying just the thermal history that bests fits the data.

Collecting a range of accepted models in a probability distribution allows us to consider different individual models such as a maximum likelihood, or maximum posterior models, or maximum posterior models, or a representative average model such as the expected model (Gallagher, 2012). The maximum likelihood model is the model of all those sampled which best fits the data. However the thermal history in this model typically contains more t-T points than the other final output model types, which may not be justified by the data and thus make the model more complex. The expected model is a weighted-mean model, where the weighting is provided by the posterior probability for each model. It has the characteristics of all models sampled in the post-burn iterations and is in general less complex than the maximum likelihood model (Gallagher, 2012). Where possible, the expected model is displayed in the modelling results in this thesis, with the exception of samples where the predictions for the expected

model deviate from the observed data by more than 10%. In such cases, the maximum likelihood model is displayed as well.

6.4 Generating a QTQt modelling file

The user interface in QTQt allows the creation of a text document which contains all the information needed to run inverse modelling of thermochronological data.

At the time of writing this thesis, AFT data from both the EDM and the LA-ICP-MS method can be implemented in QTQt. However, the previous versions of QTQt only accepted spontaneous and induced track data from the EDM. Since the LA-ICP-MS method was used in this study to determine the U content, no induced tracks were counted. In order to use QTQt before the option for the LA-ICP-MS method was included, the number of induced tracks (N_{calc}) was calculated from the weighted $^{238}U/^{43}Ca$ ratio, the counted area Ω in cm^2 and a representative value of $1x10^7$ (tracks/cm^2) for ρ_D, the track density in a standard dosimeter glass (Hurford and Green, 1982):

$$N_{calc} = \Omega * \left(^{238}U/^{43}Ca\right)_{weighted} * 1 \text{ x } 10^7$$

Equation 26

QTQt uses N_s and the calculated N_i (N_{calc}) as well as the personal LA-IPC-MS zeta factor and ρ_D to calculate the central age of the sample (section 3.2). This central age is subsequently employed in the thermal history modelling.

When entering AHe data into the QTQt interface, it should be noted that the uncorrected AHe age as calculated by QTQt is usually slightly different than the uncorrected AHe age as calculated by the non-iterative age calculation of Meesters and Dunai (2005). QTQt uses the absolute U, Th and Sm concentrations in ppm and the grains dimensions (geometry of a sphere) to calculate the AHe age. In contrast, the SUERC in-house calculation sheet uses the amount of atoms of U, Th and Sm to calculate the total ^4He production and

then calculates the AHe age without information on the mass of the grain. Due to this calculation differences in QTQt and the SUERC in-house calculation sheet, it is necessary to adjust the U concentration by typically less than 4% so that the uncorrected AHe age in QTQt match the AHe as calculated by the non-iterative method (Meesters and Dunai, 2005). Adjusting the uranium content by ~4% (which corresponds to uranium content of 0.65 ppm taken from the average uranium content in all modelled grains) is within the error margin of the grain size measurements and thus does not influence the overall result for the AHe ages.

6.5 Applying the QTQt modelling procedure in this study

All thermal models created in this thesis used the multi-kinetic annealing model of Ketcham et al. (2007a; 2007b) for fission track annealing and the RDAAM from Flowers et al. (2009) for the ^{4}He diffusivity in apatite. Additionally, the kinetic parameter D_{par} was allowed to vary within standard error (SE).

The first steps for preparing each individual modelling run are adding additional t-T constraints (e.g. U-Pb age or deposition age) and defining the model space as explained in Section 6.3. After the t-T constraints and model space were defined, the amount of MCMC iterations and the time-temperature step are selected. Usually in this thesis, the models were started with only ~10,000 iterations to explore the data and define an appropriate scale for each time-temperature step. Furthermore, it is important to check the discrepancy of the observed and predicted data before a detailed final model run is started. Sometimes, single AHe ages cannot be predicted because they are too old or young for the expected model and this "forces" the thermal model into a history which does not fit the rest of the data. In these cases, it is beneficial to experiment with removing such AHe ages to see if the remaining data yield better predictions.

For all final models, a burn-in of 200,000 iterations and 200,000 post-burn-in iterations were chosen. Burn-in means that all iterations generated in the burn-in are only created to explore the model space given by the general priors and

are subsequently discarded. Only the accepted post-burn-in (see section 6.3) models are used to generate the probability distribution for the model parameters (Gallagher, 2012).

After the modelling, several parameters were examined in order to evaluate the quality of the thermal model. The acceptance rate indicates how many of the new models, with changed time-temperature steps, were accepted as new thermal models. The general rule in this thesis, and in accordance with Gallagher (2012), was that the acceptance rate should be between 0.2 and 0.6 which are good values to explore the time – temperature space of the model.

Additionally, the log likelihood as a function of iteration (chain) should be examined. If the likelihood chain shows a steady increase or trend, then this means that the thermal model has not reach the stationary state, and so not fully explored the full model space. Then the amount of iterations should be increased, or modelling restarted from the last model of the initial run. If the likelihood chain has no obvious trends, then the thermal model space is usually well explored. The likelihood chain for all thermal history models (see Figure 7.10 to Figure 7.20) was examined and consistently flat which means the modelling space was sufficiently explored for each model.

Finally, the predictions for the expected thermal models are compared with the measured AFT and AHe ages and the kinetic parameters (e.g. D_{par}) and the measured track lengths. Usually, a discrepancy of ~10% between the predicted and observed data is good. However, as described in section 4.2.1, AHe data often exhibit large age dispersion and thus sometimes it is not possible to ensure that all the predicted AHe ages lie within 10% of the observed AHe ages.

7. Results

Overall 64 separate samples were processed for AFT and AHe dating. However, the granite samples from the Mourne Mountains (MM sample suite: four pseudo-vertical profile samples and eight from a geothermal drill core), Snowdonia (Yg-1, Yg-2, My-1 and My-2) and Pembrokeshire (Pb-3) did not yield any apatite and hence could not be analysed (and are thus not in the data tables). AFT and AHe dating was therefore undertaken on 47 samples, including four pseudo-vertical profiles (Cu, Br, IoA and Lu).

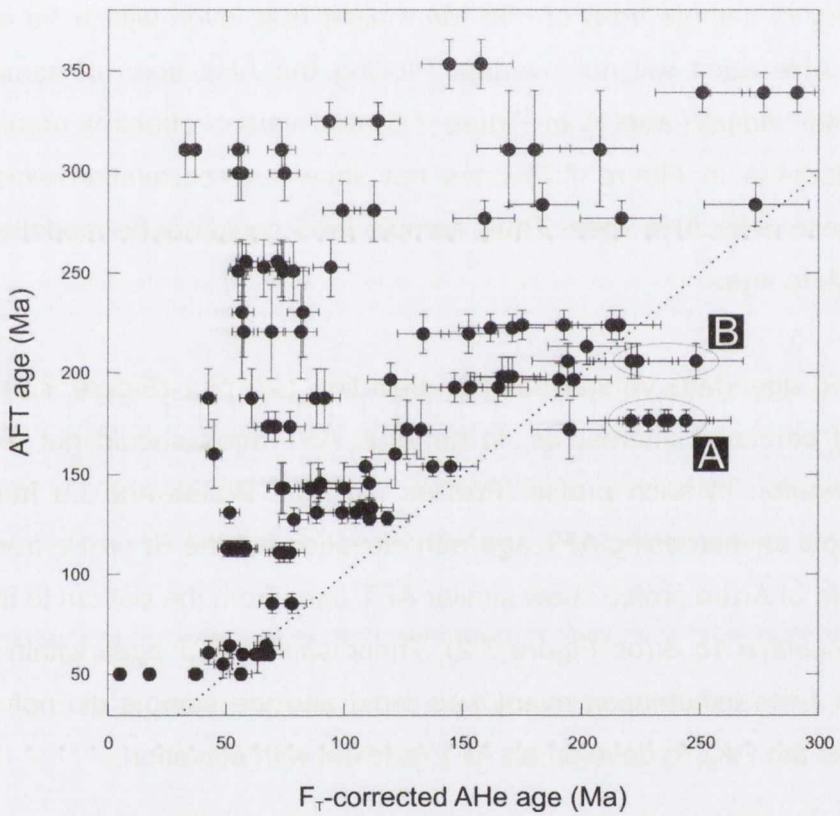


Figure 7.1: AFT age (Ma) versus F_T-corrected single grain AHe age (Ma) plot of all modelled results. Dashed line is the 1:1 ratio from AFT to Ft-corrected AHe age. Samples below the line have older AHe ages than AFT ages. A: Sample Ire-5 shows consistent older AHe than AFT ages. B: Three out of four AHe grains from sample Br-1 are older than the corresponding AFT age but only one grains is far away (out or error) from the 1:1 ratio.

The AFT results show a large variation in age from 43.3 ± 5.8 Ma (1σ) on the Isle of Arran (IoA-3) to 353.6 ± 12.1 Ma (1σ) in central Scotland (Sct-6) (Figure 7.1, Table 7-1). In most samples the AFT ages are older than the corresponding AHe ages (see Figure 7.1) but in two samples most AHe single

grain ages are older than the corresponding AFT age. Sample Ire-5 (label A in Figure 7.1) has AHe ages which are ~55 Ma older than the corresponding AFT age of 176.3 ±5.6 Ma and AHe ages in sample Br-1 (label B in Figure 7.1) are ~16 Ma older than the AFT age of 205.8 ±8.8 Ma.

In sample Br-1 both AFT and AHe ages are within 1σ error within each other with the exception of AHe grain Br-1-d with and AHe age of 248.62 ±19.89 Ma (F_T-corrected). Since the ages are within error it is still possible to model the sample as similar ages could mean a rapid exhumation event. The age discrepancy in sample Ire-5 of ~55 Ma means that, even with a 1σ error, the AFT and AHe ages will not overlap. Plotting the AHe ages of sample Ire-5 versus grain radius (label A in Figure 7.6) and versus effective uranium (eU) content (label A in Figure 7.7) does not show any correlation which could explain these older AHe ages. Thus, sample Ire-5 could not be modelled due to the older AHe ages.

In the AFT age (Ma) versus sample elevation (m) plot (Figure 7.2) are the profiles of particular interest as, in general, AFT ages should get older with higher elevation in each profile. Profiles Cu from Wales and Lu from south Ireland show an increasing AFT age with elevation but the Br profile from Wales and the Isle of Arran profile show similar AFT ages from the bottom to the top of the profile (within 1σ error; Figure 7.2). These similar AFT ages within a profile can occur if the exhumation event was rapid and the sample did not spend a long time in the PAZ to develop an AFT gradient with elevation.

In general, the single samples from Ireland and Scotland show a similar trend with increasing AFT ages with elevation. However, the correlation is weak as regional effects (e.g. regional faulting) can influence the age/elevation relationship. As shown in Figure 7.2, some samples in Ireland and Scotland, which are currently at sea level, belong to the older samples in the respective regions.

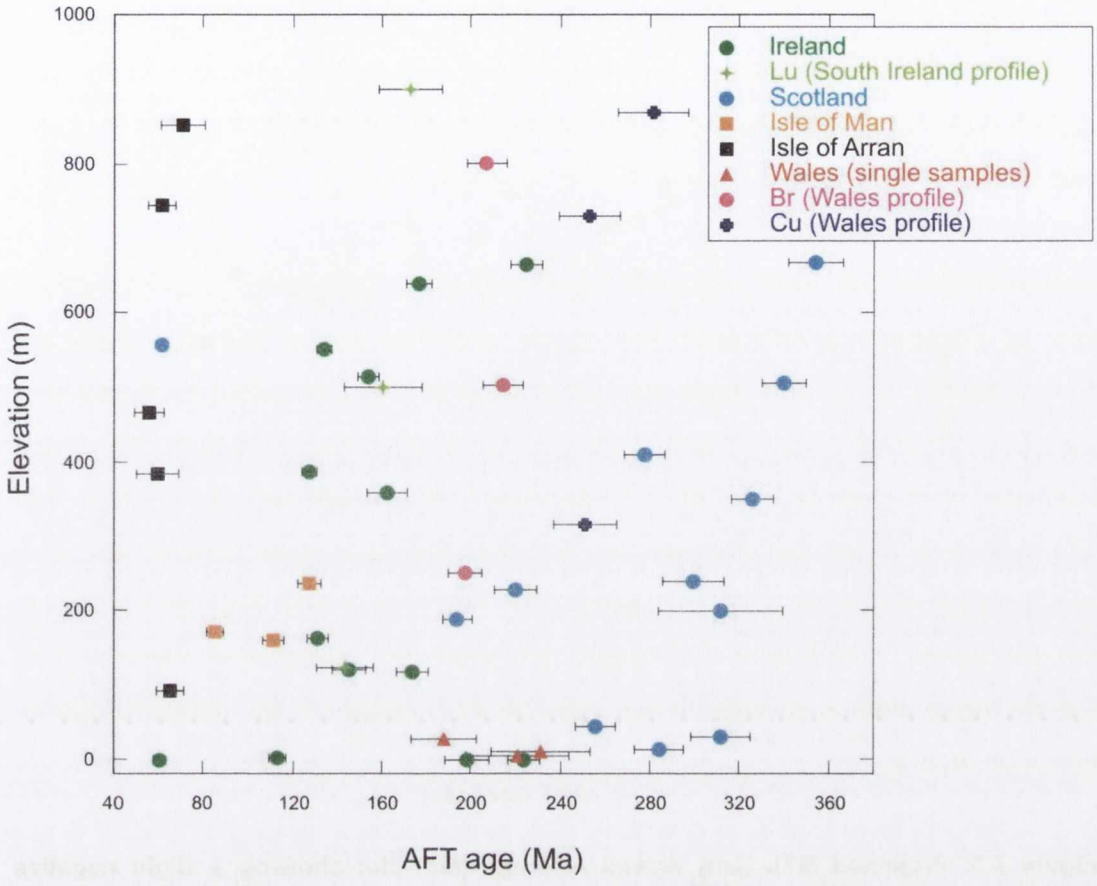


Figure 7.2: Sample elevation (m) versus AFT age (Ma) divided by region for all samples in this study. Sample profiles are separated from their corresponding region.

It was not possible to count enough tracks for the samples from the Isle of Arran and for Pb-1 and Pb-2 so the track length distributions were determined for 39 samples. The mean track lengths (MTLs) show a large range from 12.1 ± 0.21 µm (1 SE) in NW Ireland (Ire-5) to 14.71 ± 0.08 µm (1 SE) in NW Ireland (Ire-7), with a negative correlation between MTL and AFT age (Figure 7.3).

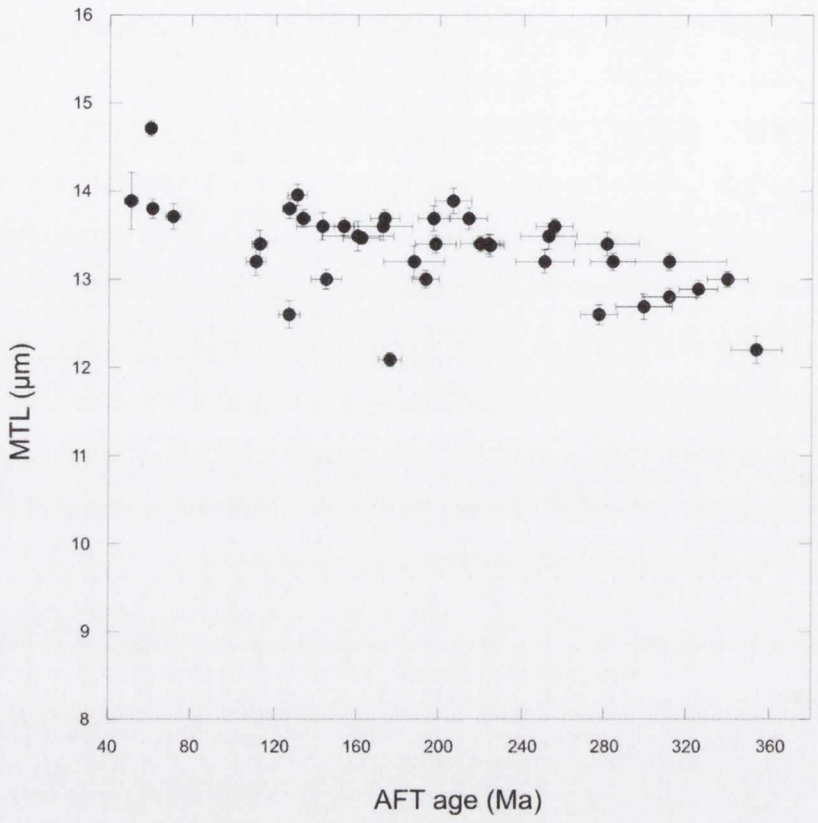


Figure 7.3: Projected MTL (µm) versus AFT age (Ma) plot showing a slight negative correlation between MTL and AFT age.

The chlorine content measured by LA-ICP-MS during the AFT dating protocol ranges from 0 to 1.4 wt % (see appendix). However, only samples Pb-2 (Pembrokeshire) and Sct-2 (Scotland) exceed 0.45 wt %, with Cl contents of 1.26 and 1.41 wt %, respectively. The mean value for the chlorine content is 0.12 wt % and this indicates that the analysed grains are fluorapatites and similar in terms of their annealing kinetics to the Durango apatite standard. The kinetic parameter D_{par} ranges from 1.3 to 2.1 µm and has a mean value of 1.6 µm (etching protocol: 5.5 N HNO_3 for 20.0s at 21°C; Carlson et al. (1999), section 3.2.1) which is consistent with the D_{par} value of ~1.66 µm for Durango apatite using the same etching protocol (1.66 µm is the Trinity laboratory mean D_{par} value for the Durango apatite). Nine out of the 47 samples failed the χ^2-test (χ^2 under 5%; Galbraith, 1981) and these nine samples (see Table 7-1) also proved difficult or even impossible to model (i.e. Ire-5 and Sct-4). They will be further discussed in section 7.1.

Overall the AFT ages, MTLs and kinetic parameters are similar to previously published AFT data for Ireland and Britain (see Figure 7.4 and additional information in Green et al., 2000; Holford et al., 2005b; Hillis et al., 2008a; Holford et al., 2010; Cogné et al., 2014).

As shown in Figure 7.4 the newly acquired data from Ireland overlaps with previously published data and only the new data from Scotland and the Cu profile from Wales (Table 7-1 and Figure 7.4) do not fall into the cluster of previously published data. That the previously published AFT ages do not exceed ~240 Ma is probably related to the fact that the samples are, mostly, from Ireland and thus to not show ages older than 240 Ma.

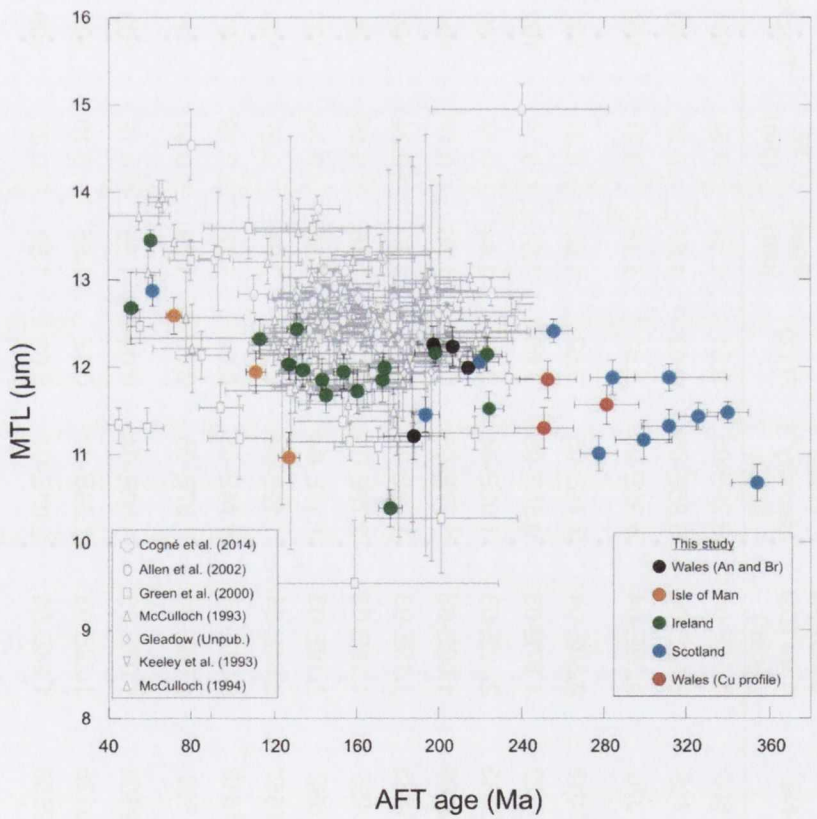


Figure 7.4: Unprojected MTL (µm) versus AFT age (Ma) plot with previously published data from Ireland (empty symbols) and data from this study divided into the different geographical regions.

Table 7-1: Apatite fission track results

Sample Name	Grains	Ns[1]	Counted Area (Ωi) (cm^2)	Track density[2] ΣpiΩi	P(χ2)	Dpar (μm)	SE (μm)	Tracks	MTL[3] (μm)	SE (μm)	SD (μm)	AFT age (Ma)	Error ±1σ (Ma)
loM 1	20	800	5.65E-04	6.25E-05	0.01	1.54	0.24	101	12.60	0.15	1.52	127.4	5.5
loM 2	21	765	6.58E-04	6.85E-05	0.02	1.67	0.22	103	13.20	0.15	1.54	111	5.0
loM 3	25	376	9.39E-04	4.33E-05	0.61	1.48	0.21	100	13.70	0.14	1.38	85.48	4.7
Ire 1	20	1018	8.30E-04	7.74E-05	0.02	1.65	0.21	102	13.96	0.12	1.18	130.7	4.9
Ire 2	23	1923	1.87E-03	9.56E-05	1.00	1.51	0.19	102	13.40	0.10	0.96	198.83	9.5
Ire 3	18	2333	2.12E-03	1.03E-04	0.25	1.44	0.17	100	13.39	0.12	1.15	224.1	7.0
Ire 4	20	2209	1.06E-03	9.77E-05	0.06	1.70	0.17	101	13.40	0.11	1.11	222.9	6.8
Ire 5	18	1883	1.15E-03	1.06E-04	0.04	1.29	0.24	100	12.10	0.21	2.07	176.30	5.6
Ire 6	21	455	1.15E-03	2.78E-05	0.15	1.46	0.46	28	13.47	0.24	1.26	162.3	8.6
Ire 7	22	692	1.19E-03	1.17E-04	0.19	1.55	0.24	100	14.71	0.08	0.77	59.97	3.1
Ire 8	20	1657	8.61E-04	1.49E-04	0.07	2.01	0.27	100	13.40	0.15	1.47	112.8	3.9
Ire 9	22	1018	8.01E-04	5.74E-05	0.83	1.78	0.19	101	13.70	0.11	1.09	173.35	7.2
Ire 10	29	358	4.68E-04	7.07E-05	0.76	1.89	0.44	17	13.90	0.32	1.34	49.98	2.9
LG 17	21	2601	1.07E-03	1.68E-04	0.09	1.55	0.15	103	13.60	0.10	1.06	153.4	4.8
LG 18	22	3125	1.22E-03	2.34E-04	0.12	1.55	0.18	102	13.70	0.11	1.16	133.2	3.6
LG 19	21	2556	1.24E-03	2.01E-04	0.08	1.52	0.21	100	13.80	0.12	1.22	127.4	3.5
LG 32	20	459	1.16E-03	3.12E-05	0.10	1.53	0.22	100	13.00	0.12	1.19	145.1	7.5
Sct 1	20	1303	5.67E-04	2.19E-04	0.16	1.63	0.24	103	13.8	0.12	1.19	60.4	2.0
Sct 2	21	622	3.96E-04	2.02E-05	0.27	2.03	0.38	104	12.7	0.14	1.43	299.1	13.8

continues next page

Sample Name	Grains	Ns[1]	Counted Area (Ωi) (cm^2)	Track density[2] ΣpiΩi	P(χ2)	Dpar (μm)	SE (μm)	Tracks	MTL[3] (μm)	SE (μm)	SD (μm)	AFT age (Ma)	Error ±1σ (Ma)
Sct 3	19	1610	6.31E-04	8.23E-05	0.02	1.79	0.28	101	13	0.10	1.04	193	7.0
Sct 4	19	2978	1.11E-03	8.94E-05	0.01	1.55	0.16	110	12.9	0.09	0.93	325	9.3
Sct 5	23	641	1.18E-03	2.88E-05	0.11	1.47	0.20	100	13.4	0.08	0.8	219.51	9.8
Sct 6	14	1821	5.16E-04	5.02E-05	0.02	1.37	0.18	100	12.2	0.15	1.45	353.6	12.1
Sct 7	19	2263	7.62E-04	8.02E-05	0.01	1.62	0.15	101	12.6	0.11	1.11	277.3	8.9
Sct 8	15	569	5.72E-04	1.80E-05	0.02	1.76	0.20	100	13.2	0.10	1.04	311.5	28.2
Sct 9	20	3646	1.04E-03	1.05E-04	0.01	1.53	0.16	103	13	0.08	0.79	339.6	9.8
Sct 10	20	1479	1.98E-03	5.68E-05	0.05	1.59	0.21	101	13.6	0.09	0.9	255.8	8.8
Sct 11	18	768	9.51E-04	2.41E-05	0.21	1.55	0.21	102	12.8	0.10	1.05	311	13.2
Sct 12	19	1270	6.83E-04	4.39E-05	0.02	1.52	0.25	100	13.2	0.10	1.04	284.1	10.7
An 1	26	171	3.78E-04	8.94E-06	1.00	1.72	0.18	98	13.2	0.18	1.82	187.7	14.9
Br 1	31	736	4.87E-04	3.56E-05	0.69	1.85	0.27	100	13.9	0.14	1.39	205.8	8.8
Br 2	29	779	7.49E-04	3.62E-05	0.87	1.73	0.23	102	13.7	0.13	1.27	213.5	9.1
Br 3	38	838	7.79E-04	4.28E-05	0.13	1.73	0.23	100	13.7	0.14	1.43	196.9	7.9
Cu 3	29	379	4.91E-04	1.33E-05	0.53	1.72	0.19	100	13.4	0.14	1.35	280.5	15.4
Cu 2	28	387	6.15E-04	1.49E-05	0.66	1.79	0.21	101	13.5	0.14	1.4	252.3	13.9
Cu 4	28	369	5.81E-04	1.43E-05	0.61	1.70	0.19	100	13.2	0.14	1.4	250.7	14.2
Pb 1	26	102	4.43E-04	4.39E-06	0.37	1.65	0.20	-	-	-	-	220.8	23.2
Pb 2	23	115	3.27E-04	4.85E-06	0.76	2.10	0.23	-	-	-	-	230.6	22.3

continues next page

Sample Name	Grains	Ns[1]	Counted Area (Ωi) (cm^2)	Track density[2] ΣpiΩi	P(χ2)	Dpar (μm)	SE (μm)	Tracks	MTL[3] (μm)	SE (μm)	SD (μm)	AFT age (Ma)	Error ±1σ (Ma)
loA 1	14	49	3.18E-04	7.12E-06	0.99	1.35	0.26	-	-		-	70.6	9.9
loA 2	21	118	8.69E-04	1.79E-05	0.06	1.37	0.21	-	-		-	61.1	6.2
loA 3	8	59	3.34E-04	1.37E-05	0.44	1.36	0.15	-	-		-	43.3	5.8
loA 4	15	106	5.00E-04	1.67E-05	0.96	1.44	0.19	-	-		-	55.3	6.4
loA 5	9	54	2.31E-04	8.04E-06	0.83	1.38	0.25	1			-	59.1	9.3
loA 6	16	112	5.93E-04	1.70E-05	0.99	1.41	0.23	-	-		-	64.9	6.4
Lu 1	20	608	3.29E-04	3.47E-05	0.72	1.62	0.15	100	13.6	0.16	1.59	172.3	7.3
Lu 3	20	662	3.00E-04	4.02E-05	0.26	1.60	0.15	100	13.5	0.16	1.64	159.9	8.7
Lu 6	20	533	3.51E-04	3.65E-05	0.99	1.62	0.19	100	13.6	0.15	1.47	143.1	6.4

Notes:
1: Number of Counted spontaneous tracks
2: Sum of the weighted $^{238}U/^{43}Ca$ ratio times the counted area
3: Mean track length projected to c-axis
SE: Standard error
SD: Standard deviation

Overall, 272 single grain analyses were undertaken for AHe dating from 46 samples. 71 of these grains were picked and analysed as part of a "broken grain" study (Beucher et al., 2013; Brown et al., 2013) from the Lugnaquilla pseudo-vertical profile (three samples). The remaining 201 grains are from 43 samples, which corresponds to approximately 5 AHe single-grain ages per sample. This includes any failed measurements due to a lack of ^{4}He, or unrealistically (40-50% older than the mean AHe age for the sample) old ages attributed to either inclusions not detected during picking or ^{4}He implantation.

110 single grain AHe ages were used for modelling, spread across the 43 samples (excluding the Lu profile grains for the broken grain analysis). The AHe age range from 3.9 ± 0.3 Ma (1σ, uncorrected) in eastern Ireland (Ire 10) to 226.3 ± 18.1 Ma on Shetland (Sct-12) and from 5.2 ± 0.4 Ma (1σ, F_T-corrected) (Ire-10) to 290.9 ±23.3 Ma in central Scotland (Sct-9) (Figure 7.1). The selection of the subset of 110 grains from the suite of all analysed grains was based on the average of the AHe ages from a single sample (Table 7-2). If one AHe age was |40-50% older or younger than the mean sample AHe age then the grain was removed. The remaining grains were chosen during the modelling step as explained in section 6.5.

Plotting the F_T-corrected AHe ages against elevation (Figure 7.5) shows a similar relationship as the AFT ages versus elevation in Figure 7.2. The pseudo-vertical profiles Cu and Br from Wales and the Lu profile from south Ireland show increasing AHe ages with elevation. The Isle of Arran profile on the other hand shows no correlation between AHe age and elevation which is probably related to a fast passing through the PRZ during exhumation. The single samples from Ireland and Scotland also show a weak positive correlation between AHe ages and elevation, similar to the AFT ages in Figure 7.2.

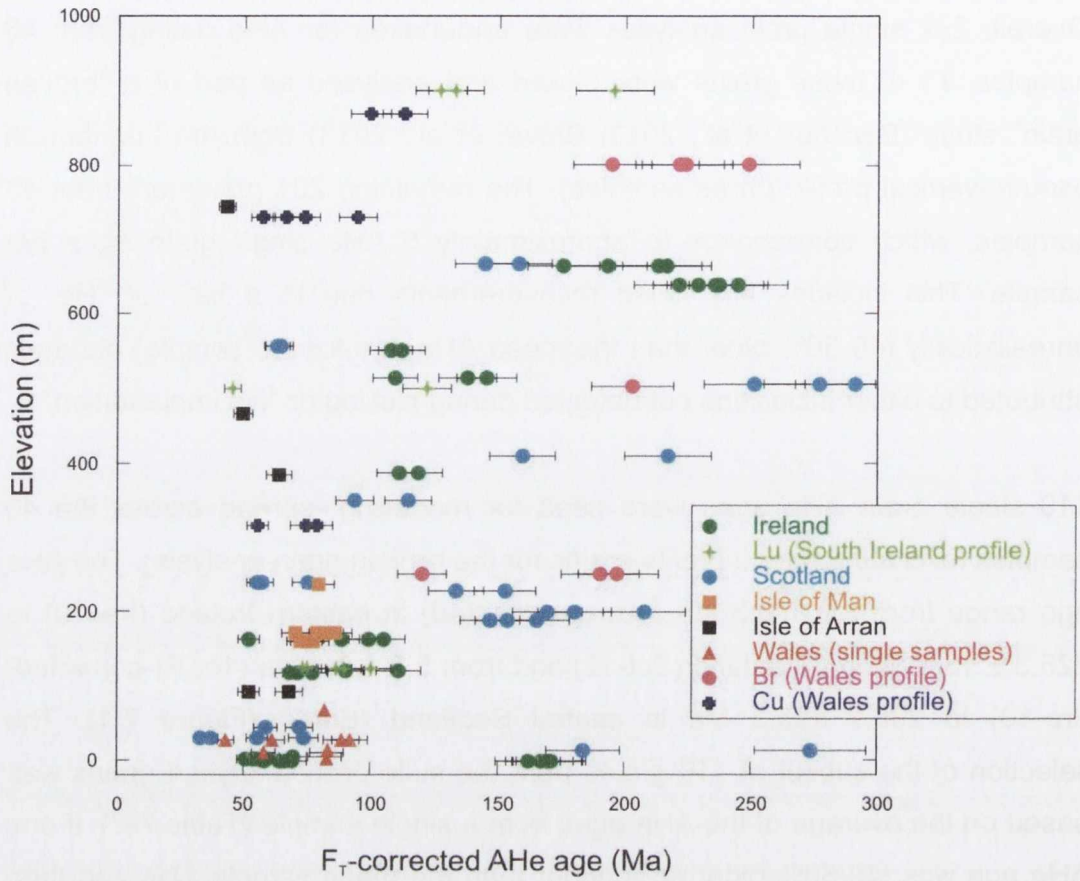


Figure 7.5: Sample elevation (m) versus single grain F_T-corrected AHe age (Ma) divided by region for all samples in this study. Sample profiles are separated from their corresponding region.

Plotting F_T-corrected AHe ages (Ma) against the single grain radius (µm) shows neither a positive nor negative correlation Figure 7.6. The region which illustrates this non-correlation between AHe age and grain radius are the samples from the Isle of Man (orange symbol; Figure 7.6). The AHe ages from the Isle of Man show a narrow range between 78.9 ±6.3 Ma and 69.6 ±5.6 Ma (both 1σ) while the radius ranges from 41 to 92 µm (Figure 7.6).

Figure 7.7 shows F_T-corrected single grain AHe ages (Ma) versus effective uranium content (eU in ppm). There is no obvious relationship between AHe age and eU if the samples are divided into regions and pseudo-vertical profiles, similar to AHe ages versus grain radius (Figure 7.6).

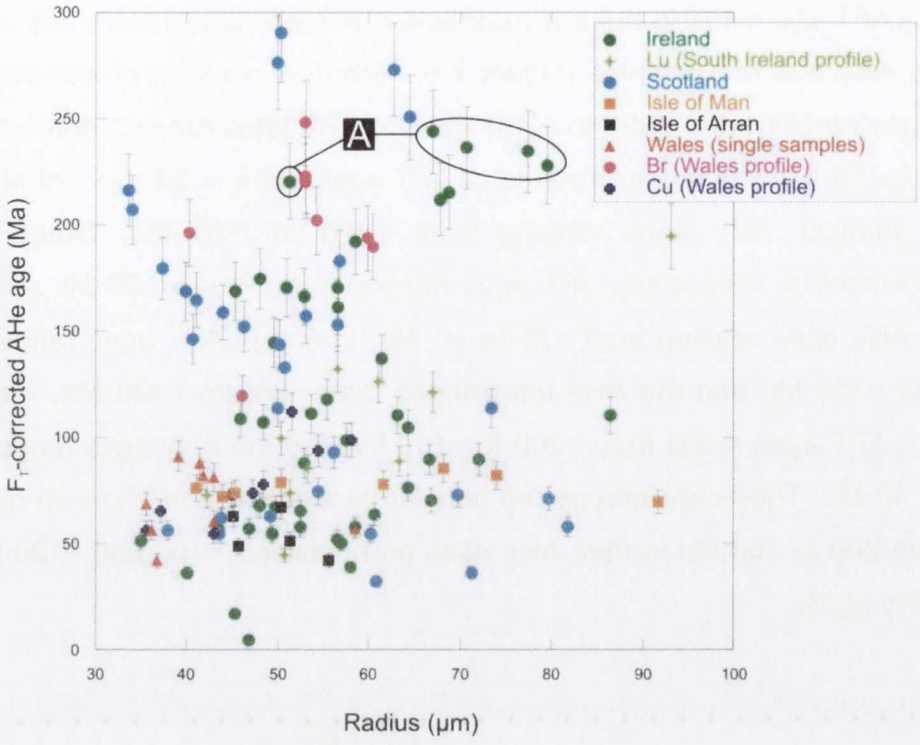


Figure 7.6: F_T-corrected AHe age (Ma) versus radius (µm) of each modelled single grain per sample used for modelling and divided into regions.

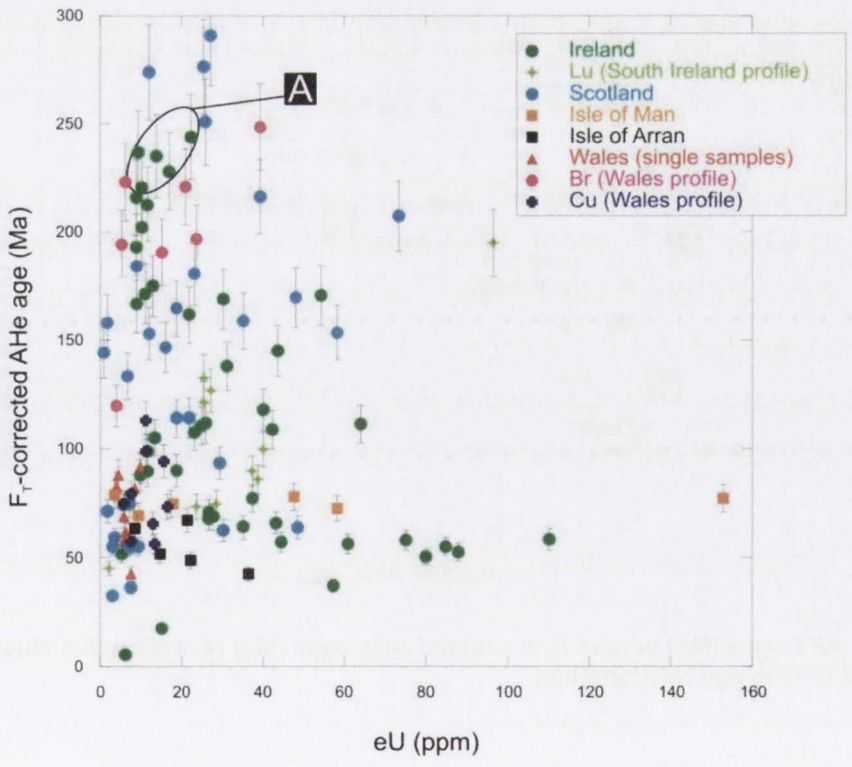


Figure 7.7: FT-corrected AHe ages (Ma) versus eU (ppm) of each modelled single grain per sample used for modelling and divided into regions.

Plotting AFT against AHe ages (F_T-corrected) reveals five clusters with similar AFT to AHe age relationships (Figure 7.8). Group A consists of samples with AFT ages ranging from ~360 to ~250 Ma and AHe ages ranging from ~300 to ~140 Ma. Group B has similar range of AFT ages (from ~330 to ~220 Ma) but much younger AHe ages ranging from ~120 to ~30 Ma. Group C is characterized by very young AFT ages ranging from ~80 to ~50 Ma and also young AHe ages ranging from ~75 to ~4 Ma. Group D AFT ages range from ~230 to ~150 Ma and the AHe age ranges from ~250 to ~120 Ma, whereas group E AFT ages range from ~200 to ~110 Ma and the AHe ages range from 150 to 40 Ma. These two groups are very close together and show an overlap between 200 to 150 Ma in their AFT ages and between ~150 and ~120 Ma in their AHe ages.

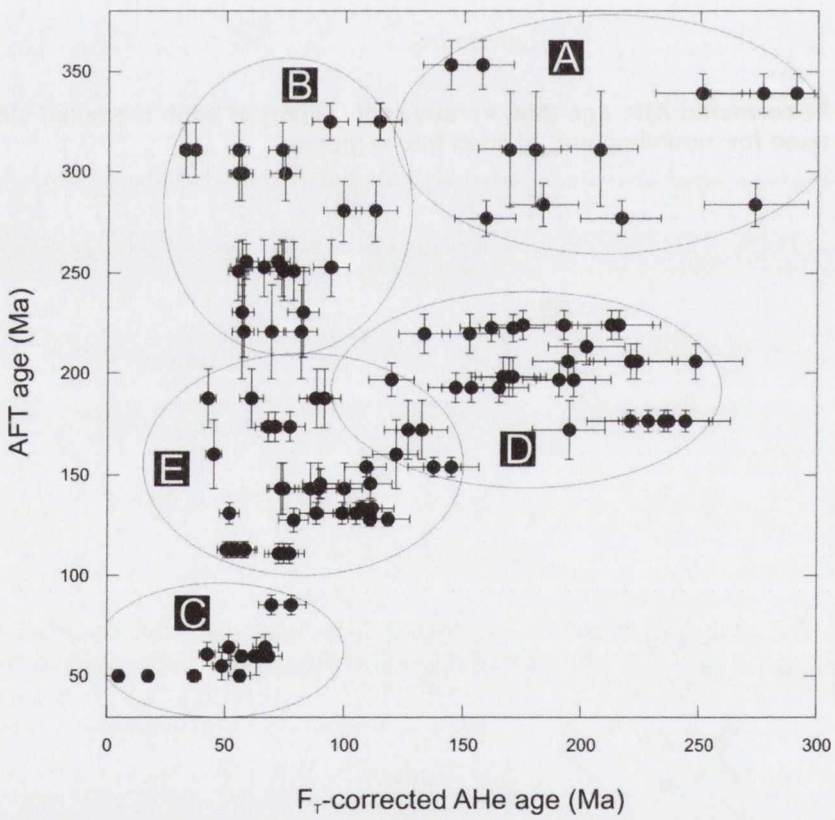


Figure 7.8: AFT ages (Ma) versus F_T-corrected AHe ages (Ma) revealing five clusters with similar AFT to AHe age relationships.

Dividing the AFT and AHe age data into five regions (Scotland, south Ireland, west and central east Ireland, Wales and the Isle of Man/Arran) reveals no

large-scale correlation between the age clusters and the geographical regions (Figure 7.9). While in general the oldest AFT ages are from Scotland followed by Wales, the AFT and AHe ages are not sufficiently characteristic of geographical regions and hence the thermal models need to be evaluated to reveal possible geographical trends. Consequently the thermal models are described in section 7.1 and are interpreted and discussed in chapter 8.

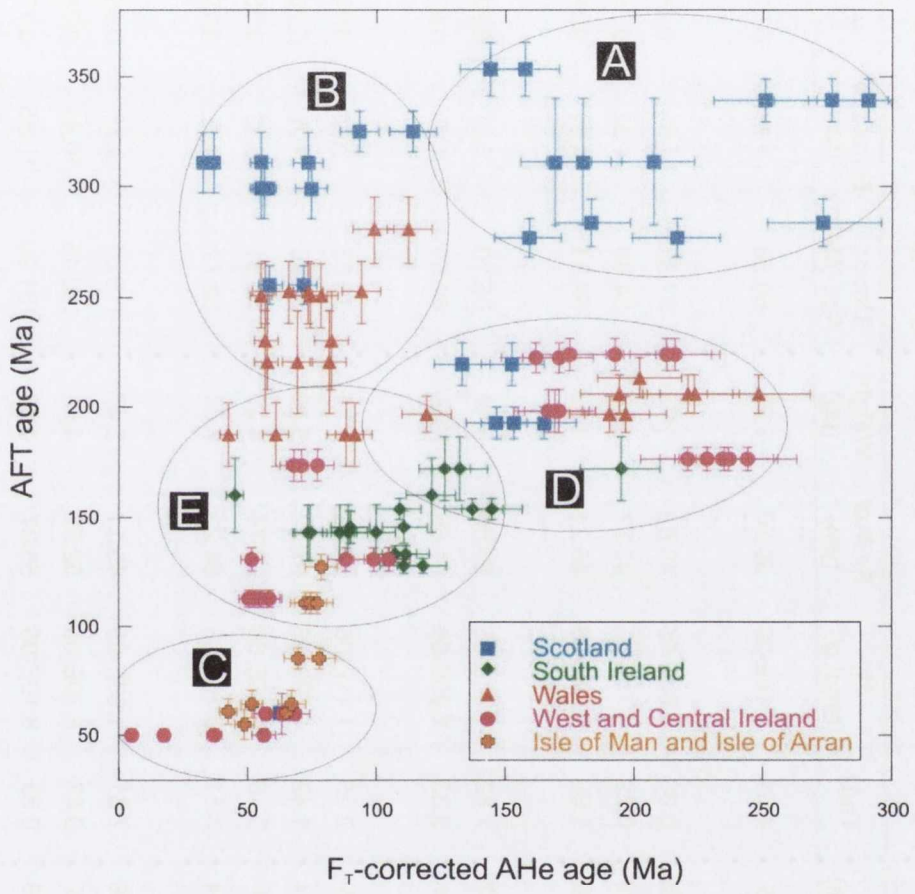


Figure 7.9: AFT ages (Ma) versus F_T-corrected AHe ages (Ma) plot comparing the five clusters revealed by the data and five regional districts (Scotland, south Ireland, west and central east Ireland, Wales and the Isle of Man/Arran).

Table 7-2: AHe age results for the modelled AHe grains. A more detailed table with all analysed grains is provided in the appendix.

Sample Name	U (ppm)	Th (ppm)	Sm (ppm)	eU (ppm)	Th/U	He (nmol g^{-1})	Radius (µm)	Weight (µg)	Uncor.[1] Age (Ma)	Error ±1σ (Ma)	F_T	Cor. Age[2] (Ma)	Error ±1σ (Ma)
loM 1													
-a	1.65	7.93	26.77	3.65	4.81	1.17E-06	50.30	3.27	60.56	4.84	0.77	78.85	6.31
loM 2													
-c	151.00	8.85	1.23	153.09	0.06	4.80E-05	40.89	1.75	57.93	4.63	0.75	77.04	6.16
-d	55.30	12.04	29.91	58.28	0.22	1.71E-05	43.77	2.20	54.08	4.33	0.75	72.60	5.81
-e	11.80	23.34	6.26	17.32	1.98	5.29E-06	45.24	2.37	56.33	4.51	0.76	74.51	5.96
loM 3													
-b	16.70	130.52	59.19	47.67	7.82	1.68E-05	61.59	6.16	65.10	5.21	0.83	78.15	6.25
-d	5.00	16.64	45.56	9.14	3.33	2.95E-06	91.66	19.92	60.65	4.85	0.87	69.63	5.57
lre 1													
-a	3.46	8.12	-3.02	5.35	2.35	1.11E-06	34.83	1.11	38.06	3.04	0.74	51.57	4.13
-b	8.80	12.51	0.00	11.74	1.42	4.79E-06	57.52	5.26	75.26	6.02	0.76	99.02	7.92
-e	5.50	17.40	3.60	9.61	3.16	3.46E-06	52.76	4.20	66.51	5.32	0.75	88.21	7.06
-f	7.40	26.00	6.40	13.54	3.51	6.10E-06	64.22	7.01	82.72	6.62	0.79	105.11	8.41
lre 2													
-c	10.90	82.94	14.41	30.46	7.61	1.93E-05	45.11	2.47	116.37	9.31	0.69	168.90	13.51
-d	7.20	6.29	14.46	8.75	0.87	6.30E-06	52.82	4.01	130.15	10.41	0.78	167.08	13.37
-e	9.90	5.20	21.06	11.23	0.53	8.19E-06	56.37	4.66	131.90	10.55	0.77	171.08	13.69
lre 3													
-a	8.15	3.63	1.77	9.01	0.45	7.60E-06	58.35	5.38	154.77	12.38	0.80	192.74	15.42

continues next page

Sample Name	U (ppm)	Th (ppm)	Sm (ppm)	eU (ppm)	Th/U	He (nmol g^{-1})	Radius (µm)	Weight (µg)	Uncor. Age (Ma)	Error ±1σ (Ma)	F_T	Cor. Age (Ma)	Error ±1σ (Ma)
-b	10.15	5.16	6.35	11.40	0.51	1.02E-05	67.71	8.47	163.60	13.09	0.77	212.74	17.02
-c	7.95	3.63	4.16	8.82	0.46	8.42E-06	68.65	8.62	174.54	13.96	0.81	216.01	17.28
-d	10.10	11.09	0.00	12.71	1.10	8.84E-06	47.86	2.93	127.08	10.17	0.73	175.04	14.00
Ire 4													
-c	10.90	47.13	5.59	22.00	4.32	1.47E-05	56.44	5.08	122.06	9.76	0.76	161.66	12.93
-d	30.10	102.72	13.09	54.30	3.41	4.01E-05	50.82	3.37	135.07	10.81	0.79	170.54	13.64
Ire 5													
-a	14.95	6.60	39.70	16.70	0.44	1.73E-05	79.44	13.38	190.81	15.27	0.84	227.97	18.24
-b	12.50	5.60	33.80	13.99	0.45	1.49E-05	77.26	12.01	195.80	15.66	0.83	235.05	18.80
-c	8.85	5.70	17.30	10.28	0.64	9.57E-06	51.21	3.63	171.07	13.69	0.78	220.46	17.64
-d	19.40	10.30	47.60	22.06	0.53	2.29E-05	67.02	8.13	186.28	14.90	0.76	243.82	19.51
-e	8.40	3.90	19.40	9.41	0.46	9.61E-06	70.65	9.39	187.82	15.03	0.79	236.84	18.95
Ire 7													
-a	22.40	92.75	16.85	44.28	4.14	9.90E-06	46.75	3.12	41.29	3.30	0.72	57.27	4.58
-b	13.80	57.93	0.24	27.42	4.20	7.25E-06	47.81	2.99	48.69	3.89	0.71	68.38	5.47
-c	18.60	70.35	9.96	35.18	3.78	9.29E-06	60.53	7.04	48.69	3.89	0.76	63.81	5.10
-e	22.20	88.18	8.81	42.97	3.97	1.13E-05	52.45	3.93	48.58	3.89	0.74	65.92	5.27
Ire 8													
-a	40.00	149.30	37.30	75.27	3.73	1.73E-05	58.44	6.40	42.44	3.39	0.73	57.97	4.64
-b	38.40	176.68	-	79.92	4.60	1.64E-05	56.87	5.50	37.86	3.03	0.75	50.48	4.04
-c	49.60	162.80	40.32	88.06	3.28	1.89E-05	56.43	5.14	39.55	3.16	0.75	52.52	4.20
-d	57.10	226.32	-	110.28	3.96	2.61E-05	52.40	3.69	43.58	3.49	0.75	58.42	4.67

continues next page

Sample Name	U (ppm)	Th (ppm)	Sm (ppm)	eU (ppm)	Th/U	He (nmol g^{-1})	Radius (µm)	Weight (µg)	Uncor. Age (Ma)	Error ±1σ (Ma)	F_T	Cor. Age (Ma)	Error ±1σ (Ma)
-e	48.80	153.35	31.50	85.00	3.14	1.84E-05	49.29	3.24	39.98	3.20	0.73	55.07	4.41
Ire 9													
-a	12.80	58.30	21.60	26.61	4.55	8.14E-06	66.79	7.77	56.40	4.51	0.80	70.95	5.68
-d	19.30	77.10	-	37.42	3.99	1.18E-05	64.15	7.80	57.98	4.64	0.75	77.11	6.17
-e	12.70	59.60	20.20	26.81	4.69	7.11E-06	49.67	3.45	48.88	3.91	0.72	67.80	5.42
Ire 10													
-a	30.74	128.14	23.95	60.97	4.17	1.22E-05	43.25	2.84	36.54	2.92	0.65	56.48	4.52
-b	3.83	11.09	-	6.43	2.90	1.36E-07	46.71	2.68	3.89	0.31	0.75	5.21	0.42
-c	4.28	46.70	4.24	15.28	10.91	1.04E-06	45.22	2.73	12.46	1.00	0.71	17.68	1.41
-d	24.92	138.04	34.70	57.53	5.54	7.51E-06	39.97	1.95	23.92	1.91	0.65	36.74	2.94
LG 17													
-a	42.20	6.70	-	43.77	0.16	2.62E-05	49.42	3.54	110.09	8.81	0.76	145.04	11.60
-b	30.00	5.50	-	31.29	0.18	1.75E-05	61.24	6.20	102.54	8.20	0.74	137.83	11.03
-e	34.00	34.80	19.30	42.27	1.02	1.76E-05	45.68	2.59	77.04	6.16	0.71	108.97	8.72
LG 18													
-a	23.95	7.30	22.40	25.78	0.30	1.19E-05	53.44	3.96	85.41	6.83	0.77	111.65	8.93
-b	22.60	2.29	27.67	23.28	0.10	9.03E-06	48.27	2.95	71.75	5.74	0.67	107.57	8.61
LG 19													
-a	24.60	1.10	20.60	24.96	0.04	1.26E-05	63.06	6.44	93.08	7.45	0.84	110.54	8.84
-d	39.50	0.80	39.20	39.88	0.02	1.98E-05	55.32	4.36	91.39	7.31	0.77	118.08	9.45
LG 32													
-a	4.50	29.96	14.86	11.62	6.66	4.73E-06	66.61	7.60	75.27	6.02	0.84	89.93	7.19

continues next page

Sample Name	U (ppm)	Th (ppm)	Sm (ppm)	eU (ppm)	Th/U	He (nmol g^{-1})	Radius (μm)	Weight (μg)	Uncor. Age (Ma)	Error ±1σ (Ma)	F_T	Cor. Age (Ma)	Error ±1σ (Ma)
-b	6.80	50.21	22.60	18.71	7.38	7.61E-06	72.09	9.87	75.08	6.01	0.83	90.13	7.21
-c	20.80	183.21	22.65	63.97	8.81	3.23E-05	86.36	16.54	93.18	7.45	0.84	111.19	8.90
Sct 1													
-a	38.50	40.72	51.51	48.33	1.06	1.19E-05	49.07	3.64	45.68	3.65	0.72	63.71	5.10
-b	26.40	15.56	23.61	30.18	0.59	7.10E-06	43.58	2.32	43.52	3.48	0.69	62.70	5.02
Sct 2													
-a	3.95	12.37	21.51	6.96	3.13	2.12E-06	54.35	4.45	56.71	4.54	0.76	74.72	5.98
-b	7.10	9.77	8.30	9.44	1.38	2.06E-06	43.47	2.38	40.28	3.22	0.73	55.11	4.41
-c	4.90	11.23	7.12	7.58	2.29	1.71E-06	37.84	1.46	41.60	3.33	0.74	56.37	4.51
Sct 3													
-b	29.50	121.47	0.00	58.05	4.12	3.89E-05	56.51	4.71	122.88	9.83	0.80	153.40	12.27
-c	9.90	36.96	0.00	18.58	3.73	1.23E-05	40.92	1.76	121.02	9.68	0.74	164.65	13.17
-d	8.20	32.72	0.00	15.89	3.99	9.31E-06	40.57	2.04	107.10	8.57	0.73	146.91	11.75
Sct 4													
-a	11.50	42.89	11.82	21.64	3.73	1.09E-05	73.42	10.99	92.94	7.44	0.81	114.60	9.17
-d	20.50	37.36	8.41	29.32	1.82	1.13E-05	56.00	5.03	71.03	5.68	0.76	93.59	7.49
-e	12.70	25.26	7.63	18.68	1.99	8.41E-06	49.82	3.49	82.86	6.63	0.73	113.82	9.11
Sct 5													
-d	5.30	6.12	0.00	6.74	1.16	3.74E-06	50.53	3.70	101.54	8.12	0.76	133.61	10.69
-e	10.50	6.16	18.04	12.04	0.59	6.67E-06	46.07	2.77	102.02	8.16	0.67	152.72	12.22

continues next page

Sample Name	U (ppm)	Th (ppm)	Sm (ppm)	eU (ppm)	Th/U	He (nmol g^{-1})	Radius (µm)	Weight (µg)	Uncor. Age (Ma)	Error ±1σ (Ma)	F_T	Cor. Age (Ma)	Error ±1σ (Ma)
Sct 6													
-a	1.88	0.21	0.00	1.93	0.11	1.30E-06	52.94	3.84	125.06	10.00	0.79	157.90	12.63
-c	1.13	-0.16	0.00	1.09	-0.14	6.45E-07	50.00	3.36	110.41	8.83	0.77	143.95	11.52
Sct 7													
-b	25.75	80.09	0.00	44.57	3.11	3.18E-05	33.48	1.06	130.74	10.46	0.60	216.45	17.32
-c	23.10	67.55	0.00	38.97	2.92	2.42E-05	43.84	2.51	113.67	9.09	0.72	158.98	12.72
Sct 8													
-a	52.00	89.45	37.99	73.21	1.72	4.97E-05	33.97	1.20	124.72	9.98	0.60	207.17	16.57
-b	15.30	33.13	37.56	23.27	2.17	1.53E-05	37.30	1.48	120.88	9.67	0.67	180.42	14.43
-d	33.20	63.13	35.07	48.21	1.90	3.13E-05	39.76	1.69	119.39	9.55	0.70	169.59	13.57
Sct 9													
-a	25.80	4.52	35.37	27.04	0.18	3.03E-05	50.14	3.68	204.76	16.38	0.70	290.86	23.27
-c	24.50	3.20	29.69	25.40	0.13	2.84E-05	49.91	3.35	204.80	16.38	0.74	276.38	22.11
-d	24.90	3.97	27.15	25.97	0.16	2.75E-05	64.44	7.91	193.09	15.45	0.77	251.09	20.09
Sct 10													
-d	1.60	1.70	4.51	2.02	1.06	6.91E-07	79.56	13.16	62.64	5.01	0.88	71.34	5.71
-e	3.10	1.73	4.97	3.53	0.56	9.84E-07	81.66	14.34	50.51	4.04	0.86	58.53	4.68
Sct 11													
-b	2.70	1.60	3.29	3.09	0.59	4.21E-07	60.64	5.81	25.37	2.03	0.78	32.45	2.60
-c	3.00	0.10	0.00	3.02	0.03	6.97E-07	60.09	5.74	42.92	3.43	0.78	55.10	4.41
-d	5.50	0.82	3.76	5.71	0.15	1.92E-06	69.60	8.79	61.98	4.96	0.84	73.62	5.89
-e	5.70	7.96	4.73	7.59	1.40	1.27E-06	71.31	9.45	30.78	2.46	0.84	36.47	2.92

continues next page

Sample Name	U (ppm)	Th (ppm)	Sm (ppm)	eU (ppm)	Th/U	He (nmol g^{-1})	Radius (μm)	Weight (μg)	Uncor. Age (Ma)	Error ±1σ (Ma)	F_T	Cor. Age (Ma)	Error ±1σ (Ma)
Sct 12													
-a	6.92	8.92	11.79	9.07	1.29	7.34E-06	56.65	4.81	146.62	11.73	0.80	183.50	14.68
-b	10.31	7.34	28.58	12.18	0.71	1.54E-05	62.76	6.38	226.26	18.10	0.83	273.59	21.89
An 1													
-a	5.80	16.70	1.00	9.73	2.88	6.58E-11	38.95	1.59	59.72	4.78	0.65	91.46	7.32
-d	1.60	13.15	0.00	4.69	8.22	4.96E-11	41.27	1.88	62.39	4.99	0.71	88.25	7.06
Br 1													
-a	3.00	12.85	21.02	6.12	4.28	2.15E-10	53.04	4.13	153.86	12.31	0.69	222.98	17.84
-c	20.10	3.40	28.01	21.04	0.17	1.28E-09	52.98	3.81	177.96	14.24	0.81	220.79	17.66
-d	38.10	3.70	12.12	39.03	0.10	1.40E-09	52.94	3.97	175.28	14.02	0.71	248.62	19.89
-e	3.70	7.60	0.84	5.49	2.05	4.29E-10	59.70	5.65	155.80	12.46	0.80	194.50	15.56
Br 2													
-e	7.20	12.50	19.00	10.23	1.74	4.29E-10	54.12	4.09	153.65	12.29	0.76	202.44	16.20
Br 3													
-a	1.20	11.10	1.91	3.82	9.25	7.58E-11	45.99	2.50	89.69	7.18	0.75	119.74	9.58
-b	22.30	6.10	0.00	23.73	0.27	5.21E-10	40.09	1.82	138.11	11.05	0.70	196.73	15.74
-e	14.60	2.40	3.50	15.18	0.16	1.24E-09	60.39	5.67	158.03	12.64	0.83	190.40	15.23
Cu 2													
-a	7.30	34.20	53.74	15.61	4.68	3.63E-10	54.25	4.52	70.02	5.60	0.74	94.37	7.55
-c	6.20	42.90	49.48	16.53	6.92	1.29E-10	44.76	2.32	50.88	4.07	0.70	73.00	5.84
-d	6.70	26.30	45.21	13.11	3.93	7.29E-11	37.08	1.45	43.61	3.49	0.66	65.68	5.25

continues next page

Sample Name	U (ppm)	Th (ppm)	Sm (ppm)	eU (ppm)	Th/U	He (nmol g^{-1})	Radius (µm)	Weight (µg)	Uncor. Age (Ma)	Error ±1σ (Ma)	F_T	Cor. Age (Ma)	Error ±1σ (Ma)
-e	6.00	30.60	55.76	13.47	5.10	4.34E-11	35.48	1.27	34.41	2.75	0.61	56.32	4.51
Cu 3													
-a	5.50	22.70	62.24	11.15	4.13	3.31E-10	51.35	3.90	85.05	6.80	0.75	112.95	9.04
-b	5.20	23.90	68.22	11.16	4.60	4.01E-10	58.05	5.03	80.25	6.42	0.81	98.83	7.91
Cu 4													
-c	3.00	17.00	49.67	7.24	5.67	5.39E-11	42.90	2.11	39.67	3.17	0.72	55.10	4.41
-d	2.80	12.50	49.98	5.99	4.46	7.99E-11	47.19	2.70	56.84	4.55	0.76	74.60	5.97
-e	3.60	15.50	48.28	7.48	4.31	1.16E-10	48.31	2.99	59.26	4.74	0.75	78.70	6.30
Pb 1													
-a	2.50	13.40	0.83	5.65	5.36	2.65E-11	35.41	1.20	44.71	3.58	0.65	68.89	5.51
-b	3.40	20.30	15.27	8.25	5.97	6.54E-11	42.87	2.11	55.05	4.40	0.67	81.80	6.54
-e	2.40	25.90	0.00	8.49	10.79	3.42E-11	35.94	1.22	37.53	3.00	0.66	56.86	4.55
Pb 2													
-b	2.10	14.80	41.79	5.79	7.05	9.62E-11	58.40	5.44	43.48	3.48	0.76	57.51	4.60
-d	2.20	7.80	27.60	4.17	3.55	4.42E-11	41.75	2.04	58.20	4.66	0.70	82.78	6.62
IoA 1													
IoA 2													
-a	13.70	92.66	197.38	36.46	6.76	6.25E-06	55.47	4.38	32.16	2.57	0.75	42.71	3.42
IoA 3													
IoA 4													

continues next page

Sample Name	U (ppm)	Th (ppm)	Sm (ppm)	eU (ppm)	Th/U	He (nmol g^{-1})	Radius (μm)	Weight (μg)	Uncor. Age (Ma)	Error ±1σ (Ma)	F_T	Cor. Age (Ma)	Error ±1σ (Ma)
-a	7.10	60.93	132.14	22.08	8.58	3.99E-06	45.53	2.42	34.04	2.72	0.70	48.98	3.92
loA 5													
-c	4.65	14.63	97.72	8.58	3.15	1.98E-06	44.92	2.81	44.40	3.55	0.70	63.25	5.06
loA 6													
-b	9.30	47.81	164.21	21.36	5.14	5.63E-06	50.29	3.60	49.92	3.99	0.74	67.46	5.40
-d	6.80	30.39	144.05	14.66	4.47	2.89E-06	51.17	3.46	37.72	3.02	0.73	51.67	4.13

Notes:
1: F_T-uncorrected AHe age
2: F_T-corrected AHe age

Apatite U-Pb ages were determined for 34 samples (Table 7-3) and range from 41 ± 56 Ma (2σ) on the Isle of Arran (IoA-3) to 1628 ± 63 Ma (Sct-11) in Northern Scotland. The relative large age uncertainty in IoA-3 is related to the low U content and young age of the Isle of Arran samples (Paleogene granite) which thus has a correspondingly low radiogenic Pb concentration in these samples. The small laser spot size (30 microns) employed in LA-ICP-MS fission track analyses also results in relatively large age uncertainties due to the low analyte volume ablated. Excluding the samples from the Paleogene Isle of Arran granite, the youngest apatite U-Pb age is 372 ± 21 Ma from the Isle of Man (IoM-3). The apatite U-Pb ages are often used as high temperature constraints in the thermal history models as discussed in sections 3.4 and 4.4.

Table 7-3: Apatite U-Pb age results.

Sample Name	Apt U-Pb age (Ma)	Error ±2σ (Ma)	MSWD
IoM 1	451	14	1.3
IoM 2	418	13	1.3
IoM 3	372	21	0.77
Ire 1	414	78	1
Ire 2	430	57	0.62
Ire 3			
Ire 4	457	36	0.77
Ire 5	415	55	0.73
Ire 6			
Ire 7	434	24	1.07
Ire 8	422	17	1.03
Ire 9	442	78	0.51
Ire 10	447	18	6.2
LG 17	400	40	0.56
LG 18	396	24	0.47
LG 19	388	23	0.6
LG 32	450	90	1.14

continues next page

Sample Name	Apt U-Pb age (Ma)	Error ±2σ (Ma)	MSWD
Sct 1	395	5	
Sct 2			
Sct 3	426	45	2.1
Sct 4	460	23	0.81
Sct 5	502	150	0.65
Sct 6			
Sct 7			
Sct 8	484	21	0.8
Sct 9	444	28	0.64
Sct 10	1120	160	2.3
Sct 11	1628	63	0.88
Sct 12	530	40	0.69
An 1	529	97	0.84
Br 1	425	17	1.5
Br 2	499	51	10.2
Br 3	498	45	6.9
Cu 3	414	92	1.2
Cu 2	496	86	1.06
Cu 4	432	80	1.3
Pb 1	507	62	1.2
Pb 2	474	89	0.62
IoA 1	51	88	1.05
IoA 2	74	76	0.63
IoA 3	41	56	0.96
IoA 4			
IoA 5			
IoA 6	58	95	1.16
Lu 1	392	6	3.1
Lu 3	392	6	3.1
Lu 6	392	6	3.1

Notes:
MSWD: Mean square weighted deviation

7.1 Thermal history modelling results

The thermal history modelling was undertaken with the modelling software QTQt (version 5.4) as explained in chapter 6. The thermal models were undertaken using 200,000 burn-in and 200,000 post burn-in iterations and present day temperature was set to be 10°C.

As annealing model for fission track dating was the multi-kinetic model of Ketcham et al. (2007a; 2007b) emplyed (explained in section 6.5). The kinetic parameter D_{par} (explained in more detail in section 3.2.8) is allowed to vary within standard error (SE) during the modelling. For modelling the radiation damage for AHe dating the RDAAM model from Flowers et al. (2009), see chapter 3.3.5, was employed.

The large variation in the AFT and AHe ages in the study area is also expressed in the diversity of the thermal history models. Thus, the study area was divided into five sub-sections based on their regional geographical location, and then further divided based on the results from the thermal history modelling.

The apatite U-Pb ages were added to the thermal model as a high temperature constraint but in the following thermal models (Figure 7.10 to Figure 7.20) the temperature range is zoomed to about 150°C (depending on sample) since the temperature range between 425°C and 120°C is poorly resolved with the used methods and the important temperature range for this study starts at about 150°C.

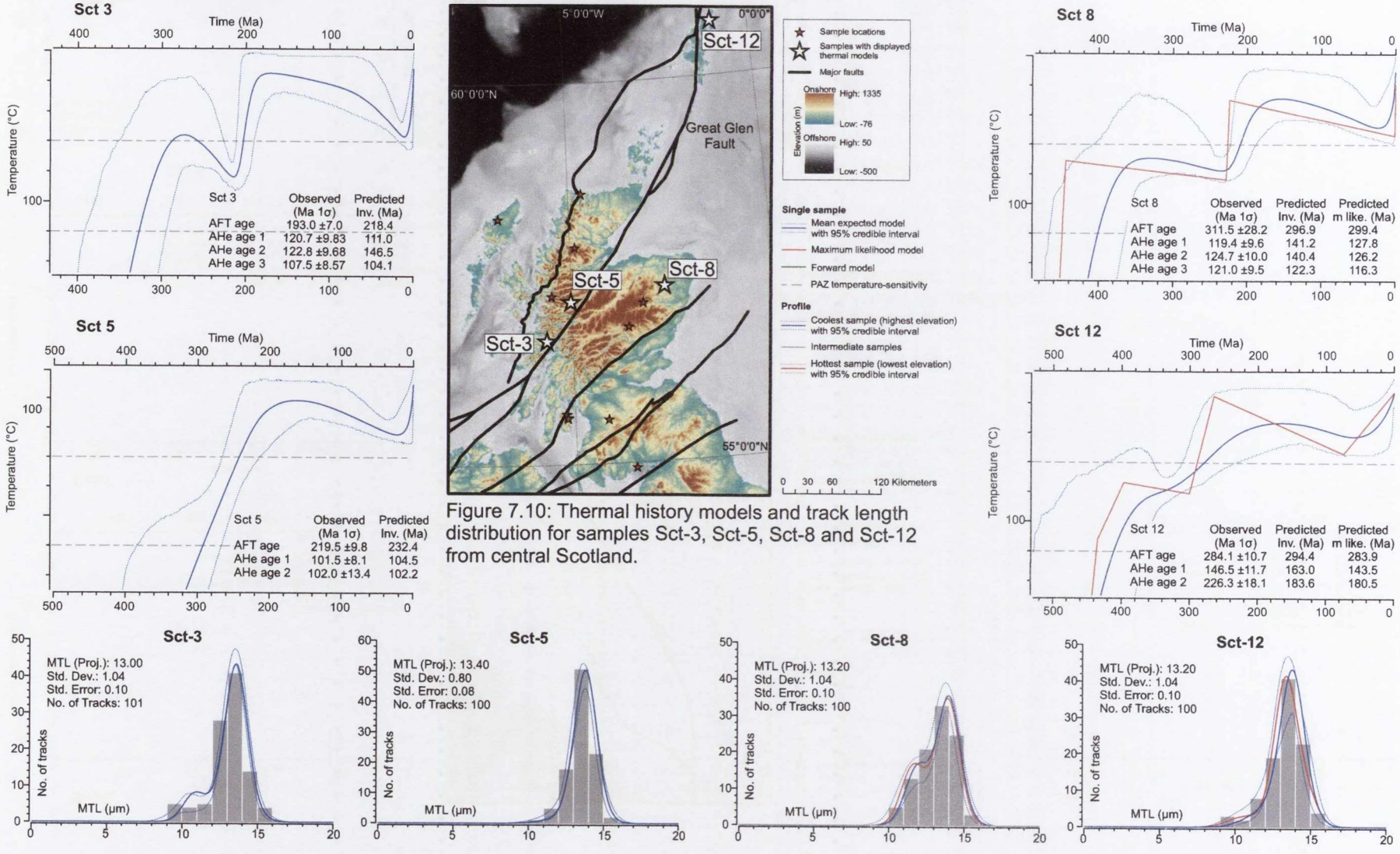


Figure 7.10: Thermal history models and track length distribution for samples Sct-3, Sct-5, Sct-8 and Sct-12 from central Scotland.

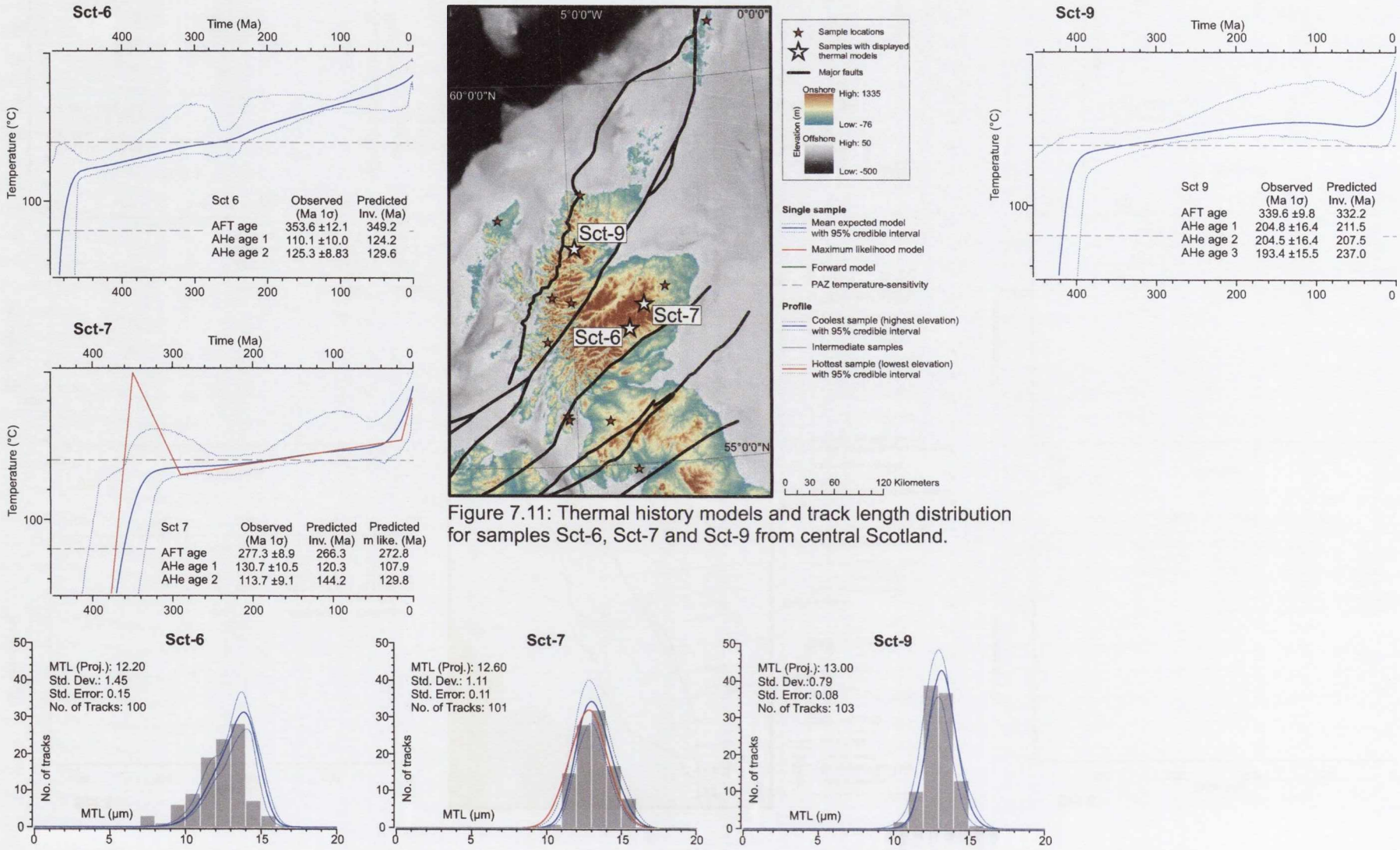


Figure 7.11: Thermal history models and track length distribution for samples Sct-6, Sct-7 and Sct-9 from central Scotland.

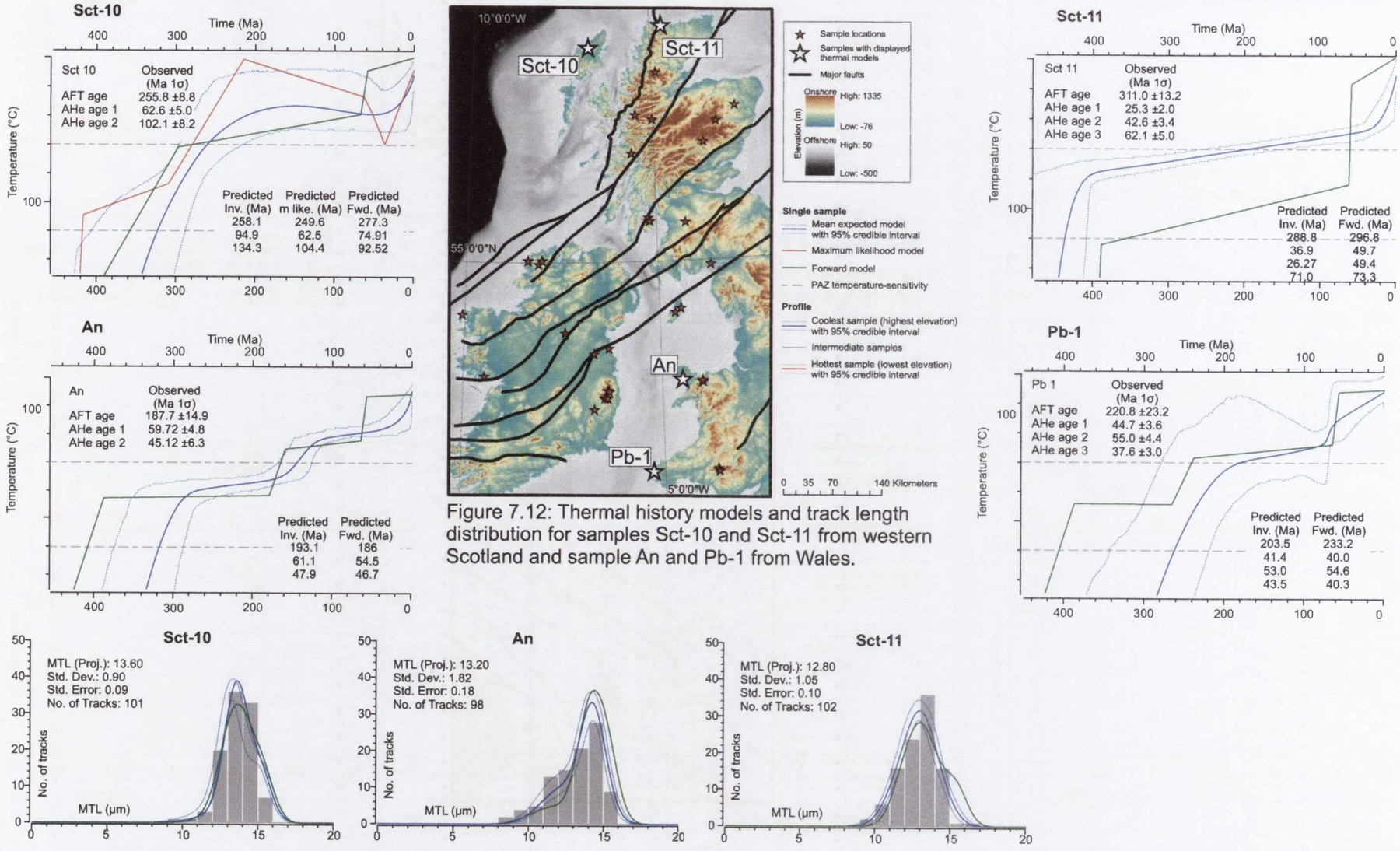
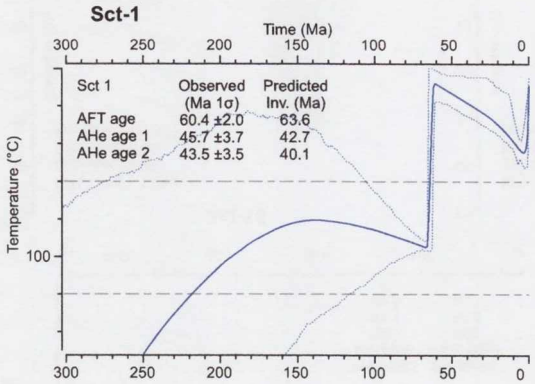
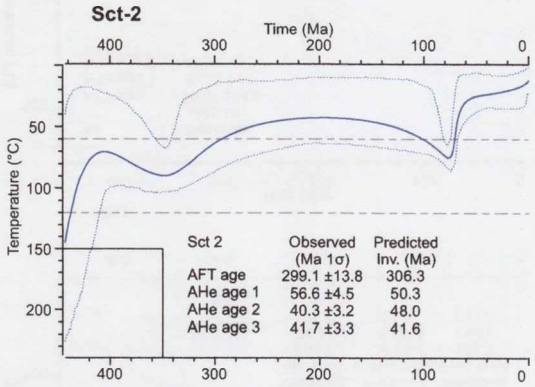


Figure 7.12: Thermal history models and track length distribution for samples Sct-10 and Sct-11 from western Scotland and sample An and Pb-1 from Wales.





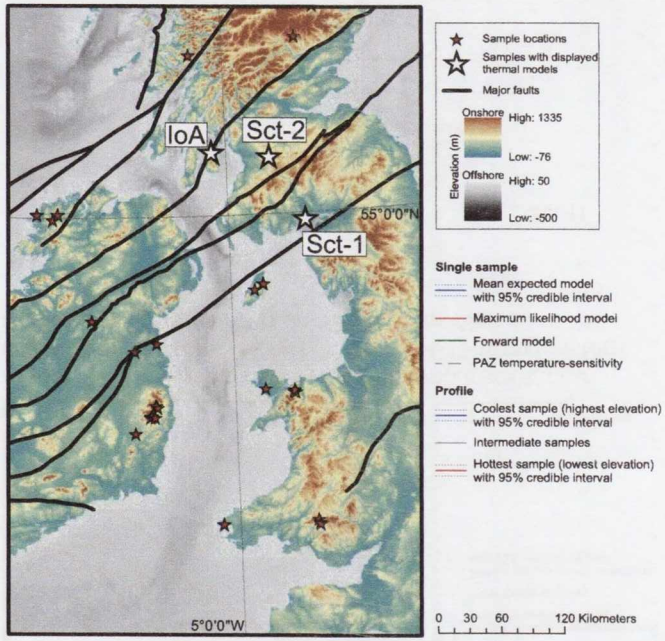
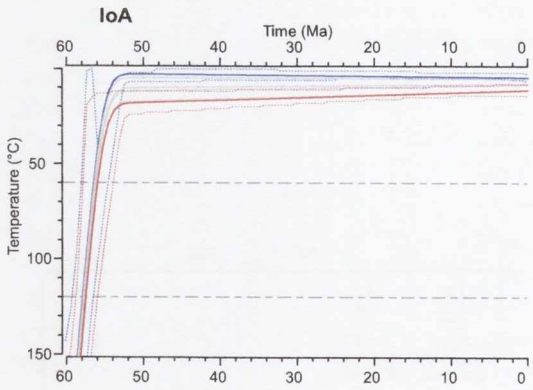
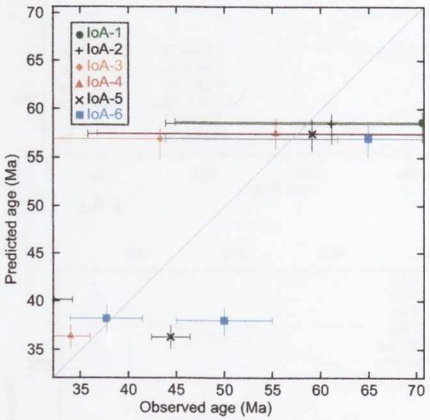
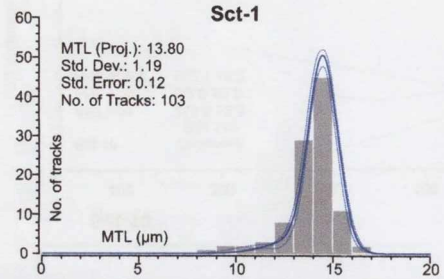
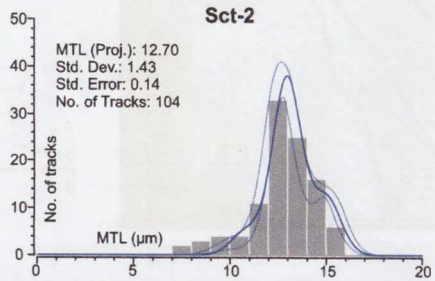


Figure 7.13: Thermal history models and track length distribution for samples Sct-1, Sct-2 and the Isle of Arran in south Scotland.









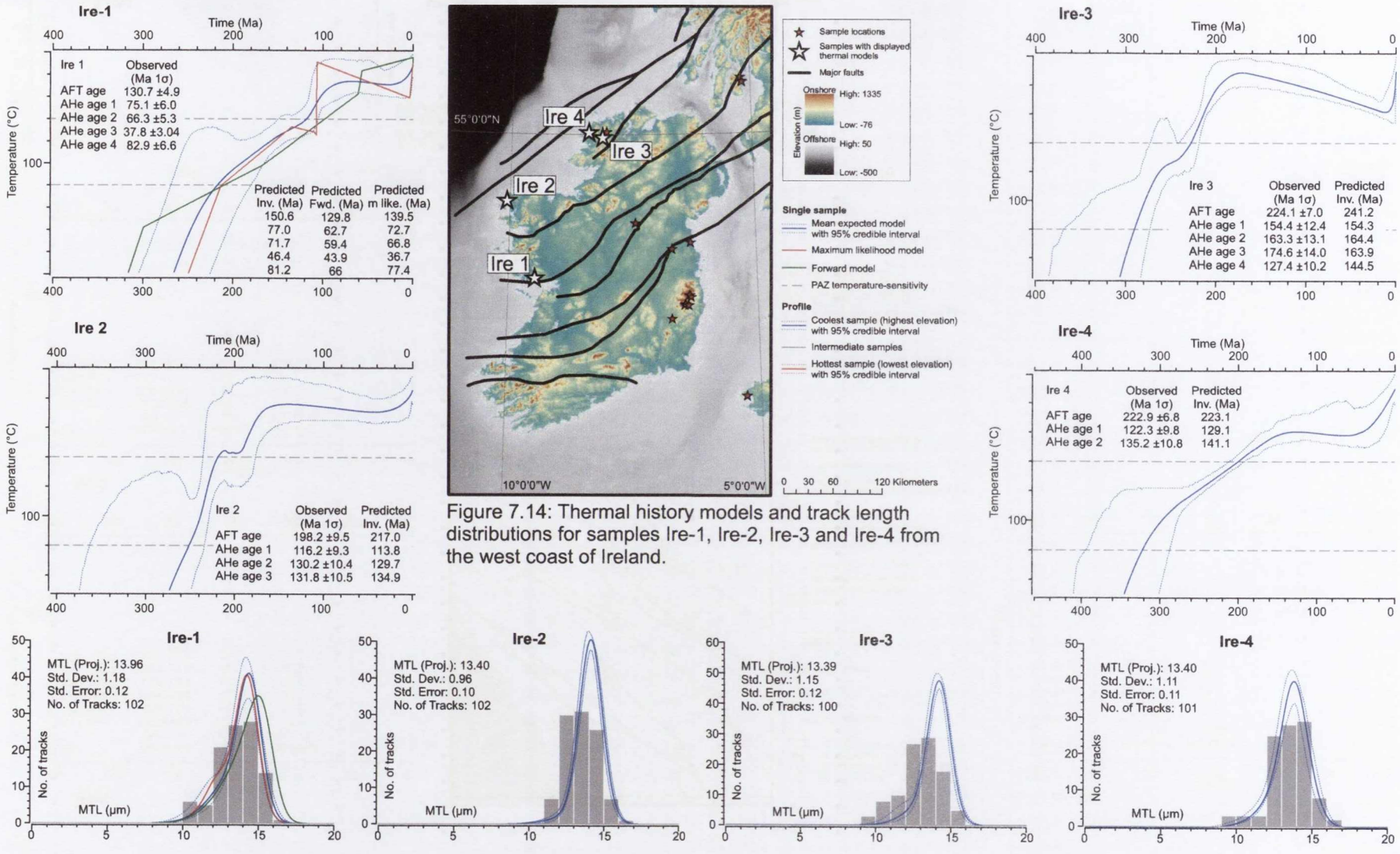


Figure 7.14: Thermal history models and track length distributions for samples Ire-1, Ire-2, Ire-3 and Ire-4 from the west coast of Ireland.

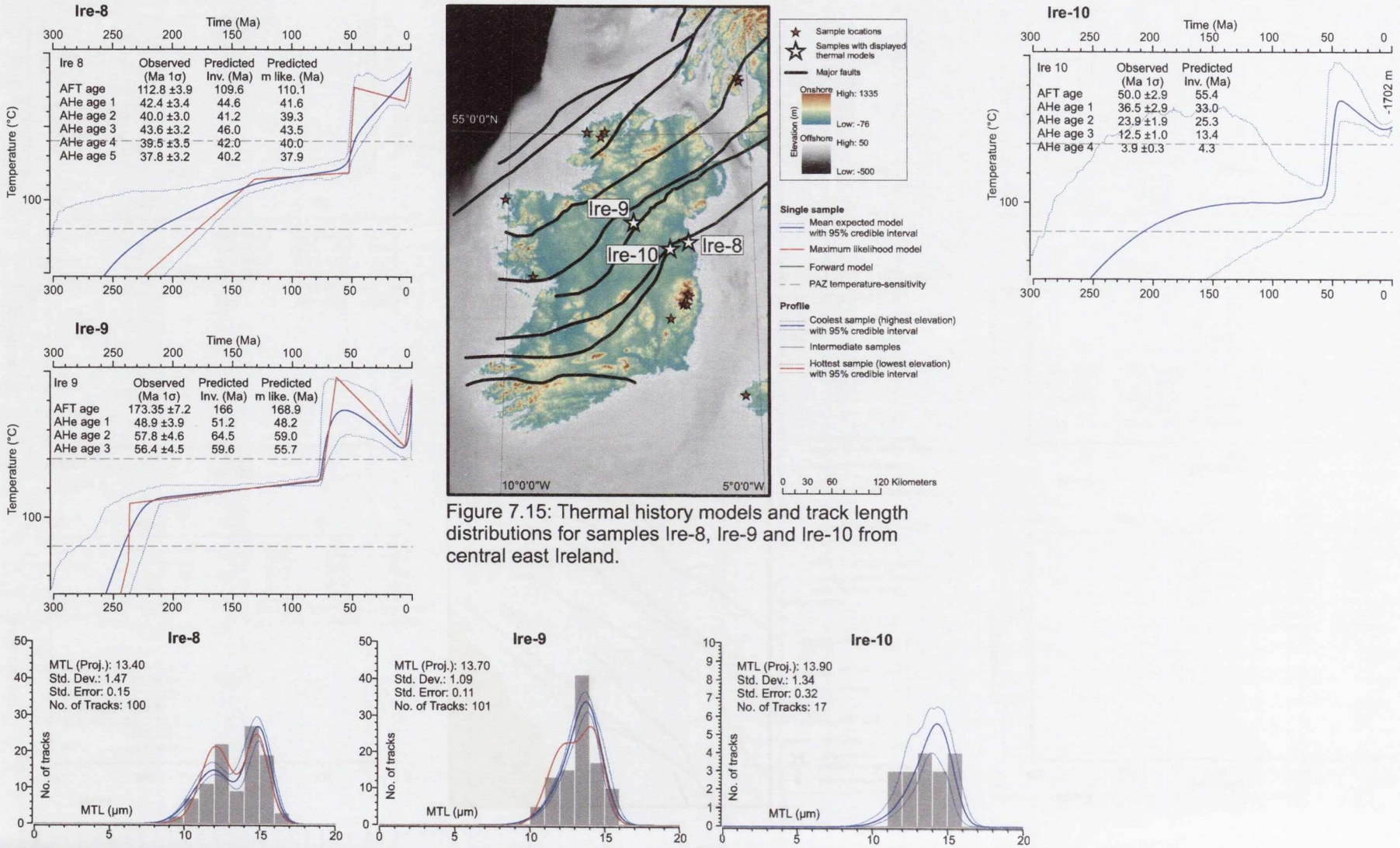


Figure 7.15: Thermal history models and track length distributions for samples Ire-8, Ire-9 and Ire-10 from central east Ireland.

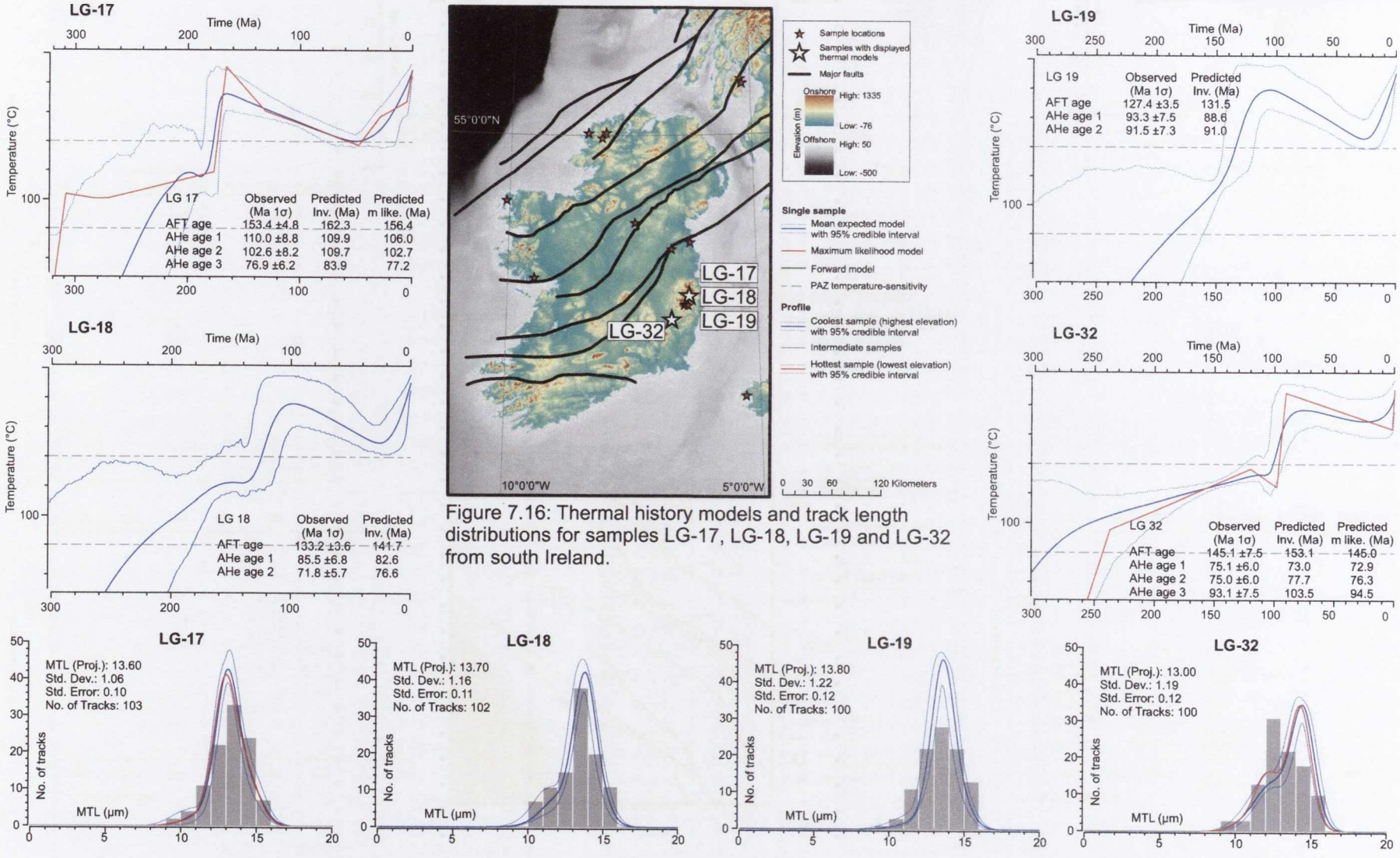
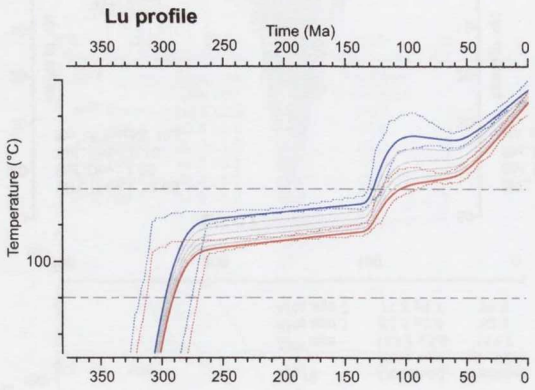
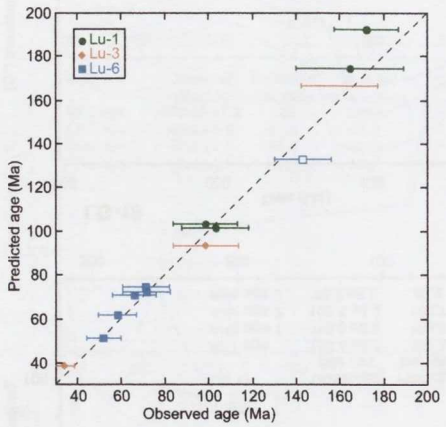


Figure 7.16: Thermal history models and track length distributions for samples LG-17, LG-18, LG-19 and LG-32 from south Ireland.





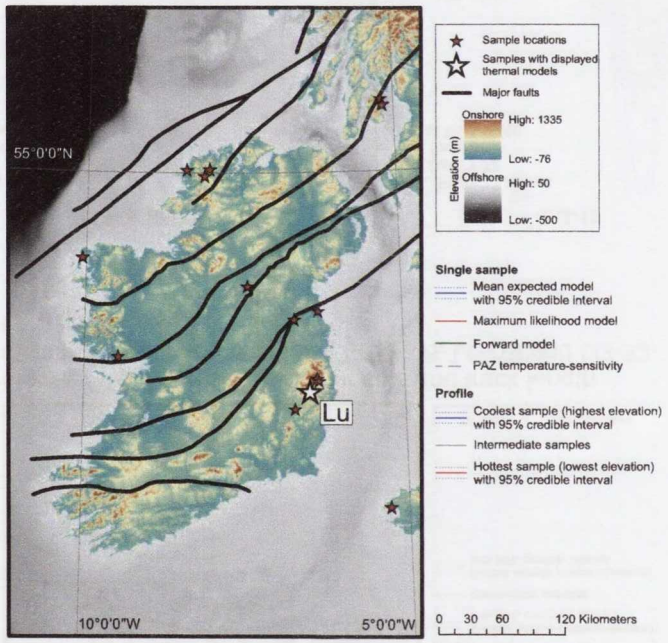
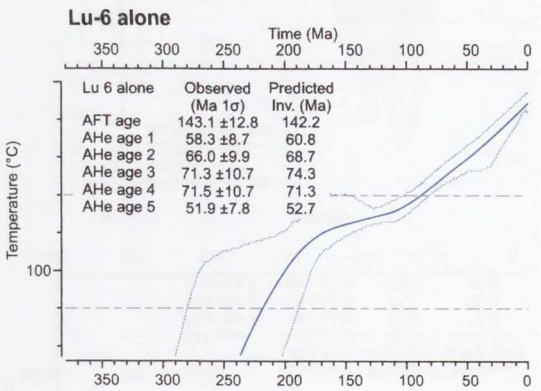
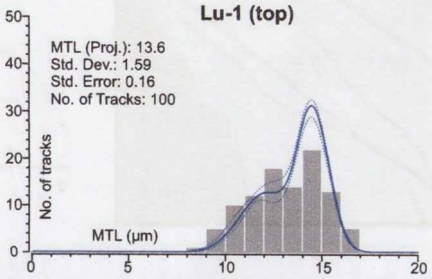
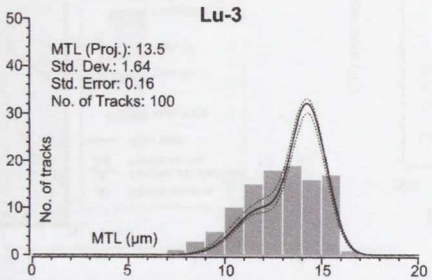
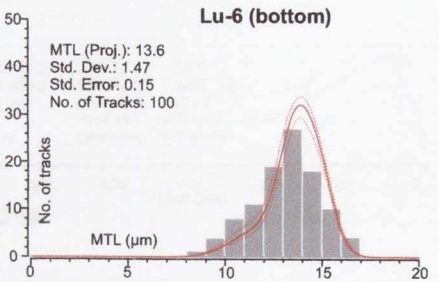


Figure 7.17: Thermal history models and track length distributions for profile Lugnaquilla (Lu) in south Ireland.









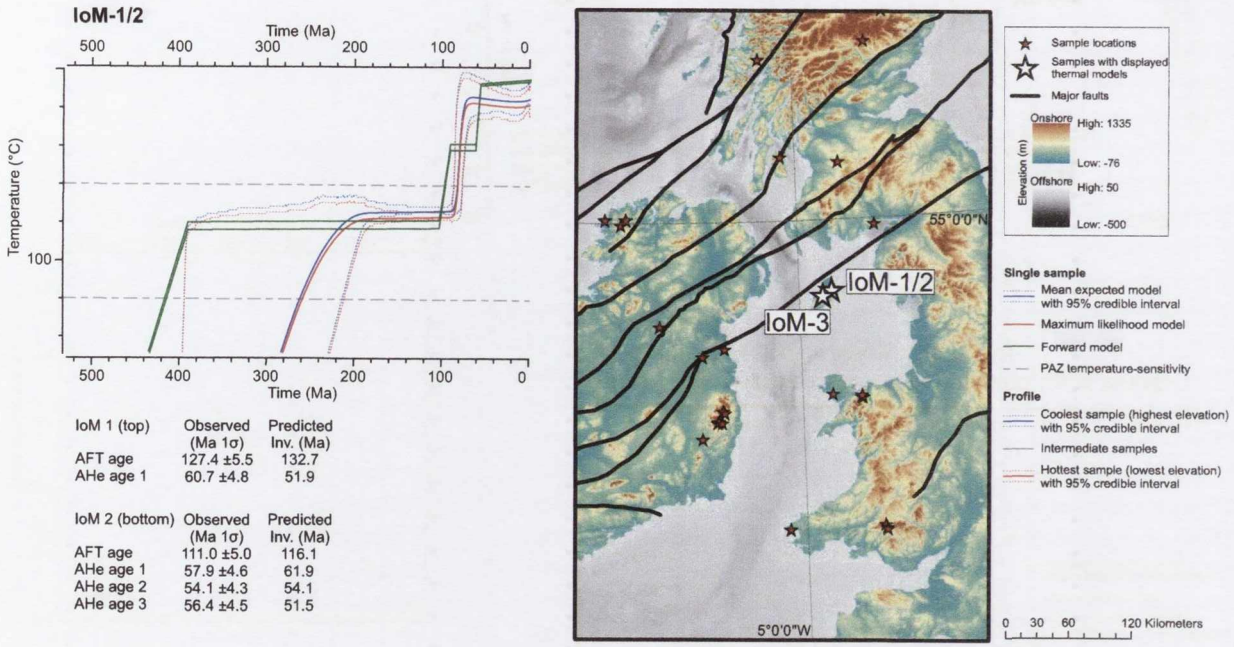
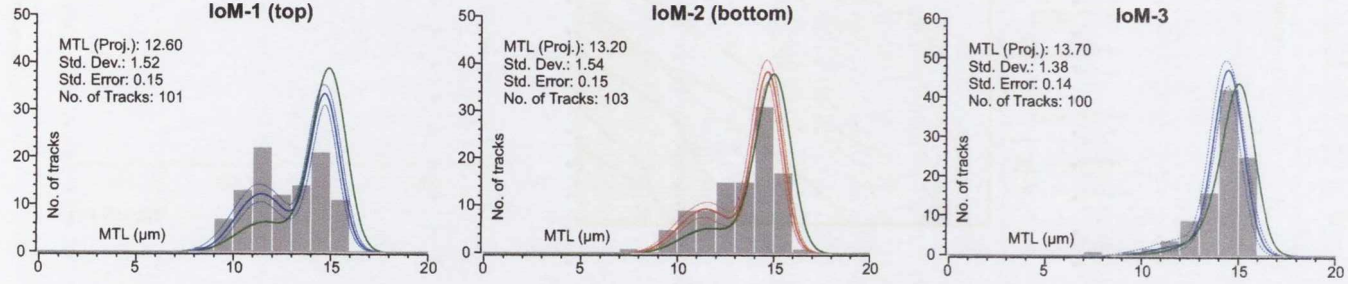


Figure 7.18: Thermal history models and track length distributions for samples IoM-1, IoM-2 and IoM-3 from the Isle of Man.



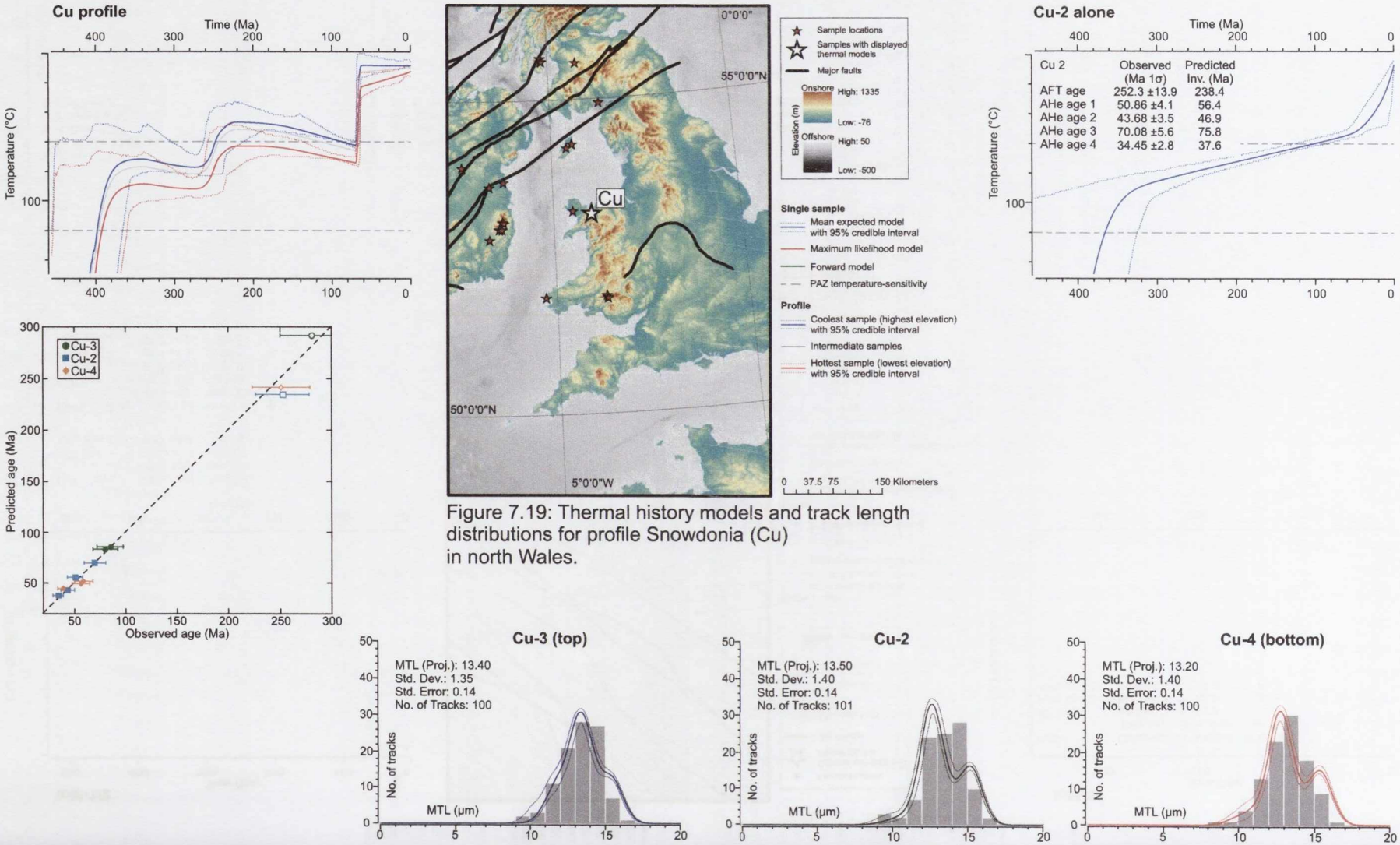
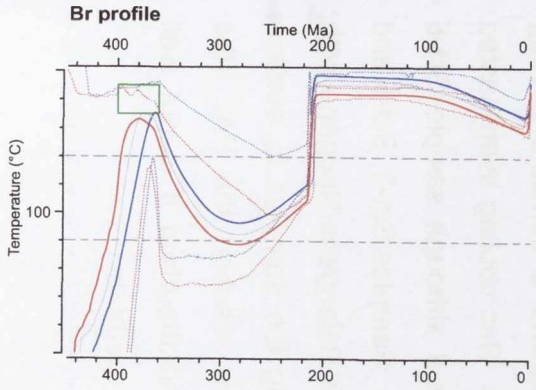
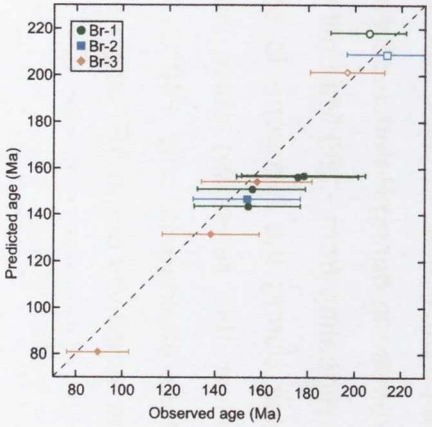


Figure 7.19: Thermal history models and track length distributions for profile Snowdonia (Cu) in north Wales.





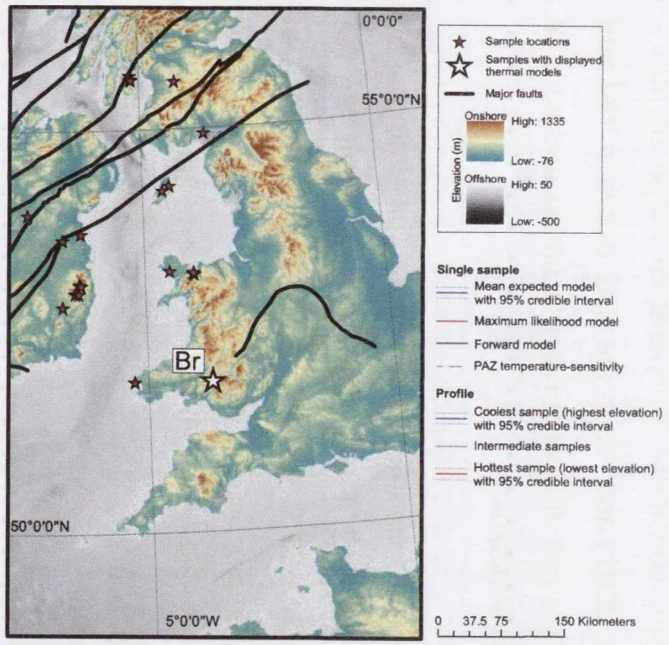
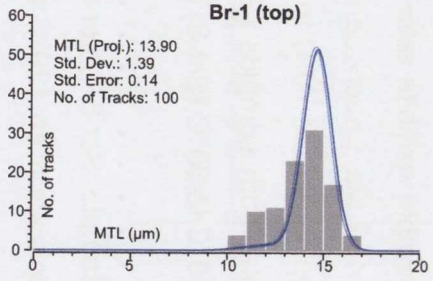
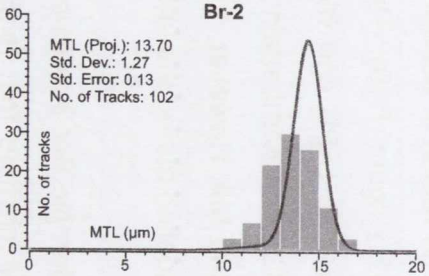
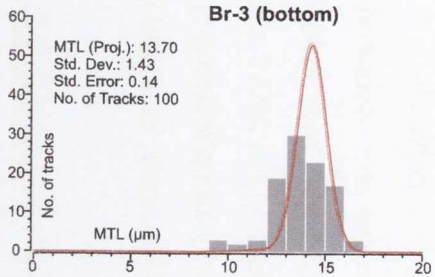


Figure 7.20: Thermal history models and track length distributions for profile Brecon Beacons (Br) in south Wales.







7.1.1 Scotland

In general, Scotland is characterized by very old AFT ages of up to 353.6 ± 12.1 Ma (1σ) (Sct-6) and a large range of AHe ages ranging from 32.5 ± 2.6 Ma (Sct-11) to 290.9 ± 23.3 Ma F_T-corrected (1σ) (Sct-9) (Figure 7.9). Sct-1 is the only sample showing a young AFT age of 60.4 ±2 Ma. Due to the large range of AHe ages, Scotland is divided into 3 different sub-sections.

7.1.1.1 Central Scotland

The region in central Scotland consists of the samples Sct-3 to Sct-9 and Sct-12 (Figure 7.10). These samples all show a relatively fast cooling from the apatite U-Pb age high temperature constraint (temperature range of 500 – 425°C, Chamberlain and Bowring, 2001) and reach the PAZ between 480 and 300 Ma. However, there are some small differences in the timing and style of cooling during the late Paleozoic to Mesozoic.

Sample Sct-3 reaches the PAZ at ~320 Ma and cools further until ~280 Ma, by which time the sample has left the PAZ. From ~280 Ma until ~220 Ma the sample exhibits slow reheating from ~60°C to 80°C. Sct-8 enters the PAZ at ~400 Ma (much earlier than in sample Sct-3) and shows a minor reheating episode from 70°C to 80°C between ~360 and 220 Ma. Between ~220 and 190 Ma, both samples (Sct-3 and Sct-8) experienced a rapid cooling event from 80°C to 30°C (Sct-8) and 20°C (Sct 3).

Sample Sct-5 enters the PAZ at ~300 Ma and shows a constant cooling episode from 120°C at ~300 Ma to 20°C at 180 Ma. This cooling event lasted until 180 Ma and appears similar to Sct-3 and Sct-8 although sample Sct-5 does not show any reheating during Paleozoic times. Samples Sct-3, Sct-5 and Sct-8 all show slow reheating from ~180 Ma until the Paleogene/Neogene with a small cooling pulse during the Neogene to bring the samples to surface temperatures. However this reheating pulse never reached the PAZ (the maximum temperature attained is only ~40°C) and therefore it is not well constrained given the sensitivity of the AFT and AHe methods.

Sample Sct-6 reaches the PAZ at ~480 Ma and shows monotonic cooling from 80 to 10°C between ~460 Ma to present day. Only the credible interval for 95% allows for a very minor amount of cooling between 200 – 240 Ma, but it is less clear than in samples Sct-3, Sct-5 and Sct-8.

Samples Sct-7 and Sct-9 enter the PAZ at ~360 and 420 Ma, respectively (Figure 7.11). Both samples show a relatively fast cooling through the PAZ. Sct-7 is already below 70°C at 320 Ma and Sct-9 reaches 60°C already at 400 Ma. Both samples subsequently cool very slowly until the Neogene where both samples show a small cooling pulse from ~40°C to the present day. However, this final cooling is well beneath the PAZ and thus difficult to constrain given the sensitivity of the AFT and AHe methods at low temperatures.

The expected model from Sct-12 reaches the PAZ at ~410 Ma (Figure 7.10) and shows a slow monotonic cooling from 120 to ~30°C between 410 to 180 Ma. Afterwards Sct-12 indicates a slow reheating from 30°C to 40°C from 180 Ma to the Paleogene/Neogene and a final undefined cooling episode to present day temperatures. The maximum likelihood model however, shows a more distinctive cooling pulse from 140°C to 20°C between 300 and 260 Ma and a subsequent reheating episode from 20°C to just under 60°C between 260 and ~70 Ma.

Sample Sct-4 yield AFT ages of 325.0 ± 9.3 Ma and the AHe ages range from 114.6 ± 9.2 Ma to 93.6 ± 7.5 Ma is located in close proximity to Sct-5 (~25 km). However, thermal modelling with QTQt did not yield any reasonable results. The time acceptance rate during the modelling procedure was below 1% and could not be improved.

7.1.1.2 Western Scotland

Samples Sct-10 and Sct-11 are located in NW Scotland (Figure 7.12). Both samples yield the oldest apatite U-Pb ages of all samples analysed at 1120 ± 160 Ma (2σ) and 1628 ± 63 Ma, respectively.

The inverse thermal history modelling of sample Sct-10 enters the PAZ at ~320 Ma and shows slow cooling to 40°C until ~200 Ma. From ~200 Ma until the Neogene, the thermal history path remains at ~40°C until a minor acceleration in cooling occurs during the Neogene. However, this last cooling pulse is not well constrained. The young AHe ages of 62.6 and 50.5 Ma (uncorrected) indicate potentially Cenozoic cooling, and therefore I also included a forward model in the thermal history (Figure 7.12). The forward model enters the PAZ at the same time as the inverse model (~320 Ma) but cools much faster and at 300 Ma is set at 60°C. Afterwards, the forward model defines monotonic cooling throughout the Late Paleozoic and Mesozoic, until 60 Ma where a distinctive cooling pulse is set based on the AHe ages. The amplitude of this cooling pulse is 35°C (from 50 to 15°C).

Sample Sct-11 shows, similar to Sct-10, monotonic cooling in the inverse model from ~400 Ma at 80°C to 10°C at present day, with a minor acceleration during the Neogene. The AHe ages in this sample range from 62.3 to 25.3 Ma and therefore I included a forward model to test the predictions for a set cooling pulse at 60 Ma. The forward model is defined as monotonic cooling through the PAZ from ~390 to ~60 Ma, with a cooling pulse of ~60°C from 80 to 20°C at 60 Ma.

7.1.1.3 South Scotland

Samples Sct-1 and Sct-2 are located in southwest Scotland (Figure 7.13) and show rather different Cenozoic thermal histories compared with central Scotland (i.e. Sct-5) (Figure 7.10).

Sample Sct-1 is significantly different from all other samples in Scotland which have a Paleozoic or older emplacement age. Sct-1 exhibits a relatively young AFT age of 60.4 ± 2.0 Ma (1σ), despite having an old and well-defined apatite U-Pb age of 395 ±5 Ma (2σ). Thus, the Paleozoic and Mesozoic thermal history is not well constrained and allows for several possible thermal histories. Nevertheless, the cooling pulse from 100°C to 10°C at ~60 Ma is well constrained by the young AFT age 60.4 ± 2.0 Ma (1σ) and AHe ages of ~63

Ma F_T-corrected (~45 Ma uncorrected). The model shows a rapid reheating from 10 to ~40°C between 60 and ~5 Ma but, this reheating episode is not well constrained given the sensitivity of the AFT and AHe methods at low temperatures.

Sample Sct-2 is one of the samples where it was not possible to determine the apatite U-Pb age. Thus, a Caledonian high temperature constraint of 400 ± 50 Ma at 200 ± 50°C was chosen. The Paleozoic thermal history for sample Sct-2 is similar to central Scotland (i.e. Sct-3). Sct-2 reaches the PAZ at ~440 Ma and cools to 70°C between ~440 and 410 Ma. Afterwards, Sct-2 shows a reheating episode of ~20°C between 410 and 350 Ma. From 350 to ~200 Ma the sample cools from 90°C to ~40°C before another reheating episode from 40°C to 80°C occurs between ~200 and 80 Ma. Between 70 and 60 Ma, Sct-2 shows another distinct cooling pulse of ~45°C which although of smaller magnitude occurs at a similar time as in sample Sct-1.

7.1.2 West and Central Ireland

AFT ages in Ireland range from 224.1 ± 7.0 Ma to 50.0 ± 2.9 Ma (both 1σ) and a mean value of ~145 Ma which is in in general younger than the AFT ages from Scotland (mean value of ~275 Ma). However, the AHe ages range from 243.8 ± 19.5 Ma to 5.2 ± 1.4 Ma (F_T-corrected; 1σ) with a mean value of ~114 Ma which is much closer to the AHe ages from Scotland (mean value of ~136 Ma).

The study areas in Ireland can be divided into three groups, i), west and NW Ireland, ii), central Ireland and iii), south Ireland.

7.1.2.1 West Ireland

Sample Ire-1 was collected from the Galway granite on the west coast of Ireland, samples Ire-2 to Ire-7 are all located in NW Ireland (Figure 5.1) but only Ire-1 to Ire-4 were modelled (Figure 7.14).

Sample Ire-5 yielded a mean AHe age of ~232.8 Ma (F_T-corrected) which is much older than the AFT age (176.3 Ma), and thus it was not possible to generate a thermal history model which predicts AHe ages older than the AFT age, even when the RDAAM model (section 3.3.5) of Flowers et al. (2009) was employed. As shown in Figure 7.6 and Figure 7.7 there is no correlation of the AHe ages in sample Ire-5 and the grain size radius or effective uranium content, respectively.

Sample Ire-6 did not yield any AHe ages and thus was not modelled as there is already a pseudo-vertical profile available nearby with AFT and AHe ages (Cogné et al., 2014) and therefore modelling only the AFT age would not yield any additional information. Sample Ire-7 was previously analysed by Stuart Bennett (Bennett, 2006) and was located in close proximity to a Paleogene dyke (0.15 m distance). The AFT and AHe ages were reset during the emplacement of the dyke between 62.6 ± 0.3 and 59.6 ± 0.3 Ma (Ganerød et al., 2010).

The inverse model for sample Ire-1 enters the PAZ at 220 Ma and shows constant cooling from 120°C to ~70°C between 220 to 120 Ma. Between 120 and 100 Ma the cooling accelerates from 70 to 20°C. From 100 Ma the thermal model shows a reheating pulse from 20°C to 40°C before a final cooling phase occurs during the Neogene, but this reheating and final cooling episode within the last ~40°C is not well constrained. Due to the young AHe ages of 82.9 to 37.8 Ma (uncorrected), a forward model was included into the thermal history modelling to test for a possible Cenozoic cooling pulse which is not visible in the inverse thermal history model. The forward model tested enters the PAZ at 200 Ma and shows monotonic cooling from 120°C to 40°C at 60 Ma followed by a cooling pulse of less than 20°C. This cooling phase is much smaller than in the other samples where a forward model was tested (i.e. Sct-10 and Sct-11).

Samples Ire-2 to Ire-4 yield very similar thermal histories compared with the samples from central Scotland (i.e. Sct-3). After cooling from the apatite U-Pb high-temperature age constraint (temperature range of 500 – 425°C;

Chamberlain and Bowring, 2001) the samples reach the PAZ at different times but all show cooling between 270 and 220 Ma.

Sample Ire-2 reaches the PAZ at ~240 Ma and rapidly cools from 120°C to 60°C at 220 Ma (Figure 7.14). From 220 to 190 Ma the sample remains at 60°C before it starts cooling again from 60°C to 30°C between 190 and 160 Ma. From 160 Ma to the Neogene, the sample remains at roughly at ~30°C with only a small amount of reheating until the Neogene. This reheating and final cooling to present-day temperatures is very small and poorly constrained.

Samples Ire-3 and Ire-4 both enter the PAZ between 290 Ma and 280 Ma and both samples cool to ~80°C between 280 and ~275 Ma (Figure 7.14). However, sample Ire-3 remains at ~80°C from 280 to 240 Ma and then shows a distinctive cooling episode from 80 to ~15°C between 240 and 180 Ma. From 180 Ma to the Neogene Ire-3 shows reheating from 15°C to 40°C, with a final cooling pulse during the Neogene. Sample Ire-4 on the other hand shows constant cooling from ~80°C to ~30°C between ~275 and 110 Ma. Between 110 and ~50 Ma the sample exhibits a reheating pulse to about 40°C before the final cooling episode. However, in both samples the Cenozoic thermal history is not well constrained.

7.1.2.2 Central east Ireland

Samples Ire-8 to Ire-10 are located at the east coast of Ireland and central Ireland (Figure 7.15). Ire-10 is from a borehole (1702 m depth) from Tara Mines in Navan, County Meath, north east of Dublin. This region is characterized by relatively young AFT age with a mean value of ~107 Ma and a mean AHe age of ~50.5 Ma (F_T-corrected). These young AHe ages are much younger than the other samples in Ireland which show a mean AHe age value of ~132 Ma. Furthermore, all three samples show a strong and rapid cooling pulse between 60 and 50 Ma which also does not occur elsewhere in Ireland.

Sample Ire-8 enters the PAZ at ~220 Ma and slowly cools from 120 to 80°C between 220 and 60 Ma (Figure 7.15). At ~60 Ma the sample shows a strong

cooling episode which is more obvious in the maximum likelihood model than in the expected model. The expected model shows strong cooling from ~80°C to 60°C between ~60 and 50 Ma and subsequently constant cooling from 50 Ma to the present day. The maximum likelihood model prefers a much more pronounced cooling pulse from 90 to ~25°C at around 50 Ma. Afterwards, the maximum likelihood model shows a reheating event from ~25°C to 35°C until the Neogene where a final cooling pulse occurs. The credible interval clearly allows for constant cooling and a reheating event during Cenozoic times, but it is not well constrained since the temperature does not reach 40°C.

Sample Ire-9 reaches the PAZ at 240 Ma and cools relatively quickly to ~90°C between 240 and 220 Ma (Figure 7.15). Afterwards, the sample shows a decrease in the cooling rate and the temperature decreases from ~90 to 70°C between 220 and ~70 Ma. Between 70 and 60 Ma the sample shows a distinctive cooling pulse from 70°C to 30°C in the expected model and from 70°C to 10°C in the maximum likelihood model. Both models show a reheating pulse to 50°C from 60 Ma to the Neogene before the final cooling pulse to present-day temperature occurs. However, both the Paleozoic reheating episode and the final cooling pulse are not well constrained.

Sample Ire-10 is a sandstone from a borehole (1702 m depth) in central east Ireland (Figure 7.15). The Paleozoic and Mesozoic thermal history is not well constrained at this location due to the young AFT age of 50 ±2.9 Ma (1σ). The thermal history model enters the PAZ at ~210 Ma and slowly cools from 120°C to just under 100°C between 210 and ~60 Ma. Between 60 and 50 Ma the samples show a very rapid and well constrained cooling pulse from ~100°C to ~30°C and shows a reheating episode during the Paleogene/Neogene to ~45°C which is the assumed present day temperature (based on a geothermal gradient of ~25°C/km).

7.1.3 South Ireland

Samples LG-17 to LG-19, LG-32 (Figure 7.16) and the Lu profile (Figure 7.17) were all collected from the Leinster batholith in SE Ireland. The Lu profile was

sampled and analysed by N. Cogné, and thus the thermal model for this profile is not included in the results. However this sample is still discussed as the sample is very close to LG-17 to LG-19. I analysed 71 AHe ages from the Lu profile but due to computational difficulties (only 1000 modelling iterations in 72 hours in QTQt) in applying the broken grain model of Beucher et al. (2013), a thermal history model could not be constructed.

Sample LG-18 and LG-19 have a very similar thermal history (Figure 7.16). LG-18 enters the PAZ at ~220 Ma and cools to 80°C between ~220 and 160 Ma. Between 160 and 140 Ma the thermal model remains at 80°C before another cooling episode from 80°C to 20°C between 140 and 100 Ma occurs. The thermal model shows a reheating episode to 50°C took place between 100 Ma and the Neogene subsequent cooling to surface temperatures.

This reheating and final cooling episode is very similar to LG-19 where reheating from 20 to ~50°C occurs between 110 Ma and the Neogene (Figure 7.16). However, the Mesozoic thermal history is slightly different. LG-19 enters the PAZ at 190 Ma and shows constant cooling from 120 to 20°C between 190 and 110 Ma. Nevertheless, the credible interval allows for the same thermal history as in LG-18.

Sample LG-17 is in very close proximity to LG-18 and LG-19 but the thermal history is different (Figure 7.16). LG-17 reaches the PAZ at 240 Ma and cools to ~80°C at 200 Ma. The expected model shows a small reheating pulse between 200 and 180 Ma of ~5°C but this reheating episode is not visible in the maximum likelihood model. Between ~180 and 170 Ma the thermal model shows a rapid cooling pulse in the expected and maximum likelihood model from ~85°C to 30°C in the expected and to ~5°C in the maximum likelihood model. Both models show a reheating episode from 30°C and 5°C, respectively, to 60°C between 170 and 50 Ma. From 50 Ma both models show a final cooling pulse to present-day temperatures.

Sample LG-32 is located to the southwest of the other samples of the Leinster batholith (Figure 7.16). The expected thermal model enters the PAZ at ~280 Ma

and slowly cools to about 70°C at 110 Ma. The sample remains close to 70°C with a very small reheating episode for 10 Ma until the thermal model shows a cooling episode from ~70°C to 20°C between 100 and 90 Ma. Afterwards, the model exhibits reheating to about 40°C from 90 Ma to the Neogene before the final cooling pulse to present-day temperatures occurs. However, this reheating and cooling pulse between 20 and 40°C is not well constrained.

The Lu profile enters the PAZ at about 290 Ma and cools to ~80°C for the uppermost sample by 240 Ma (Figure 7.17). Afterwards, the thermal model shows a very slow cooling phase from 80 to 60°C between 240 and 130 Ma, and then from 130 to ~100 Ma a cooling pulse of 20°C occurs. From ~100 to 60 Ma the profile remains at ~40°C (uppermost sample) but at 60 Ma a final cooling pulse to present-day temperatures takes place.

To show the advantage of using vertical profile modelling, a single sample from the Lu profile (Lu-6) was modelled alone. Lu 6 alone reaches the PAZ at ~240 Ma which is 50 Ma later than using the vertical profile (Figure 7.17). Between 240 and 140 Ma the sample cools with a constantly decreasing cooling rate from 120 to ~70°C. From 140 Ma to the present day, the thermal model shows monotonic cooling without any indication of reheating or increased cooling episodes, which occurs in the vertical profile at ~60 Ma. The difference between the profile and the single sample modelling will be discussed in chapter 8.

7.1.4 Isle of Man and Isle of Arran

The Isle of Arran (IoA) is located in southwest Scotland (Figure 7.13) and the Isle of Man (IoM) in the centre of the Irish Sea (Figure 7.18).

The profile from the Isle of Arran is from a Paleogene intrusion ($^{40}Ar/^{39}Ar$ age of 59.35 ±0.6 Ma; Ganerød et al., 2010) and the mean value of ~59 Ma for the AFT ages from the profile is comparable with Sct-1 (AFT 59.4 ± 2 Ma (1σ)) and Ire 10 (50 ± 2.9 Ma(1σ)). The thermal model shows rapid cooling between 60 and 50 Ma but it is not well constrained due to the low amount of apatite grains counted (only one sample with 21 grains) and the relatively low track density,

which is roughly an order of magnitude lower than the most other samples analysed (Table 7-1).

The Isle of Man (IoM) samples were collected at two separate localities and comprise three samples in total (Figure 7.18). IoM-1 and IoM-2 were collected from the same granite body in the northwest of the island and were modelled together but only have a vertical separation of ~80 m. The thermal models for both locations are very similar. The thermal models for IoM-1 and IoM-2 enter the PAZ at ~240 Ma and cool subsequently to ~80°C at 200 Ma (Figure 7.18). The model remains at 80°C until ~80 Ma where a prominent cooling pulse of ~60°C occurs. The thermal model for IoM-3 takes the same path until Paleogene times compared with IoM-1 and IoM-2 but, instead of remaining at 20°C from 80 Ma until the present day, IoM-3 shows reheating to 40°C until the Neogene where a final cooling pulse to present-day temperatures occurs (Figure 7.18). However, in both locations the final path from 80 Ma to present day is difficult to constrain given the sensitivity of the AFT and AHe methods at low temperatures.

7.1.5 Wales

The dataset from Wales comprises samples An and the Cu profile in north Wales, and samples Pb-1 and Pb-2 as well as the Br profile in south Wales (Figure 5.1).

The thermal history of the Cu profile in northern Wales shows, similar to central Scotland (Figure 7.19) (i.e. Sct-6 and Sct-8), rapid cooling from high temperatures constrained by apatite U-Pb ages (between 496 ±86 and 414 ±19 Ma (2σ)) until ~70°C for the top sample of the profile at ~370 Ma. From 370 to 260 Ma the profile shows a minor reheating episode of ~10°C before another cooling episode from 80°C to ~50°C occurs between 260 and 220 Ma (Figure 7.19). This cooling episode is followed by another reheating event of 10°C magnitude which occurs between 220 and ~60 Ma. At ~60 Ma the profile shows a rapid cooling pulse from 60°C to 10°C where the samples remain until the present day. Importantly, the cooling pulse at 60 Ma is not visible if the samples

from the profile are modelled alone (see example Cu-2 in Figure 7.19). The thermal history model for Cu-2 alone shows simple monotonic cooling from 100°C at 340 Ma until 50°C at 40 Ma where a small acceleration in the cooling rate occurs until the present day. The difference between the Cu profile and the Cu single sample modelling will be discussed in chapter 8.

Sample An in northern Wales is very similar to west Scotland (i.e. Sct-10 and Sct-11) in that the inverse thermal history models show slow monotonic cooling (Figure 7.12). Sample An enters the PAZ at ~320 Ma and cools to 80°C at 280 Ma. Between 280 and 160 Ma the samples shows monotonic cooling from 80°C to 70°C (Figure 7.12). The credible interval of the expected model indicates an increase of the cooling rate between 160 and 120 Ma and the sample cools from 70°C to ~40°C. From 120 Ma to the late Paleogene, the sample shows minimal cooling of less than 10°C until the cooling accelerates from ~40 Ma to the present day. Since the AHe ages are, like in western Scotland, very young (59.7 to 45.1 Ma uncorrected) I added a forward model to the thermal history (Figure 7.12). The forward model enters the PAZ at 410 Ma, similar to Sct-10 and remains at 80°C from 390 to 180 Ma. Between 180 and 160 Ma the sample cools from 80°C to 50°C and afterwards, between 160 and ~60 Ma, the sample cools an additional 10°C. A final cooling pulse is set at 60 Ma from 40°C to 10°C and remains at 10°C until the present day.

The samples from Pembrokeshire (Pb-1 and Pb-2) were only 10 metres apart and yield virtually identical AFT and AHe ages within error (AFT age: 220.8 ±23.2 and 230.6 ±22.3 Ma, both 1σ) and thus only sample Pb-1 was modelled. The inverse model for sample Pb-1 reaches the PAZ at ~260 Ma from where the sample slowly cools from 120°C to 60°C at 180 Ma with a constantly decreasing cooling rate between 260 and 180 Ma (Figure 7.12). The sample cools slowly from 60°C to 40°C between 180 and ~70 Ma where a very small increase in the cooling rate from 40°C to 30°C is visible. From ~70 Ma to the present day the thermal model slows monotonic cooling to 10°C. The small increase in cooling rate at ~70 Ma and the similarities to samples An, Sct-10 and Sct-11 led me to create a forward model. The forward model was included to examine if a more pronounced cooling episode during Cenozoic times was

possible. The best fits to the forward model are found when it enters the PAZ much earlier than in the inverse model which would be consistent with the An and Cu samples in Wales (Figure 7.12). A cooling pulse for ~40°C (80°C to 60°C) is set between 260 and 240 Ma followed by continuous cooling from 60°C to 40°C between 240 and 60 Ma. Around 60 Ma another cooling pulse is set from 40°C to 10°C where the sample remains until the present day.

The profile from south Wales was sampled in the Brecon Beacons (Br) (Figure 7.20). These samples consist of Lower Devonian sandstones compared to the majority of the other samples in this study which are typically Caledonian igneous rocks. Thus, instead of the apatite U-Pb age, the start of the thermal history employed a depositional age of ~400 – 380 Ma (Figure 7.20) (Wellman et al., 1998). Following deposition, the samples show reheating between 380 to 280 Ma to at least 100°C for the top sample in the profile. Between 280 and 220 Ma the samples slowly cool from 100 to 80°C and this slow cooling is followed by a rapid cooling pulse between 220 and 200 Ma from 80 to 10°C (Figure 7.20). This strong cooling event is followed by a period of static temperatures until ~100 Ma when the sample slowly reheats to ~30°C until the Neogene, before a final rapid cooling pulse occurred. However, this last reheating and cooling pulse during Late Cenozoic times took place below 40°C and is therefore not well constrained.

Figure 7.21 summarises all *major* cooling events revealed by the thermal history modelling from Paleozoic to Paleogene (to some degree Neogene) times based on geographical regions. As shown in Figure 7.21 the onset of cooling is different for the geographical regions. Scotland and parts of Wales (Cu profile) shows mainly Paleozoic onset of cooling while Ireland and the Isle of Man show mainly Mesozoic cooling events. Early Cenozoic cooling (marked with the grey box in Figure 7.21) occurs across the geographical regions and will be discussed in more detail chapter 8.4.

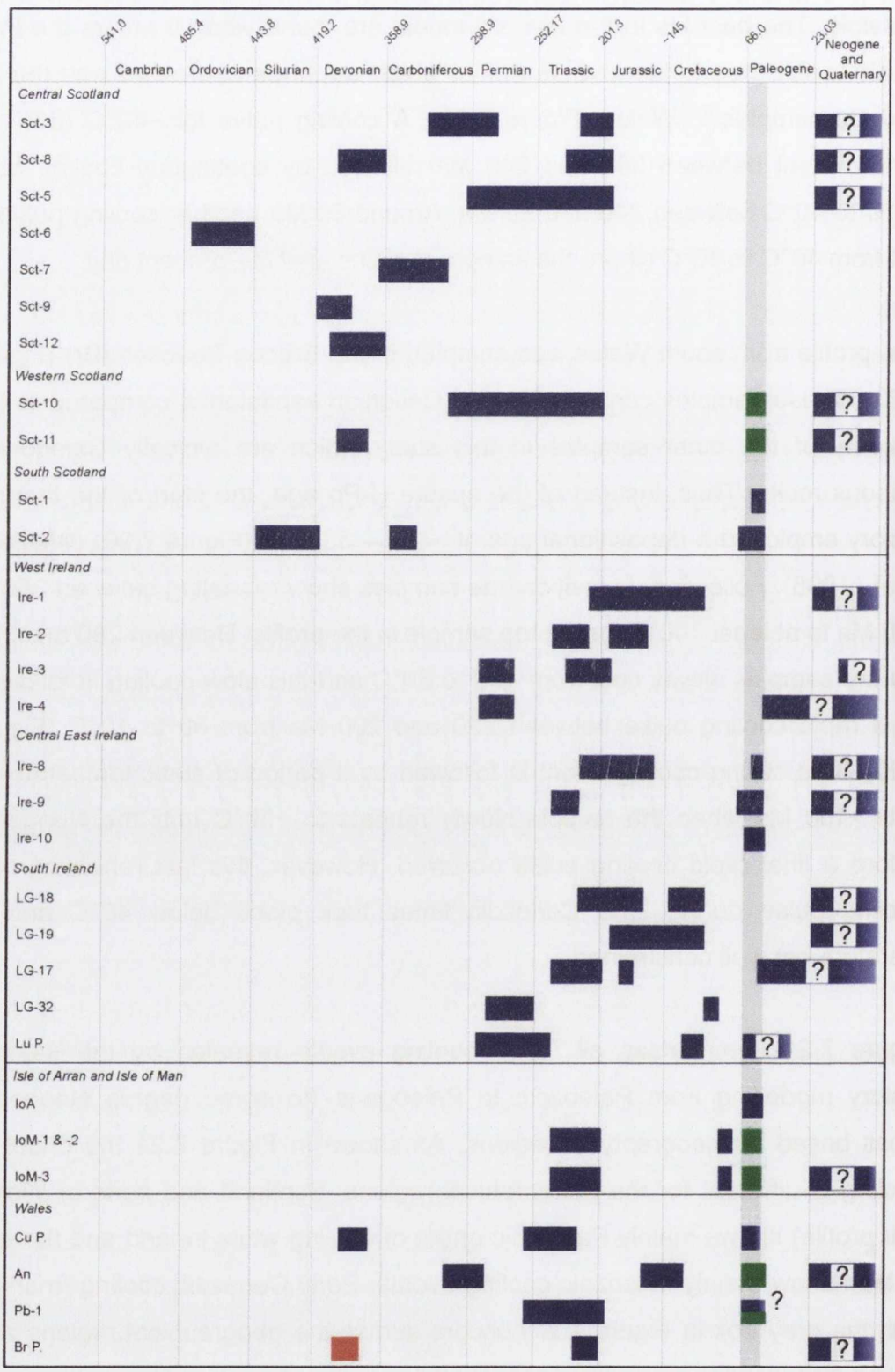


Figure 7.21: Summary figure of all *major* cooling events revealed by thermal history modelling divided into regions. Blue: Cooling events. Green: Cooling events from forward modelling. Red: Depositional age. P.: sample profiles. Grey box represents the proposed timeframe for mantle-driven processes during early Paleogene. Cooling events labeled with a question mark are below recorded below 40°C and thus not well constraint.

8. Discussion

The thermal history modelling results described in chapter 7 reveal different phases of cooling in the thermal history of Britain and Ireland from the early Paleozoic through to Cenozoic times (Figure 7.21). If the timing of cooling in the thermal history models is coincident with known *major* tectonic events, then it is possible that the cooling episode in question was caused by the respective tectonic event. Several major tectonic events occurred during the Phanerozoic geological history of Britain and Ireland including the Caledonian orogeny, the Variscan orogeny, the break-up of Pangea, Mesozoic rifting followed by exhumation during Cenozoic times which is likely either related to far-field stresses or mantle-driven processes as discussed in the introduction (see chapters 1 and 2). To determine the exhumation history of Ireland and Britain, the spatial patterns in the timing of cooling and reheating episodes in the thermal history models are linked below with the timing of *major* regional tectonic events. The synthesis and discussion in this chapter is therefore divided into five sections based on the regional timing of the major tectonic events: i) Caledonian tectonism and post-Caledonian exhumation; ii) Carboniferous deposition and Variscan exhumation; iii) Pangea break-up and Mesozoic rifting events; iv) early Cenozoic exhumation and v) Neogene exhumation.

It is important to note that the large "closure" temperature differences between the apatite U-Pb method (500 - 425°C) and the low-temperature AFT (120 - 60°C) and AHe dating methods (85 - 40°C) used in this thesis means that the thermal history models are poorly constrained between 425°C and 120°C. Thus, the early cooling history of the thermal history models following the high-temperature constraint has to be assessed with caution, because the expected model (the blue path in the models presented in Chapter 7) may not necessarily represent the actual cooling path taken by the sample. The credible interval (the zone where 95% of the thermal models pass though) hence can be very large, especially for samples with much younger AFT ages than their corresponding apatite U-Pb age i.e. sample Sct-1 from southern Scotland.

Nevertheless, it is possible to make observations about the early portions of the thermal history in Ireland and Britain, particularly for samples where the AFT age is "close" to the apatite U-Pb age. One example is sample Sct-9 from the Northern Highlands with an apatite U-Pb age of 444.0 ± 28.0 Ma (2σ) and an AFT age of 339.6 ± 9.8 Ma (1σ) (Figure 7.11). On the other hand, where the AFT age and the respective apatite U-Pb age are separated by a large time gap, the Paleozoic history cannot be resolved in detail. For example, sample Sct-1 in southern Scotland has an AFT age of 60.4 ± 2.0 Ma (1σ) and an apatite U-Pb age of 395.0 ±5.0 Ma (2σ), and therefore the thermal history model cannot resolve the Paleozoic or Mesozoic history (Figure 7.13). Therefore, the pre-late Mesozoic thermal histories are only discussed as far as the thermal history models allow for an interpretation, and the late Mesozoic and Cenozoic exhumation histories will be interpreted in more detail.

8.1 Caledonian and post-Caledonian exhumation

As explained above, it is not possible to resolve the thermal history within the temperature range between 425°C and 120°C. Thus, by default the thermal model will always show relatively constant cooling from the apatite U-Pb high-temperature constraint until the samples reach the PAZ where the AFT method is sensitive. Thus, the cause for the cooling from 500 - 425°C to 120°C is ambiguous and all thermal models are cut at about 150°C to increase the resolution of the temperature range where AFT and AHe dating are sensitive. Cooling from the apatite U-Pb high-temperature constraint to 120°C for Caledonian igneous samples (the most common sample type in this study) most likely represents a combination of cooling following emplacement (thermal relaxation) and subsequent cooling related to exhumation.

At least seven samples in central Scotland (Sct-2, Sct-6 to Sct-9, Sct-11 and Sct-12 and the Snowdonia (Cu) profile in north Wales show relatively rapid cooling from their respective apatite U-Pb high-temperature constraint at ~425°C to 120°C within less than 100 Ma (Figure 8.1). This relatively rapid cooling indicates these samples experienced cooling related to thermal relaxation followed by a subsequent exhumation pulse. Most of these samples

reached the PAZ between 440 and 390 Ma. Only sample Sct-6 exhibits a much earlier cooling phase at ~480 Ma, while sample Sct-7 exhibits a late cooling phase at ~360 Ma. The cooling episode at ~480 Ma in sample Sct-6 clearly cannot be much younger due to the very old AFT age of 353.6 Ma ±12.1 Ma (1σ). This ~480 Ma cooling episode correlates with the first phase of the Caledonian orogeny (the Grampian phase: 475 - 460 Ma; Dewey and Shackleton, 1984). However, the credible interval for Sct-7 allows the sample to reach the PAZ at ~400 Ma and therefore it is difficult to distinguish between Caledonian or post-Caledonian exhumation.

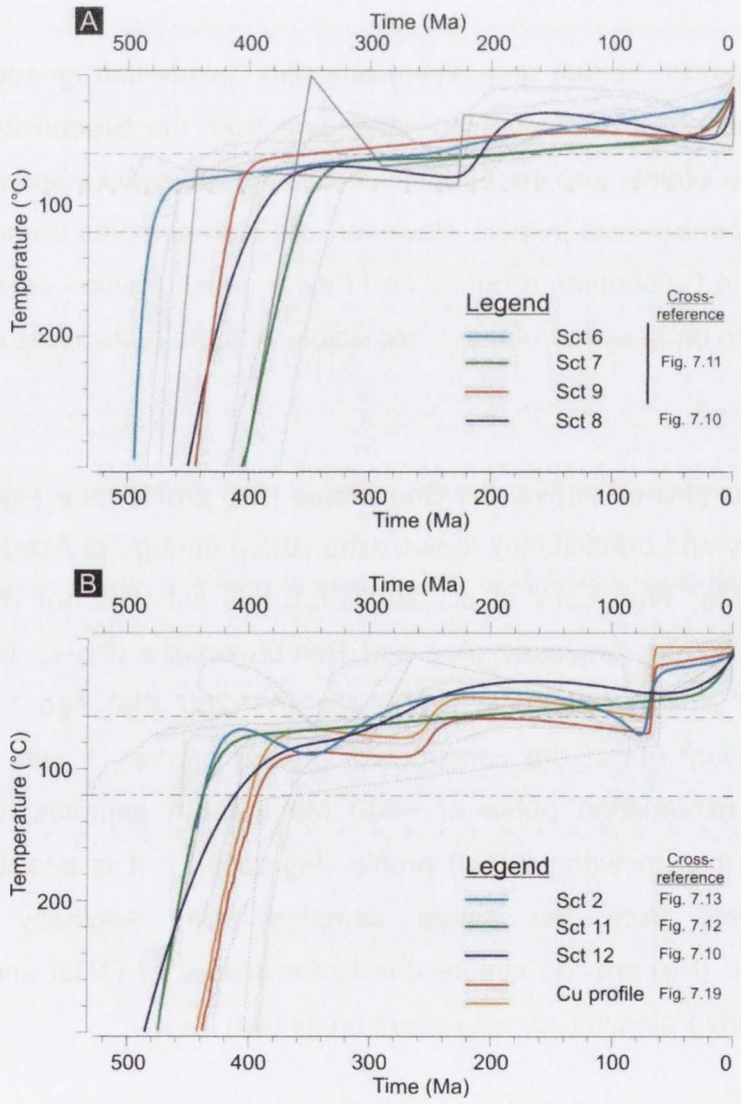


Figure 8.1: Thermal history models from seven samples in Scotland and the Snowdonia (Cu) profile in Wales. Cross-referenced are the thermal models with predictions and TLD, where available.

Samples Sct-2 and Sct-11 reach the PAZ at ~440 Ma which corresponds with the Scandian event of the Caledonian orogeny (Figure 8.1a) (~435 - 425 Ma; Thigpen et al., 2013). This is an appropriate mechanism to explain the exhumation of sample Sct-11 which is situated in NW Scotland close to the Moine Thrust Zone where Scandian deformation is pervasive; however Scandian deformation is minor southeast of the Great Glen Fault and is unlikely to be responsible for the cooling pulse observed in sample Sct-2. Samples Sct-8, Sct-9, Sct-12 and the Snowdonia (Cu) profile enter the PAZ between 410 and 390 Ma (Figure 8.1b), which corresponds in time with the end stages of the Acadian orogeny (~405 - 390 Ma; Woodcock et al., 2007).

Most samples from Ireland and Wales are also Caledonian igneous samples, with the exception of the Devonian sandstone from the Brecon Beacons (Br) profile in south Wales, and the Ordovician-Silurian greywacke borehole sample (Ire-10) from central-east Ireland. However, the Irish samples do not reach the PAZ during the Caledonian orogeny and thus any exhumation associated with the Caledonian orogeny in Ireland is not visible with the techniques employed in this study.

In Wales, as explained above, the Snowdonia (Cu) profile (see Figure 7.19 for thermal history and predictions) shows exhumation during the Acadian orogeny (~405 - 390 Ma; Woodcock et al., 2007) but this event is not visible in the inverse models from Anglesey (An) and Pembrokeshire (Pb-1). Both inverse models show a late Paleozoic (~300 Ma to ~260 Ma; see Figure 7.12) exhumation event but in the constructed forward models, it was possible to generate an exhumation pulse at ~400 Ma in both samples, which does coincide with the Snowdonia (Cu) profile (Figure 8.2). It is possible that the inverse models from the single samples from Anglesey (An) and Pembrokeshire (Pb) are too simple due to the nature of QTQt and could not resolve the early Paleozoic cooling event on its own.

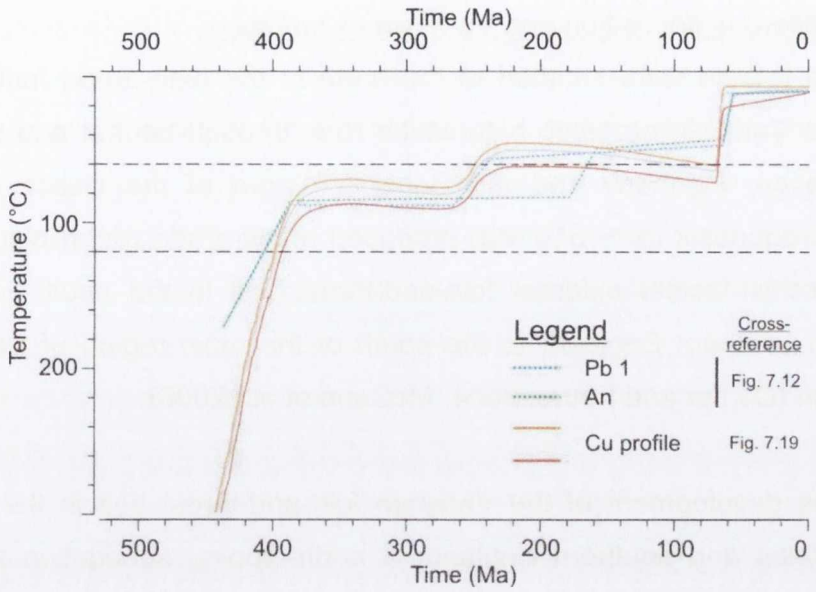


Figure 8.2: Thermal history models from Wales. The constructed forward models for Anglesey (An; green dashed line) and Pembrokeshire (Pb-1; blue dashed line) are compatible with the inverse model from the Snowdonia profile (Cu; red and orange line) profile. Cross-referenced are the thermal models with predictions and TLD, where available.

Table 8-1 shows the observed AFT and AHe ages for samples An and Pb-1 as well as the predictions for inverse and forward modelling with QTQt. Both, inverse and forward model, do fit the observed ages within error which means both thermal models are possible explanations for their respective locations.

Table 8-1: Observed ages and predictions from the inverse and forward model with QTQt from samples Anglesey (An) and Pembrokeshire (Pb-1) in Wales.

Sample Name		Observed ages (Ma, 1σ)	Predicted Inv. model (Ma)	Predicted Fwd. model (Ma)
An	AFT age	187.7 ±14.9	193.1	186
	AHe age 1	59.72 ±4.8	61.1	54.5
	AHE age 2	45.12 ±6.3	47.9	46.7
Pb-1	AFT age	220.8 ±23.2	203.5	233.2
	AHe age 1	44.7 ±3.6	41.4	40.0
	AHE age 2	55.0 ±4.4	53.0	54.6
	AHe age 3	37.6 ±3.0	43.5	40.3

Notes:
Inv.: Inverse model with QTQt
Fwd.: Forward model with QTQt

8.2 Carboniferous deposition and Variscan exhumation

Britain and Ireland were situated to the north of the high-grade metamorphic core of the Variscan orogenic belt, which runs through central and northwest Spain, France, Germany and the Bohemian area of the Czech Republic. Varsican orogenesis (at ~ 310 Ma) produced a low-grade (deep diagenetic to the greenschist-facies) external fold-and-thrust belt in the south of Ireland, Wales and southern England, to the south of the main region of Caledonian deformation (Cartier and Faure, 2004; McCann et al., 2006).

Prior to the development of the Variscan fold-and-thrust belt in the south of Ireland, Wales and southern England, a north-dipping subduction zone had been established through central France and southern Germany by the early Carboniferous. This gave rise to back-arc extension and the establishment of major Carboniferous depocentres in Britain and Ireland. These depocentres comprise much of Ireland, along with northern England (the Pennine Basin), the Devon-Cornwall Basin in Southern England and the Midland Valley of Scotland, and were separated by important, long-lived palaeogeographical barriers, the Wales–London–Brabant High and the Southern Uplands High.

Thus the time period from ~360 Ma to 310 Ma can be considered a relatively "quiet" tectonic setting, with reburial during Carboniferous times in Ireland and the portions of Britain listed above. This is shown by the thermal history model of sample Sct-2 from the margins of the Midland Valley/Southern Uplands zone in southern Scotland which shows reheating between ~360 to 310 Ma (Figure 8.3), which is attributed to the deposition of Carboniferous rocks in the Midland Valley associated with Carboniferous dextral transtension and associated emplacement of alkali volcanics (Woodcock and Strachan, 2012).

A similar reheating event from ~360 to 280 Ma is also apparent in the late Devonian sandstone profile from the Brecon Beacons (Br), which shows reheating above 120°C (Figure 8.3). This is compatible with the bituminous to anthracite rank of Carboniferous coals in the adjacent South Wales coalfield (Bevins et al., 1996). Thus, although the exact amount of reheating cannot be determined as the AFT and AHe ages were, at least partially reset (see Figure

7.20 and Figure 8.3), the reheating event seen in the Brecon Beacons is probably caused by a combination of Carboniferous burial, similar to sample Sct-2 in the Midland Valley, and crustal thickening due to the Variscan orogeny affecting the southern parts of Ireland, Wales and south England at ~310 Ma (Quinn et al., 2005, see below). It is difficult to separate these two closely-spaced events from each other as AFT and AHe dating is insensitive at temperatures above 120°C.

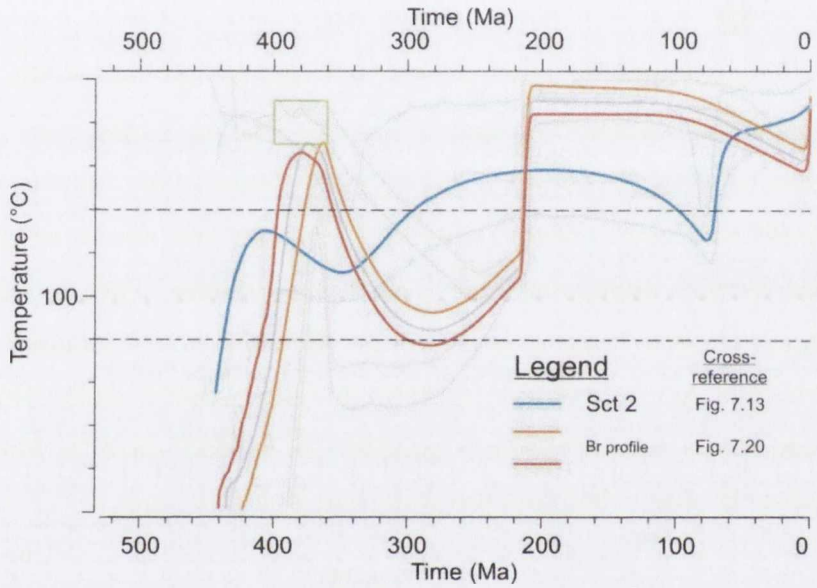


Figure 8.3: Carboniferous reheating in Southern Scotland (Sct-2) and in the Brecon Beacons profile (Br) from south Wales. Cross-referenced are the thermal models with predictions and TLD, where available.

The timing of Variscan deformation in the low-grade, external fold-and-thrust belt of southern Ireland (part of the Variscan Rhenohercyian tectonic zone) is estimated at 310 Ma (predominantly ductile deformation) to 300 Ma (predominantly brittle deformation) based on ^{40}Ar-^{39}Ar dating of metamorphic white mica (Quinn et al., 2005). North of the fold-and-thrust belt and the so-called "Variscan Front" (Chapter 2), deformation is localised and partitioned into predominantly dextral strike-slip movements on earlier Caledonian structures such as the Highland Boundary and Southern Uplands faults (Woodcock and Strachan, 2012). Far-field (up to 1000 km) effects of Variscan Orogenesis are recognised as far northwards into the Devonian Orcadian Basin of NW Scotland, Orkney and Shetland, where Late Carboniferous dextral strike-slip

reactivation of the Great Glen Fault, and its continuation into Shetland, the Walls Boundary Fault, led to the development of small-scale folds and thrusts (Seranne, 1992). Hence samples Sct-3, Sct-5, Sct-10 from Scotland and Ire-3, Ire-4, LG-32 and the Lugnaquilla (Lu) profile from Ireland, which all show cooling between ~310 to 280 Ma (Figure 8.4), are attributed to post-Variscan exhumation, even though they lie to the north of the Variscan front.

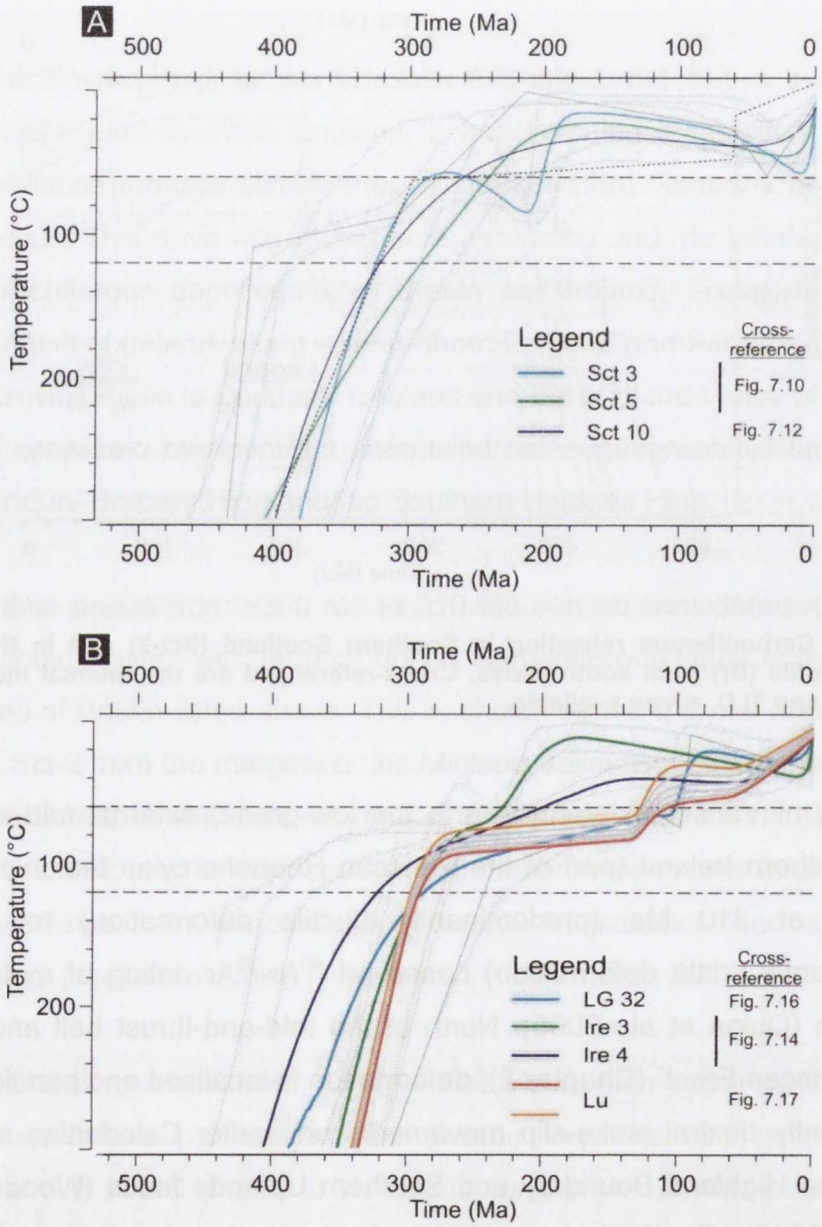


Figure 8.4: Thermal history models which show post-Variscan exhumation despite the fact that they lie north of the Variscan front. Cross-referenced are the thermal models with predictions and TLD, where available.

8.3 Pangea break-up and Mesozoic rifting event

The thermal history models reveal a complex late Permian to mid-Cretaceous cooling history which lasted over 160 Ma. Different cooling phases occurred from ~260 – 240 Ma (late Permian - early Triassic), ~220 – 200 Ma (late Triassic), 190 – 180 Ma (early Jurassic) and 125 – 100 Ma (mid-Cretaceous).

The reason for this rather differentiated cooling history across Ireland and Britain is related to the complicated break-up of Pangea and the subsequent initiation of rifting in the North Atlantic region. The break-up of Pangea started during the late Permian to early Triassic between the Barents Sea and the Norwegian-Greenland Sea rift (Figure 2.6a; Peacock, 2004) which corresponds to the first recognized cooling pulse documented in this dataset between ~260 and 240 Ma. The break-up is followed by a complicated system of southward-propagating rifts from the North Atlantic where they connect with a second major rift system in the Central Atlantic (Ziegler and Stampfli, 2001; Peacock, 2004) during the early Jurassic (Figure 2.6b) into the Cretaceous (Figure 2.7b) (section 2.1.3). Consequently, rifting does not occur everywhere at the same time, which is evident in the different Mesozoic rifting histories of the offshore basins and sub-basins of the Irish Sea system (see chapter 2.3.2, 2.3.3). It seems highly plausible that the variable exhumation histories seen in the thermal history models from the onshore regions are associated with the diachronous Mesozoic rifting histories evident in the adjacent offshore basins. Thus, onshore Mesozoic exhumation histories are linked with timing of Mesozoic rifting in the adjacent offshore basins, to test if a relationship between rifting and exhumation exists.

8.3.1 South Ireland

Samples LG-17 to 19 from the Leinster Granite show cooling between ~200 to 180 Ma (early Jurassic) which is contemporaneous with the deposition of clastic sediments of Sinemurian age (199.3 ± 0.3 to 190.8 ± 1.0 Ma) in the Celtic Sea Basin to the south (Figure 8.5) (Shannon and Naylor, 1998) and up to 2.7 km of lower Jurassic syn-rift sediments on the west flank (Bray fault) of the Kish Bank Basin to the northeast (Naylor et al., 1993). A similar early Jurassic pulse of

cooling is recognized in the Galtee Mountains and Mount Leinster by Cogné et al., (Cogné et al., 2016; see appendix) and in samples across Ireland by Green et al. (2000). The deposition of syn-rift sediments indicates that this cooling pulse in southern Ireland was caused by exhumation and is linked to rifting in the adjacent offshore basins.

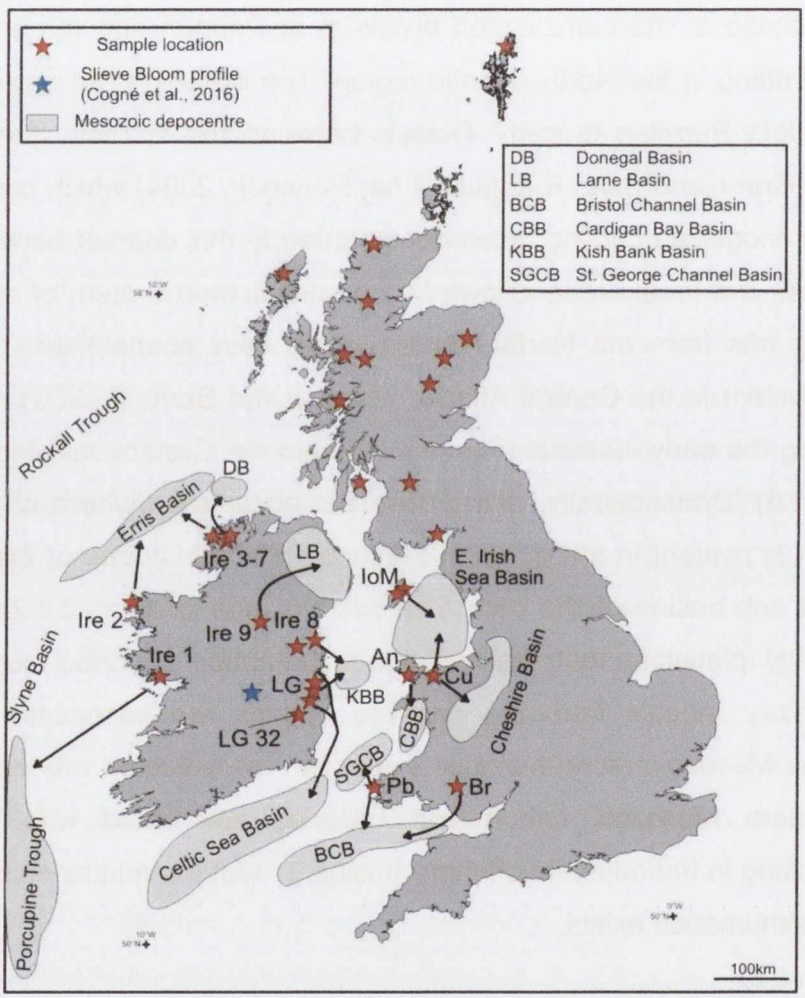


Figure 8.5: Onshore exhumation linked with syn-rift sedimentation in the adjacent offshore basins. Arrows show which adjacent offshore basins contain syn-rift sediments of the same age as exhumation is proposed by thermal models. The Paleozoic and Mesozoic exhumation is explained in more detail in chapter 9.1.

Sample LG-32 is located ~25 km away (to the southwest) from the other LG samples (Figure 5.1) and does not show this early Jurassic cooling event. It is possible that some regional tectonic break (i.e. differential fault movement)

resulted in this region not experiencing the same early Jurassic exhumation history as the other LG samples to the northeast. A very limited early Jurassic exhumation phase was also recognized by Cogné et al. (2016 ;see appendix) in the Slieve Bloom profile in central Ireland (Figure 8.5). This limited amount of Mesozoic rifting in central Ireland indicates that the rift-related exhumation was focussed at areas close to the offshore basins and did not extend into central Ireland (Cogné et al., 2016).

A second Mesozoic cooling pulse in south Ireland occurred between ~125 and 100 Ma (mid-Cretaceous) and is visible in samples LG-18, LG-19, LG-32 and the Lugnaquilla (Lu) profile (Figure 7.16 and Figure 7.17). Only sample LG-17 in south Ireland shows an earlier cooling pulse at ~165 Ma which is probably related to the older AHe ages (Figure 7.16). Holford et al. (2005b) recognized this ~125 and 100 Ma early Cretaceous cooling episode in the Central and East Irish Sea Basin and Green et al. (2000) onshore Ireland. However, unlike the first early Jurassic cooling pulse, this cooling episode cannot be linked to rifting in the offshore basins. Neither the north St. George's Channel Basin (Welch and Turner, 2000a; Williams et al., 2005) nor the Kish Bank Basin (Naylor et al., 1993) show any record of rifting or deposition of Cretaceous successions. AFT and vitrinite reflectance data from the Central and East Irish Sea Basin suggest that early Cretaceous cooling was related to a phase of exhumation (Holford et al., 2005b) and likely associated with extension at the Atlantic Margin due to onset of seafloor spreading in the Bay of Biscay (Keen et al., 1977; Ziegler, 1989) and major changes in the vector of African plate motion at ~131 Ma and ~84 Ma, linked to the Eo-Alpine orogeny (e.g. Handy et al., 2010).

8.3.2 Central east Ireland

Samples Ire-8 to Ire-10 come from central east Ireland. Ire-10 is the borehole sample (1702 m) from Tara Mines near Navan with an AFT age of 50.0 ± 2.9 Ma (1σ) and the Mesozoic thermal history is therefore not constrained. Sample Ire-9 is located in central Ireland and shows a distinct cooling pulse during the mid-Triassic (~240 Ma), whereas the thermal history model for sample Ire-8,

located directly on the east coast, is under constrained during Mesozoic times and allows for cooling at ~240 Ma or at a later stage during the mid-Jurassic.

Both exhumation events, during the mid-Triassic and mid-Jurassic, are similar to the events recognized in south Ireland (section 8.3.1) and were also caused by rifting in the adjacent basins. Ire-9 is close to the Larne Basin in Northern Ireland which is now mostly buried beneath the Antrim Lava Group (Figure 8.5). Previous studies have shown that the basin formed under the same extensional regime as the Irish Sea Basin system (Coward, 1995) and hosts Permo-Triassic successions up to 2.9 km thick (Holford et al., 2009a).

Sample Ire-8 allows for a Permo-Triassic exhumation pulse however, the maximum likelihood model (Figure 7.15) prefers Jurassic exhumation. This Jurassic exhumation event would be consistent with the deposition of Jurassic syn-rift sediments up to 2.7 km thick on the west flank of the Kish Bank Basin (Naylor et al., 1993), which is to the southeast of the sample location of Ire-8 (Figure 8.5). Nevertheless, the Kish Bank Basin was also a depocentre during Permo-Triassic times and shows reactivation of faults, especially on its western margin (Naylor et al., 1993), which means that Mesozoic exhumation on the east coast of Ireland is polyphase and not represented by one discrete event.

8.3.3 West Ireland

The Irish Atlantic offshore basins consist of several small basins and some larger basins such as the Slyne, Erris, Rockall and Porcupine Basin (Figure 1.3 and Figure 8.5). In some basins, such as the Rockall Basin, the exact timing of extension, igneous activity and the sedimentological evolution are poorly understood due to the limited amount of boreholes and seismic data available (i.e., Haughton et al., 2005), although there are more data available for the Slyne, Erris, and the northern portion of the Porcupine Basin (Shannon and Naylor, 1998). Connecting the onshore cooling phases with offshore rifting phases is complicated by the polyphase (Permo-Triassic to Jurassic) rifting history of the Irish Atlantic basins, which can be exacerbated in regions where

there is a lack of seismic data and thick Cenozoic successions are present (Shannon and Naylor, 1998; Haughton et al., 2005).

Samples Ire-1 to Ire-4 (Figure 7.14) are all located on the west coast of Ireland, with sample numbers increasing to the north from central west Ireland (Galway, Ire-1) to NW Ireland (Donegal, Ire-3,-4) (Figure 5.1). Sample Ire-3 has a general Caledonian high temperature constraint of 475 ± 75°C between 450 and 350 Ma and Ire-4 yields an apatite U-Pb age of 457 ± 36 Ma (2σ) as high temperature constraint. Sample Ire-3 reaches the PAZ AT ~290 Ma and a second cooling pulse at between 240 and 200 Ma, whereas sample Ire-4 enters the PAZ at ~320 Ma and experienced subsequently monotonic cooling throughout Mesozoic times. Although the 320 to 290 Ma cooling pulse postulated in the thermal models would appear compatible with post-Variscan exhumation, NW Ireland was not affected by the Variscan fold-and-thrust belt (Graham, 2009b) and it does not correlate with the development of the Irish Atlantic offshore basins, which initiated during Permo-Triassic times ~50 Ma later (Shannon and Naylor, 1998). The cause of this early high temperature portion of the cooling history in samples Ire-3 and Ire-4 is therefore somewhat uncertain.

The track length distribution (TLD) of Ire-3 and Ire-4 show a considerable amount of short tracks (<11 µm), which means that the sample had to spend a significant portion of time in the PAZ to generate these short tracks. This also explains the difference between the cooling pulse of ~310 - 290 Ma derived from the thermal history model and the younger AFT age of ~224.1 ± 7 Ma for sample Ire-3 and 222.9 ± 6.8 Ma for sample Ire-4 (both 1σ error). Nevertheless, the AFT ages in this study are older than the published AFT ages by Cogné et al. (2014) for the same region, which range from 200.1 ± 17.8 Ma to 167.8 ± 13 Ma (both 2σ). The discrepancy between the AFT ages in this study and the previously published ages from Cogné et al. (2014) could be related to some local faulting between the sample locations of Cogné et al. (2014) and the sample location in this study Figure 5.1.

Furthermore, samples Ire-1 and Ire-3 show subsequent Mesozoic cooling between at ~210 Ma and sample Ire-2 two cooling pulses at ~240 and ~190 Ma (late Triassic to early Jurassic). These cooling events can be linked with clastic deposition in the Donegal and Erris Basins (Figure 8.5) which contain Triassic (700 and 300 m thick respectively) and Lower Jurassic successions, (Shannon and Naylor, 1998). Furthermore, Triassic and Jurassic sediments are also known in the North Porcupine Basin which is another potential depocentre for material eroded from western Irish onshore (Figure 8.5) (Shannon and Naylor, 1998). Thus, the Triassic to Jurassic onshore cooling episode was likely caused by exhumation related to rifting in the adjacent offshore basins as in south Ireland and Wales. Sample Ire-1 from the Galway Granite shows another cooling pulse at ~110 Ma (Cretaceous) which cannot be linked with rifting in the offshore basins and is probably related to a phase of exhumation associated with extension at the Atlantic Margin (Holford et al., 2005b) as described in section 8.3.1.

The observation by Cogné et al. (2014) that the Mesozoic cooling along the western Irish onshore becomes younger to the south is still valid. However, the results from this study suggest that exhumation on the west coast of Ireland is related to extension caused by polyphase rift-shoulder uplift in the offshore basins, similar to the samples in central east and south Ireland (section 8.3.2), instead of southward propagating rift-shoulder uplift during mid-Mesozoic rift proposed by Cogné et al. (2014). However, Cogné et al. (2014) used several pseudo-vertical profiles from the west coast of Ireland while in this thesis only single samples were used. Thus, the results from the pseudo-vertical profiles are probably more reliable than the single sample modelling.

8.3.4 Wales and Isle of Man

During Permo-Triassic times (~260 to 240 Ma), the whole Irish Sea Basin system was affected by rifting associated with extensional break-up of the Pangean supercontinent, which led to the development of several basins within the Irish Sea region containing up to 3 km of syn-rift Permo-Triassic clastic successions (Shannon and Naylor, 1998).

The late Permian to early Triassic cooling pulse in Snowdonia (Cu; Figure 7.19) and on the Isle of Man (IoM; Figure 7.18) is coeval with a significant rifting phase in the East Irish Sea Basin and the Cheshire Basin (Figure 8.5) (Rowley and White, 1998). As QTQt naturally prefers simpler solutions (see chapter 6.2), some forward models were constructed for both locations on the Isle of Man and it is possible to generate thermal models which are compatible with an early Cretaceous (~110 Ma) cooling pulse which is a widely detected cooling episode in the Central and East Irish Sea Basin (Holford et al., 2005b) and onshore Ireland (Green et al., 2000). The cause for cooling at ~110 Ma cannot be linked with rifting in the offshore basins and is instead probably related to a phase of exhumation associated with extension at the Atlantic Margin (Holford et al., 2005b) as described in section 8.3.1.

In Pembrokeshire, late Permian to early Triassic cooling is contemporaneous with the opening of the Bristol Channel to the south during the Permo-Triassic (Kamerling, 1979), and with the opening of the St George's Channel Basin to the north during Triassic (Figure 8.5) (Welch and Turner, 2000b). In Anglesey, the cooling pulse occurs during the early Jurassic (~190 to 180 Ma) which is contemporaneous with rifting and the deposition of 1.3 km Lower Jurassic clastic sediments in the Cardigan Bay Basin (Figure 8.5) (Shannon and Naylor, 1998). In southeast Wales, the late Triassic cooling pulse recognized in the Brecon Beacons (Br) profile is contemporaneous with deposition of Upper Triassic rocks which rest uncomfortably on Devonian and Carboniferous successions in in the Bristol Channel Basin (Figure 8.5) (Kamerling, 1979).

The onshore Mesozoic exhumation history in Wales is rather complex and related to rifting in the adjacent offshore basins and lasted for ~160 Ma. Despite its rather complicated history, the Mesozoic exhumation history is in good agreement with previously published results from NW Wales by Holford et al. (2005a) and the timing of rifting and clastic deposition in the immediately adjacent offshore basins.

8.3.5 Scotland

With the exception of samples Sct-3, Sct-5 and Sct-8 (Figure 7.10), Scotland seems rather unaffected by Pangaea break-up and subsequent Mesozoic rifting, with most samples from Scotland generally showing slow cooling during Paleozoic and Mesozoic times, with no obvious cooling event between ~260 to 100 Ma. Sample Sct-3 shows a *reheating* pulse between ~280 and 220 Ma, while samples Sct-3 and Sct-8 both show a cooling pulse between 210 and 200 Ma. Sample Sct-5 shows no cooling pulse but monotonic cooling through the PAZ between ~280 and ~240 Ma. Interestingly, these three samples are the samples with the lowest elevation in central Scotland at between 190 and 230 m above sea level. The causes for the cooling events at Sct-3, Sct-5 and Sct-8 are not known but below two possible explanations are evaluated.

One possibility is that Scotland was reburied beneath a veneer of Carboniferous and Permian sediments which caused partial reheating in the lowest elevation samples in central Scotland (Sct-3 and Sct-5 from the Northern Highlands and Sct-8 from Central Highlands). At least in the Midland Valley and Southern Uplands, some Carboniferous and some scattered Permian outcrops are still preserved. However, there are virtually no remnants of Carboniferous or younger rocks north of the Midland Valley and most samples north of the Midland Valley were colder than the temperature sensitivity window of the AFT and AHe methods during Carboniferous and Permian times. Thus, if Carboniferous and/or Permian sediments were deposited north of the Midland Valley and were subsequently removed between deposition and the present-day, then they were not thick enough to reheat most of the Scottish Highland massif to temperature where AFT and AHe dating would be affected, with the exception of samples Sct-3 and Sct-8.

It is also possible that no Carboniferous and/or Permian sediments were deposited on the Scottish massif and that the Mesozoic cooling seen in samples Sct-3, Sct-5 and Sct-8 represents local, small-scale tectonic events. In particular, samples Sct-3 and Sct-5 are in the vicinity of the Great Glen Fault (GGF), separating the Northern Highland from the Central Highland blocks. This major fault has had a long, complicated reactivation history (Le Breton et

al., 2013) and influences the development of the Inner Moray Firth Basin. During Triassic times, the Inner Moray Firth Basin shows dextral strike-slip movement along the GGF of about 8 km (Le Breton et al., 2013), which could have caused exhumation along the GGF at sample locations Sct-3 and Sct-5 (see GGF and sample location in Figure 7.10).

8.3.6 Overall Mesozoic exhumation history

The Mesozoic exhumation history in Ireland and Britain is complex and lasted over 160 Ma, from the late Permian (260 Ma) to mid-Cretaceous (100 Ma). The onshore exhumation from the late Permian to mid-Jurassic shows a clear relationship between exhumation and rifting in the adjacent offshore basins which is linked with the break-up of Pangea and the subsequent initiation of rifting in the North Atlantic region (Figure 8.5). The Cretaceous cooling in Ireland and Britain cannot be linked with rifting in the adjacent basins. Previous studies based on AFT and vitrinite reflectance data (Holford et al., 2005b) showed that exhumation occurs contemporaneous with extension on the Atlantic Margin associated with the onset of seafloor spreading in the Bay of Biscay during the Aptian ~118 Ma (Keen et al., 1977; Ziegler, 1989) and the onset of the Eo-Alpine orogeny (Eo-Alpine event ~140 - 84 Ma; Handy et al., 2010).

8.4 Early Cenozoic exhumation

As explained in chapter 1, identifying the timing and spatial pattern of Cenozoic exhumation is the main focus of this study. The timing and spatial pattern of exhumation is key in distinguishing between exhumation caused by far-field stresses and mantle-driven processes. The early Cenozoic cooling pulse evident in some thermal history models is interpreted as recording a pulse of exhumation. Only in samples Ire-7, which is adjacent to a Paleogene dyke (distance to dyke 0.15 m) and the Isle of Arran (IoA) profile, a Paleogene intrusion, can the cooling also be related to thermal relaxation following the emplacement of a hot igneous body which will be discussed below.

Investigating the early Cenozoic cooling pulses in the thermal models reveals an interesting pattern. Samples which display evidence for distinct (50 - 90°C) early Cenozoic cooling are Ire-8, Ire-9 and Ire-10 on the central east coast of Ireland (Figure 7.15), samples Sct-1, Sct-2 and the Isle of Arran samples in southern Scotland (Figure 7.13), the Isle of Man samples (Figure 7.18) and the Cu profile in north Wales (Figure 7.19). This indicates a focused cooling event which occurred around the onshore margins of the Irish Sea basin system. Furthermore, samples An and Pb-1 from Wales and samples Sct-10 and Sct-11 from western Scotland allow ~30 - 50°C cooling in their forward models (Figure 7.12) which means early Cenozoic cooling is possible at this locations. This early Cenozoic cooling pulse is not visible in northwest Ireland, central Scotland or the Brecon Beacon profile (Br) in south Wales.

Based on this pattern in the thermal models, the early Cenozoic cooling history is divided into four different zones, which are here assigned colours depending on the intensity of the cooling signal visible in the thermal models (Figure 8.7). These are:

i) the red zone (50 - 90°C of cooling), which represents a distinct cooling pulse during early Cenozoic times which is visible in inverse thermal models for pseudo-vertical profiles (i.e. IoA) and *also* in single samples (i.e. Ire-9)

ii) the yellow zone (35 - 50°C of cooling), which represents only an early Cenozoic cooling event if a pseudo-vertical profile is employed (i.e. Cu profile) or in forward modelling of single samples (i.e. Sct-10 or Pb-1),

iii) the green zone (20 - 35°C of cooling), which does not show a discrete early Cenozoic cooling pulse but instead only a slight increase in the cooling rate at ~60 Ma and

iv) the white zone (<20°C of cooling), which shows no sign of early Cenozoic cooling.

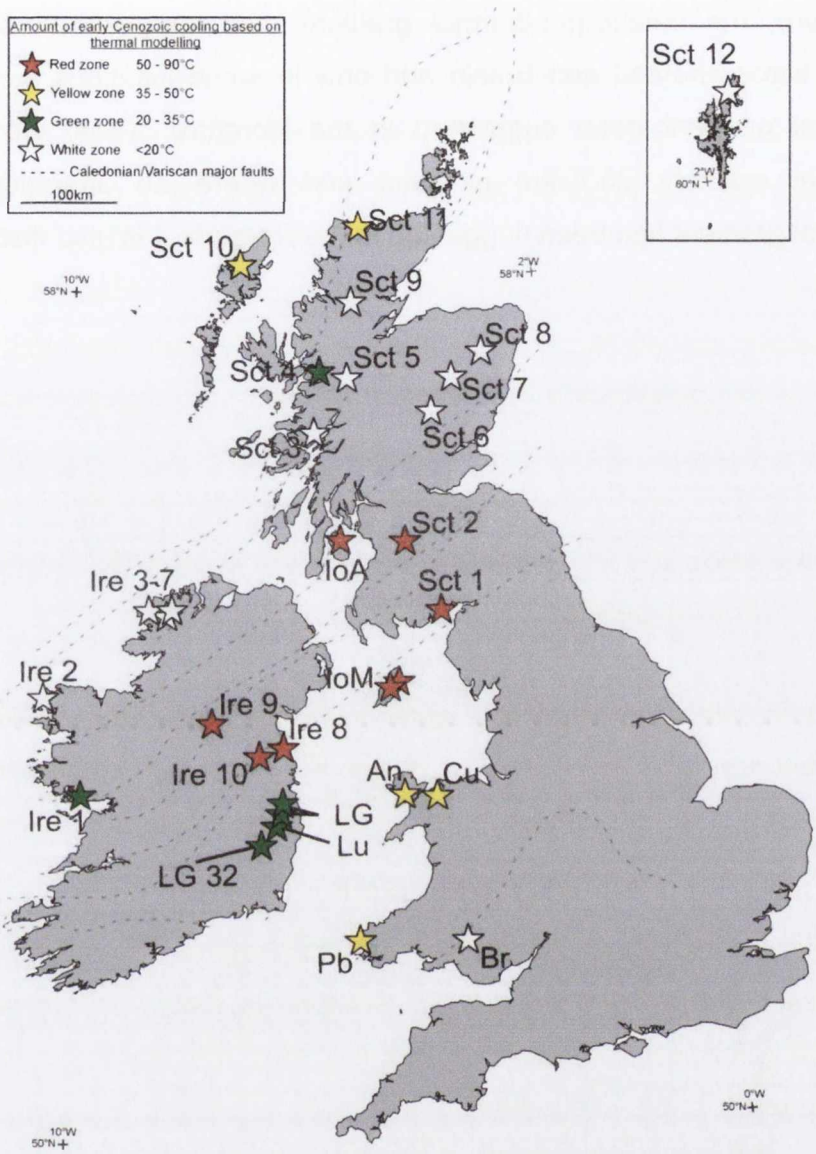


Figure 8.6: Map of Britain and Ireland with sample location coloured based on their amount of early Cenozoic cooling.

Assuming the modelled early Cenozoic cooling events represent phases of exhumation, then, the amount of exhumation for each sample and zone can be calculated using a paleo-geothermal gradient. For this study a paleo-geothermal gradient of 25°C/km was used. This gradient is only an assumption as the actual value for early Paleogene times is not measureable and might have varied through time. But, a suggested paleogeothermal gradient of 25°C/km for Ireland and Britain seems appropriate as it is neither an active rift zone, which commonly have a geothermal gradient of ~30°C/km and more, nor is an old craton with a relative low geothermal gradient of ~15°C/km.

Furthermore, the palaeo-geothermal gradient may have varied at different locations across Ireland and Britain and only in some locations has a paleo-geothermal gradient been suggested in the literature. Thus, the assumed geothermal gradient 25°C/km is used and where an alternative paleo-geothermal gradient has been suggested in the literature it is also discussed.

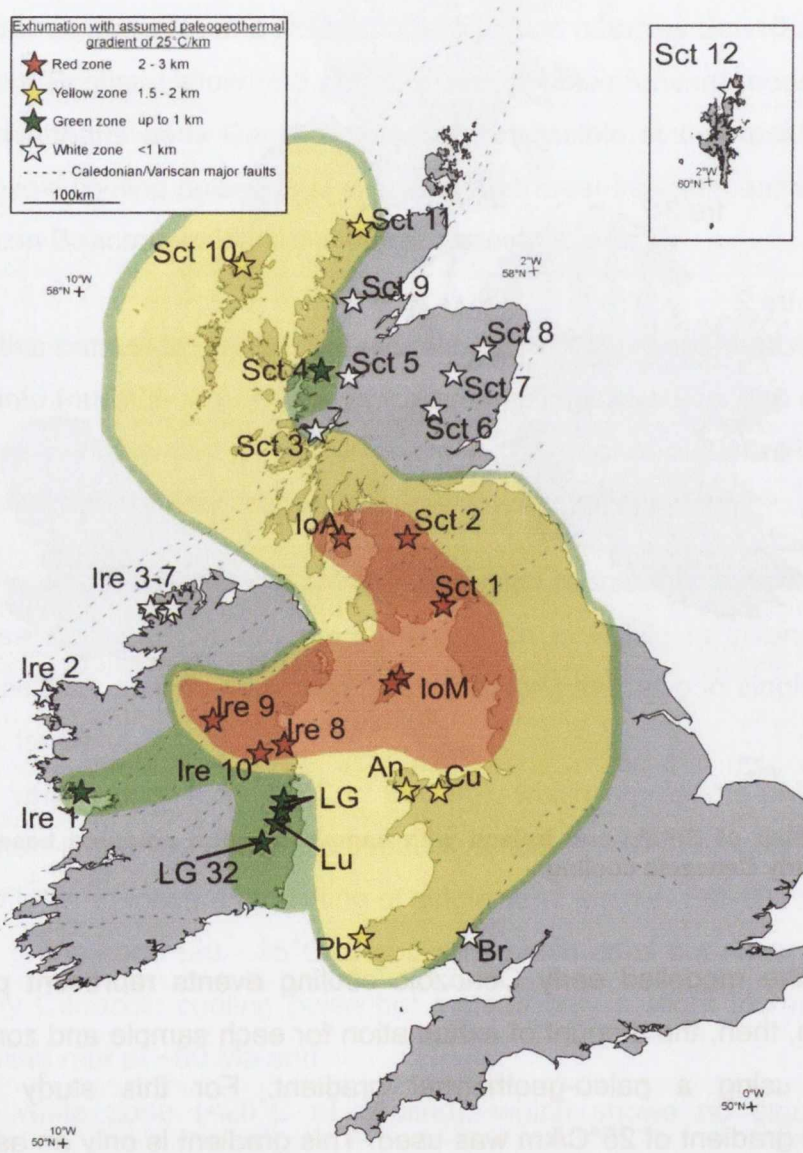


Figure 8.7: Proposed early Cenozoic exhumation map of Britain and Ireland with sample locations divided into three coloured zones based on their magnitude of exhumation. Exhumation is derived from modelled cooling events and an assumed paleo-geothermal gradient of 25°C/km.

8.4.1 Red zone exhumation

The red zone encompasses samples from southern Scotland and the Isle of Arran (Sct-1, Sct-2 and IoA), central east Ireland (Ire-8, Ire-9 and Ire-10) and the Isle of Man (IoM-1/2 and IoM-3). The zone is characterized by a distinct cooling pulse at ~60 Ma in the thermal history models, very young AHe ages generally around 60 Ma (Figure 8.8) and AFT ages from 299.1 ± 13.8 Ma (1σ) in the Midland Valley (Sct-2) to 50 ± 2.9 Ma (1σ) in central east Ireland (Ire-10) (excluding the Isle of Arran early Palaeogene Northern Granite). The samples from the red zone in Figure 8.7 are all single samples (sample IoM-1/2 are treated as a single sample due to the minor ~80 m difference in elevation), and show a sharp (~5 Ma in the thermal model; Figure 7.18) Early Cenozoic exhumation pulse, which is not visible in thermal history models from any other *single* samples in Ireland or Britain. In the samples from southern Scotland and central east Ireland, the exhumation event occurs at ~60 Ma, whereas at the Isle of Man the event occurs at ~80 Ma which is 10 to 20 Ma older than the other samples in this zone.

The largest amount of inferred exhumation is recognized in sample Sct-1 in the Southern Uplands of southern Scotland with up to ~3 km of exhumation at ~60 Ma calculated using the assumed paleo-geothermal gradient (Figure 8.7). Similar Cenozoic AFT ages and magnitudes of exhumation were reported in earlier fission track studies from the Pennines, the Lake District, Cheshire Basin and the East Irish Sea Basin (Pennines, Green, 1986; Cheshire Basin, Lewis et al., 1992; East Irish Sea Basin, Green et al., 1997 and Holford et al., 2005; Lake District, Green, 2002). However, previous studies based on vitrinite reflectance data (Green et al., 1997; Green, 2002) have shown that the Lake District and East Irish Sea Basin might have experienced a much higher paleo-geothermal gradient at ~60 Ma of 61°C/km and 50°C/km, respectively (Green, 2002; Holford et al., 2005b). Thus, the cooling from ~100°C to 10°C during early Paleogene in sample Sct-1 might be a combination of cooling due to exhumation and cooling from an elevated paleo-geothermal gradient to the present-day geothermal gradient (i.e. 33°C/km in the Cheshire Basin, Green et al., 1997). Assuming the elevated paleo-geothermal gradient proposed by Green et al. (2002) for the Lake District is applicable for the sample location of

Sct-1, then the amount of exhumation would be ~1.5 km during early Cenozoic. The range from 3 to 1.5 km is probably the upper and lower limit of exhumation for south-west Scotland.

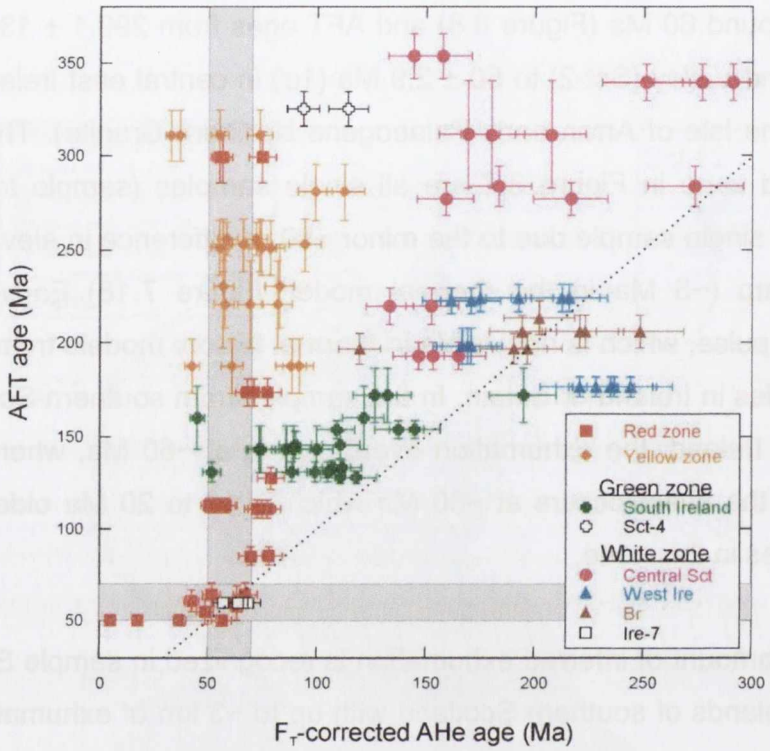


Figure 8.8: AFT (Ma) versus F_T-corrected AHe (Ma) plot divided into zones based on the intensity of early Cenozoic exhumation. The white zone is further divided into Scotland, west Ireland and the Brecon Beacons (Br) profile in Wales, to emphasize that each region (Ireland, Scotland and Wales) contains samples which do not show early Cenozoic exhumation. Ire-7 is considered separately because this sample did not experience early Cenozoic exhumation but thermal relaxation following the emplacement of a nearby Palaeogene dyke. Dashed line: AFT and AHe ages 1:1 ratio.

Sample Sct-2 in the Midland Valley in south Scotland exhibits ~2 km exhumation (Figure 8.7) using the assumed geothermal gradient of 25°C/km at ~60 Ma, which is smaller than in sample Sct-1 from the Southern Uplands calculated with the same assumed geothermal gradient.

The amount of Paleogene exhumation experienced by the Isle of Arran (IoA) granite is difficult to constrain due to its Paleogene intrusion age. However, the amount of exhumation can be predicted from the emplacement depth, which

was estimated to be 2 to 3 km by England (1992). Assuming the granite was emplaced in 2 to 3 km depth (England, 1992) and is now at the surface, the granite must have been exhumed by at least 2 to 3 km since emplacement. Since the thermal model indicates rapid cooling at ~60 Ma it is likely that the amount of early Paleogene exhumation is similar to the emplacement depth.

Samples from the Isle of Man (IoM) show slightly older AHe ages with a mean age of 77.4 Ma (F_T-corrected) compared to the rest of the samples in the red zone with a mean age of 54.2 Ma. If exhumation on the Isle of Man happened in a single event, then the amount of exhumation would be between 2.5 and 3 km, similar to Sct-1 in south Scotland or Ire-10 in central east Ireland (Figure 8.7). However, according to the thermal models (Figure 7.18), the exhumation event would have occurred at ~80 Ma and thus predates the early Cenozoic exhumation event seen in other locations in the red zone. Thus, to determine if this cooling pulse at ~80 Ma could be divided into two cooling events at ~100 and ~60 Ma, which would be in agreement with the rest of the thermal history models from the red zone, forward modelling was successfully applied to both samples from the Isle of Man (section 7.1.4).

This approach of separating one cooling event into two is viable as the Bayesian modelling approach of QTQt naturally prefers simpler solutions, and hence it is difficult for QTQt to resolve two separate cooling pulses which occur within a short period of time. Based on the results from the forward model, it is possible that the Isle of Man experienced two exhumation events during the mid- to late Cretaceous at 100 Ma and the early Cenozoic at 60 Ma, and that each pulse represents roughly 1.5 and 1.2 km of exhumation, respectively. However, is has to be emphasised that these two cooling pulses are derived from the forward model and thus, were manually constructed, and hence the actual magnitude of each exhumation pulse might be different. While the amount of exhumation on the Isle of Man in the two pulses is smaller than in other samples from the red zone at ~1.5 km, the total amount of exhumation on the Isle of Man is similar to south Scotland and central east Ireland, at between 2 to 3 km (Figure 8.7).

The samples in central east Ireland (Ire-8 to Ire-10) experienced exhumation of ~2 km (Figure 8.7) between 70 and 50 Ma, which is a similar magnitude compared with sample Sct-2 in the Midland Valley of Scotland. Only sample Ire-10 from a borehole in central east Ireland (1702 m depth) has experienced 2.5 to 3 km of exhumation which is more similar to Sct-1 in the Southern Uplands (Figure 8.7).

Assuming that the Isle of Man experienced two separate exhumation events, all samples in the red zone show a clear pulse of early Cenozoic exhumation with a magnitude of 2 to 3 km at ~60 Ma (Figure 8.7) which is contemporaneous with the emplacement of early Cenozoic igneous centres across Northern Ireland, Scotland, the Isle of Arran, the Irish Sea system and south to the Isle of Lundy in the Bristol Channel (Thorpe et al., 1990).

8.4.2 Yellow zone exhumation

The yellow zone comprises samples from Wales (Cu profile, samples An and Pb-1) and western Scotland (samples Sct-10 and Sct-11). This zone is characterized by a wide range in AFT ages from 187.7 Ma on Anglesey (An) to 311.0 Ma in western Scotland (Sct 11) compared to relatively young AHe ages with a mean age of 69.5 Ma (Figure 8.8).

Modelling the sample from Anglesey (An), Pembrokeshire (Pb) and the two samples from west Scotland (Sct-10 and Sct-11) does not show a distinctive early Cenozoic exhumation event as in the red zone. However, as shown in figure Figure 8.8, the AHe ages from the yellow zone overlap with the AHe ages from the red zone. The mean AHe age in the yellow zone is only about 10 Ma older than in the red zone (which yields an average AHe age of ~58.7 Ma). Nevertheless, the thermal history models from the red zone show a clear exhumation pulse at ~60 Ma which is not visible in the yellow zone.

In general, the AFT ages are older in the yellow zone compared to the red zone (Figure 8.8). However sample, Sct-2 in the red zone (from the Midland Valley of Southern Scotland) shows an old AFT age of 299.1 ± 13.8 Ma (1σ) which is

similar to the oldest AFT age in the yellow zone of 311 ± 13.2 Ma (1σ) from (sample Sct-11 in western Scotland). Since all samples in the red zone show very young AHe ages (~58.7 Ma) independently of their AFT age, which range from 50.0 ± 2.9 Ma to 299.1 ± 13.8 Ma (both at the 1σ level and excluding the Isle of Arran early Palaeogene Northern granite), it is a justified assumption that the AHe system can still record an exhumation event where the AFT ages are already, in some cases, insensitive. If the young AHe ages in the red zone represent an exhumation pulse, then it is likely that the young AHe ages in the yellow zone also represent the same exhumation pulse, even if the pulse is not visible in the thermal history models of single samples. Therefore, all samples in the yellow zone where an early Cenozoic exhumation event in the inverse thermal history models is absent, were forward modelled to test for the possibility of an exhumation event at 60 Ma. In both Wales and western Scotland, is it possible to construct forward models that show a clear cooling pulse at ~60 Ma.

The best-fit forward models yield a ~60 Ma cooling pulse from 40°C to 10°C for single samples from Anglesey (An) in north Wales and Pembrokeshire (Pb-1) in south Wales, which can be interpreted as representing ~1.5 km of exhumation at ~60 Ma. Sample Sct-10 from the Outer Hebrides cooled at ~60 Ma from 50°C to 15°C, which corresponds to ~1.2 km of exhumation with the assumed paleogeothermal gradient of 25°C/km, whereas at the same time, sample Sct-11 from the Northern Highlands experienced a much more distinct cooling pulse from 80°C to 20°C, which corresponds to ~2.5 km of exhumation. The much higher amount of exhumation of 2.5 km in sample Sct-11 during early Cenozoic times can be either related to the location of the sample within the Moine Thrust Zone (MTZ), which could indicate that this major fault was reactivated causing enhanced Cenozoic exhumation, or that the constructed forward model for Sct-11 is too simple with monotonic cooling from mid-Devonian (~390 Ma) to early Cenozoic times (~60 Ma). A more complex thermal history might reduce the amount of early Cenozoic exhumation needed to generate the same thermal history.

If the cooling pulses constructed in the forward models for Sct-10, Sct-11, An and Pb-1 are real, then the exhumation was likely smaller than in the red zone since the inverse models in QTQt were not able to resolve these cooling pulses. Hence, sample Sct-11 in western Scotland experienced closer to ~1.5 km exhumation rather than 2.5 km as a stronger exhumation event would probably be much more pronounced in the inverse thermal model and this is neither the case for the samples from western Scotland (Sct-10 and Sct-11) nor from Anglesey (An) or Pembrokeshire (Pb-1).

The Cu profile from Snowdonia, north Wales, shows a pronounced exhumation pulse at ~60 Ma of ~2 km and, hence, could be included in the red or yellow zone. However, modelling of *single* samples from the Cu profile reveals no clear exhumation pulse during early Cenozoic times (Figure 7.19). As example, sample Cu-2 from Snowdonia was modelled separately and shows a similar thermal history to the sample from Anglesey (An) in north Wales (see Figure 7.12 and description in section 7.1.5). Thus, single sample modelling (Cu-2) implies that the exhumation pulse in Snowdonia is not as pronounced as in the red zone (i.e. the northern margins of the Irish Sea system). Therefore, the Cu profile is assigned to the yellow zone, as the early Cenozoic exhumation event in the thermal history models requires a pseudo-vertical profile to recognize the early Cenozoic exhumation event. North Wales experienced ~2 km of exhumation at ~60 Ma based on this inverse model from Snowdonia (Cu profile). The Snowdonia profile is probably the best sample to account for the amount of exhumation in the yellow zone, as it is the only sample where exhumation is pronounced in the inverse model during Cenozoic times. Early Cenozoic exhumation estimates from the other samples from Wales and western Scotland were based on forward models, and thus the amount of exhumation is dependent on how the forward model was constructed.

Based on the forward models from west Scotland and Wales as well as the inverse model from Snowdonia, the assumed amount of exhumation in the yellow zone is 1.5 to 2 km during early Cenozoic times (Figure 8.7).

8.4.3 Green zone

The green zone consists of samples from south east Ireland (Lu profile, samples LG-17 to LG-19 and LG-32), sample Sct-4 in Scotland and sample Ire-1 from western Ireland (Figure 8.7). The AFT ages in this zone range from 172.3 ± 14.6 Ma to 127.4 ± 3.5 Ma (both 1σ) (excluding Sct-4 due to its very old AFT age of 325.0 ± 9.3 Ma) and the mean AHe age is 104.5 Ma (including Sct-4) (Figure 8.8). This zone therefore shows neither a clear early Cenozoic event like the red zone, nor Cenozoic AHe ages like the yellow zone.

The Lugnaquilla (Lu) profile, from the Leinster granite, (Figure 7.17) shows a cooling event from 80°C to 60°C between ~130 and 100 Ma for the lowest sample in the profile. The profile then remains at these temperatures until ~60 Ma, where it starts cooling again to present-day temperatures. This onset of increased cooling could indicate some degree of early Cenozoic exhumation similar to the red and yellow zone, but even when employing the profile modelling approach in QTQt, the event is not strong enough to cause significant amounts of early Cenozoic exhumation. Furthermore, this increased cooling occurs at the limits of the temperature sensitivities of the AFT and particularly the AHe systems, and is thus not well constrained.

Samples LG-17 to LG-19 and LG-32 are, like the Lu profile, located in south east Ireland (southern Leinster granite batholith) (Figure 5.1). Comparing the thermal history models shows that sample LG-17 indicate a cooling pulse at ~50 Ma, with samples LG-18 and LG-19 yielding a Neogene cooling pulse. Only sample LG-32 does not show a reheating and cooling pulse during Cenozoic times. However, Figure 8.8 shows that the AFT and AHe ages of these samples all plot within the same cluster within the green zone. Only sample Sct-4 shows a much older AFT age of 325.0 ± 9.3 Ma (1σ) and does not fall into this cluster Figure 8.8. Thus, it is likely that the samples experienced a similar thermal history as the Lugnaquilla profile, and indeed their late Mesozoic thermal histories are very similar (section 7.1.3, 8.3.1).

Determining the amount of early Cenozoic exhumation in the green zone is difficult, as all thermal models from this zone were already below 60°C and thus

cooler than the PAZ of the AFT dating method and at the temperature sensitivity limit the AHe method. The most reliable thermal history model to determine the amount of Cenozoic exhumation in the green zone is probably the Lugnaquilla profile (Figure 7.17), as the inverse modelling of a pseudo-vertical profile is better constrained than in a single sample (see section 1.2). At 60 Ma, the uppermost sample (i.e. lowest temperature sample) in the Lugnaquilla profile was already at 35°C, which means that the maximum total amount of early Cenozoic exhumation did not exceed ~1 km, assuming a paleogeothermal gradient of 25°C/km. Thus, it is possible that the green zone experienced up to 1 km of Cenozoic exhumation, but a stronger Cenozoic exhumation event is unlikely based on the available data set.

Interestingly, the samples from south-eastern Ireland are the only sample suite which show a positive correlation between FT-corrected AHe age and effective uranium content (eU) (Figure 8.9). Positive eU-AHe correlations are diagnostic of He trapping due to radiation damage for most thermal histories (section 3.3.5; Flowers et al., 2009).

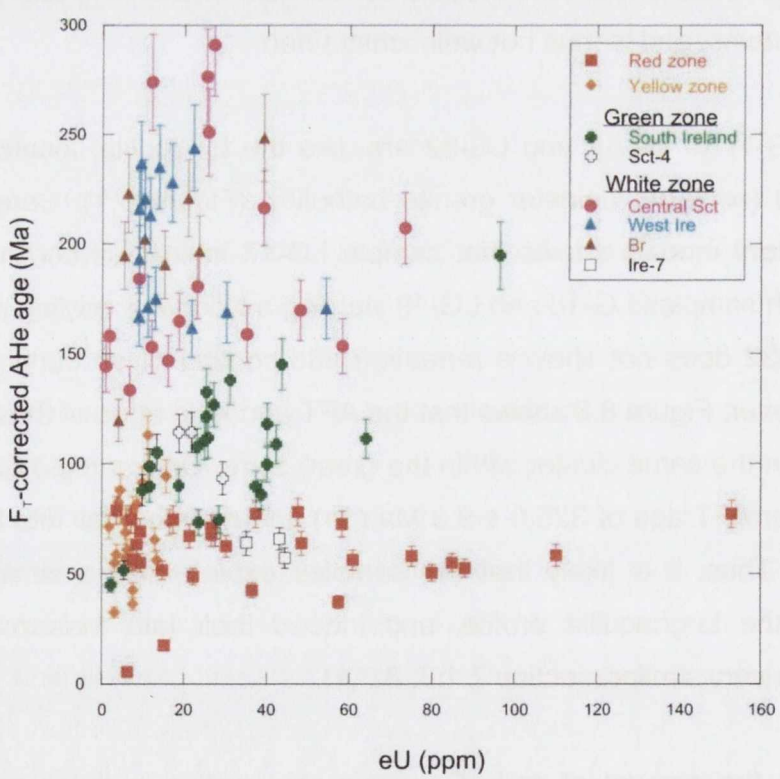


Figure 8.9: Single grain F_T-corrected AHe age (Ma) versus eU (ppm) plot.

Sample Ire-1 is from the Galway Granite on the west coast of Ireland and was sampled at an elevation of 165 m. Figure 8.8 shows that sample Ire-1 plots in the same cluster of AFT versus F_T-corrected AHe ages as the Leinster Granite samples from south-eastern Ireland. The AHe ages from Ire-1 have a mean value of ~86 Ma, which is similar to the lowest sample of the Lugnaquilla (Lu) profile with a mean value of ~85 Ma at an elevation of 126 m. Thus, a similar thermal history can be expected, but conducting a forward model shows that the predictions for an exhumation event at ~60 Ma are worse than the inverse model which shows an exhumation event at ~120 Ma. Thus, it is unlikely that Ire-1 experienced a significant early Cenozoic exhumation pulse, particularly when compared to samples in the yellow zone. Plotting the single grain ages from Ire-1 against grain radius Figure 8.10 shows some correlation between age and grain size but only if the smallest grain (~35 µm) is considered. Otherwise the grains are close together and above the average grain size. Therefore, it can be ruled out that the young AHe ages in Ire-1 are only derived from small AHe grains. The relatively young AHe ages and the similarity to the lowest sample in the Lugnaquilla profile means that some (up to 1 km) early Cenozoic exhumation cannot be definitively ruled out.

Sample Sct-4 is located in the Northern Highlands of Scotland, close to sample Sct-5 (Figure 5.1) and yields an AFT age of 325 ± 9.3 Ma (1σ) and AHe ages from 114.6 ± 9.2 to 93.6 ± 7.5 Ma (both 1σ). As shown in Figure 8.8, sample Sct-4 has a much older AFT age than the samples from southern Ireland but comparing the AHe age from Sct-4 with the other samples in Figure 8.8 shows that the AHe ages are comparable with samples from Snowdonia (Cu-3 AHe ages: 113 ± 9 Ma and 98.8 ± 7.9 Ma) in the yellow zone and samples from south-eastern Ireland including the Lu profile (mean AHe age of ~104.5 Ma). Unfortunately it was not possible to model this sample due to the low acceptance rate of the thermal history models as explained in chapter 7.1.1.1. Nevertheless it is included in the green zone as a potential location which may have experienced minor (up to 1 km) early Cenozoic exhumation at ~ 60 Ma, similar to the Lugnaquilla (Lu) profile.

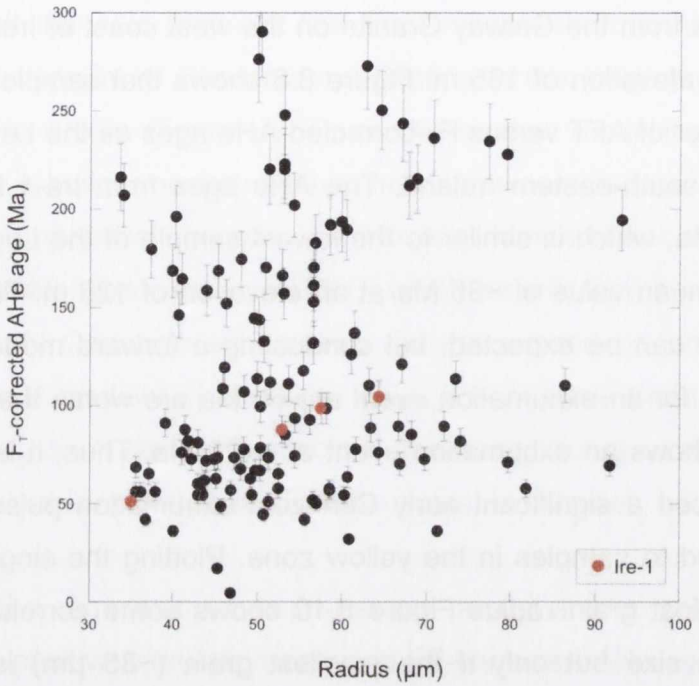


Figure 8.10: Sample Ire-1 compared to the bulk of the single grain F_T-corrected AHe ages (Ma) versus radius (µm).

8.4.4 Non-coloured study area (white zone)

The white zone encompasses samples from NW Ireland (Ire-2 to Ire-4 and Ire-7), central Scotland (Sct-3, Sct-5 to Sct-9 and Sct-12) and the Brecon Beacons (Br) profile in south Wales (Figure 8.7). This zone is characterized by relatively old AFT ages with a mean value of ~246 Ma, and AHe ages with a mean value of ~191 Ma (Figure 8.8) (excluding sample Ire-7 due to its proximity to a Paleogene dyke).

The white zone shows no evidence for early Cenozoic cooling and thus exhumation. There is also no indication that would suggest that an early Cenozoic exhumation event is "hidden" within the thermal history models, unlike the thermal history models from the yellow and green zone. This means, if early Cenozoic exhumation took place in this region, then the total amount of Cenozoic exhumation was not sufficient enough to affect AFT or AHe ages. Mass balance calculations of Paleogene submarine fans from the Northern North Sea Basins indicate less than 1 km of uplift for the East Shetland

Platform and the Scottish Highlands massif (Den Hartog Jager et al., 1993). This is in agreement with the AFT and AHe ages as less than 1 km of exhumation would not affect the AFT and AHe ages from the central Scottish Highlands. Only sample Ire-7 in NW Ireland shows cooling at ~60 Ma, but the sample is from the aureole of a Paleogene dyke (0.15 m; Bennett, 2006). The emplacement of the dyke reset the AFT and AHe systems, thus, cooling during early Paleogene at Ire-7 is not related to exhumation but thermal relaxation following the emplacement of the dyke. Thus, Ire-7 is included into the white zone despite falling into the ~60 Ma range of the red zone Figure 8.8.

Overall, the white zone shows no obvious sign of early Cenozoic cooling and therefore no pronounced exhumation event. However, less than 1 km exhumation may still have occurred, as recognized by mass balance calculations from the northern North Sea Basin (Den Hartog Jager et al., 1993), but the AFT and AHe dating methods are not sensitive enough to identify such small amounts of exhumation.

Comparing the proposed early Cenozoic exhumation with previously published AFT, AHe, compaction and subsidence models (Figure 8.11) reveal a similar pattern, however the interpretation is different. As shown in Figure 8.11, the red zone, highest amount of exhumation (2 – 3 km), overlaps with previously published focal point in the East Irish Sea Basin proposed by Jones et al. (2003). Furthermore, a compiled dataset by Hillis et al. (2008a) also matched closely with the proposed exhumation zones. However, there are some local differences for example in the Celtic Sea Basin (Figure 8.11). Persano et al. (2007) published AFT and AHe ages from western Scotland which do not match in magnitude with the proposed exhumation zones but the trend is similar show higher exhumation in the yellow zone than in the green/white zone. Previously published data from the west coast of Ireland (Cogné et al., 2014) shows no visible sign of early Cenozoic exhumation and thus matches the results from this thesis.

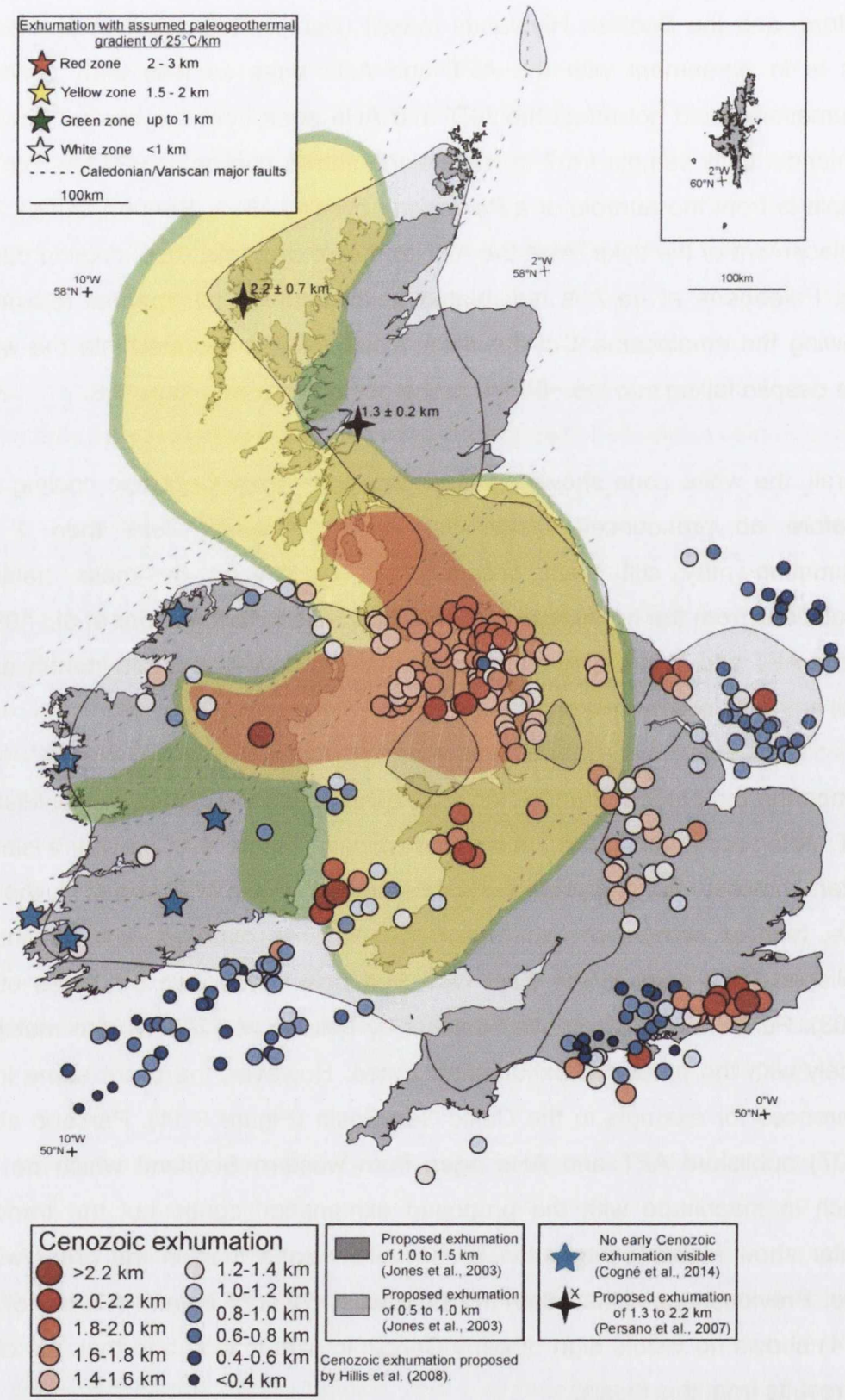


Figure 8.11: Proposed early Cenozoic exhumation divided into three zones based on magnitude of exhumation compared with results from previous studies.

8.5 Neogene cooling

The Neogene thermal history in Ireland and Britain is difficult to determine. There are no surface samples with AFT ages younger than 60.4 ± 2.0 Ma (1σ) (Sct-1), if the results from the Isle of Arran are excluded due to the low amount of counted grains and track lengths. Thus, the AFT ages cannot provide much useful information about the Neogene cooling history. The AHe ages show a larger range of young ages, ranging from the 5.2 ± 0.4 Ma age from the Ire-10 borehole (at a depth of 1702 m), but in general the AHe ages are not younger than early Paleogene in age (Paleocene to early Eocene). Thus, the AHe dating technique also struggles to resolve any potential Neogene cooling events.

Nevertheless, many thermal models from Ireland (LG-17 to LG-19, LG-32, Ire-1, Ire-3, Ire-4, Ire-9 and Ire-10), Scotland (Sct-1, Sct-3, Sct-5 and Sct-8), Wales (Br profile) and the Isle of Man (IoM-3) show a reheating event during the Paleogene, and a subsequent cooling pulse to present-day temperatures. In some models, the reheating event is very pronounced, with a magnitude of up to nearly 40°C (i.e. LG-17 and Sct-3). Only samples LG-17 and Sct-3 reached temperatures of 60°C during the reheating event in the Paleogene and Neogene, respectively, but no samples significantly exceeded 60°C and passed entirely into the PAZ. Samples Ire-2, Ire-4, LG-32 and IoM-3 exhibit only small amounts of reheating (up to 10°C in the mean expected model), while sample Ire-8 shows a change in the shape of the credible interval which could indicate some amount of reheating during the Paleogene/Neogene but still exhibits constant cooling in the mean expected model.

The thermal models from Anglesey (An) in north Wales and samples Sct-6, Sct-7, Sct-9 to Sct-12 from Scotland show monotonic cooling throughout Cenozoic times and only a slight increase in the cooling rate during the Neogene, but this may be related to the fact that the samples are forced to be at 10 ±10°C at present-day and in fact does not represent an actual cooling pulse. The 10°C present-day surface temperature for Ireland and Britain is only an approximation as the global mean temperature is ~15°C. However, Ireland and Britain are situated at around ~55°N so it is likely that the mean temperature is lower than 15° C.

Samples Pb-1 from Wales, Sct-2 in south Scotland and the Lu profile in Ireland all show some cooling at ~60 Ma or an increased cooling rate (Lu profile), and then exhibit monotonic cooling to present-day temperatures from 60 Ma. A similar thermal history with a cooling pulse before 60 Ma and at ~60 Ma is visible in IoM-1/2 from the Isle of Man, the Isle of Arran profile (IoA) and in the Cu profile in north Wales. However, these three locations reach close to present-day temperatures already between ~70 to ~60 Ma and remain at this temperature until the present-day.

Comparison of all the thermal history models for Neogene cooling shows no real spatial trend. Samples from all geographical regions, Ireland, Wales and Scotland, show both a reheating and cooling event as well as monotonic cooling in the Cenozoic. The same is true for samples which showed early Cenozoic exhumation. Samples Ire-9 from central east Ireland and Sct-1 from southern Scotland in the red zone (i.e. enhanced early Cenozoic cooling) show a Paleogene/Neogene reheating and cooling event, whereas the Cu profile from the yellow zone and the Isle of Man (IoM-1/2) from the red zone which again had experienced significant early Cenozoic exhumation do not show a reheating event during Paleogene/Neogene. Thus, there is no correlation between samples that experienced early Cenozoic cooling and Neogene cooling or vice versa.

The main spatial trend in the Neogene exhumation pattern is that the majority of the Irish samples tend to show a Neogene pulse which is supported by AFT and AHe thermal models from Cogné et al. (2014) who proposed a final pulse of Neogene cooling for the west coast of Ireland, probably related to compression at the plate margin and, possibly, enhanced erosion linked to Pleistocene glaciation.

On the other hand, the majority of Scottish samples tend to show monotonic cooling and no final Neogene exhumation pulse. Interestingly, the three samples from central Scotland that show a Paleogene/Neogene reheating and cooling event are samples Sct-3, Sct-5 and Sct-8 which are the lowest elevation samples in central Scotland (from 190 m for sample Sct-3 to 230 m for sample

Sct-5). However, this is not the case for the samples Sct-10 and Sct-11 in western Scotland which are at low elevations of 45 and 30 m respectively, and show only an increased cooling rate during the Cenozoic. However, all thermal models with Paleogene/Neogene reheating and cooling are cooler than the apatite PAZ and only enter the uppermost (i.e. lowest temperature) portion of the AHe temperature-sensitivity window (the PRZ). Hence all models are not well constrained and it is difficult to determine if the Neogene cooling is an actual exhumation event or just an artefact related to the modelling process (Gunnell, 2000; Redfield, 2010).

8.6 Causes for early Cenozoic exhumation

The analysis of the thermal history models from Ireland and Britain shows a clear exhumation event focused around the Irish Sea system during early Cenozoic times (Figure 8.12). The highest amount of exhumation of up to 3 km with an assumed paleogeothermal gradient of 25°C/km is recognized in the northern part of the East Irish Sea Basin (Figure 8.12a) and decreases to the north, south and west. As explained in chapter 1, the timing, magnitude and spatial distribution of early Cenozoic exhumation in Ireland and Britain, and particularly the Irish Sea region, remains highly contentious but focuses on two competing hypotheses.

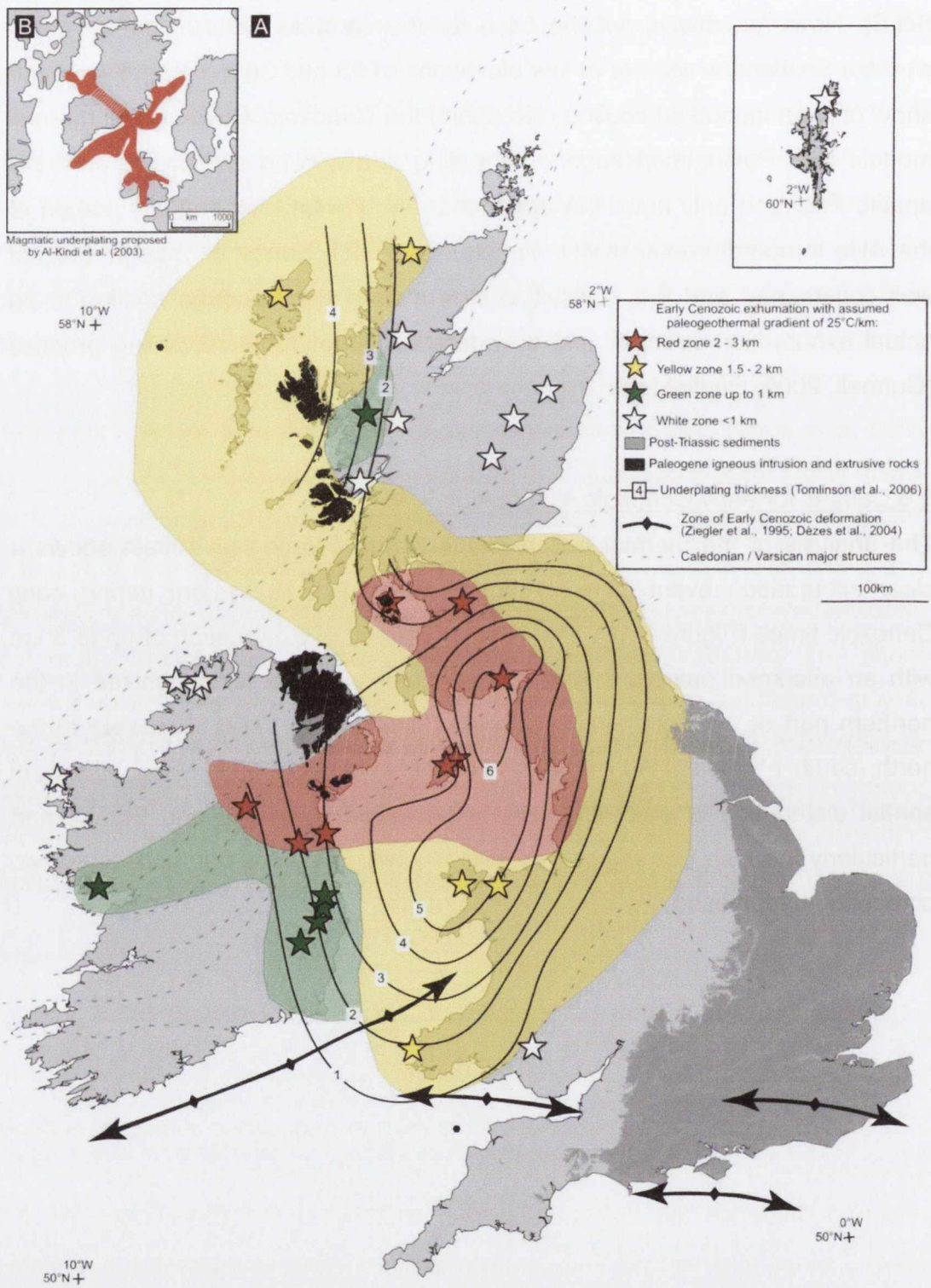


Figure 8.12: Map of Ireland and Britain showing focused early Cenozoic exhumation colour-coded according to the inferred magnitude of the exhumation pulse. The locus of early Cenozoic exhumation is compared with the postulated zone of magmatic underplating as proposed by Al-Kindi et al. (2003) and Tomlinson et al. (2006).

The first hypothesis is based on far-field stress originating from the opening of the Atlantic Ocean, the collision of the African and Eurasian plate or both, respectively (Figure 1.1) (i.e. Cloetingh et al., 1990; Lewis et al., 1992; Ziegler et al., 1995; Green et al., 2001a; Doré et al., 2002; Green et al., 2002; Holford et al., 2005b; Hillis et al., 2008a; Holford et al., 2009b). The second hypothesis links early Cenozoic exhumation with mantle-driven processes associated with the development of the proto-Iceland mantle plume, including magmatic underplating, the isostatic response associated with mechanical erosion or thinning of the lithosphere, or dynamically-supported uplift (Figure 1.2; i.e. White and Lovell, 1997; Jones et al., 2002; Al-Kindi et al., 2003; Jones and White, 2003; Arrowsmith et al., 2005; Davis et al., 2012).

The main arguments in favour for the far-field stress hypothesis are based on Cenozoic inversion events seen in the offshore basins, and predicts a variable spatial and temporal (i.e. throughout the Cenozoic) exhumation pattern of varying magnitude (see section 1.3 and 1.5 as well as Figure 1.5a for further details) across Ireland, Britain and their offshore basins (i.e. Holford et al., 2005b; Hillis et al., 2008a). On the other hand, exhumation associated with mantle-driven processes would lead to a ~60 Ma exhumation event focused on the postulated position of the mantle activity (see chapter 1.4 for further details) on the Irish Sea region (i.e. Jones et al., 2001).

8.6.1 Far-field stress hypothesis

The focused exhumation pattern evident in Figure 8.12a is not compatible with a spatially and temporally variable exhumation and localized inversion pattern associated with compressional far-field stress which has been proposed by several authors for the Irish Sea system (Holford et al., 2005b; Hillis et al., 2008a). Thus, it is unlikely that compressional far-field stress was the primary cause for early Cenozoic exhumation. The exhumation pattern seen in Figure 8.12a is not linked with any major faults which would most likely have been reactivated during compressional stress. However, some local fault reactivation must have occurred, which is evident in Northern Ireland where the late Paleogene Mourne Mountains granite (~56 Ma; Gamble et al., 1999) is now at

the surface and in close proximity (~15 km) to the early Paleogene Antrim Lava Group (62.6 – 59.6 Ma; Ganerod et al., 2010). Assuming a similar emplacement depth for the Mourne Mountains granite as for the Isle of Arran granite, the southern part of Northern Ireland must have experienced 2-3 km of exhumation since the emplacement of the Mourne Mountains granite. In contrast, the older Antrim Lava Group (between 62.3 – 59.6 Ma; Ganerød et al., 2010) only experienced between ~0.7 to ~1.2 km of exhumation, based on burial depth estimates from the Upper Cretaceous limestones overlain by the Antrim Lava Group (Maliva and Dickson, 1997). Differential exhumation of a depth of ~1.8 to ~2.3 km across the short (~5-10 km) horizontal distance separating the two units strongly suggests faulting as a mechanism (fault zone of the Southern Upland Fault; Figure 2.4), although flexural doming as a result of the Mourne Mountains granite intrusion cannot be excluded.

Compiled AFT, VR and compaction data for southern England suggest multiple small-scale (less than 10 km apart) phases of exhumation with magnitudes of up to ~1 km during the Cretaceous, Paleogene and Neogene (Hillis et al., 2008a). Hillis et al. (2008a) argue that variable small-scale exhumation would be inconsistent with a first-order scale exhumation event related to a mantle-driven processed associated with the proto-Iceland mantle plume. However, recent studies have shown that also plume-related exhumation can cause small-wavelength exhumation patterns. These short-wavelength exhumation patterns can be driven by dynamic supported uplift which can cause relatively localised upwelling arising from small density anomalies in the upper mantle (Braun, 2010), or due to interaction between the plume and lithosphere (Burov and Cloetingh, 2009). The latter can cause mechanical erosion of the plate and reduce the stress needed for folding due to thermal and structural weakening of the lithosphere (Burov and Cloetingh, 2009). Modelling suggest that these effects can cause mantle plume-related exhumation on a much smaller wavelength (even less than 100 km) than previously assumed (typically on the order of ~1000 km; Burov and Cloetingh, 2009).

The exhumation in Britain and Ireland is also not restricted to areas of known Cenozoic shortening (Figure 8.12a), for example the Wessex/Weald Basin, the

South Celtic Sea Basin, the St George's Channel Basin, the Sole Pit Basin, and the Moray Firth Basin (Van Hoorn, 1987a; Dèzes et al., 2004; Mackay et al., 2005; Williams et al., 2005). Additionally, the total amount of Cenozoic shortening expected to cause between 1 to 3 km of exhumation is on the order of 130 to 230 km shortening across Britain and Ireland (>1000 km distance; White et al., 2013). In the southern Ireland and Britain, most basins such as the Wessex/Weald Basin, the South Celtic Sea Basin and the St. George's Channel Basin have experienced only ~4 km shortening over a distance of ~200 km (Blundell, 2002). Even if the amount of shortening is doubled to 8 km, by assuming that half the shortening is concealed in small-scale deformation, accommodated by shear-stress in soft sediments (White et al., 2013) or by reverse displacement and subsequent removal of evidence for inversion by later erosional phases (Holford et al., 2009c), then the amount of Cenozoic shortening would be at least an order of magnitude (i.e. ten times) too small to cause the observed amount of exhumation of between 1 to 3 km (White et al., 2013).

If exhumation was controlled by compressional far-field stress which caused localized and variable Cenozoic exhumation and inversion, then where exhumation is reduced or absent, the development of small-scale Cenozoic sedimentary traps would be expected. Furthermore, deposition of the eroded material in the nearest offshore basin would be likely, which is seen in the Mesozoic history of the offshore basins and the thermal history models derived from the adjacent uplifting onshore massifs. However, the East Irish Sea Basin does not contain any Cenozoic sediments (Shannon and Naylor, 1998), while the Cenozoic successions in the Central Irish Sea Basin, St. George's Channel Basin and the Celtic Sea Basin only reach thicknesses of up to 1 km. The absence of Cretaceous and Cenozoic rocks in the Irish Sea Basin requires a regional-scale exhumation event which cannot be explained by localized exhumation associated with variable compressional far-field stress during early Cenozoic times. Given the exhumation pattern displayed in Figure 8.12a, it is clear that exhumation is focused around the Irish Sea system. While compressional far-field stress might have caused some small-magnitude,

localized exhumation, it is clearly not the primary cause for Cenozoic exhumation.

8.6.2 Mantle-driven exhumation

If tectonic processes such as compression or extension are not responsible for the early Cenozoic exhumation in Ireland and Britain, then it is likely that exhumation is linked with mantle-driven processes such as dynamic supported uplift, isostatic response to thinning of the lithosphere or magmatic underplating (see chapter 1.4). Several studies have suggested that the early Cenozoic exhumation in Ireland and Britain is related to mantle-driven processes originating from the proto-Iceland mantle plume (White and Lovell, 1997; Jones et al., 2002; Al-Kindi et al., 2003; Jones and White, 2003; Arrowsmith et al., 2005; Tomlinson et al., 2006; Davis et al., 2012).

Most studies which have postulated the presence of the proto-Iceland plume underneath the Irish Sea region have employed geophysical, subsidence or sedimentological studies (see Figure 8.12b and correlation of clastic fan systems with exhumation; see chapter 2.5) whereas AFT and vitrinite reflectance (VR) data have usually been used to support the compressional far-field stress hypothesis (see chapter 2.4). However, Persano et al. (2007) employed AFT and AHe dating on two pseudo-vertical profiles from the Outer Hebrides and the Central Highlands of Scotland respectively. Their results suggest an early Cenozoic (~60 Ma) exhumation pulse which they linked with magmatic underplating. A more recent AFT and AHe study by Cogné et al. (2014) from western Ireland does not show any early Cenozoic cooling pulse. However the western coast of Ireland is situated outside the proposed area of early Cenozoic exhumation as seen by the thermal history models from samples Ire-1 to Ire-4 in this study (Figure 7.14).

The pattern of early Cenozoic exhumation in this study (Figure 8.12a) is in good agreement with previously published exhumation patterns from subsidence analysis (Jones et al., 2002) as well as the distribution of crustal underplating deduced from the locations of free-air gravity anomalies (Arrowsmith et al.,

2005) and seismic receiver function analyses (i.e. Tomlinson et al., 2006). All these studies support the hypothesis of mantle-driven exhumation in Ireland and Britain caused by the proto-Iceland mantle plume.

Today, the Iceland mantle plume is situated beneath eastern Iceland but reconstructions of relative plate motions indicate that the proto-Iceland mantle plume was situated beneath Greenland at ~60 Ma (Figure 8.12b) (Lawver and Müller, 1994). This plate reconstruction is supported by the simultaneous emplacement of igneous rocks on the NW and SE margins of the Greenland craton (Ganerød et al., 2010), across the Rockall Trough (Archer et al., 2005) and in western Scotland, Northern Ireland and into the Irish Sea region (Figure 8.12a). The latter are part of the British Irish Paleogene Igneous Province (BIPIP) which was emplaced between ~63 and 55 Ma (Chambers et al., 2005). $^{3}He/^{4}He$ ratios in olivine from the Skye Lava Field basalts, a component of the BIPIP, are up to 22 times higher than the normal atmospheric ratio, which suggests an origin from a deep-seated mantle source such as a plume, even though the plume head was beneath Greenland during the emplacement of the BIPIP (Stuart et al., 2000). The BIPIP follows a path from the Rockall Trough, along the western margin of Scotland from St. Kilda, the Outer Hebrides, Skye, Isle of Mull, Isle of Arran, the Antrim Lava Group and the Mourne Mountains in Northern Ireland, the Fleetwood dyke swarm (K-Ar whole rock ages: 65.5 ± 1.0 to 61.4 ± 0.8 Ma; Arter and Fagin, 1993; Jackson et al., 1995) in the East Irish Sea Basin and the Lundy granite in the Bristol Channel (Figure 2.8 and Figure 8.12a). Furthermore, NW-SE trending Paleocene dykes are also found in NW Ireland and in southern Scotland (Figure 1.1).

Comparing the above mentioned studies, the path of the BIPIP and the exhumation pattern revealed in this study, it is likely that the proto-Iceland mantle plume, situated beneath Greenland at ~60 Ma, extended laterally to the NW and SE edges of the Greenland craton. The Greenland craton is strong and thick, and weak zones in the base of the lithosphere (i.e. lithospheric-scale detachments or portions of thinner lithosphere), likely facilitated "fingers" of hot mantle material to travel south from the plume head beneath Greenland following the path as described for the emplacement of the BIPIP (Figure 8.12b;

Al-Kindi et al., 2003) into the Irish Sea region where the focus of early Cenozoic exhumation took place.

Al-Kindi et al. (2003) analysed wide-angle seismic profiles across the Iapetus Suture and imaged a ~6 km thick high-velocity zone which they interpreted as a zone of magmatic underplating beneath the Irish Sea region. Based on this profile, Tomlinson et al. (2006) developed contour lines for the zone of magmatic underplating derived from receiver-function modelling. Their contoured map shows a maximum thickness of 7 km magmatic underplating beneath the northern part of the East Irish Sea Basin system, which is in good agreement with the maximum amount of exhumation recognized in this study (Figure 8.12a) (up to 3 km at Sct-1 on the Southern Uplands). Furthermore, several studies suggest that the injection of hot melt occurred in pulsed cycles (i.e. White and Lovell, 1997; Al-Kindi et al., 2003) which would explain the periodicities in the deposition of clastic fans in the offshore basins, especially in the East Shetland Basin (Thomas and Coward, 1995) and the Porcupine Basin (White and Lovell, 1997).

Several studies have suggested that transient dynamically-supported uplift caused by the presence of a hot convective sheet in the upper asthenospheric mantle may have been the dominant form of Early Cenozoic uplift on this segment of the NW European margin. Jones et al. (2002) analysed the present-day dynamically-supported uplift around Iceland and its surrounding areas to infer the amount of dynamically-supported uplift caused by the proto-Iceland mantle plume. Today, the Iceland plume causes 1.5 to 2 km dynamically-supported uplift around Iceland and ~0.5 km on the NW European shelf (e.g. Ireland and Britain). Similar amounts are inferred for the proto-Iceland mantle plume and its effect on Ireland and Britain during early Cenozoic times. Recent analysis from p-wave anomalies beneath the Irish Sea region show a low-velocity zone in the mantle (~120 to 160 km depth; Arrowsmith et al., 2005) which correlates with a long-wavelength gravity high. This is interpreted as a present-day "finger" of low-density (hot) asthenosphere originating from the modern Iceland plume and thus causing some dynamically-supported uplift in the Irish Sea region (Arrowsmith et al., 2005; Rickers et al., 2013). These

studies suggest that a similar hot convective sheet in the upper asthenospheric mantle could have caused the early Cenozoic exhumation event around the Irish Sea region (Davis et al., 2012). It is not possible to discriminate between magmatic underplating, dynamically- supported uplift or the isostatic response to mechanical erosion of the lithosphere given the resolution of the AFT and AHe methods. All mechanisms are plausible and as explained in chapter 1, usually more than one process is active at once.

On a more regional scale, the outcrop pattern of post-Triassic sedimentary rocks on a geological map of Britain and Ireland suggest a south-east directed tilting of Britain during early Cenozoic times (Figure 2.8 and Figure 8.12a) (Cope, 1994). Furthermore, post-Cretaceous drainage systems and the heavy mineral assemblage of Paleogene sands in the Hampshire Basin indicate transport from Scotland to the south-east, which implies that NW of Britain was being uplifted relative to the south-east (Morton, 1982; Cope, 1994).

Overall, the early Cenozoic exhumation map created from the thermal history models is in good agreement with previously published maps for magmatic underplating, the path across Northern Britain and Ireland of the BIPIP and the south-east tilting of Britain and its drainage patterns. This strongly suggests that exhumation was caused by a mantle-driven process and not compressional far-field stress.

8.7 Early Cenozoic deposition centres

As explained above, small-scale exhumation events would most likely lead to deposition of sediments in the respective adjacent offshore basin or to the development of sedimentary traps of early Cenozoic age. However, the Irish Sea Basin system contains no younger sediments than early Jurassic in the East Irish Sea Basin and the Solway Firth Basin (Shannon and Naylor, 1998). To the south, the Central Irish Sea Basin, St George's Channel Basin and the Celtic Sea Basin only contain up to 1 km of Cenozoic sediments and the oldest Cenozoic rocks are Eocene successions in the St. George's Channel Basin (Williams et al., 2005). This indicates that the whole Irish Sea Basin system was

subject to exhumation during the early Paleogene, and no sediments were deposited. This large-scale exhumation is in contradiction to the proposed small-scale variations in exhumation in the far-field stress hypothesis (Hillis et al., 2008a). The sediment had to be transported further away into the offshore basins to the south of Britain and Ireland, such as the western Irish Atlantic margin (the Porcupine and Rockall basins) and the North Sea (Figure 1.3), which makes mass balance calculations more challenging.

The basins to the south of the Irish Sea region cannot account for the amount of early Cenozoic exhumation proposed for the Irish Sea Basin system (Figure 1.3). The Celtic Sea Basin only contains up to 1 km of Cenozoic sediments (Robinson et al., 1981), the St. George's Channel Basin only locally up to 1 km (Tappin et al., 1994; Williams et al., 2005) and the Bristol Channel Basin only contains a scattered Cenozoic sedimentary record and up to ~1 km of early Cenozoic exhumation is reported by previous AFT studies (Glen et al., 2005; Holford et al., 2005b). Additionally, Williams et al. (2005) suggested between ~1 and 1.5 km of exhumation for the St. George's Channel Basin during early Cenozoic times which could explain the relatively small amount of Cenozoic sediments.

The largest depocentres of Cenozoic rocks are located in the western Irish offshore basins - the Porcupine and Rockall basins. The Rockall Basin contains up to 6 km (Haughton et al., 2005) and the Porcupine Basin up to 7 km (Croker and Klemperer, 1989) of Cretaceous and Cenozoic sediments. The Porcupine Basin also shows a clear change from basin-wide carbonate to clastic sedimentation during the late Cretaceous to early Paleogene (Shannon, 1992). Besides the uplift of the Porcupine High, the clastic sediments could have been derived from the exhumed Irish Sea region by sediment transport routing systems passing from the Irish Sea into the western Irish offshore basins probably via the Paleo-Shannon. A Paleo-Shannon river system would explain how sediments from the Irish Sea region could be transported into the western Irish offshore basins as significant (i.e., >0.5-1.0 km depth) early Cenozoic exhumation is absent on the west coast of Ireland.

The Rockall Basin is located to the NW of the Irish massif and the Irish Sea region. It contains up to ~6 km of Mesozoic and Cenozoic sediments (Haughton et al., 2005). The sedimentological evolution is poorly understood due to the limited amount of boreholes in the Rockall Basin (Haughton et al., 2005), but it is possible that the Rockall Basin served as a depocentre during early Cenozoic times as shown by mass balance calculations (Jones et al., 2002). The North Channel between Northern Ireland and Scotland does not contain any Cenozoic sediments, but could have functioned as a sediment routing system between the uplifted source area in the Irish Sea region and Cenozoic depocentres in the Rockall Trough.

In northern England (e.g. the Lake District and the Midland Shelf), it is likely that most of the eroded sediments during the early Cenozoic were Cretaceous chalk, Jurassic shales and Carboniferous limestones, which would explain the lack of clastic sediments in the adjacent offshore basins (Den Hartog Jager et al., 1993). In particular there are no early Cenozoic submarine fans in the southern North Sea which suggests a lack of siliciclastic input during the early Cenozoic (Den Hartog Jager et al., 1993).

On the other hand, mass balance calculations from Paleogene submarine fans in the northern North Sea suggest less than 1 km of uplift of the East Shetland Platform and the Scottish Highlands occurred (Den Hartog Jager et al., 1993). Holford et al. (2010) suggested multiple phases of exhumation in NW Scotland at 65 - 60 Ma, 40 - 25 Ma and 15 - 10 Ma. Their event summary shows reheating during the Cenozoic and Neogene of up to 90°C and ~75°C, respectively. However, in this study, the thermal history models from northern Scotland do not support multiple phases of Cenozoic exhumation. Additionally as the far more thermally-sensitive AHe dating technique was employed in this study (in contrast to Holford et al., 2010), reheating to ~90°C is unlikely as the AHe dating would yield much younger ages than is detected for most parts of the Scottish massif. In fact, with the exception of the forward models in Sct-10 and Sct-11, none of the samples in this study north of the Highland Boundary Fault show any clear sign of Cenozoic cooling. Additionally, Paleocene/Eocene sequences in the Northern North Sea show only a small number of submarine

fans after ~52 Ma, which indicates only small amounts of exhumation during the Eocene and younger (Den Hartog Jager et al., 1993).

9. Conclusions

The goal of this thesis is to investigate the Mesozoic and early Cenozoic exhumation history of Ireland and Britain. The debate about the exhumation history has focussed mainly on two competing hypotheses: i) exhumation caused by mantle-driven processes associated with the development of the proto-Iceland mantle plume (Figure 1.2) (i.e. White and Lovell, 1997; Jones and White, 2003; Tiley et al., 2004; Persano et al., 2007), and ii) exhumation related to compressional forces associated with the effects of the opening of the North Atlantic Ocean and the Alpine collision (Figure 1.1) (Ziegler et al., 1995; Green et al., 2002; Holford et al., 2005b; Japsen et al., 2007; Hillis et al., 2008a; Holford et al., 2009b). The main difference between these two hypotheses is their spatial and temporal exhumation pattern. Exhumation related to mantle-driven processes would yield an asymmetric dome-like structure centred on the Irish Sea region at ~60 Ma (Al-Kindi et al., 2003; Jones and White, 2003), whereas exhumation associated with compressional stress would result in spatially and temporally variable late Cretaceous to Neogene exhumation (Ziegler et al., 1995; Green et al., 2002; Holford et al., 2005b; Japsen et al., 2007; Hillis et al., 2008a; Holford et al., 2009b).

Therefore, in this thesis a combination of AFT and AHe dating was employed to distinguish between these two hypotheses. Both techniques have the advantage that they can be applied in the absence of strata straddling the time of exhumation as is the case for the Irish Sea region, where onshore Cenozoic rocks are sparse to non-existent. The AFT and AHe results were subsequently modelled in the software package QTQt (Gallagher, 2012).

Sample locations were selected to include the region putatively affected by the Proto-Iceland mantle plume along with neighbouring regions, so that the limits of a possible plume-related Cenozoic exhumation could be determined. The sample area encompasses the region around the Irish Sea and extended into Wales, central and western Ireland and Scotland. Where possible, pseudo-vertical profiles were taken to improve the thermal history modelling.

Overall, 47 samples were analysed for AFT and AHe dating, including four pseudo-vertical profiles (Snowdonia (Cu), Brecon Beacons (Br), Isle of Arran (IoA) and Lugnaquilla (Lu); Figure 5.1). The AFT results show a large variation in age from 43.3 ± 5.8 Ma (1σ) on the Isle of Arran (IoA-3) to 353.6 ± 12.1 Ma (1σ) in central Scotland (Sct-6) (Figure 7.1). Out of a total of 272 AHe single grain analysis 110 were used for modelling spread across the 43 samples (excluding the Lu profile grains for the broken grain analysis). The AHe age range from 3.9 ± 0.3 Ma (1σ, uncorrected) in eastern Ireland (Ire 10) to 226.3 ± 18.1 Ma on Shetland (Sct-12) and from 5.2 ± 0.4 Ma (1σ, F_T-corrected) (Ire-10) to 290.9 ±23.3 Ma in central Scotland (Sct-9).

9.1 Paleozoic and Mesozoic exhumation

The thermal history modelling reveals different phases of cooling in the thermal history of Britain and Ireland from the early Paleozoic through to Cenozoic times. The Paleozoic cooling events are associated with the Caledonian and post-Caledonian exhumation across Scotland and the Snowdonia (Cu) profile in Wales. The forward models from Anglesey (An) and Pembrokeshire (Pb-1) also allow for a possible Acadian (~405 - 390 Ma; Woodcock et al., 2007) exhumation pulse similar to the Snowdonia profile, but the inverse models prefer a post-Variscan exhumation event (~300 Ma to ~260 Ma).

The time period from ~360 Ma to 310 Ma can be considered a relatively quiescent tectonic setting, with reburial during Carboniferous times in Ireland and northern England (the Pennine Basin), the Devon-Cornwall Basin in Southern England and the Midland Valley of Scotland. This is shown by the thermal history model of sample Sct-2 from the margins of the Midland Valley/Southern Uplands zone in southern Scotland which shows reheating between ~360 to ~310 Ma (Figure 8.3) which is attributed to the deposition of Carboniferous rocks in the Midland Valley associated with Carboniferous dextral transtension and associated emplacement of alkali volcanics (Woodcock and Strachan, 2012). Furthermore, the late Devonian sandstone profile from the Brecon Beacons (Br) which shows reheating between ~360 to ~280 Ma (Figure 8.3) which is compatible with the bituminous to anthracite rank

of Carboniferous coals in the adjacent South Wales coalfield (Bevins et al., 1996).

The thermal models reveal a complex late Permian to mid-Cretaceous cooling history which lasted over 160 Ma. Different cooling phases occurred from ~260 – ~240 Ma (late Permian - early Triassic), ~220 – ~200 Ma (late Triassic), 190 – ~180 Ma (early Jurassic) and 125 – ~100 Ma (mid-Cretaceous). Late Permian to mid-Jurassic onshore exhumation in Ireland and Wales shows a relationship between exhumation and rifting in the immediately adjacent offshore basins (Figure 8.5) which is related to the complicated break-up of Pangea and the subsequent initiation of rifting in the North Atlantic region. With the exception of samples Sct-3, Sct-5 and Sct-8, Scotland seems rather unaffected by Pangaea break-up and subsequent Mesozoic rifting, with most samples from Scotland generally showing slow cooling during Paleozoic and Mesozoic times. Interestingly, the three samples from the Northern (Sct-3 and Sct-5) and Central Highlands (Sct-8) are the samples with the lowest elevation in these regions at between 190 and 230 m above sea level. Thus, cooling could represent either some local fault reactivation for example of the Great Glen Fault (GGF; Le Breton et al., 2013), or Scotland was reburied beneath a thin veneer of Carboniferous and Permian sediments which caused partial reheating in the lowest elevation samples in central Scotland.

The Cretaceous cooling in Ireland and Britain cannot be linked with rifting in the adjacent basins. However, previous studies based on AFT and vitrinite reflectance data (Holford et al., 2005b) showed that exhumation occurs contemporaneous with extension on the Atlantic Margin associated with the onset of seafloor spreading in the Bay of Biscay (Keen et al., 1977; Ziegler, 1989) and major changes in the vector of African plate motion at ~84 Ma and ~131 Ma, also linked to the Eo-Alpine orogeny (e.g., Handy et al., 2010).

9.2 Early Cenozoic exhumation

The early Cenozoic exhumation history of Ireland and Britain reveals a strongly focused exhumation pattern centred on the northern part of the Irish Sea

system (Figure 8.7) and is divided into four different zones based on the thermal history models. The zones are assigned colours depending on magnitude of the early Cenozoic exhumation signal (Figure 8.7), and the amount of exhumation is calculated with an assumed paleogeothermal gradient of 25°C/km. The zones of early Cenozoic exhumation are:

i) The red zone shows a distinct exhumation pulse during early Cenozoic times which is visible in inverse thermal models for pseudo-vertical profiles (i.e. IoA) and *also* single samples (i.e. Ire-9). The suggested amount of early Cenozoic exhumation ranges from ~2 to ~3 km.

ii) The yellow zone shows only an early Cenozoic exhumation event if a pseudo-vertical profile is employed (i.e. Cu profile) or in forward modelling of single samples (i.e. Sct-10 or Pb-1). The suggested amount of early Cenozoic exhumation ranges from ~1.5 to ~2 km.

iii) The green zone does not show a discrete early Cenozoic cooling pulse but instead only a slight increase in the cooling rate at ~60 Ma. The green zone potentially experienced up to 1 km of early Cenozoic exhumation.

iv) The white zone which shows no sign of early Cenozoic exhumation. However, small amount of exhumation are difficult to identify due to the temperature sensitivity of AFT and AHe dating. Thus, the white zone can still have experienced early Cenozoic exhumation but probably less than ~1 km as proposed for Scotland from mass balance calculations of Paleogene submarine fans in the northern part of the North Sea (Den Hartog Jager et al., 1993).

This focused exhumation pulse at ~60 Ma around the Irish Sea region is not compatible with a spatially and temporally variable exhumation and localized inversion pattern associated with compressional far-field stress which has been proposed by several authors for the Irish Sea system (Holford et al., 2005b; Hillis et al., 2008a). Thus, it is unlikely that compressional far-field stress was the primary cause for early Cenozoic exhumation. On the other hand, the focused nature of the exhumation event is in good agreement with previously published exhumation patterns deduced from subsidence analysis (Figure 2.10;

Jones et al., 2002), and the extent of crustal underplating proposed from analysis of free-air gravity anomalies (Arrowsmith et al., 2005) and proposed magmatic underplating based on seismic receiver function analysis (Figure 8.12; Tomlinson et al., 2006) which all proposed mantle-driven processes as cause of exhumation. Furthermore, the timing of exhumation is synchronous with the emplacement of the BIPIP between ~63 and 55 Ma (Chambers et al., 2005) which yield helium isotope ratios ($^3He/^4He$) 22 times higher than the atmospheric ratio, which is appropriate for magmas derived from a mantle plume source (Stuart et al., 2000).

Thus, the early Cenozoic exhumation in Ireland and Britain was most likely caused by mantle-driven processes associated with the development of the proto-Iceland mantle plume. An elongate body of hot mantle material extended from beneath Greenland to beneath the Irish Sea region, emplacing a magmatic body into or beneath the lower crust corresponding approximately to the present-day limits of the BIPIP (Al-Kindi et al., 2003; Tomlinson et al., 2006). This study identifies the emplacement of this magmatic body as the main cause of early Cenozoic exhumation. It is also possible that a component of the observed early Cenozoic exhumation was caused by dynamically supported uplift and mechanical erosion of the lithosphere which causes short-wavelength (<1000 km) exhumation (sections 1.4, 8.6.2).

The AFT and AHe dating systems are not temperature-sensitive enough to resolve the Neogene thermal history in Ireland and Britain from surface samples, but the presented thermal histories suggest small amounts of Neogene exhumation for Ireland, whereas the Scottish samples tend to show monotonic cooling during the Neogene.

One key point of this study is that, in order to resolve small amounts (<1.5 km) it is necessary to combine AFT and AHe dating and, were possible, analyse boreholes and vertical profiles which greatly improves the resolution of the thermal models.

10. Suggestions for future work

Ireland and Britain are well covered by existing AFT studies (Green, 1986; Green et al., 2000; Green et al., 2001a; Allen et al., 2002; Holford et al., 2005b; Holford et al., 2008; Holford et al., 2010). However, the results from this study show that to resolve the early Cenozoic exhumation history, a combination of AFT and AHe dating is necessary, and needs to be combined with vertical profile modelling. Previous to this study, only (Persano et al., 2007) had applied forward modelling of AHe ages on two profiles in west and central Scotland, while (Cogné et al., 2014) deployed a combination of AFT and AHe dating on vertical profiles from western Ireland. Thus, there is a lack of AHe data from this sector of the NW European margin, which is *key* to resolving the small amounts of exhumation involved. This study focused on the proposed centre of early Cenozoic exhumation around the Irish Sea region, as the west coast of Ireland was already well covered by Cogné et al. (2014). Thus, the centre and the western limits of the zone of early Cenozoic exhumation are well defined. However, early Cenozoic exhumation in Scotland, southern and eastern England, in particular, are not well constrained.

AFT ages of ~60 Ma from northern England (Lake District and Pennines) are similar to sample Sct-1 (60.4 ±2.0 Ma) from the Southern Uplands and imply a strong early Cenozoic exhumation event (i.e. Green et al., 2002). Despite evidence of an elevated paleogeothermal gradient of up to 55 - 61°C/km in the Lake District during the Early Cenzoic, there was clearly substantial Early Cenzoic exhumation in northern England. Thus, future studies should focus on investigating the eastern limits of early Cenozoic exhumation in northern England by employing AFT and AHe dating on vertical profiles. Furthermore, additional studies on the paleogeothermal gradient around the Lake District region could better constrain the amount of early Cenozoic exhumation in the northern part of the Irish Sea Basin. Sample Sct-2 from the Midland Valley shows a clear early Cenozoic exhumation pulse, whereas samples from the Central Highlands show no indication of any Cenozoic event. Thus, future analysis should focus on AFT and AHe dating of the transition zone between the Midland Valley and the Central Highlands to detect the northern limit of the

early Cenozoic exhumation pulse centred on the northern part of the Irish Sea region. Sample Pb-1 from Pembrokeshire experienced up to ~1.5 km of early Cenozoic exhumation derived from the forward model. Additionally, in the Bristol Channel the Paleogene intrusion of Lundy indicates that the mantle-driven exhumation may have extended as far as south as Lundy. Future studies should explore if the early Cenozoic exhumation event also extends south of the Bristol Channel into south-west England, and potentially even as far as Brittany. Samples Sct-10 from the Hebrides and Sct-11 from the Northern Highlands indicate early Cenozoic exhumation in their forward models. However, both samples are only single samples, thus it is important to sample vertical profiles from NW Scotland supplement the earlier work of Persano et al. (2007) and prove that the forward models are also supported by inverse models.

In addition to the improvements on the onshore sample locations it is also important to collect offshore boreholes, if possible. As seen in this study, the temporal resolution of AFT and AHe dating from surface samples alone is typically insufficient to detect the low magnitudes of exhumation common to passive margins. Collecting vertical profiles with both AFT and AHe data could greatly improve the predictions of eroded material, especially in the Irish Sea Basin system.

Furthermore, it is also necessary to improve the annealing models for AFT dating and the diffusion models for AHe dating. Advanced annealing/diffusion models could greatly influence the thermal models and, thus, the prediction for exhumation.

11. Acknowledgements

I would like to thank my supervisor Dave Chew for his support regarding my PhD and personal life. Furthermore, I would like to thank you for the countless comments and discussions. Without your help the completion of this study would not have been possible.

I would also like to thank:

Nathan and Chris for endless discussions and comments about the results and the fieldwork in Wales. Additionally, I would like to thank Nathan for his help with the modelling. Without your help the results would not look as good as they do look now.

Luca and Vincent for our frequent Costa visits and the good time we had talking about our funding.

Tobi for putting up with me as a flatmate for two years and the great evenings watching countless movies.

Abi, Ben, and Kieran for their welcome in the first year and the good advice on what to do in Dublin and who to talk to if I had any questions.

Mike, Kyle, Gavin, Clare, Saskia, Edel, Paul, Antoinette, Meabh, Anthea and the other postgraduate students for the fun evenings in the pub.

Mags, Frank, Noel, Maura and Neil for their good natured help with ordering things, sample preparation and answering a lot of questions.

My parents for supporting me my whole life and especially since I moved abroad. Without your help it would have been much more difficult.

And last but not least, Sabrina my girlfriend for all the support over the past five years since I moved to Ireland, and especially the last few months when I was

busy writing this thesis. It has been nearly three years since we moved together and I wouldn't want to miss a single day.

12. References

Al-Kindi, S., White, N., Sinha, M., England, R., and Tiley, R., 2003, Crustal trace of a hot convective sheet: Geology, v. 31, no. 3, p. 207–210.

Allen, P.A., Bennett, S.D., Cunningham, M.J.M., Carter, A., Gallagher, K., Lazzaretti, E., Galewsky, J., Densmore, A.L., Phillips, W.E.A., Naylor, D., and Hach, C.S., 2002, The post-Variscan thermal and denudational history of Ireland: Geological Society, London, Special Publications, v. 196, no. 1, p. 371–399, doi: 10.1144/GSL.SP.2002.196.01.20.

Allen, M.B., and Davies, C.E., 2007, Unstable Asia: active deformation of Siberia revealed by drainage shifts: Basin Research, v. 19, no. 3, p. 379–392, doi: 10.1111/j.1365-2117.2007.00331.x.

Andrews, I.J., Long, D., Richards, P.C., Thomson, A.R., Brown, S., Chesher, J.A., and McCormac, M., 1990, The geology of the Moray Firth: HMSO.

Anell, I., Thybo, H., and Artemieva, I.M., 2009, Cenozoic uplift and subsidence in the North Atlantic region: Geological evidence revisited: Tectonophysics, v. 474, no. 1–2, p. 78–105, doi: 10.1016/j.tecto.2009.04.006.

Antignano, A., and Manning, C.E., 2008, Fluorapatite solubility in H2O and H2O-NaCl at 700 to 900°C and 0.7 to 2.0 GPa: Chemical Geology, v. 251, no. 1–4, p. 112–119, doi: 10.1016/j.chemgeo.2008.03.001.

Archer, S.G., Bergman, S.C., Iliffe, J., Murphy, C.M., and Thornton, M., 2005, Palaeogene igneous rocks reveal new insights into the geodynamic evolution and petroleum potential of the Rockall Trough, NE Atlantic Margin: Basin Research, v. 17, no. 1, p. 171–201, doi: 10.1111/j.1365-2117.2005.00260.x.

Arrowsmith, S.J., Kendall, M., White, N., VanDecar, J.C., and Booth, D.C., 2005, Seismic imaging of a hot upwelling beneath the British Isles: Geology, v. 33, no. 5, p. 345–348, doi: 10.1130/G21209.1.

Arter, G., and Fagin, S.W., 1993, The Fleetwood Dyke and the Tynwald fault zone, Block 113/27, East Irish Sea Basin, *in* Petroleum Geology of Northwest Europe: Proceedings of the 4th Conference, Geological Society of London, p. 835–843.

Baker, D., 1976, Structural implications of plate tectonics for Moine Thrust zone, NW Scotland: Transactions-American Geophysical Union, v. 57, no.

4, p. 334–334.

Balestrieri, M.L., Stuart, F.M., Persano, C., Abbate, E., and Bigazzi, G., 2005, Geomorphic development of the escarpment of the Eritrean margin, southern Red Sea from combined apatite fission-track and (U–Th)/He thermochronometry: Earth and Planetary Science Letters, v. 231, no. 1–2, p. 97–110, doi: 10.1016/j.epsl.2004.12.011.

Barbarand, J., Carter, A., Wood, I., and Hurford, T., 2003a, Compositional and structural control of fission-track annealing in apatite: Chemical Geology, v. 198, no. 1–2, p. 107–137, doi: 10.1016/S0009-2541(02)00424-2.

Barbarand, J., Hurford, T., and Carter, A., 2003b, Variation in apatite fission-track length measurement: Implications for thermal history modelling: Chemical Geology, v. 198, no. 1–2, p. 77–106, doi: 10.1016/S0009-2541(02)00423-0.

Barbarand, J., and Pagel, M., 2001, Importance of the chemistry to characterise apatite fission-track annealing: Comptes Rendus de l'Academie des Sciences Series IIA Earth and Planetary Science, v. 332, no. 4, p. 259–265.

Barr, F.T., 1966, Upper Cretaceous foraminifera from the Ballydeenlea chalk, County Kerry, Ireland: Paleontology, v. 9, p. 492–510.

Baumer, A., Ganteaume, M., and Klee, W.E., 1985, Determination of OH ions in hydroxyfluorapatites by infrared spectroscopy: Bulletin de minéralogie, v. 108, no. 2, p. 145–152.

Bennett, S.D., 2006, Tertiary Dykes in Northwest Ireland: Field Occurrence, Emplacement Mechanisms, Host Rock Deformation, and Post-emplacement Strain and Denudation: Trinity College Dublin.

Bergman, S.C., and Corrigan, J., 1996, Compositional variation of natural apatites subjected to fission track analysis, *in* International Workshop on Fission-Track Dating, University of Gent, August, p. 26–30.

Bernet, M., 2005, Fission-track Analysis of Detrital Zircon: Reviews in Mineralogy and Geochemistry, v. 58, no. 1, p. 205–237, doi: 10.2138/rmg.2005.58.8.

Beucher, R., Brown, R.W., Roper, S., Persano, C., Stuart, F., and Fitzgerald, P., 2013, Natural age dispersion arising from the analysis of broken crystals. Part I: Theoretical basis and implications for the apatite (U-Th)/He

thermochronometer: Geochimica et Cosmochimica Acta, v. 122, p. 478–497, doi: 10.1016/j.gca.2013.05.041.

Bevins, R.E., Horák, J.M., Evans, A.D., and Morgan, R., 1996, Palaeogene dyke swarm, NW Wales: evidence for Cenozoic sinistral fault movement: Journal of the Geological Society, v. 153, no. 2, p. 177–180.

Bhandari, N., Bhat, S.G., Lal, D., Rajagopalan, G., Tamhane, A.S., and Venkatavaradan, V.S., 1971, Fission fragment tracks in apatite: recordable track lengths: Earth and Planetary Science Letters, v. 13, no. 1, p. 191–199, doi: 10.1016/0012-821X(71)90123-3.

Bird, P., 1979, Continental delamination and the Colorado Plateau: J. geophys. Res, v. 84, no. B13, p. 7561–7571.

Blundell, D.J., 2002, Cenozoic inversion and uplift of southern Britain: Special Publication-Geological Society of London, v. 196, p. 85–102.

Bonvalot, S., Balmino, G., Brias, A., Kuhn, M., Peyrefitte, A., Vales, N., Biancale, R., Gabalda, G., Moreaux, G., Reinquin, F., and Sarrailh, M., 2012, World Gravity Map.:

Boyce, J.W., and Hodges, K.V., 2005, U and Th zoning in Cerro de Mercado (Durango, Mexico) fluorapatite: Insights regarding the impact of recoil redistribution of radiogenic 4He on (U–Th)/He thermochronology: Chemical Geology, v. 219, no. 1, p. 261–274, doi: 10.1016/j.chemgeo.2005.02.007.

Braun, J., 2010, The many surface expressions of mantle dynamics: Nature Geoscience, v. 3, no. 12, p. 825–833, doi: 10.1038/ngeo1020.

Braun, J., Van Der Beek, P., and Batt, G., 2006, Quantitative thermochronology: numerical methods for the interpretation of thermochronological data: Cambridge University Press.

Le Breton, E., Cobbold, P.R., and Zanella, A., 2013, Cenozoic reactivation of the Great Glen Fault, Scotland: additional evidence and possible causes: Journal of the Geological Society, v. 170, no. 3, p. 403–415, doi: 10.1144/jgs2012-067.

Brodie, J., and White, N., 1994, Sedimentary basin inversion caused by ingneous underplating: Geology, v. 22, p. 147–150.

Brodie, J., and White, N., 1995, The link between sedimentary basin inversion and igneous underplating: Geological Society, London, Special Publications, v. 88, no. 1, p. 21–38, doi: 10.1144/GSL.SP.1995.088.01.03.

Broughan, F.M., Naylor, D., and Anstey, N.A., 1989, Jurassic rocks in the Kish Bank Basin: Irish Journal of Earth Sciences, p. 99–106.

Brown, R.W., Beucher, R., Roper, S., Persano, C., Stuart, F., and Fitzgerald, P., 2013, Natural age dispersion arising from the analysis of broken crystals. Part I: Theoretical basis and implications for the apatite (U-Th)/He thermochronometer: Geochimica et Cosmochimica Acta, v. 122, p. 478–497, doi: 10.1016/j.gca.2013.05.041.

Brown, R., Gallagher, K., and Duane, M., 1994, A quantitative assessment of the effects of magmatism on the thermal history of the Karoo sedimentary sequence: Journal of African Earth Sciences, v. 18, no. 3, p. 227–243, doi: 10.1016/0899-5362(94)90007-8.

Burov, E., and Cloetingh, S., 2009, Controls of mantle plumes and lithospheric folding on modes of intraplate continental tectonics: Differences and similarities: Geophysical Journal International, v. 178, no. 3, p. 1691–1722, doi: 10.1111/j.1365-246X.2009.04238.x.

Carlson, R.W., 2011, Absolute Age Determinations: Radiometric BT - Encyclopedia of Solid Earth Geophysics, *in* Gupta, H.K. ed., Springer Netherlands, Dordrecht, p. 1–8.

Carlson, W.D., Donelick, R.A., and Ketcham, R.A., 1999, Variability of apatite fission-track annealing kinetics: I. Experimental results: American Mineralogist, v. 84, p. 1213–1223.

Cartier, C., and Faure, M., 2004, The Saint-Georges-sur-Loire olistostrome, a key zone to understand the Gondwana-Armorica boundary in the Variscan belt (Southern Brittany, France): International Journal of Earth Sciences, v. 93, no. 6, p. 945–958, doi: 10.1007/s00531-004-0398-3.

Cawood, P.A., Strachan, R.A., Merle, R.E., Millar, I.L., Loewy, S.L., Dalziel, I.W.D., Kinny, P.D., Jourdan, F., Nemchin, A.A., and Connelly, J.N., 2014, Neoproterozoic to early Paleozoic extensional and compressional history of East Laurentian margin sequences: The Moine Supergroup, Scottish Caledonides: Geological Society of America Bulletin, v. 127, no. 3–4, p. 349–371, doi: 10.1130/B31068.1.

Chamberlain, K.R., and Bowring, S.A., 2000, Apatite–feldspar U–Pb thermochronometer: a reliable, mid-range (~450°C), diffusion-controlled system: Chemical Geology, v. 172, no. 1–2, p. 173–200, doi:

10.1016/S0009-2541(00)00242-4.

Chambers, L.M., Pringle, M.S., and Parrish, R.R., 2005, Rapid formation of the Small Isles Tertiary centre constrained by precise 40Ar/39Ar and U–Pb ages: Lithos, v. 79, no. 3–4, p. 367–384, doi: 10.1016/j.lithos.2004.09.008.

Chapman, T.J., Broks, T.M., Corcoran, D. V., Duncan, L.A., and Dancer, P.N., 1999, Petroleum Geology of Northwest Europe: Proceedings of the 5th Conference: Geological Society of London.

Cherniak, D.J., 2000, Rare earth element diffusion in apatite: Geochimica et Cosmochimica Acta, v. 64, no. 22, p. 3871–3885, doi: 10.1016/S0016-7037(00)00467-1.

Cherniak, D.J., and Watson, E.B., 2000, Pb diffusion in zircon: Chemical Geology, v. 172, no. 1, p. 5–24.

Chew, D.M., 2009, Grampian Orogeny, *in* Holland, C.H. and Sanders, I.S. eds., The Geology of Ireland, Dunedin Academic Press, Edinburgh, p. 69–94.

Chew, D.M., and Donelick, R. a, 2012, Chapter 12: Combined apatite fission track and U-Pb dating by LA-ICP-MS and its application in apatite provenance analysis: Mineralogical Association of Canada Short Course 42, , no. May, p. 219–247.

Chew, D.M., Petrus, J.A., and Kamber, B.S., 2014, U-Pb LA-ICPMS dating using accessory mineral standards with variable common Pb: Chemical Geology, v. 363, p. 185–199, doi: 10.1016/j.chemgeo.2013.11.006.

Chew, D.M., and Stillman, C.J., 2009, Late Caledonian orogeny and magmatism, *in* Holland, C.H. and Sanders, I.S. eds., The Geology of Ireland, Dunedin Academic Press, Edinburgh, p. 143–174.

Chew, D.M., and Strachan, R.A., 2014, The Laurentian Caledonides of Scotland and Ireland: Geological Society, London, Special Publications, v. 390, no. 1, p. 45–91, doi: 10.1144/SP390.16.

Chew, D.M., Sylvester, P.J., and Tubrett, M.N., 2011, U-Pb and Th-Pb dating of apatite by LA-ICPMS: Chemical Geology, v. 280, no. 1–2, p. 200–216, doi: 10.1016/j.chemgeo.2010.11.010.

Clayton, G., Haughey, N., Sevastopulo, G.D., and Burnett, R., 1989, Thermal maturation levels in the Devonian and Carboniferous rocks of Ireland: Geological Survey of Ireland.

Clift, P.D., and Turner, J., 1998, Paleogene igneous underplating and

subsidence anomalies in the rockall-Faeroe-Shetland area: Marine and Petroleum Geology, v. 15, no. 3, p. 223–243, doi: 10.1016/S0264-8172(97)00056-1.

Cloetingh, S., Gradstein, F.M., Kooi, H., Grant, A.C., and Kaminski, M., 1990, Plate reorganization: a cause of rapid late Neogene subsidence and sedimentation around the North Atlantic? Journal of the Geological Society, v. 147, no. 3, p. 495–506, doi: 10.1144/gsjgs.147.3.0495.

Cobbold, P.R., Rossello, E. a., Roperch, P., Arriagada, C., Gomez, L. a., and Lima, C., 2007, Distribution, timing, and causes of Andean deformation across South America: Geological Society, London, Special Publications, v. 272, no. 1, p. 321–343, doi: 10.1144/GSL.SP.2007.272.01.17.

Cochrane, R., Spikings, R.A., Chew, D., Wotzlaw, J.F., Chiaradia, M., Tyrrell, S., Schaltegger, U., and Van der Lelij, R., 2014, High temperature (>350 °C) thermochronology and mechanisms of Pb loss in apatite: Geochimica et Cosmochimica Acta, v. 127, p. 39–56, doi: 10.1016/j.gca.2013.11.028.

Cogné, N., Chew, D., and Stuart, F., 2014, The thermal history of the Western Irish onshore: v. 16, p. 3522, doi: 10.1144/jgs2014-026.

Cogné, N., Doepke, D., Chew, D., Stuart, F.M., and Mark, C., 2016, Measuring plume-related exhumation of the British Isles in Early Cenozoic times: Earth and Planetary Science Letters, v. 456, p. 1–15, doi: 10.1016/j.epsl.2016.09.053.

Cogné, N., Gallagher, K., and Cobbold, P.R., 2011, Post-rift reactivation of the onshore margin of southeast Brazil: Evidence from apatite (U–Th)/He and fission-track data: Earth and Planetary Science Letters, v. 309, no. 1–2, p. 118–130, doi: 10.1016/j.epsl.2011.06.025.

Cogné, N., Gallagher, K., Cobbold, P.R., Riccomini, C., and Gautheron, C., 2012, Post-breakup tectonics in southeast Brazil from thermochronological data and combined inverse-forward thermal history modeling: Journal of Geophysical Research, v. 117, no. B11, p. B11413, doi: 10.1029/2012JB009340.

Cope, J.C.W., 1994, A latest Cretaceous hotspot and the southeasterly tilt of Britain: Journal of the Geological Society, v. 151, no. 6, p. 905–908, doi: 10.1144/gsjgs.151.6.0905.

Cope, J.C.W., 1984, The Mesozoic history of Wales: Proceedings of the

Geologists' Association, v. 95, no. 4, p. 373–385, doi: 10.1016/S0016-7878(84)80067-X.

Corcoran, D. V, and Clayton, G., 2001, Interpretation of vitrinite reflectance profiles in sedimentary basins, onshore and offshore Ireland: Geological Society, London, Special Publications, v. The Petrol, no. 188, p. 61–90, doi: 10.1144/GSL.SP.2001.188.01.04.

Corcoran, D. V., and Doré, A.G., 2005, A review of techniques for the estimation of magnitude and timing of exhumation in offshore basins: Earth-Science Reviews, v. 72, no. 3–4, p. 129–168, doi: 10.1016/j.earscirev.2005.05.003.

Coward, M.P., 1995, Structural and tectonic setting of the Permo-Triassic basins of northwest Europe: Geological Society, London, Special Publications, v. 91, no. 1, p. 7–39, doi: 10.1144/GSL.SP.1995.091.01.02.

Coward, M.P., 1990, The Precambrian, Caledonian and Variscan framework to NW Europe: Geological Society, London, Special Publications, v. 55, no. 1, p. 1–34, doi: 10.1144/GSL.SP.1990.055.01.01.

Coxon, P., and McCarron, S.G., 2009, Tertiary and Quaternary (until 11,700 years before 2000), *in* Holland, C.H. and Sanders, I.S. eds., The Geology of Ireland, Dunedin Academic Press, Edinburgh, p. 355–396.

Croker, P.F., and Klemperer, S.L., 1989, Structure and stratigraphy of the Porcupine Basin: relationships to deep crustal structure and the opening of the North Atlantic, *in* Tankard, A.. and Balkwill, H.R. eds., Extensional tectonics and stratigraphy of the North Atlantic margins, American Association of Petroleum Geologists, Tulsa, p. 445–459.

Crowley, K.D., Cameron, M., and Schaefer, R.L., 1991, Experimental studies of annealing of etched fission tracks in fluorapatite: Geochimica et Cosmochimica Acta, v. 55, no. 5, p. 1449–1465, doi: 10.1016/0016-7037(91)90320-5.

Dancer, P.N., Algar, S.T., and Wilson, I.R., 1999, Petroleum Geology of Northwest Europe: Proceedings of the 5th Conference: Geological Society of London.

Dancer, P.N., Kenyon-Roberts, S.M., Downey, J.W., Baillie, J.M., Meadows, N.S., and Maguire, K., 2005, The Corrib gas field, offshore west of Ireland, *in* Petroleum Geology: North-West Europe and Global Perspectives –

Proceedings of the 6th Petroleum Geology Conference, Geological Society of London, p. 1035–1046.

Davis, M.W., White, N.J., Priestley, K.F., Baptie, B.J., and Tilmann, F.J., 2012, Crustal structure of the British Isles and its epeirogenic consequences: Geophysical Journal International, v. 190, no. 2, p. 705–725, doi: 10.1111/j.1365-246X.2012.05485.x.

Dewey, J.F., 2000, Cenozoic tectonics of western Ireland: Proceedings of the Geologists' Association, v. 111, no. 4, p. 291–306, doi: 10.1016/S0016-7878(00)80086-3.

Dewey, J.F., and Shackleton, R.M., 1984, A model for the evolution of the Grampian tract in the early Caledonides and Appalachians: Nature, v. 312, no. 5990, p. 115–121, doi: 10.1038/312115a0.

Dewey, J.F., and Strachan, R.A., 2003, Changing Silurian-Devonian relative plate motion in the Caledonides: sinistral transpression to sinistral transtension: Journal of the Geological Society, v. 160, no. 2, p. 219–229, doi: 10.1144/0016-764902-085.

Dèzes, P., Schmid, S.M., and Ziegler, P.A., 2004, Evolution of the European Cenozoic Rift System: interaction of the Alpine and Pyrenean orogens with their foreland lithosphere: Tectonophysics, v. 389, no. 1–2, p. 1–33, doi: 10.1016/j.tecto.2004.06.011.

Dobson, K.J., 2006, The zircon (U-Th)/He thermochronometer: development and application of thermochronometers in igneous provinces: University of Glasgow, 282 p.

Dodson, M.H., 1973, Closure temperature in cooling geochronological and petrological systems: Contributions to Mineralogy and Petrology, v. 40, p. 259–274, doi: 10.1007/BF00373790.

Donelick, R.A., 1993, A method of fission-track analysis utilizing bulk chemical etching of apatite: Patent 5,267,274: US Patent and Trademark Off., Washington, DC,.

Donelick, R.A., 1991, Crystallographic orientation dependence of mean etchable fission track length in apatite: An empirical model and experimental observations: American Mineralogist, v. 76, p. 83–91.

Donelick, R.A., Ketcham, R.A., and Carlson, W.D., 1999, Variability of apatite fission-track annealing kinetics: II. Crystallographic orientation effects:

American Mineralogist, v. 84, p. 1224–1234.

Donelick, R.A., and Miller, D.S., 1991, Enhanced tint fission track densities in low spontaneous track density apatites using 252Cf-derived fission fragment tracks: A model and experimental observations: International Journal of Radiation Applications and Instrumentation. Part D. Nuclear Tracks and Radiation Measurements, v. 18, no. 3, p. 301–307, doi: 10.1016/1359-0189(91)90022-A.

Donelick, R.A., O'Sullivan, P.B., and Ketcham, R.A., 2005, Apatite Fission-Track Analysis: Reviews in Mineralogy and Geochemistry, v. 58, no. 1, p. 49–94, doi: 10.2138/rmg.2005.58.3.

Doré, A.G., Cartwright, J.A., Stoker, M.S., Turner, J.P., and White, N.J., 2002, Exhumation of the North Atlantic margin: introduction and background: Geological Society, London, Special Publications, v. 196, no. 1, p. 1–12, doi: 10.1144/GSL.SP.2002.196.01.01.

Doré, A.G., Lundin, E.R., Jensen, L.N., Birkeland, Ø., Eliassen, P.E., and Fichler, C., 1999, Principal tectonic events in the evolution of the northwest European Atlantic margin: Geological Society, London, Petroleum Geology Conference series, v. 5, p. 41–61, doi: 10.1144/0050041.

Dore, A.G., Lundin, E.R., Kusznir, N.J., and Pascal, C., 2008, Potential mechanisms for the genesis of Cenozoic domal structures on the NE Atlantic margin: pros, cons and some new ideas: Geological Society, London, Special Publications, v. 306, no. 1, p. 1–26, doi: 10.1144/SP306.1.

Dunai, T.J., Bikker, A., and Meesters, A.G.C., 2003, Decomp: a user friendly forward modeling program for (U-Th)/He low-temperature geochronology: EGS - AGU - EUG Joint Assembly,.

Ehlers, T.A., and Farley, K.A., 2003, Apatite (U-Th)/He thermochronometry: Methods and applications to problems in tectonic and surface processes: Earth and Planetary Science Letters, v. 206, no. 1–2, p. 1–14, doi: 10.1016/S0012-821X(02)01069-5.

England, R.W., 1992, The genesis, ascent, and emplacement of the Northern Arran Granite, Scotland: Implications for granitic diapirism: Geological Society of America Bulletin, v. 104, no. 5, p. 606–614, doi: 10.1130/0016-7606(1992)104.

Evans, A., and Clayton, G., 1998, The geological history of the Ballydeenlea

Chalk Breccia, County Kerry, Ireland: Marine and Petroleum Geology, v. 15, no. 4, p. 299–307, doi: 10.1016/S0264-8172(98)00024-5.

Farley, K.A., 2002, (U-Th)/He Dating: Techniques, Calibrations, and Applications: Reviews in Mineralogy and Geochemistry, v. 47, no. 1, p. 819–844, doi: 10.2138/rmg.2002.47.18.

Farley, K.A., 2000, Helium diffusion from apatite: General behavior as illustrated by Durango fluorapatite: Journal of Geophysical Research: Solid Earth, v. 105, no. B2, p. 2903–2914, doi: 10.1029/1999JB900348.

Farley, K.A., and Stockli, D.F., 2002, (U-Th)/He Dating of Phosphates: Apatite, Monazite, and Xenotime: Reviews in Mineralogy and Geochemistry, v. 48, no. 1, p. 559–577, doi: 10.2138/rmg.2002.48.15.

Farley, K.A., Wolf, R.A., and Silver, L.T., 1996, The effects of long alpha-stopping distances on (U-Th)/He ages: Geochimica et Cosmochimica Acta, v. 60, no. 21, p. 4223–4229, doi: 10.1016/S0016-7037(96)00193-7.

Faure, M., Leloix, C., and Roig, J., 1997, Polycyclic evolution of the Hercynian belt: Bulletin de la Société Géologique de France, v. 168, no. 6, p. 695–705.

Fleischer, R.L., Price, P.B., and Walker, R.M., 1975, Nuclear tracks in solids: principles and applications: Univ of California Press.

Floodpage, J., Newman, P., and White, J., 2001, Hydrocarbon prospectivity in the Irish Sea area: insights from recent exploration of the Central Irish Sea, Peel and Solway basins: Geological Society, London, Special Publications, v. 188, no. 1, p. 107–134, doi: 10.1144/GSL.SP.2001.188.01.06.

Flowers, R.M., Ketcham, R.A., Shuster, D.L., and Farley, K.A., 2009, Apatite (U-Th)/He thermochronometry using a radiation damage accumulation and annealing model: Geochimica et Cosmochimica Acta, v. 73, no. 8, p. 2347–2365, doi: 10.1016/j.gca.2009.01.015.

Foeken, J., Stuart, F.M., Dobson, K.J., Persano, C., and Vilbert, D., 2006, A diode laser system for heating minerals for (U-Th)/He chronometry: Geochemistry, Geophysics, Geosystems, v. 7, no. 4.

Friedlander, G., Macias, E.S., and Kennedy, J.W., 1981, Nuclear and radiochemistry: John Wiley & Sons.

Galbraith, R.F., 1981, On statistical models for fission track counts: Journal of the International Association for Mathematical Geology, v. 13, no. 6, p.

471–478, doi: 10.1007/BF01034498.

Galbraith, R.F., 2005, Statistics for fission track analysis: CRC Press.

Galbraith, R.F., and Laslett, G.M., 1993, Statistical models for mixed fission track ages: Nuclear Tracks and Radiation Measurements, v. 21, no. 4, p. 459–470, doi: 10.1016/1359-0189(93)90185-C.

Gallagher, K., 2015, QTQt User Guide v5.4.5R: , p. 62.

Gallagher, K., 2012, Transdimensional inverse thermal history modeling for quantitative thermochronology: Journal of Geophysical Research, v. 117, no. B2, p. B02408, doi: 10.1029/2011JB008825.

Gallagher, K., Brown, R., and Johnson, C., 1998, Fission track analysis and its applications to geological problems: Annual Review of Earth and Planetary Sciences, v. 26, no. 1, p. 519–572, doi: 10.1146/annurev.earth.26.1.519.

Gallagher, K., Charvin, K., Nielsen, S., Sambridge, M., and Stephenson, J., 2009, Markov chain Monte Carlo (MCMC) sampling methods to determine optimal models, model resolution and model choice for Earth Science problems: Marine and Petroleum Geology, v. 26, no. 4, p. 525–535, doi: 10.1016/j.marpetgeo.2009.01.003.

Gallagher, K., Stephenson, J., Brown, R., Holmes, C., and Ballester, P., 2005a, Exploiting 3D Spatial Sampling in Inverse Modeling of Thermochronological Data: Reviews in Mineralogy and Geochemistry, v. 58, no. 1, p. 375–387, doi: 10.2138/rmg.2005.58.14.

Gallagher, K., Stephenson, J., Brown, R., Holmes, C., and Fitzgerald, P., 2005b, Low temperature thermochronology and modeling strategies for multiple samples 1: Vertical profiles: Earth and Planetary Science Letters, v. 237, no. 1–2, p. 193–208, doi: 10.1016/j.epsl.2005.06.025.

Gamble, J.A., Wysoczanski, R.J., and Meighan, I.G., 1999, Constraints on the age of the British Tertiary Volcanic Province from ion microprobe U-Pb (SHRIMP) ages for acid igneous rocks from NE Ireland: Journal of the Geological Society, v. 156, no. 2, p. 291–299, doi: 10.1144/gsjgs.156.2.0291.

Ganerød, M., Smethurst, M.A., Torsvik, T.H., Prestvik, T., Rousse, S., McKenna, C., Van Hinsbergen, D.J.J., Hendriks, B.W.H., Ganerød, M., Smethurst, M.A., Torsvik, T.H., Prestvik, T., Rousse, S., McKenna, C., et al., 2010, The North Atlantic Igneous Province reconstructed and its

relation to the Plume Generation Zone: The Antrim Lava Group revisited: Geophysical Journal International, v. 182, no. 1, p. 183–202, doi: 10.1111/j.1365-246X.2010.04620.x.

Gautheron, C., and Tassan-Got, L., 2010, A Monte Carlo approach to diffusion applied to noble gas/helium thermochronology: Chemical Geology, v. 273, no. 3–4, p. 212–224, doi: 10.1016/j.chemgeo.2010.02.023.

Gautheron, C., Tassan-Got, L., Barbarand, J., and Pagel, M., 2009, Effect of alpha-damage annealing on apatite (U–Th)/He thermochronology: Chemical Geology, v. 266, no. 3–4, p. 157–170, doi: 10.1016/j.chemgeo.2009.06.001.

Gautheron, C.E., Tassan-Got, L., and Farley, K.A., 2006, (U–Th)/Ne chronometry.:

Gleadow, A.J.W., and Duddy, I.R., 1981, A natural long-term track annealing experiment for apatite: Nuclear Tracks, v. 5, no. 1–2, p. 169–174, doi: 10.1016/0191-278X(81)90039-1.

Glen, R.A., Hancock, P.L., and Whittaker, A., 2005, Basin inversion by distributed deformation: the southern margin of the Bristol Channel Basin, England: Journal of Structural Geology, v. 27, no. 12, p. 2113–2134, doi: 10.1016/j.jsg.2005.08.006.

Graham, J.R., 2009a, Devonian, *in* Holland, C.H. and Sanders, I.S. eds., The Geology of Ireland, Dunedin Academic Press, Edinburgh, p. 175–214.

Graham, J.R., 2009b, Variscan deformation and metamorphism, *in* Holland, C.H. and Sanders, I.S. eds., The Geology of Ireland, Dunedin Academic Press, Edinburgh, p. 295–310.

Gray, J., 2013, Petroleum prospectivity of the principal sedimentary basins on the United Kingdom Continental Shelf Petroleum prospectivity of the principal sedimentary basins on the United Kingdom Continental Shelf.:

Green, P.F., 2002, Early Tertiary paleo-thermal effects in northern England: Reconciling results from apatite fission track analysis with geological evidence: Tectonophysics, v. 349, no. 1–4, p. 131–144, doi: 10.1016/S0040-1951(02)00050-1.

Green, P.F., 1986, On the thermo-tectonic evolution of Northern England: evidence from fission track analysis: Geological Magazine, v. 123, no. 5, p. 493, doi: 10.1017/S0016756800035081.

Green, P.F., 1988, The relationship between track shortening and fission track age reduction in apatite: combined influences of inherent instability, annealing anisotropy, length bias and system calibration: Earth and Planetary Science Letters, v. 89, no. 3–4, p. 335–352, doi: 10.1016/0012-821X(88)90121-5.

Green, P.F., Duddy, I.R., and Bray, R.J., 1997, Variation in thermal history styles around the Irish Sea and adjacent areas: implications for hydrocarbon occurrence and tectonic evolution: Geological Society, London, Special Publications, v. 124, no. 1, p. 73–93, doi: 10.1144/GSL.SP.1997.124.01.06.

Green, P.F., Duddy, I.R., Bray, R.J., Duncan, W.I., and Corcoran, D. V, 2001a, The influence of thermal history on hydrocarbon prospectivity in the Central Irish Sea Basin: The Petroleum Exploration of Ireland's Offshore Basins, v. 188, p. 171–188, doi: 10.1144/GSL.SP.2001.188.01.09.

Green, P.F., Duddy, I.R., Gleadow, A.J.W., Tingate, P.R., and Laslett, G.M., 1986, Thermal annealing of fission tracks in apatite: 1. A qualitative description: Chemical Geology: Isotope Geoscience section, v. 59, p. 237–253.

Green, P.F., Duddy, I.R., and Hegarty, K.A., 2002, Quantifying exhumation from apatite fission-track analysis and vitrinite reflectance data: precision, accuracy and latest results from the Atlantic margin of NW Europe: Geological Society, London, Special Publications, v. 196, no. 1, p. 331–354, doi: 10.1144/GSL.SP.2002.196.01.18.

Green, P.F., Duddy, I.R., Hegarty, K.A., Bray, R.J., Sevastopulo, G., Clayton, G., and Johnston, D., 2000, The post-Carboniferous evolution of Ireland: evidence from Thermal History Reconstruction: Proceedings of the Geologists' Association, v. 111, no. 4, p. 307–320, doi: 10.1016/S0016-7878(00)80087-5.

Green, P.F., Duddy, I.R., Laslett, G.M., Hegarty, K.A., Gleadow, A.J.W., and Lovering, J.F., 1989, Thermal annealing of fission tracks in apatite 4. Quantitative modelling techniques and extension to geological timescales: Chemical Geology: Isotope Geoscience Section, v. 79, no. 2, p. 155–182, doi: 10.1016/0168-9622(89)90018-3.

Green, P.F., and Hurford, A.J., 1984, Thermal neutron dosimetry for fission

track dating: Nuclear Tracks and Radiation Measurements (1982), v. 9, no. 3–4, p. 231–241, doi: 10.1016/0735-245X(84)90190-X.

Green, P.F., Thompson, K., and Hudson, J.D., 2001b, Recognition of tectonic events in undeformed regions; contrasting results from the Midland Platform and East Midlands Shelf, Central England: Journal of the Geological Society, v. 158, no. 1, p. 59–73, doi: 10.1144/jgs.158.1.59.

Green, P.F., Westaway, R., Manning, D.A.C., and Younger, P.L., 2012, Cenozoic cooling and denudation in the North Pennines (northern England, UK) constrained by apatite fission-track analysis of cuttings from the Eastgate Borehole: Proceedings of the Geologists' Association, v. 123, no. 3, p. 450–463, doi: 10.1016/j.pgeola.2011.11.003.

Guenthner, W.R., Reiners, P.W., Ketcham, R.A., Nasdala, L., and Giester, G., 2013, Helium diffusion in natural zircon: Radiation damage, anisotropy, and the interpretation of zircon (U-Th)/He thermochronology: American Journal of Science, v. 313, no. 3, p. 145–198.

Gunnell, Y., 2000, Apatite fission track thermochronology: an overview of its potential and limitations in geomorphology: Basin Research, v. 12, no. 2, p. 115–132.

Hacker, B.R., Kelemen, P.B., and Behn, M.D., 2015, Continental Lower Crust: Annual Review of Earth and Planetary Sciences, v. 43, no. 1, p. 167–205, doi: 10.1146/annurev-earth-050212-124117.

Hall, A., and Bishop, P., 2002, Scotland's denudational history: an integrated view of erosion and sedimentation at an uplifted passive margin: Exhumation of the North Atlantic Margin: Timing, Mechanisms and Implications for Petroleum Exploration, v. 196, no. 1, p. 271–290, doi: 10.1144/GSL.SP.2002.196.01.15.

Hallis, L.J., Taylor, G.J., Nagashima, K., and Huss, G.R., 2012, Magmatic water in the martian meteorite Nakhla.:

Handy, M.R., Schmid, S.M., Bousquet, R., Kissling, E., and Bernoulli, D., 2010, Reconciling plate-tectonic reconstructions of Alpine Tethys with the geological-geophysical record of spreading and subduction in the Alps: Earth-Science Reviews, v. 102, no. 3–4, p. 121–158, doi: 10.1016/j.earscirev.2010.06.002.

Hanna, G.C., Westcott, C.H., Lemmel, H.D., Leonard, B.R.J., Story, J.S., and

Attree, P.M., 1969, Revision of values for the 2200 m/s neutron constants for four fissile nuclides:

Harland, W.B., and Gayer, R.A., 1972, The Arctic Caledonides and earlier Oceans: Geological Magazine, v. 109, no. 4, p. 289–314, doi: 10.1017/S0016756800037717.

Harlov, D.E., and Förster, H.-J., 2004, Fluid-induced nucleation of (Y+REE)-phosphate minerals within apatite: Nature and experiment. Part II. Fluorapatite: American Mineralogist, v. 88, no. 8–9, p. 1209–1229, doi: 10.2138/am-2003-8-905.

Den Hartog Jager, D., Giles, M.R., and Griffiths, G.R., 1993, Petroleum Geology of Northwest Europe: Proceedings of the 4th Conference: Geological Society of London.

Hasebe, N., Barbarand, J., Jarvis, K., Carter, A., and Hurford, A.J., 2004, Apatite fission-track chronometry using laser ablation ICP-MS: Chemical Geology, v. 207, no. 3–4, p. 135–145, doi: 10.1016/j.chemgeo.2004.01.007.

Haughton, P.D.W., Praeg, D., Shannon, P.M., Harrington, G., Higgs, K., Amy, L., Tyrrell, S., and Morrissey, T., 2005, First results from shallow stratigraphic boreholes on the eastern flank of the Rockall Basin, offshore western Ireland: Geological Society, London, Petroleum Geology Conference series, v. 6, p. 1077–1094, doi: 10.1144/0061077.

Herbert-Smith, M., 1979, The Age of the Tertiary Deposits of the Llanbedr Mochras Farm Borehole as Determined from Palynological Studies:

Higgs, K., and Beese, A.P., 1986, A Jurassic Microflora from the Colbond Clay of Cloyne, County Cork: Irish Journal of Earth Sciences, v. 7, no. 2, p. 99–109.

Hillis, R.R., 1995, Regional Tertiary Exhumation in and around the United Kingdom: Geological Society, London, Special Publications, v. 88, no. 1, p. 167–190, doi: 10.1144/GSL.SP.1995.088.01.11.

Hillis, R.R., Holford, S.P., Green, P.F., Doré, A.G., Gatliff, R.W., Stoker, M.S., Thomson, K., Turner, J.P., Underhill, J.R., and Williams, G.A., 2008a, Cenozoic exhumation of the southern British Isles: Geology, v. 36, no. 5, p. 371–374, doi: 10.1130/G24699A.1.

Hillis, R.R., Sandiford, M., Reynolds, S.D., and Quigley, M.C., 2008b, Present-

day stresses, seismicity and Neogene-to-Recent tectonics of Australia's "passive" margins: intraplate deformation controlled by plate boundary forces: Geological Society, London, Special Publications, v. 306, no. 1, p. 71–90, doi: 10.1144/SP306.3.

Holford, S.P., Green, P.F., Hillis, R.R., Turner, J.P., and Stevenson, C.T.E., 2009a, Mesozoic-Cenozoic exhumation and volcanism in Northern Ireland constrained by AFTA and compaction data from the Larne No. 2 borehole: Petroleum Geoscience, v. 15, no. 3, p. 239–257, doi: 10.1144/1354-079309-840.

Holford, S.P., Green, P.F., Hillis, R.R., Underhill, J.R., Stoker, M.S., and Duddy, I.R., 2010, Multiple post-Caledonian exhumation episodes across NW Scotland revealed by apatite fission-track analysis: Journal of the Geological Society, v. 167, no. 4, p. 675–694, doi: 10.1144/0016-76492009-167.

Holford, S., Green, P., and Turner, J., 2005a, Palaeothermal and compaction studies in the Mochras borehole (NW Wales) reveal early Cretaceous and Neogene exhumation and argue against regional Palaeogene uplift in the southern Irish Sea: Journal of the Geological Society, v. 162, no. 5, p. 829–840, doi: 10.1144/0016-764904-118.

Holford, S.P., Green, P.F., Turner, J.P., Williams, G.A., Hillis, R.R., Tappin, D.R., and Duddy, I.R., 2008, Evidence for kilometre-scale Neogene exhumation driven by compressional deformation in the Irish Sea basin system: Geological Society, London, Special Publications, v. 306, no. 1, p. 91–119, doi: 10.1144/SP306.4.

Holford, S.P., Hillis, R.R., Green, P.F., Duddy, I.R., Turner, J.P., and Stoker, M.S., 2009b, Regional intraplate exhumation episodes related to plate-boundary deformation: Bulletin of the Geological Society of America, v. 121, no. 11–12, p. 1611–1628, doi: 10.1130/B26481.1.

Holford, S., Turner, J., and Green, P., 2005b, Reconstructing the Mesozoic – Cenozoic exhumation history of the Irish Sea basin system using apatite fission track analysis and vitrinite reflectance data, *in* Dore, A.G. and Vining, B.A. eds., Petroleum Geology: North-West Europe and Global Perspectives - Proceedings of the 6th Petroleum Geology Conference, Geological Society, p. 1095–1110.

Holford, S.P., Turner, J.P., Green, P.F., and Hillis, R.R., 2009c, Signature of cryptic sedimentary basin inversion revealed by shale compaction data in the Irish Sea, western British Isles: Tectonics, v. 28, doi: 10.1029/2008tc002359.

Holland, C.H., and Sanders, I.S. (Eds.), 2009, The Geology of Ireland: Dunedin Academic Press, Edinburgh.

Holliday, D.W., 1993, Mesozoic cover over northern England: interpretation of apatite fission track data: Journal of the Geological Society, v. 150, no. 4, p. 657–660, doi: 10.1144/gsjgs.150.4.0657.

Van Hoorn, B., 1987a, Structural evolution, timing and tectonic style of the Sole Pit inversion: Tectonophysics, v. 137, no. 1–4, p. 239–284, doi: 10.1016/0040-1951(87)90322-2.

Van Hoorn, B., 1987b, The south Celtic Sea/Bristol Channel Basin: origin, deformation and inversion history: Tectonophysics, v. 137, no. 1–4, p. 309–334, doi: 10.1016/0040-1951(87)90325-8.

House, M.A., Farley, K.A., and Stockli, D., 2000, Helium chronometry of apatite and titanite using Nd-YAG laser heating: Earth and Planetary Science Letters, v. 183, no. 3–4, p. 365–368, doi: 10.1016/S0012-821X(00)00286-7.

Hudec, M.R., and Jackson, M.P. a., 2002, Structural segmentation, inversion, and salt tectonics on a passive margin: Evolution of the Inner Kwanza Basin, Angola: Geological Society of America Bulletin, v. 114, no. 10, p. 1222–1244, doi: 10.1130/0016-7606(2002)114<1222:SSIAST>2.0.CO;2.

Hurford, A.J., and Green, P.F., 1982, A users' guide to fission track dating calibration: Earth and Planetary Science Letters, v. 59, no. 2, p. 343–354, doi: 10.1016/0012-821X(82)90136-4.

Hurford, A.J., and Green, P.F., 1983, The zeta age calibration of fission-track dating: Chemical Geology, v. 41, p. 285–317, doi: 10.1016/S0009-2541(83)80026-6.

Hurley, P.M., 1952, Alpha ionization damage as a cause of low helium ratios: Eos, Transactions American Geophysical Union, v. 33, no. 2, p. 174–183.

Jackson, D.I., Jackson, A.A., Evans, D., Wingfield, R.T.R., Barnes, R.P., and Arthur, M.J., 1995, United Kingdom offshore regional report: the geology of the Irish Sea: British Geological Survey,.

Jaffey, A.H., Flynn, K.F., Glendenin, L.E., Bentley, W.C., and Essling, A.M., 1971, Precision Measurement of Half-Lives and Specific Activities of U 235 and U 238: Physical Review C, v. 4, no. 5, p. 1889–1906, doi: 10.1103/PhysRevC.4.1889.

Japsen, P., 2000, Investigation of multi-phase erosion using reconstructed shale trends based on sonic data. Sole Pit axis, North Sea: Global and Planetary Change, v. 24, no. 3–4, p. 189–210, doi: 10.1016/S0921-8181(00)00008-4.

Japsen, P., Green, P.F., Nielsen, L.H., Rasmussen, E.S., and Bidstrup, T., 2007, Mesozoic–Cenozoic exhumation events in the eastern North Sea Basin: a multi-disciplinary study based on palaeothermal, palaeoburial, stratigraphic and seismic data: Basin Research, v. 19, no. 4, p. 451–490, doi: 10.1111/j.1365-2117.2007.00329.x.

Johnston, S., Dore, A.G., and Spencer, A.M., 2001, The Mesozoic evolution of the southern North Atlantic region and its relationship to basin development in the south Porcupine Basin, offshore Ireland: Geological Society, London, Special Publications, v. 188, no. 1, p. 237–263, doi: 10.1144/GSL.SP.2001.188.01.14.

Jones, S.M., and White, N., 2003, Shape and size of the starting Iceland plume swell: Earth and Planetary Science Letters, v. 216, no. 3, p. 271–282, doi: 10.1016/S0012-821X(03)00507-7.

Jones, S.M., White, N., Clarke, B.J., Rowley, E., and Gallagher, K., 2002, Present and past influence of the Iceland Plume on sedimentation: Geological Society, London, Special Publications, v. 196, no. 1, p. 13–25, doi: 10.1144/GSL.SP.2002.196.01.02.

Jones, S.M., White, N., and Lovell, B., 2001, Cenozoic and Cretaceous transient uplift in the Porcupine Basin and its relationship to a mantle plume: Geological Society, London, Special Publications, v. 188, no. 1, p. 345–360, doi: 10.1144/GSL.SP.2001.188.01.20.

Kamerling, P., 1979, The geology and hydrocarbon habitat of the Bristol Channel Basin: Journal of Petroleum Geology, v. 2, no. 1, p. 75–93.

Keen, C.E., Hall, B.R., and Sullivan, K.D., 1977, Mesozoic evolution of the Newfoundland Basin: Earth and Planetary Science Letters, v. 37, no. 2, p. 307–320, doi: 10.1016/0012-821X(77)90176-5.

Ketcham, R.A., 2005a, Forward and Inverse Modeling of Low-Temperature Thermochronometry Data: Reviews in Mineralogy and Geochemistry, v. 58, no. 1, p. 275–314, doi: 10.2138/rmg.2005.58.11.

Ketcham, R.A., 2005b, The role of crystallographic angle in characterizing and modeling apatite fission-track length data: Radiation Measurements, v. 39, no. 6, p. 595–601, doi: 10.1016/j.radmeas.2004.07.008.

Ketcham, R.A., Carter, A., Donelick, R.A., Barbarand, J., and Hurford, A.J., 2007a, Improved measurement of fission-track annealing in apatite using c-axis projection: American Mineralogist, v. 92, no. 5–6, p. 789–798.

Ketcham, R.A., Carter, A., Donelick, R.A., Barbarand, J., and Hurford, A.J., 2007b, Improved modeling of fission-track annealing in apatite: American Mineralogist, v. 92, no. 5–6, p. 799–810, doi: 10.2138/am.2007.2281.

Ketcham, R.A., Donelick, R.A., and Carlson, W.D., 1999, Variability of apatite fission-track annealing kinetics; III, Extrapolation to geological time scales: American Mineralogist, v. 84, no. 9, p. 1235–1255, doi: 10.2138/am-1999-0903.

Ketcham, R.A., Donelick, R.A., and Donelick, M.B., 2000, AFTSolve: A program for multi-kinetic modeling of apatite fission-track data: Geological Materials Research, v. 2, no. 1, p. 1–32.

Ketcham, R.A., Gautheron, C., and Tassan-Got, L., 2011, Accounting for long alpha-particle stopping distances in (U-Th-Sm)/He geochronology: Refinement of the baseline case: Geochimica et Cosmochimica Acta, v. 75, no. 24, p. 7779–7791, doi: 10.1016/j.gca.2011.10.011.

Kroner, U., and Romer, R.L., 2013, Two plates - Many subduction zones: The Variscan orogeny reconsidered: Gondwana Research, v. 24, no. 1, p. 298–329, doi: 10.1016/j.gr.2013.03.001.

Laslett, G.M., Gleadow, A.J.W., and Duddy, I.R., 1984, The relationship between fission track length and track density in apatite: Nuclear Tracks and Radiation Measurements (1982), v. 9, no. 1, p. 29–38, doi: 10.1016/0735-245X(84)90019-X.

Laslett, G.M., Green, P.F., Duddy, I.R., and Gleadow, A.J.W., 1987, Thermal annealing of fission tracks in apatite 2. A quantitative analysis: Chemical Geology: Isotope Geoscience section, v. 65, no. 1, p. 1–13, doi: 10.1016/0168-9622(87)90057-1.

Lawver, L.A., and Müller, R.D., 1994, Iceland hotspot track: Geology, v. 22, no. 4, p. 311–314, doi: 10.1130/0091-7613(1994)022<0311:IHT>2.3.CO;2.

Lederer, C.M., Hollander, J.M., and Perlman, I., 1967, Table of isotopes:

Lefort, J.-P., 1989, Basement Correlation Across the North Atlantic: Springer Science & Business Media.

Lewis, C., Green, P., Carter, A., and Hurford, A., 1992, Elevated K/T palaeotemperatures throughout Nortwest England: three kilometres of Tertiary erosion? Earth and Planetary Science Letters, v. 112, p. 131–145, doi: 10.1016/0012-821X(92)90012-K.

Lithgow-Bertelloni, C., and Silver, P.G., 1998, Dynamic topography, plate driving forces and the African superswell: Nature, v. 395, no. 6699, p. 269–272.

Mackay, L.M., Turner, J., Jones, S.M., and White, N.J., 2005, Cenozoic vertical motions in the Moray Firth Basin associated with initiation of the Iceland Plume: Tectonics, v. 24, no. 5, doi: 10.1029/2004TC001683.

Maclennan, J., and Lovell, B., 2002, Control of regional sea level by surface uplift and subsidence caused by magmatic underplating of Earth's crust: Geology, v. 30, no. 8, p. 675, doi: 10.1130/0091-7613(2002)030<0675:CORSLB>2.0.CO;2.

Maddox, S.J., Blow, R., and Hardman, M., 1995, Hydrocarbon prospectivity of the Central Irish Sea Basin with reference to Block 42/12, offshore Ireland: Geological Society, London, Special Publications, v. 93, no. 1, p. 59–77, doi: 10.1144/GSL.SP.1995.093.01.08.

Magara, K., 1976, Thickness of removed sedimentary-rocks, paleopore pressure, and paleotemperature, southwestern part of western Canada basin: AAPG Bulletin-American association of Petroleum Geologists, v. 60, no. 4, p. 554–565.

Maliva, R.G., and Dickson, J.A.D., 1997, Ulster White Limestone Formation (Upper Cretaceous) of Northern Ireland: effects of basalt loading on chalk diagenesis: Sedimentology, v. 44, no. 1, p. 105–112, doi: 10.1111/j.1365-3091.1997.tb00426.x.

Mark, C., Cogné, N., and Chew, D., 2016, Tracking exhumation and drainage divide migration of the western Alps: a test of the apatite U-Pb thermochronometer as a detrital provenance tool: GSA Bulletin, v. In

Press, no. X, p. 1–22, doi: 10.1130/B31351.1.

Matte, P., 1991, Accretionary history and crustal evolution of the Variscan belt in Western Europe: Tectonophysics, v. 196, no. 3–4, p. 309–337, doi: 10.1016/0040-1951(91)90328-P.

Matte, P., 2001, The Variscan collage and orogeny (480-290 Ma) and the tectonic definition of the Armorica microplate: a review: Terra Nova, v. 13, no. 2, p. 122–128, doi: 10.1046/j.1365-3121.2001.00327.x.

McCann, T., Pascal, C., Timmerman, M.J., Krzywiec, P., Lopez-Gomez, J., Wetzel, L., Krawczyk, C.M., Rieke, H., and Lamarche, J., 2006, Post-Variscan (end Carboniferous-Early Permian) basin evolution in Western and Central Europe: Geological Society, London, Memoirs, v. 32, no. 1, p. 355–388, doi: 10.1144/GSL.MEM.2006.032.01.22.

McCulloch, A.A., 1993, Apatite fission track results from Ireland and the Porcupine basin and their significance for the evolution of the North Atlantic: Marine and Petroleum Geology, v. 10, no. 6, p. 572–590, doi: 10.1016/0264-8172(93)90060-6.

McDonnell, A., and Shannon, P.M., 2001, Comparative Tertiary stratigraphic evolution of the Porcupine and Rockall basins: Geological Society, London, Special Publications, v. 188, no. 1, p. 323–344, doi: 10.1144/GSL.SP.2001.188.01.19.

McDowell, F.W., McIntosh, W.C., and Farley, K.A., 2005, A precise 40Ar–39Ar reference age for the Durango apatite (U–Th)/He and fission-track dating standard: Chemical Geology, v. 214, no. 3–4, p. 249–263, doi: 10.1016/j.chemgeo.2004.10.002.

McHone, J.G., 2000, Non-plume magmatism and rifting during the opening of the central Atlantic Ocean: Tectonophysics, v. 316, no. 3–4, p. 287–296, doi: 10.1016/S0040-1951(99)00260-7.

McKenzie, D., 1984, A possible mechanism for epeirogenic uplift: Nature, v. 307, no. 5952, p. 616–618, doi: 10.1038/307616a0.

McKenzie, D., 1978, Some remarks on the development of sedimentary basins: Earth and Planetary Science Letters, v. 40, no. 1, p. 25–32, doi: 10.1016/0012-821X(78)90071-7.

McKerrow, W.S., MAC Niocaill, C., and Dewey, J.F., 2000, The Caledonian Orogeny redefined: Journal of the Geological Society, v. 157, no. 6, p.

1149–1154, doi: 10.1144/jgs.157.6.1149.

McQuillin, R., Donato, J., and Tulstrup, J., 1982, Development of basins in the Inner Moray Firth and the North Sea by crustal extension and dextral displacement of the Great Glen Fault: Earth and Planetary Science Letters, v. 60, no. 1, p. 127–139, doi: 10.1016/0012-821X(82)90028-0.

Meesters, A.G.C.A., and Dunai, T.J., 2005, A noniterative solution of the (U-Th)/He age equation: Geochemistry, Geophysics, Geosystems, v. 6, no. 4, p. 4–6, doi: 10.1029/2004GC000834.

Meesters, A.G.C.A., and Dunai, T.J., 2002a, Solving the production–diffusion equation for finite diffusion domains of various shapes Part II. Application to cases with α-ejection and nonhomogeneous distribution of the source: Chemical Geology, v. 186, no. 1–2, p. 57–73, doi: 10.1016/S0009-2541(01)00423-5.

Meesters, A.G.C.A., and Dunai, T.J., 2002b, Solving the production – diffusion equation for finite diffusion domains of various shapes Part I . Implications for low-temperature (U-Th)/He thermochronology: Chemical Geology, v. 186, p. 333–344, doi: 10.1016/S0009-2541(01)00422-3.

Mitchell, I., 2004, The Geology of Northern Ireland: Our Natural Foundation:

Moore, J.G., 1992, A syn-rift to post-rift transition sequence in the Main Porcupine Basin, offshore western Ireland: Geological Society, London, Special Publications, v. 62, no. 1, p. 333–349, doi: 10.1144/GSL.SP.1992.062.01.26.

Moore, A., Blenkinsop, T., and Cotterill, F. (Woody), 2008, Controls on post-Gondwana alkaline volcanism in Southern Africa: Earth and Planetary Science Letters, v. 268, no. 1–2, p. 151–164, doi: 10.1016/j.epsl.2008.01.007.

Morgan, W.J., 1972, Deep mantle convection plumes and plate motions: AAPG bulletin, v. 56, no. 2, p. 203–213.

Morton, A.C., 1982, Heavy minerals of Hampshire Basin Palaeogene strata: Geological Magazine, v. 119, no. 5, p. 463, doi: 10.1017/S0016756800026819.

Morton, A.C., and Hallsworth, C.R., 1999, Processes controlling the composition of heavy mineral assemblages in sandstones: Sedimentary Geology, v. 124, no. 1, p. 3–29.

Mosar, J., Lewis, G., and Torsvik, T., 2002, North Atlantic sea-floor spreading rates: implications for the Tertiary development of inversion structures of the Norwegian-Greenland Sea: Journal of the Geological Society, v. 159, no. 5, p. 503–515, doi: 10.1144/0016-764901-093.

Mudge, D.C., and Jones, S.M., 2004, Palaeocene uplift and subsidence events in the Scotland-Shetland and North Sea region and their relationship to the Iceland Plume: Journal of the Geological Society, v. 161, no. 3, p. 381–386, doi: 10.1144/0016-764903-038.

Murdoch, L.M., Musgrove, F.W., and Perry, J.S., 1995, Tertiary uplift and inversion history in the North Celtic Sea Basin and its influence on source rock maturity: Geological Society, London, Special Publications, v. 93, no. 1, p. 297–319.

Murphy, F.C., Anderson, T.B., Daly, J.S., Gallagher, V., Graham, J.R., Harper, D.A.T., Johnston, J.D., Kennan, P.S., Kennedy, M.J., Long, C.B., Morris, J.H., O'Keeffe, W.G., Parkes, M., Ryan, P.D., et al., 1991, An Appraisal of Caledonian Suspect Terranes in Ireland: Irish Journal of Earth Sciences, v. 11, no. 1, p. 11–41.

Nance, R.D., Gutiérrez-Alonso, G., Keppie, J.D., Linnemann, U., Murphy, J.B., Quesada, C., Strachan, R.A., and Woodcock, N.H., 2010, Evolution of the Rheic Ocean: Gondwana Research, v. 17, no. 2–3, p. 194–222, doi: 10.1016/j.gr.2009.08.001.

Naylor, D., Haughey, N., Clayton, G., and Graham, J.R., 1993, The Kish Bank Basin, offshore Ireland, *in* Petroleum Geology of Northwest Europe: Proceedings of the 4th Conference, Geological Society of London, p. 845–855.

Naylor, D., and Shannon, P.M., 2005, Petroleum Geology: North-West Europe and Global Perspectives – Proceedings of the 6th Petroleum Geology Conference: Geological Society of London.

Nielsen, S.B., Paulsen, G.E., Hansen, D.L., Gemmer, L., Clausen, O.R., Jacobsen, B.H., Balling, N., Huuse, M., and Gallagher, K., 2002, Paleocene initiation of Cenozoic uplift in Norway: Geological Society, London, Special Publications, v. 196, no. 1, p. 45–65, doi: 10.1144/GSL.SP.2002.196.01.04.

Nielsen, S.B., Stephenson, R., and Thomsen, E., 2007, Dynamics of Mid-

Palaeocene North Atlantic rifting linked with European intra-plate deformations.: Nature, v. 450, no. 7172, p. 1071–1074, doi: 10.1038/nature06379.

Nürnberg, D., and Müller, R.D., 1991, The tectonic evolution of the South Atlantic from Late Jurassic to present: Tectonophysics, v. 191, no. 1–2, p. 27–53, doi: 10.1016/0040-1951(91)90231-G.

O'Sullivan, P.B., and Parrish, R.R., 1995, The importance of apatite composition and single-grain ages when interpreting fission track data from plutonic rocks: a case study from the Coast Ranges, British Columbia: Earth and Planetary Science Letters, v. 132, no. 1, p. 213–224.

Paton, C., Hellstrom, J., Paul, B., Woodhead, J., Hergt, J., Kosler, J., Fonneland, H., Sylvester, P., Tubrett, M., Pedersen, R., Jackson, S.E., Pearson, N.J., Griffin, W.L., Belousova, E.A., et al., 2011, Iolite: Freeware for the visualisation and processing of mass spectrometric data: Journal of Analytical Atomic Spectrometry, v. 26, no. 12, p. 2508, doi: 10.1039/c1ja10172b.

Paul, T.A., and Fitzgerald, P.G., 1992, Transmission electron microscopic investigation of fission tracks in fluorapatite: American Mineralogist, v. 77, p. 336–344.

Peacock, D.C.P., 2004, The post-Variscan development of the British Isles within a regional transfer zone influenced by orogenesis: Journal of Structural Geology, v. 26, no. 12, p. 2225–2231, doi: http://dx.doi.org/10.1016/j.jsg.2004.05.005.

Persano, C., Barfod, D.N., Stuart, F.M., and Bishop, P., 2007, Constraints on early Cenozoic underplating-driven uplift and denudation of western Scotland from low temperature thermochronometry: Earth and Planetary Science Letters, v. 263, no. 3–4, p. 404–419, doi: 10.1016/j.epsl.2007.09.016.

Petrus, J.A., and Kamber, B.S., 2012, VizualAge: A Novel Approach to Laser Ablation ICP-MS U-Pb Geochronology Data Reduction: Geostandards and Geoanalytical Research, v. 36, no. 3, p. 247–270, doi: 10.1111/j.1751-908X.2012.00158.x.

Praeg, D., Stoker, M.S., Shannon, P.M., Ceramicola, S., Hjelstuen, B., Laberg, J.S., and Mathiesen, A., 2005, Episodic Cenozoic tectonism and the

development of the NW European "passive" continental margin: Marine and Petroleum Geology, v. 22, no. 9–10, p. 1007–1030, doi: 10.1016/j.marpetgeo.2005.03.014.

Quinn, D., Meere, P.A., and Wartho, J.-A., 2005, A chronology of foreland deformation: ultra-violet laser 40Ar/39Ar dating of syn/late-orogenic intrusions from the Variscides of southwest Ireland: Journal of Structural Geology, v. 27, no. 8, p. 1413–1425, doi: 10.1016/j.jsg.2005.02.003.

Ravenhurst, C., Roden, M.K., Willett, S.D., and Miller, D.S., 1992, Dependence of fission track annealing on apatite crystal chemistry. 7th Int, *in* Workshop Fission-Track Thermochronology, Philadelphia,.

Redfield, T.F., 2010, On apatite fission track dating and the Tertiary evolution of West Greenland topography: Journal of the Geological Society, v. 167, no. 2, p. 261–271, doi: 10.1144/0016-76492009-036.

Reiners, P.W., 2005, Past, Present, and Future of Thermochronology: Reviews in Mineralogy and Geochemistry, v. 58, no. 1, p. 1–18, doi: 10.2138/rmg.2005.58.1.

Reiners, P.W., and Farley, K.A., 2001, Influence of crystal size on apatite (U-Th)/He thermochronology: An example from the Bighorn Mountains, Wyoming: Earth and Planetary Science Letters, v. 188, p. 413–420, doi: 10.1016/S0012-821X(01)00341-7.

Richmond, L.K., and Williams, B.P.J., 2015, A new terrane in the Old Red Sandstone of the Dingle Peninsula, SW Ireland: Geological Society, London, Special Publications, v. 180, no. 1, p. 147–183, doi: 10.1144/GSL.SP.2000.180.01.09.

Rickers, F., Fichtner, A., and Trampert, J., 2013, The Iceland-Jan Mayen plume system and its impact on mantle dynamics in the North Atlantic region: Evidence from full-waveform inversion: Earth and Planetary Science Letters, v. 367, p. 39–51, doi: 10.1016/j.epsl.2013.02.022.

Ritchie, J.D., Gatliff, R.W., and Richards, P.C., 1999, Early Tertiary magmatism in the offshore NW UK margin and surrounds (A. J. Fleet & S. A. R. Boldy, Eds.): Geological Society, London.

Roberts, J.H., Gold, R., and Armani, R.J., 1968, Spontaneous-Fission Decay Constant of U 238: Physical Review, v. 174, no. 4, p. 1482–1484, doi: 10.1103/PhysRev.174.1482.

Robinson, K.W., Shannon, P.M., and Young, D.G.G., 1981, The Fastnet Basin: an integrated analysis: Petroleum Geology of the Continental Shelf of North-West Europe, Heyden, London, p. 432–444.

Rogers, N., van Staal, C.R., McNicoll, V., Pollock, J., Zagorevski, A., and Whalen, J., 2006, Neoproterozoic and Cambrian arc magmatism along the eastern margin of the Victoria Lake Supergroup: A remnant of Ganderian basement in central Newfoundland? Precambrian Research, v. 147, no. 3, p. 320–341, doi: 10.1016/j.precamres.2006.01.025.

Rowley, E., and White, N., 1998, Inverse modelling of extension and denudation in the East Irish Sea and surrounding areas: Earth and Planetary Science Letters, v. 161, no. 1–4, p. 57–71, doi: 10.1016/S0012-821X(98)00137-X.

Rutherford, E., 1905, Present problems in radioactivity: Popular Science Monthly, p. 1–34.

Ryan, M.C., Helland-Hansen, W., Johannessen, E.P., and Steel, R.J., 2009, Erosional vs. accretionary shelf margins: The influence of margin type on deepwater sedimentation: An example from the Porcupine Basin, offshore western Ireland: Basin Research, v. 21, no. 5, p. 676–703, doi: 10.1111/j.1365-2117.2009.00424.x.

Schoene, B., 2013, U-Th-Pb Geochronology:

Schoene, B., and Bowring, S.A., 2007, Determining accurate temperature–time paths from U–Pb thermochronology: An example from the Kaapvaal craton, southern Africa: Geochimica et Cosmochimica Acta, v. 71, no. 1, p. 165–185, doi: 10.1016/j.gca.2006.08.029.

Scotese, C.R., and Langford, R.P., 1995, Pangea and the Paleogeography of the Permian, *in* Scholle, P.A., Peryt, T.M., and Ulmer-Scholle, D.S. eds., The Permian of Northern Pangea Paleogeography, Paleoclimates, Stratigraphy, Volume 1, Springer Berlin Heidelberg, Berlin, Heidelberg, p. 3–19.

Scotese, C.R., and McKerrow, W.S., 1990, Revised World maps and introduction: Geological Society, London, Memoirs, v. 12, no. 1, p. 1–21, doi: 10.1144/GSL.MEM.1990.012.01.01.

Seranne, M., 1992, Devonian extensional tectonics versus Carboniferous inversion in the northern Orcadian basin: Journal of the Geological Society,

v. 149, no. 1, p. 27–37, doi: 10.1144/gsjgs.149.1.0027.

Shannon, P.M., 1992, Early Tertiary submarine fan deposits in the Porcupine Basin, offshore Ireland: Geological Society, London, Special Publications , v. 62, no. 1, p. 351–373, doi: 10.1144/GSL.SP.1992.062.01.27.

Shannon, P.M., Jacob, A.W.B., O'Reilly, B.M., Hauser, F., Readman, P.W., and Makris, J., 1999, Structural setting, geological development and basin modelling in the Rockal Trough, *in* Fleet, A.J. and Boldy, S.A.R. eds., Petroleum Geology of Northwest Europe: Proceedings of the 5th Conference, Geological Society of London, London, p. 421–431.

Shannon, P.M., and Naylor, D., 1998, An Assessment of Irish Offshore Basins and Petroleum Plays: Journal of Petroleum Geology, v. 21, no. April, p. 125–152, doi: 10.1306/BF9AB7A1-0EB6-11D7-8643000102C1865D.

Shuster, D.L., and Farley, K.A., 2009, The influence of artificial radiation damage and thermal annealing on helium diffusion kinetics in apatite: Geochimica et Cosmochimica Acta, v. 73, no. 1, p. 183–196, doi: 10.1016/j.gca.2008.10.013.

Shuster, D.L., Flowers, R.M., and Farley, K.A., 2006, The influence of natural radiation damage on helium diffusion kinetics in apatite: Earth and Planetary Science Letters, v. 249, no. 3–4, p. 148–161, doi: 10.1016/j.epsl.2006.07.028.

Simms, M.J., 2009, Permian and Mesozoic, *in* Holland, C.H. and Sander, I.S. eds., The Geology of Ireland, Dunedin Academic Press, Edinburgh, p. 311–332.

Simms, M.J., and Boulter, M.C., 2000, Oligocene cave sediments in Co. Cork: implications for reconstructing the Tertiary landscape of southwest Ireland: Proceedings of the Geologists' Association, v. 111, no. 4, p. 363–372, doi: 10.1016/S0016-7878(00)80092-9.

Sleep, N.H., 1990, Hotspots and mantle plumes: Some phenomenology: Journal of Geophysical Research, v. 95, no. B5, p. 6715, doi: 10.1029/JB095iB05p06715.

Soper, N.J., Strachan, R.A., Holdsworth, R.E., Gayer, R.A., and Greiling, R.O., 1992, Sinistral transpression and the Silurian closure of Iapetus: Journal of the Geological Society, v. 149, no. 6, p. 871–880, doi: 10.1144/gsjgs.149.6.0871.

Spiegel, C., Kohn, B., Belton, D., Berner, Z., and Gleadow, A., 2009, Apatite (U–Th–Sm)/He thermochronology of rapidly cooled samples: The effect of He implantation: Earth and Planetary Science Letters, v. 285, no. 1–2, p. 105–114, doi: 10.1016/j.epsl.2009.05.045.

Spiegel, C., Kohn, B., Raza, A., Rainer, T., and Gleadow, A., 2007, The effect of long-term low-temperature exposure on apatite fission track stability: A natural annealing experiment in the deep ocean: Geochimica et Cosmochimica Acta, v. 71, no. 18, p. 4512–4537, doi: 10.1016/j.gca.2007.06.060.

Stach, E., Mackowsky, M.T.H., Teichmüller, M., Taylor, G.H., Chandra, D., and Teichmüller, R., 1982, Stach's Textbook of Coal Petrology: Berlin.

Steiger, R.H., and Jäger, E., 1977, Subcommission on geochronology: Convention on the use of decay constants in geo- and cosmochronology: Earth and Planetary Science Letters, v. 36, no. 3, p. 359–362, doi: 10.1016/0012-821X(77)90060-7.

Stoker, M.S., Holford, S.P., Hillis, R.R., Green, P.F., and Duddy, I.R., 2010, Cenozoic post-rift sedimentation off northwest Britain: Recording the detritus of episodic uplift on a passive continental margin: Geology, v. 38, no. 7, p. 595–598, doi: 10.1130/g30881.1.

Stoker, M.S., Hoult, R.J., Nielsen, T., Hjelstuen, B.O., Laberg, J.S., Shannon, P.M., Praeg, D., Mathiesen, A., van Weering, T.C.E., and McDonnell, A., 2005a, Sedimentary and oceanographic responses to early Neogene compression on the NW European margin: Marine and Petroleum Geology, v. 22, no. 9–10, p. 1031–1044, doi: 10.1016/j.marpetgeo.2005.01.009.

Stoker, M.S., Praeg, D., Hjelstuen, B.O., Laberg, J.S., Nielsen, T., and Shannon, P.M., 2005b, Neogene stratigraphy and the sedimentary and oceanographic development of the NW European Atlantic margin: Marine and Petroleum Geology, v. 22, no. 9–10, p. 977–1005, doi: 10.1016/j.marpetgeo.2004.11.007.

Stolfova, K., and Shannon, P.M., 2009, Permo-Triassic development from Ireland to Norway: basin architecture and regional controls: Geological Journal, v. 44, no. 6, p. 652–676, doi: 10.1002/gj.1187.

Stuart, F.M., Ellam, R.M., Harrop, P.J., Fitton, J.G., and Bell, B.R., 2000, Constraints on mantle plumes from the helium isotopic composition of

basalts from the British Tertiary Igneous Province: Earth and Planetary Science Letters, v. 177, no. 3–4, p. 273–285, doi: 10.1016/S0012-821X(00)00050-9.

Tappin, D.R., Chadwick, R.A., Jackson, A.A., Wingfield, R.T.R., and Smith, N.J.P., 1994, The geology of Cardigan Bay and the Bristol Channel: HMSO, London.

Thigpen, J.R., Law, R.D., Loehn, C.L., Strachan, R.A., Tracy, R.J., Lloyd, G.E., Roth, B.L., and Brown, S.J., 2013, Thermal structure and tectonic evolution of the Scandian orogenic wedge, Scottish Caledonides: integrating geothermometry, deformation temperatures and conceptual kinematic-thermal models: Journal of Metamorphic Geology, v. 31, no. 8, p. 813–842, doi: 10.1111/jmg.12046.

Thomas, D.W., and Coward, M.P., 1995, Late Jurassic-Early Cretaceous inversion of the northern East Shetland Basin, northern North Sea: Geological Society, London, Special Publications, v. 88, no. 1, p. 275–306, doi: 10.1144/GSL.SP.1995.088.01.16.

Thomson, S.N., Gehrels, G.E., Ruiz, J., and Buchwaldt, R., 2012, Routine low-damage apatite U-Pb dating using laser ablation-multicollector-ICPMS: Geochemistry, Geophysics, Geosystems, v. 13, no. 2, doi: 10.1029/2011GC003928.

Thorpe, R.S., Tindle, A.G., and Gledhill, A., 1990, The petrology and origin of the Tertiary Lundy granite (Bristol Channel, UK): Journal of Petrology, v. 31, no. 6, p. 1379–1406.

Tiley, R., White, N., and Al-Kindi, S., 2004, Linking Paleogene denudation and magmatic underplating beneath the British Isles: Geological Magazine, v. 141, no. 3, p. 345–351, doi: 10.1017/S0016756804009197.

Tomlinson, J.P., Denton, P., Maguire, P.K.H., and Booth, D.C., 2006, Analysis of the crustal velocity structure of the British Isles using teleseismic receiver functions: Geophysical Journal International, v. 167, no. 1, p. 223–237, doi: 10.1111/j.1365-246X.2006.03044.x.

Torsvik, T.H., and Rehnström, E.F., 2003, The Tornquist Sea and Baltica-Avalonia docking: Tectonophysics, v. 362, no. 1–4, p. 67–82, doi: 10.1016/S0040-1951(02)00631-5.

Turner, J.P., Green, P.F., Holford, S.P., and Lawrence, S.R., 2008, Thermal

history of the Rio Muni (West Africa)–NE Brazil margins during continental breakup: Earth and Planetary Science Letters, v. 270, no. 3–4, p. 354–367, doi: 10.1016/j.epsl.2008.04.002.

Tyrrell, S., Haughton, P.D.W., and Daly, J.S., 2007, Drainage reorganization during breakup of Pangea revealed by in-situ Pb isotopic analysis of detrital K-feldspar: Geology, v. 35, no. 11, p. 971, doi: 10.1130/G4123A.1.

Unrug, R., Harańczyk, C., and Chocyk-Jamińska, M., 1999, Easternmost Avalonian and Armorican–Cadomian terranes of central Europe and Caledonian–Variscan evolution of the polydeformed Kraków mobile belt: geological constraints: Tectonophysics, v. 302, no. 1–2, p. 133–157, doi: 10.1016/S0040-1951(98)00278-9.

Vrolijk, P., Donelick, R.A., Queng, J., and Cloos, M., 1992, Testing models of fission track annealing in apatite in a simple thermal setting: site 800, leg 129, *in* Proceedings of the Ocean Drilling Program, Scientific Results, Ocean Drilling Program College Station, TX, p. 169–176.

Wagner, G.A., 1979, Correction and interpretation of fission track ages, *in* Lectures in Isotope Geology, Springer, p. 170–177.

Wagner, G.A., 1968, Fission track dating of apatites: Earth and Planetary Science Letters, v. 4, no. 5, p. 411–415, doi: 10.1016/0012-821X(68)90072-1.

Wagner, G.A., and Van den Haute, P., 1992, Fission-track Dating: Kluwer Academic Publishers, Dordrecht.

Waldron, J.W.F., Schofield, D.I., Brendan Murphy, J., and Thomas, C.W., 2014a, How was the iapetus ocean infected with subduction? Geology, v. 42, no. 12, p. 1095–1098, doi: 10.1130/G36194.1.

Waldron, J.W.F., Schofield, D.I., Dufrane, S.A., Floyd, J.D., Crowley, Q.G., Simonetti, A., Dokken, R.J., and Pothier, H.D., 2014b, Ganderia–Laurentia collision in the Caledonides of Great Britain and Ireland: Journal of the Geological Society, v. 171, no. 4, p. 555–569, doi: 10.1144/jgs2013-131.

Walker, G.P.L., 1995, Flood basalts versus central volcanoes and the British Tertiary volcanic Province: Geological Society, London, Memoirs, v. 16, no. 1, p. 195–202, doi: 10.1144/GSL.MEM.1995.016.01.20.

Walsh, A., Knag, G., Morris, M., Quinquis, H., Tricker, P., Bird, C., and Bower, S., 1999, Petroleum geology of the Irish Rockall Trough – a frontier

challenge, *in* Fleet, A.J. and Boldy, S.A.R. eds., Petroleum Geology of Northwest Europe: Proceedings of the 5th Conference, Geological Society of London, London, p. 433–444.

Watts, W.A., 1957, A Tertiary deposit in county Tipperary: Scientific Proceedings of the Royal Dublin Society, v. 27, p. 308–311.

Welch, M.J., and Turner, J.P., 2000a, Triassic-Jurassic development of the St. George's Channel basin offshore Wales, UK: Marine and Petroleum Geology, v. 17, no. 6, p. 723–750, doi: 10.1016/S0264-8172(00)00017-9.

Welch, M.J., and Turner, J.P., 2000b, Triassic–Jurassic development of the St. George's Channel basin, offshore Wales, UK: Marine and Petroleum Geology, v. 17, no. 6, p. 723–750, doi: 10.1016/S0264-8172(00)00017-9.

Wellman, C.H., Thomas, R.G., Edwards, D., and Kenrick, P., 1998, The Cosheston Group (Lower Old Red Sandstone) in southwest Wales: age, correlation and palaeobotanical significance: Geological Magazine, v. 135, no. 3, p. 397–412.

White, N., and Lovell, B., 1997, Measuring the pulse of a plume with the sedimentary record: Nature, v. 4192, no. 1995, p. 1995–1998, doi: 10.1038/43151.

White, N.J., Mackay, L.M., Jones, S.M., Lovell, J.P.B., and Davis, M.W., 2013, Reply to comment by Hillis et al. (2013): Geophysical Journal International, v. 194, no. 2, p. 680–682, doi: 10.1093/gji/ggt132.

White, R., and McKenzie, D., 1989, Magmatism at rift zones: The generation of volcanic continental margins and flood basalts: Journal of Geophysical Research, v. 94, no. B6, p. 7685, doi: 10.1029/JB094iB06p07685.

Whitehouse, M.J., Claesson, S., Sunde, T., and Vestin, J., 1997, Ion microprobe U□Pb zircon geochronology and correlation of Archaean gneisses from the Lewisian Complex of Gruinard Bay, northwestern Scotland: Geochimica et Cosmochimica Acta, v. 61, no. 20, p. 4429–4438, doi: 10.1016/S0016-7037(97)00251-2.

Williams, G.A., Turner, J.P., and Holford, S.P., 2005, Inversion and exhumation of the St. George's Channel basin, offshore Wales, UK: Journal of the Geological Society, v. 162, no. 1, p. 97–110, doi: 10.1144/0016-764904-023.

Wolf, R.A., Farley, K.A., and Kass, D.M., 1998, Modeling of the temperature

sensitivity of the apatite (U – Th)/He thermochronometer: Chemical Geology, , no. 148, p. 105–114.

Wolf, R.A., Farley, K.A., and Silver, L.T., 1996, Helium diffusion and low-temperature thermochronometry of apatite: Geochimica et Cosmochimica Acta, v. 60, no. 21, p. 4231–4240, doi: 10.1016/S0016-7037(96)00192-5.

Woodcock, N.H., Soper, N.J., and Strachan, R.A., 2007, A Rheic cause for the Acadian deformation in Europe: Journal of the Geological Society, v. 164, no. 5, p. 1023–1036, doi: 10.1144/0016-76492006-129.

Woodcock, N., and Strachan, R. (Eds.), 2012, Geological History of Britain and Ireland: John Wiley & Sons, Ltd, Chichester, UK.

Woodland, A.W., 1971, The Llanbedr (Mochras Farm) Borehole: HM Stationery Office.

Yates, F., 1934, Contingency Tables Involving Small Numbers and the χ2 Test: Supplement to the Journal of the Royal Statistical Society, v. 1, no. 2, p. 217, doi: 10.2307/2983604.

Young, E.J., Myers, A.T., Munson, E.L., and Conklin, N.M., 1969, Mineralogy and geochemistry of fluorapatite from Cerro de Mercado, Durango, Mexico: US Geological Survey Professional Paper, v. 650, no. D, p. D84–D93.

Zeigler, J.F., 1977, Helium stopping powers and ranges in all elemental matter:

Zeitler, P.K., Herczeg, A.L., McDougall, I., and Honda, M., 1987, U-Th-He dating of apatite: A potential thermochronometer: Geochimica et Cosmochimica Acta, v. 51, no. 10, p. 2865–2868, doi: 10.1016/0016-7037(87)90164-5.

Ziegler, P.A., 1989, Evolution of the North Atlantic—an overview: American Association of Petroleum Geologists Memoir, v. 46, p. 111–129.

Ziegler, P.A., Cloetingh, S., and van Wees, J.-D., 1995, Dynamics of intra-plate compressional deformation: the Alpine foreland and other examples: Tectonophysics, v. 252, no. 1–4, p. 7–59, doi: 10.1016/0040-1951(95)00102-6.

Ziegler, P.A., and Dezes, P., 2006, Crustal evolution of Western and Central Europe: Geological Society, London, Memoirs, v. 32, no. 1, p. 43–56, doi: 10.1144/GSL.MEM.2006.032.01.03.

Ziegler, P.A., and Stampfli, G.M., 2001, Late Paleozoic Early Mesozoic plate boundary reorganisation : collapse of the Variscan orogen and opening of

Neotethys: Natura Bresciana, v. 25, p. 17–34.

Zoback, M. Lou, 1992, First- and second-order patterns of stress in the lithosphere: The World Stress Map Project: Journal of Geophysical Research, v. 97, no. B8, p. 11703, doi: 10.1029/92JB00132.

13. Appendix

The full data appendix is available from the CD included with this thesis, and can also be downloaded from http://www.tara.tcd.ie/.